JPL Quarterly Technical Review

Volume 1 January 1972 Number 4

Papers on:

Atmospheric Entry
Orbits and Trajectories
Planetary Atmospheres
Propulsion
Structural Engineering
Telecommunications

Abstracts of:

Technical Reports
Technical Memorandums
JPL Quarterly Technical Review
Open Literature Reporting

Jet Propulsion Laboratory/California Institute of Technology

JPL Quarterly Technical Review

Volume 1 January 1972 Number 4

Contents

Bibliography of Current Reporting

N72-17888

JPL Quarterly Technical Review Volume 1, Number 4 January 1972

Nonstationary Envelope Process and First Excursion Probability

J.-N. Yang

Engineering Mechanics Division

A definition of the envelope of nonstationary random processes is proposed. The establishment of the envelope definition makes it possible to simulate the nonstationary random envelope directly. The envelope statistics, such as the density function, the joint density function, the moment function, and the level crossing rate, relevant to the analyses of the catastrophic failure, fatigue, and crack propagation of structures, are derived. Applications of the envelope statistics to the prediction of structural reliability under random loadings are demonstrated in detail.

Introduction

It is well known that loadings to structures, such as earthquakes, oceanographical wave forces, strong gust loadings, aircraft impact loadings during landing, spacecraft excitations resulting from booster engine ignition or shutdown, etc., are nonstationary random processes. Because of the relative severity of such random excitations, the prediction of structural safety or failure becomes an important task of structural analysis, design, and test.

In stationary random vibration, the envelope process plays an important role in the prediction of the catastrophic failure (e.g., References 1 and 2) fatigue failure, and crack propagation (e.g., Reference 3). Similarly, the nonstationary envelope process is expected to have important application to the prediction of structural failure under nonstationary random excitations.

The purpose of this article is (1) to establish a definition of the envelope of nonstationary random processes so that the nonstationary random envelope processes can be simulated efficiently with the aid of a digital computer, and (2) to derive relevant envelope statistics useful in the prediction of structural reliability.

The definition of stationary random envelope proposed by Rice (Reference 4) and Cramer and Leadbetter (Reference 5) is extended herein to the envelope of nonstationary random processes possessing evolutionary power

spectral densities (e.g., References 6 and 7). The establishment of the nonstationary random envelope makes it possible to simulate the envelope, peaks, and troughs of a nonstationary random process directly (Reference 8). Statistics of envelope processes, such as the density function, the joint density function, the moment function, and the upcrossing rate of a barrier level, relevant to the analyses of the catastrophic failure probability, fatigue, and crack propagation, are derived. On the basis of these envelope statistics, approximate solutions to the first excursion probability are obtained.

Sample functions of the structural response and envelope to strong gust loadings or earthquake excitation are simulated, and applications to the prediction of structural reliability are demonstrated in detail.

Nonstationary Envelope Processes

Consider a real nonstationary gaussian random process $X(t)$ with mean zero and an evolutionary power spectral density. Then, $X(t)$ has a spectral representation:

$$X(t) = \int_{-\infty}^{\infty} A(t, \omega) e^{-i\omega t} d\bar{X}(\omega) \tag{1}$$

where $A(t,\omega)$ is a deterministic function of time t and frequency ω, called the oscillatory function. $d\bar{X}(\omega)$ is an orthogonal random process with mean zero and

$$\left.\begin{aligned} E\,[d\bar{X}(\omega_1) d\bar{X}^*(\omega_2)] &= 0, \quad \omega_1 \neq \omega_2 \\ E\,[|d\bar{X}(\omega)|^2] &= S(\omega)\, d\omega \end{aligned}\right\} \tag{2}$$

in which the asterisk denotes the complex conjugate; $S(\omega)$ is, in general, the power spectral density of a suitable stationary random process $\underline{X}(t)$,

$$\underline{X}(t) = \int_{-\infty}^{\infty} e^{-i\omega t} d\bar{X}(\omega) \tag{3}$$

where $e^{i\omega t} d\bar{X}(\omega)$ is the elementary oscillation of $\underline{X}(t)$. It is further assumed that $X(t) = 0$ for $t<0$ so that $A(t,\omega) = 0$ for $t<0$.

Since $X(t)$ is a real process, the real value autocorrelation function $R_x(t_1,t_2)$ of $X(t_1)$ and $X(t_2)$ can be shown as

$$R_x(t_1, t_2) = \int_0^\infty |A(t_1, \omega)|\,|A(t_2, \omega)| \cos\,[\omega(t_1 - t_2) + \delta(t_1, \omega) - \delta(t_2, \omega)]\; G(\omega)d\omega \tag{4}$$

where $G(\omega)$ is the one-sided spectral density of $\underline{X}(t)$ (Equation 3), i.e., $G(\omega) = 2S(\omega)$ for $\omega > 0$, and

$$\delta(t, \omega) = \tan^{-1}\,[\mathrm{Im}A(t, \omega)/\mathrm{Re}A(t, \omega)] \tag{5}$$

in which $\mathrm{Im}A(t,\omega)$ and $\mathrm{Re}A(t,\omega)$ are the imaginary part and the real part of $A(t,\omega)$, respectively.

Furthermore, since $X(t)$ is real, Equation 1 can be written as (Reference 5)

$$X(t) = \int_0^\infty |A(t, \omega)| \left\{\cos\,[\omega t + \delta(t, \omega)]\; dU(\omega) + \sin\,[\omega t + \delta(t, \omega)]\; dV(\omega)\right\} \tag{6}$$

where $dU(\omega)$ and $dV(\omega)$ are real orthogonal processes with mean zero, and

$$E\,[dU(\omega)^2] = E\,[dV(\omega)^2] = G(\omega)d\omega \tag{7}$$

and $dU(\omega)$ and $dV(\omega)$ are mutually orthogonal.

Following Cramer and Leadbetter, the stationary random process $\underline{X}(t)$ (Equation 3) is passed through a filter with gain $g(\omega)$,

$$g(\omega) = \begin{cases} \underline{i}, & \omega < 0 \\ 0, & \omega = 0 \\ -\underline{i}, & \omega > 0 \end{cases} \tag{8}$$

to obtain a stationary process $\hat{\underline{X}}(t)$ with elementary oscillation $g(\omega)e^{i\omega t}d\bar{X}(\omega)$. Then, one forms the nonstationary random process $\hat{X}(t)$ as follows:

$$\hat{X}(t) = \int_{-\infty}^{\infty} A(t, \omega)g(\omega)e^{\underline{i}\omega t}d\bar{X}(\omega) \tag{9}$$

Since $X(t)$ is real, it follows from Equation 9 that $\hat{X}(t)$ is real, and it can be written as

$$\hat{X}(t) = \int_0^\infty |A(t, \omega)| \{\sin [\omega t + \delta(t, \omega)]\, dU(\omega) - \cos [\omega t + \delta(t, \omega)]\, dV(\omega)\} \tag{10}$$

The envelope $V(t)$ of $X(t)$ is defined as

$$V(t) = [X^2(t) + \hat{X}^2(t)]^{1/2} \tag{11}$$

where it is clear that

$$\left.\begin{aligned} V(t) &\geq |X(t)| \\ V(t) &= |X(t)|, \quad \text{when } \hat{X}(t) = 0 \end{aligned}\right\} \tag{12}$$

This definition of envelope (Equation 12) is originally due to Rice (Reference 4).

Equation 6 states that the nonstationary random process $X(t)$ is a superposition (in the frequency domain) at each time t of elementary components

$$|A(t, \omega)| \{\cos [\omega t + \delta(t, \omega)]\, dU(\omega) + \sin [\omega t + \delta(t, \omega)]\, dV(\omega)\} = F(t, \omega) \cos [\omega t + \delta(t, \omega) + \psi(\omega)]$$

while Equation 10 states that $X(t)$ is a superposition of elementary components

$$|A(t, \omega)| \{\sin [\omega t + \delta(t, \omega)]\, dU(\omega) - \cos [\omega t + \delta(t, \omega)]\, dV(\omega)\} = \Gamma(t, \omega) \sin [\omega t + \delta(t, \omega) + \psi(\omega)]$$

Therefore, the envelope definition in Equation 11 can be appreciated by noting that the elementary component of $X(t)$ is 90 deg out of phase with the elementary component of $\hat{X}(t)$ and

$$|\cos [\omega t + \delta(t, \omega) + \psi(\omega)]| = 1$$

whenever

$$\sin [\omega t + \delta(t, \omega) + \psi(\omega)] = 0$$

The autocorrelation function $R_{\hat{x}}(t_1,t_2)$ of $\hat{X}(t)$ (Equation 10) can easily be shown to be equal to the autocorrelation function $R_x(t_1,t_2)$ of $X(t)$ (Equation 4).

The correlation function $E[X(t_2)\hat{X}(t_1)]$ between $X(t_2)$ and $\hat{X}(t_1)$ can be shown as

$$E[X(t_2)\hat{X}(t_1)] = \int_0^\infty |A(t_1, \omega)|\,|A(t_2, \omega)| \sin [\omega(t_1 - t_2) + \delta(t_1, \omega) - \delta(t_2, \omega)]\, G(\omega) d\omega \tag{13}$$

Therefore, the covariance matrix Λ of $X(t_2)$, $\hat{X}(t_2)$, $X(t_1)$ and $\hat{X}(t_1)$ can be written as

$$\Lambda = \begin{bmatrix} (\sigma_2)^2 & 0 & \sigma_1\sigma_2\rho & \sigma_1\sigma_2\lambda \\ 0 & (\sigma_2)^2 & -\sigma_1\sigma_2\lambda & \sigma_1\sigma_2\rho \\ \sigma_1\sigma_2\rho & -\sigma_1\sigma_2\lambda & (\sigma_1)^2 & 0 \\ \sigma_1\sigma_2\lambda & \sigma_1\sigma_2\rho & 0 & (\sigma_1)^2 \end{bmatrix} \tag{14}$$

where $\sigma_1 = \sigma(t_1)$ and $\sigma_2 = \sigma(t_2)$ are the standard deviations of $X(t_1)$ and $X(t_2)$, respectively, and ρ and λ are nondimensional quantities as follows:

$$\left.\begin{aligned} \rho &= (\sigma_1)^{-1}(\sigma_2)^{-1} \int_0^\infty |A(t_1, \omega)|\,|A(t_2, \omega)|\, G(\omega) \cos [\omega(t_1 - t_2) + \delta(t_1, \omega) - \delta(t_2, \omega)]\, d\omega \\ \lambda &= (\sigma_1)^{-1}(\sigma_2)^{-1} \int_0^\infty |A(t_1, \omega)|\,|A(t_2, \omega)|\, G(\omega) \sin [\omega(t_1 - t_2) + \delta(t_1, \omega) - \delta(t_2, \omega)]\, d\omega \end{aligned}\right\} \tag{15}$$

With the aid of the definition of envelope given in Equation 11 and the covariance matrix Λ given in Equation 14, the probability density function $f_v(x;t_1)$ of $V(t_1)$ and the joint density function $f_{vv}(x,y;t_2,t_1)$ of $V(t_2)$ and $V(t_1)$ can be shown as

$$f_v(x;t_1) = [x/(\sigma_1)^2] \exp[-x^2/2(\sigma_1)^2] \tag{16}$$

$$f_{vv}(x,y;t_2,t_1) = \frac{xy}{(\sigma_1)^2(\sigma_2)^2(1-r^2)} I_0\left[\frac{xyr}{\sigma_1\sigma_2(1-r^2)}\right] \times \exp\left\{-\frac{x^2(\sigma_1)^2 + y^2(\sigma_2)^2}{2(\sigma_1)^2(\sigma_2)^2(1-r^2)}\right\} \tag{17}$$

where $I_0[D]$ is the zero-order modified Bessel function of the first kind and

$$r = [\rho^2 + \lambda^2]^{1/2} \tag{18}$$

The moment function of $V(t_1)$ and $V(t_2)$ can be shown as

$$E[V^v(t_1)V^\eta(t_2)] = [2(\sigma_1)^2]^{v/2}[2(\sigma_2)^2]^{\eta/2}\Gamma\left(1+\frac{v}{2}\right) \times \Gamma\left(1+\frac{\eta}{2}\right){}_2F_1\left(-\frac{v}{2},-\frac{\eta}{2};1;r^2\right) \tag{19}$$

where $\Gamma(\bullet)$ and ${}_2F_1(\bullet)$ denote the gamma function and the hypergeometric function, respectively.

Furthermore, the envelope crossing rate $N(t_1,\alpha)$ of a barrier level α at time t_1 can be shown as

$$N(t_1,\alpha) = \frac{\alpha\sqrt{\Delta}}{\sqrt{2\pi}(\sigma_1)^2} \exp\left[-\frac{\alpha^2[\Delta + C^2/4(\sigma_1)^2]}{2(\sigma_1)^2\Delta}\right]\left\{1 + \frac{\sqrt{\pi}C\alpha}{2\sqrt{2\Delta}(\sigma_1)^2} \times \exp\left[\frac{C^2\alpha^2}{8(\sigma_1)^4\Delta}\right]\operatorname{erf}\left[-\frac{C\alpha}{2\sqrt{2\Delta}(\sigma_1)^2}\right]\right\} \tag{20}$$

where

$$\left.\begin{aligned}
&\Delta = \bar{\lambda}_2 - [(\bar{\lambda}_1)^2/(\sigma_1)^2] - [C^2/4(\sigma_1)^2] - Q \\
&\bar{\lambda}_j = \int_0^\infty |A(t_1, \omega)|^2 G(\omega)(\omega + \delta')^j d\omega, \qquad j = 1, 2 \\
&\delta' = \partial\delta(t_1, \omega)/\partial t_1 \\
&C = 2\int_0^\infty [|A(t_1, \omega)|\, \partial|A(t_1, \omega)|/\partial t_1] G(\omega) d\omega = 2E[X(t_1)\dot{X}(t_1)] \\
&Q = \int_0^\infty [\partial|A(t_1, \omega)|/\partial t_1]^2 G(\omega) d\omega
\end{aligned}\right\} \quad (21)$$

When $A(t,\omega)$ is a slowly varying function of time t,

$$C^2/(\sigma_1)^2 \ll \Delta$$

$$Q \ll \Delta$$

$$\delta' \ll \omega$$

$$\Delta \simeq \bar{\lambda}_2 - [(\bar{\lambda}_1)^2/(\sigma_1)^2]$$

Therefore, Equation 20 becomes

$$N(t_1, \alpha) \simeq \frac{\alpha\sqrt{\Delta}}{\sqrt{2\pi}(\sigma_1)^2} \exp\,[-\alpha^2/2(\sigma_1)^2] \quad (22)$$

It can easily be shown that the nonstationary envelope process $V(t)$ defined in Equation 11 degenerates into the stationary envelope process of Cramer and Leadbetter (Reference 5) when $X(t)$ is stationary; in which case,

$$A(t, \omega) = 1$$

$$t_1 - t_2 = \tau$$

$$\sigma_1 = \sigma_2 = \sigma$$

$$\delta(t_1, \omega) = 0$$

and Equations 16, 17, 19, and 20 degenerate into the formulas associated with the stationary random processes.

Consider a linear time-invariant system characterized by an impulse response function $h(t)$, or by a frequency response function $H(\omega)$, under the

excitation $X(t)$ given in Equation 1. The response process $Y(t)$ can also be expressed as a spectral representation (e.g. Reference 7):

$$Y(t) = \int_{-\infty}^{\infty} M(t, \omega) e^{i\omega t} dX(\omega) \tag{23}$$

$$M(t, \omega) = \int_0^t h(\tau) A(t - \tau, \omega) e^{-i\omega\tau} d\tau \tag{24}$$

where the assumption has been made that the system is at rest initially.

Therefore, the envelope $V_y(t)$ of the response process $Y(t)$ is as follows:

$$V_y(t) = [Y^2(t) + \hat{Y}^2(t)]^{1/2} \tag{25}$$

in which $Y(t)$ and $\hat{Y}(t)$ are in the forms of Equations 6 and 10, respectively, with $A(t,\omega)$ replaced by $M(t,\omega)$.

First Excursion Probability and Numerical Example

The probability that the structural response exits the safe domain of performance for the first time within the time interval $[0,T]$ is called the first excursion probability. The first excursion probability of a structure under random loadings has received considerable attention among engineers because of its direct relation to the structural safe performance and design. We shall discuss here the applications of nonstationary envelope statistics derived previously to the prediction of the first excursion probability of structures under random disturbances.

Let $h(t,\alpha)$ be the failure rate at time t of a gaussian random structural response $X(t)$ with mean zero and threshold levels $\pm\alpha$. The first excursion probability $F(T,\alpha)$ of the structure within the time interval $[0,T]$ can be written as

$$F(T, \alpha) = 1 - \exp\left[-\int_0^T h(t, \alpha) dt\right] \tag{26}$$

The simplest approximation, called the Poisson approximation, assumes that the events of crossings of the threshold level are independent. Hence,

$$h(t, \alpha) \simeq 2\nu^+(t, \alpha) \tag{27}$$

in which $\nu^+(t,\alpha)$ is the upcrossing rate of the level α at time t by $X(t)$. The expression of $\nu^+(t,\alpha)$ has been given, for instance, in References 7 and 9.

Another approximation is to replace the upcrossing rate $\nu^+(t,\alpha)$ by the envelope crossing rate $N(t,\alpha)$ and assume that the events of envelope crossings are independent, i.e.,

$$h(t,\alpha) \simeq N(t,\alpha) \tag{28}$$

where $N(t,\alpha)$ is given by Equation 20 or 22.

The approximation obtained in Reference 10 can be generalized to the nonstationary random processes as follows:

$$h(t,\alpha) \simeq \nu^+(t,\alpha)\,\frac{1-\exp\left[-N(t,\alpha)/2\nu^+(t,\alpha)\right]}{1-\left[\nu^+(t,\alpha)/\nu^+(t,0)\right]} \tag{29}$$

Furthermore, the approximations based on the extreme point process (References 1 and 2) can also be generalized to the nonstationary random processes, since the joint density function (Equation 17) of the envelope process has been derived. It is noted that the establishment of nonstationary envelope statistics (Equation 17) sheds considerable light on the difficult problems of nonstationary first excursion probability. Further applications of envelope statistics based on the extreme point process (References 1 and 2) will be reported in the near future.

The structural response to strong gust loadings or earthquake excitations discussed in Reference 9 is considered here. Using the definition of envelope established previously (Equation 25) and the simulation method proposed in Reference 8, the structural response $X(t)$ and its envelope $V(t)$ are simulated on a digital computer. Sample functions of $X(t)$ and $V(t)$ are given in Figure 1. It is observed from Figure 1 that the envelope practically passes through all the peak values and the absolute values of all troughs of $X(t)$.

The first excursion probability based on (1) the independent level crossing (Equation 27) of $X(t)$, (2) the independent envelope crossing (Equation 28), and (3) the generalization of Reference 10 (Equation 29) are summarized in Table 1 and plotted in Figure 2. Previous results obtained in References 11 and 12 are also given in Figure 2 for the purpose of comparison.

It is observed from Table 1 that the approximation based on envelope crossing does produce a slight improvement over Equation 27 when the threshold level α is not too high. For the high threshold level, however, Equation 28 results in a worse approximation. This phenomenon is well known in the stationary random process when the average clump size is smaller than unity. It can be observed from Figure 2 that the approximation of Equation 29 gives results close to the simulation results (Reference 11).

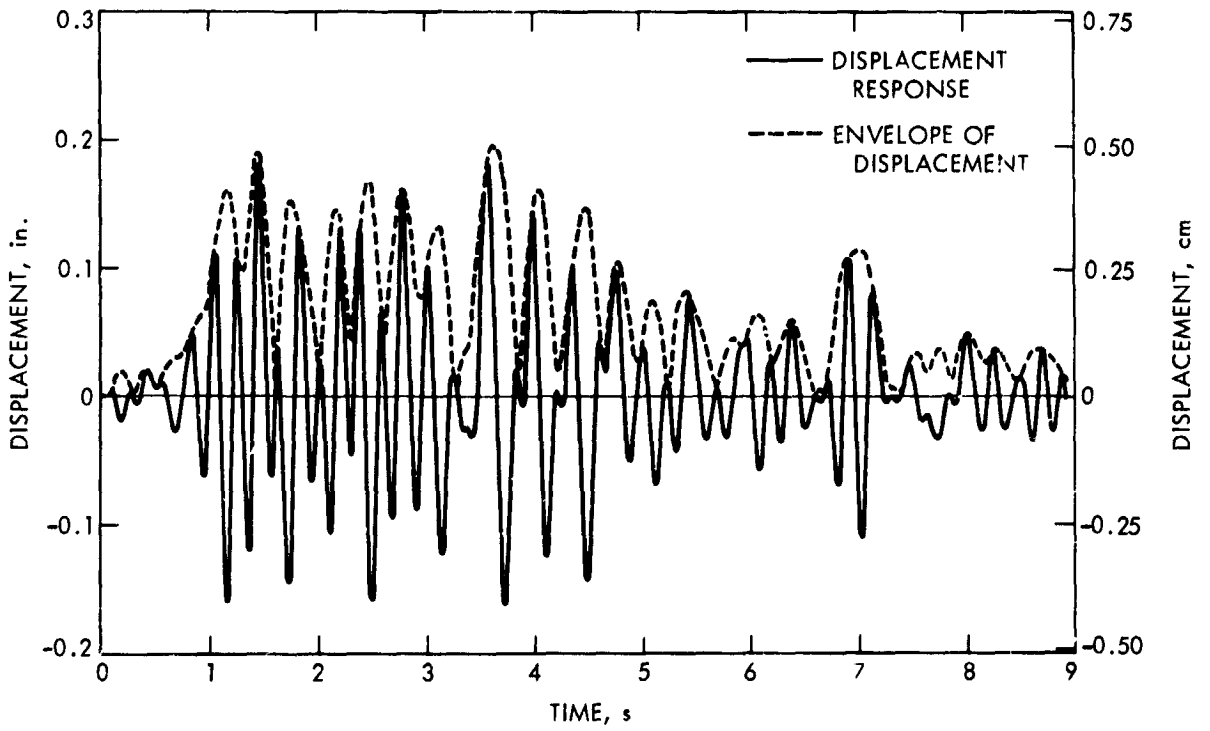

Figure 1. Sample functions of structural response and its envelope to nonstationary random excitation

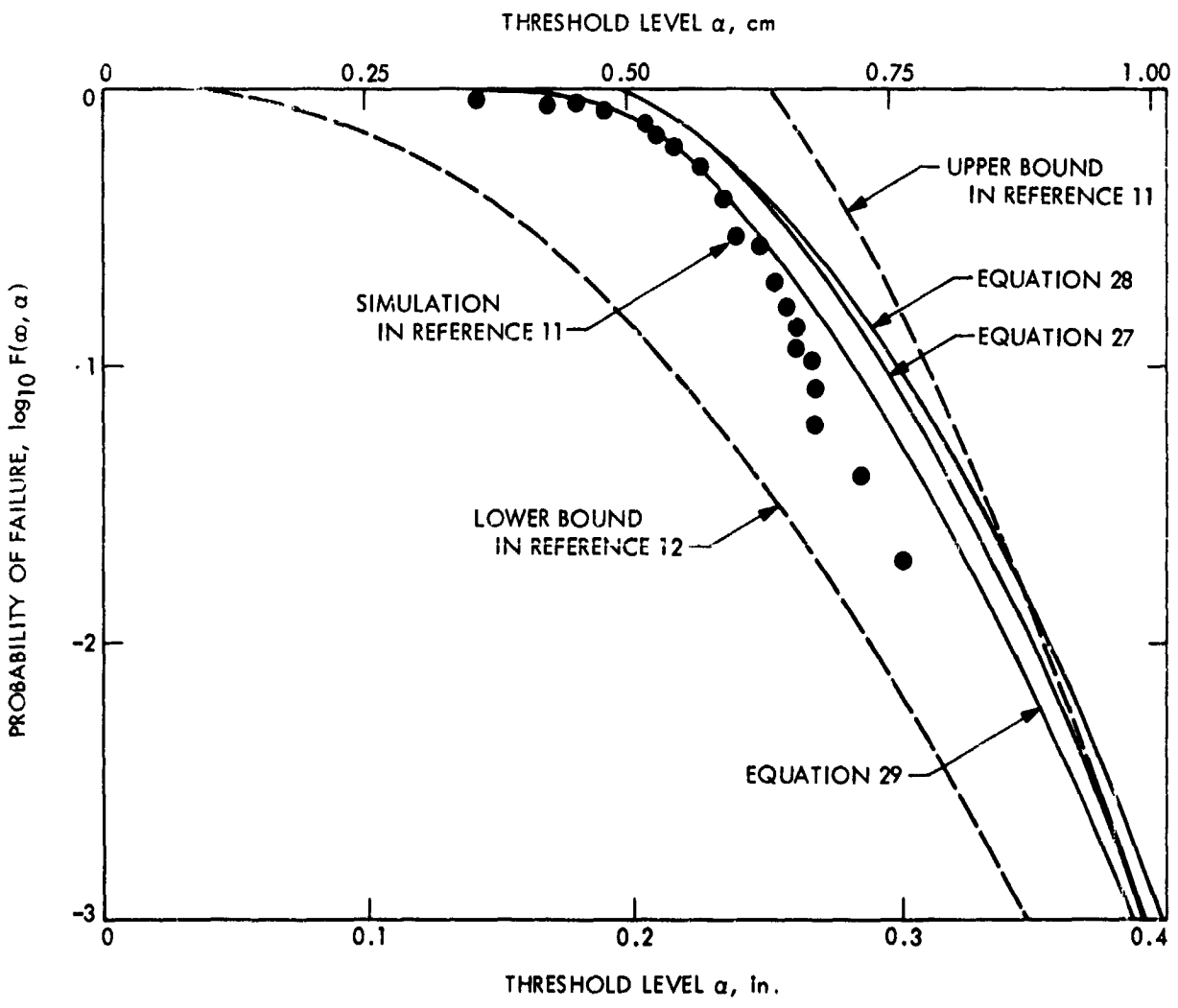

Figure 2. Probability of structural failure vs threshold level

Table 1. Probability of failure

Approximation	Barrier levels				
	0.38 cm (0.15 in.)	0.51 cm (0.20 in.)	0.64 cm (0.25 in.)	0.76 cm (0.30 in.)	0.89 cm (0.35 in.)
Equation 27	0.9998	0.8958	0.3776	0.073	0.0091
Equation 28	0.9961	0.8551	0.3900	0.089	0.0128
Equation 29	0.9931	0.7496	0.2678	0.052	0.0069

Concluding Remarks

A definition of the envelope of nonstationary random processes possessing evolutionary power spectra has been presented. The envelope definition enables one to simulate the nonstationary envelope process directly. The envelope statistics, such as the moment function, the joint density function, and the level crossing rate, relevant to the analysis of the first excursion probability, fatigue, and crack propagation, have been derived. Based on the envelope statistics, approximate solutions to the first excursion probability have been obtained.

References

1. Yang, J.-N., and Shinozuka, M., "On the First Excursion Probability in Stationary Narrow-Band Random Vibration," paper 71-APM-19, presented at the Applied Mechanics Conference, University of Pennsylvania, Pa., June 23–25, 1971, to appear in *J. Appl. Mech.*

2. Yang, J.-N., and Shinozuka, M., "On the First Excursion Probability in Stationary Narrow-Band Random Vibration II," paper to be presented at the Applied Mechanics Conference, La Jolla, Calif., June 26–28, 1972, to appear in *J. Appl. Mech.*

3. Yang, J.-N., and Heer, E., "Reliability of Randomly Excited Structures," *AIAA*, Vol. 9, No. 7, pp. 1262–1268, July 1971.

4. Rice, S. O., "Mathematical Analysis of Random Noise," in *Selected Papers on Noise and Stochastic Processes*. Edited by N. Wax. Dover Publications, Inc., New York, 1955.

5. Cramer, H., and Leadbetter, M. F., *Stationary and Related Stochastic Processes*. John Wiley & Sons, Inc., New York, 1967.

6. Priestley, M. B., "Power Spectral Analysis of Nonstationary Random Processes," *J. Sound Vib.*, Vol. 6, pp. 86–97, 1967.

7. Howell, L. J., and Lin, Y. K., "Response of Flight Vehicles to Nonstationary Atmospheric Turbulence," *Proceedings of the AIAA/ASME 12th Structures, Structural Dynamics and Materials Conference, Anaheim, California, April 19–21, 1971.*

8. Yang, J.-N., "Simulation of Random Envelope Processes," to be presented at the ASCE National Meeting on Structural Engineering, Cleveland, Ohio, April 1972.

9. Shinozuka, M., and Yang, J.-N., "Peak Structural Response to Nonstationary Random Excitations," *J. Sound Vib.*, Vol. 16, No. 4, pp. 505–517, June 1971.

10. Vanmarcke, E. H., *First Passage and Other Failure Criteria in Narrow-Band Random Vibration: A Discrete State Approach,* MIT Research Report No. R69-68. Massachusetts Institute of Technology, Dept. of Engineering, Cambridge, Mass., 1969.

11. Shinozuka, M., and Sato, Y., "Simulation of Nonstationary Random Processes," *J. Eng. Mech. Div., ASCE,* Vol. 93, No. EM1, pp. 11–40, 1967.

12. Shinozuka, M., and Yang, J.-N., "On the Bound of First-Excursion Probability," *J. Eng. Mech. Div., ASCE,* Vol. 95, No. EM2, pp. 363–377, Apr. 1969.

N72-17889

JPL Quarterly Technical Review Volume 1, Number 4 January 1972

Nonequilibrium Ionization Measurements in Hydrogen–Helium Mixtures

L. P. Leibowitz

Environmental Sciences Division

Time-resolved emission measurements of several atomic line and continuum radiation channels have been made behind the incident shock wave of the JPL electric arc shock tube. Test times and nonequilibrium ionization times were obtained for shock velocities up to 2.5×10^4 m/s in a 0.2 H_2 – 0.8 He gas mixture. The shock-heated test gas was found to be free from driver gas contamination, and the test times were adequate to achieve steady-state conditions. An activation energy of 4 eV was obtained from the nonequilibrium ionization time measurements. Modifications to experimental technique to determine the effect of test gas impurity level on ionization time measurements are discussed.

Introduction

The existence of nonequilibrium flow during Jupiter entry could have a considerable effect on entry vehicle heating. An atmospheric entry probe sent to Jupiter must withstand very large aerodynamic heating upon entering the Jupiter atmosphere. Heating rates based on the assumption that the shock-heated gases are in chemical equilibrium cannot be relied upon until the ionization kinetics of the shock-heated Jupiter atmospheric gases are understood. By measuring in the shock tube the time that is required to reach equilibrium behind shock waves in hydrogen–helium mixtures, the thickness of the nonequilibrium shock layer surrounding a Jupiter entry probe can be estimated. An electric arc shock tube built at JPL to simulate Jupiter entry conditions has been described by W. A. Menard (Reference 1). In the present investigation, the fluid flow produced in a hydrogen–helium mixture by the electric arc shock tube was studied and nonequilibrium relaxation times were measured. Measurements have been made of emission intensities for atom lines and continuum radiation as a function of time behind the incident shock wave. Characteristic ionization times and flow test times have been obtained as a function of shock velocity and initial pressure. These results are discussed and future plans are presented.

Experimental Technique

The emitted radiation from important species present in the H_2–He test gas and in the helium driver gas has been simultaneously measured as a function of time behind the incident shock wave of the JPL electric arc shock tube (Reference 1). Spectral intervals were selected in order to follow the chemical reactions in the test gas, to determine the length of the slug of test gas, and to determine whether there was any mixing between the test gas and the driver gas. It was necessary to determine spectral intervals for continuum measurements that were free from impurity radiation and to identify the strongest radiators in the driver gas. Spectrograms of the time-integrated emission from a shock-heated 0.2 H_2 – 0.8 He gas mixture were obtained using a modified Baush and Lomb grating spectrograph with 2.0×10^{-6} (20 Å/mm) dispersion. A series of spectrograms were taken over the wavelength range 250 to 900 nm (2500 to 9000 Å) using Polaroid Type 107 film for the shorter wavelengths and Polaroid Type 413 film for wavelengths larger than 600 nm. Lines from hydrogen and helium were identified on the spectrograms; however, the most intense radiation was from metal atom lines due to impurities in the driver gas.

Time-resolved emission measurements were made of five spectral intervals. Channels were selected to observe radiation from the H_β line, atomic hydrogen continuum, a helium line, a portion of a hydrogen molecular band, and an atomic line from chromium, which is an impurity introduced into the driver gas by the vaporization of a stainless-steel trigger wire. The spectrometer was a Jarrell Ash Model 75-000 with a 0.75-m focal length and a dispersion of approximately 1.0×10^{-6} (10 Å/mm). The spectral interval of each channel and a schematic drawing of the optical system are shown in Figure 1. The five photomultipliers used were RCA Type 1P28A, and the photomultipliers and electronic circuits were each tested and found to have a response time of less than 0.2 μs. The time resolution of the optical system was less than the photomultiplier response time for the shock velocities studied in this investigation.

The test gas was a 0.2 H_2 – 0.8 He mixture of Prep grade gases prepared by Matheson, Inc. The shock tube was pumped down to approximately 3.99×10^{-2} N/m^2 (3×10^{-4} torr) before each run.

Results

Shock tube runs were made over the range of shock velocities, U_s, from 1.6×10^4 to 2.5×10^4 m/s and for initial pressure of 33.3 and 133 N/m^2 (0.25 and 1.0 torr). The output signals from the five photomultipliers were recorded on three Tektronix 555 oscilloscopes. Oscillograms obtained from a typical shot are shown in Figure 2. The signals from all channels reached a maximum slope rapidly and then asymptotically approached an equilibrium level without an intermediate overshoot. The He line channel and H_2 band channel produced intensity profiles similar to the H continuum channel. It was concluded that H continuum was the primary source of radiation for these channels. The Cr signal profiles were similar to the continuum channel

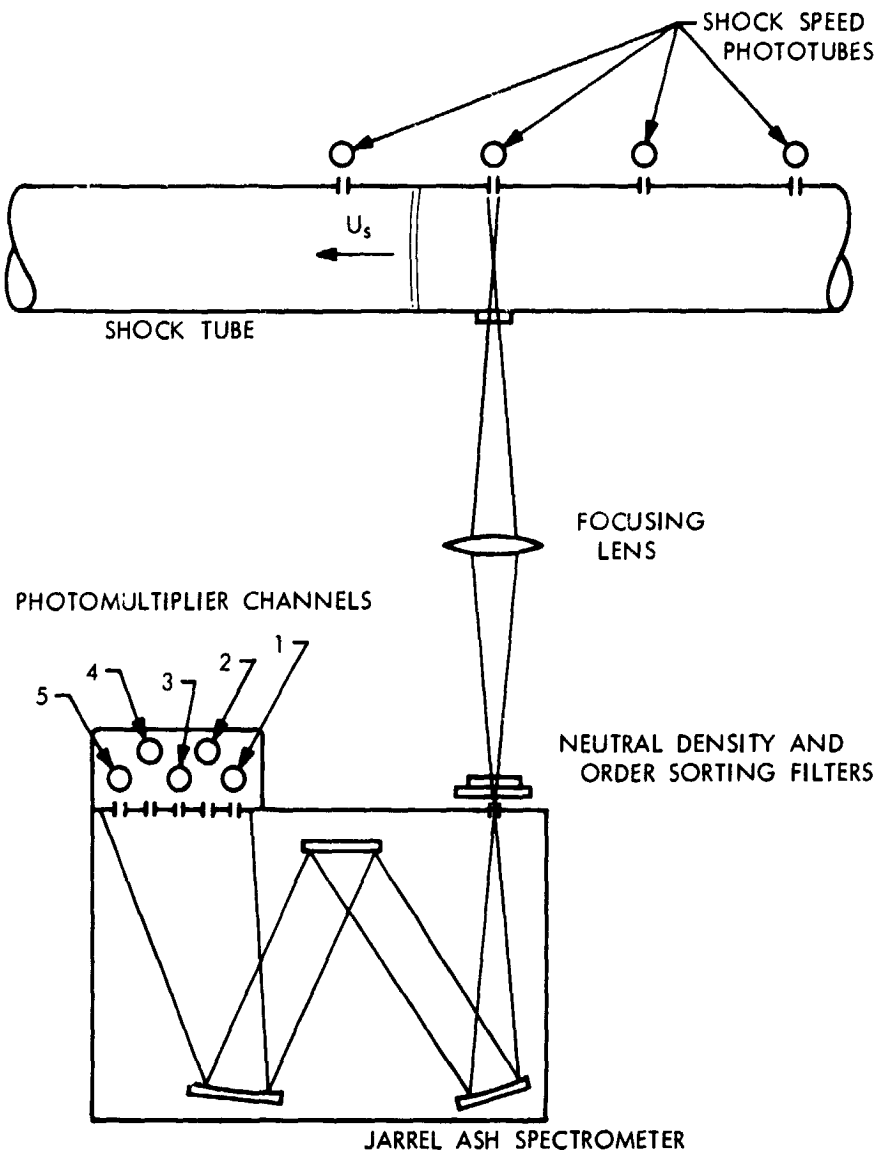

SPECTRAL INTERVALS

CHANNEL	λ, nm	Δλ, nm	SPECIES
1	425.4	0.5	Cr
2	447.1	0.5	He
3	462.8	1.0	H_2
4	486.1	0.5	$H\beta$
5	514.5	1.0	$H^+ + e$

Figure 1. Schematic diagram of optical system

until arrival of the contact surface, at which point there was a rapid and large increase in the signal level. The sudden rise in the Cr signal occurs at the same time as the sudden decrease in the H_β signal. This marks the interface between the driver gas and the test gas. The decay of the H_β signal over several microseconds indicates that there is a mixing region between the driver and test gases. It was concluded from the Cr and H_β signals that an impurity-free slug of test gas with measurable test time was formed in the JPL electric arc shock tube. Test times obtained for initial pressures p_1 = 33.3 N/m^2 and p_1 = 133 N/m^2 are shown in Figure 3. The curves in the figure are for test times calculated assuming constant values for test slug length l_t; reasonable agreement between calculated and experimental data can be seen. These test slug lengths are considerably smaller than the shock

tube diameter of 0.152 m and are several times smaller than the slug lengths that can be obtained from the test time measurements of Reference 1. This may be due, in part, to the sensitivity of the Cr channel in resolving the arrival of the driver gas.

Both the H continuum and the H_β line signals showed similar rise times. The rise time was defined as the time at which a line drawn through the maximum slope of the signal intersected the plateau signal level. The quantity $(H_2)^\circ \tau_{ion}$ is plotted as a function of $1/T_2$ in Figure 4, where τ_{ion} is the rise time of the continuum signal in shock fixed coordinates, $(H_2)^\circ$ is the frozen molar concentration of H_2 immediately behind the shock wave, and T_2 is the corresponding temperature. A reasonable fit to the $p_1 = 33.3$ N/m^2 data can be made by a straight line whose slope gives an activation energy of 4 eV. The values of τ_{ion} measured with $p_1 = 133$ N/m^2 were found to differ from the values measured with $p_1 = 33.3$ N/m^2 by a factor approximately equal to the ratio of the initial pressures. Thus, τ_{ion} was found to be independent of the initial pressure.

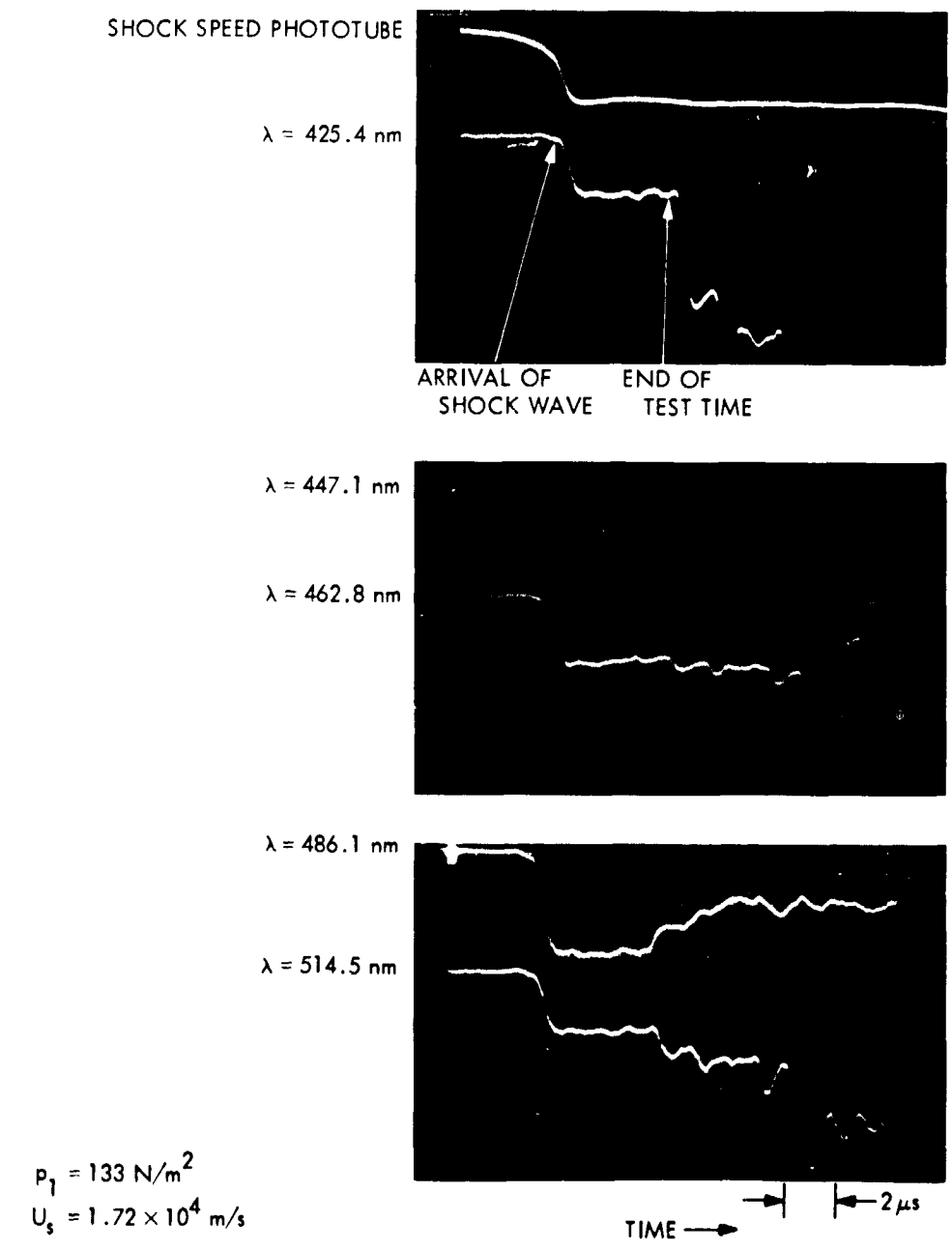

Figure 2. Photomultiplier signals as a function of time for typical shot

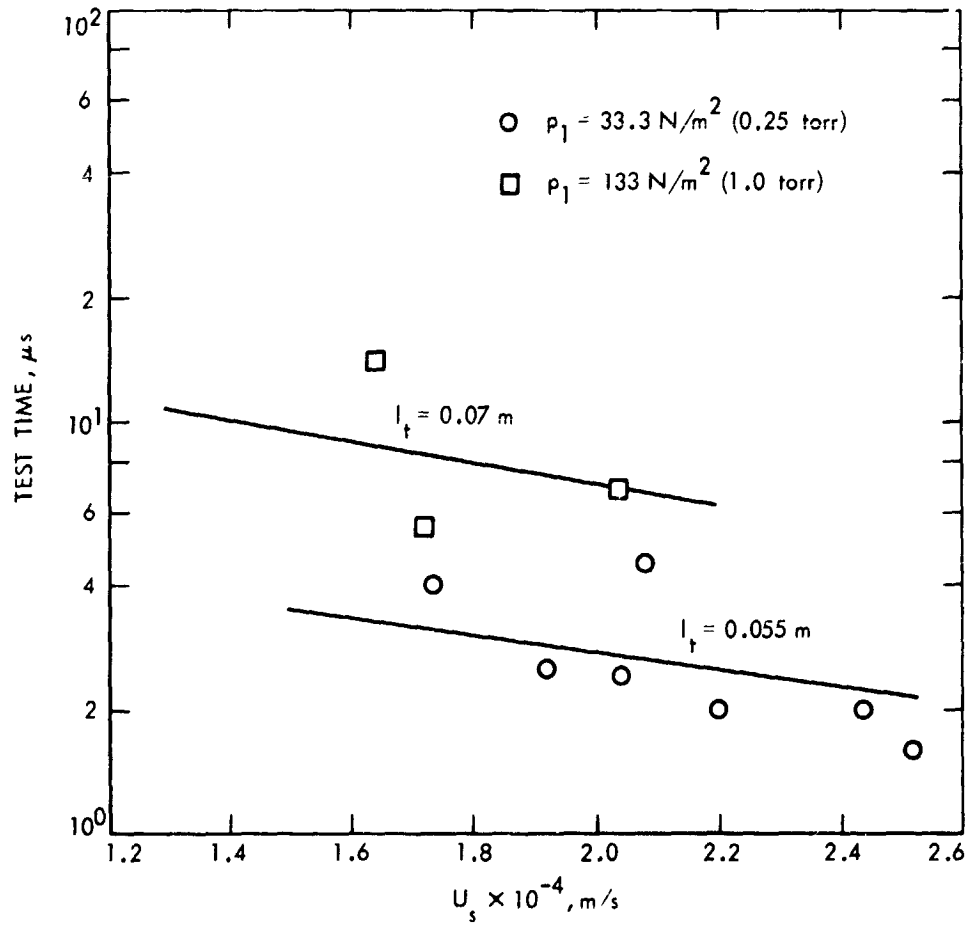

Figure 3. Test time measurements as a function of shock velocity

TOP

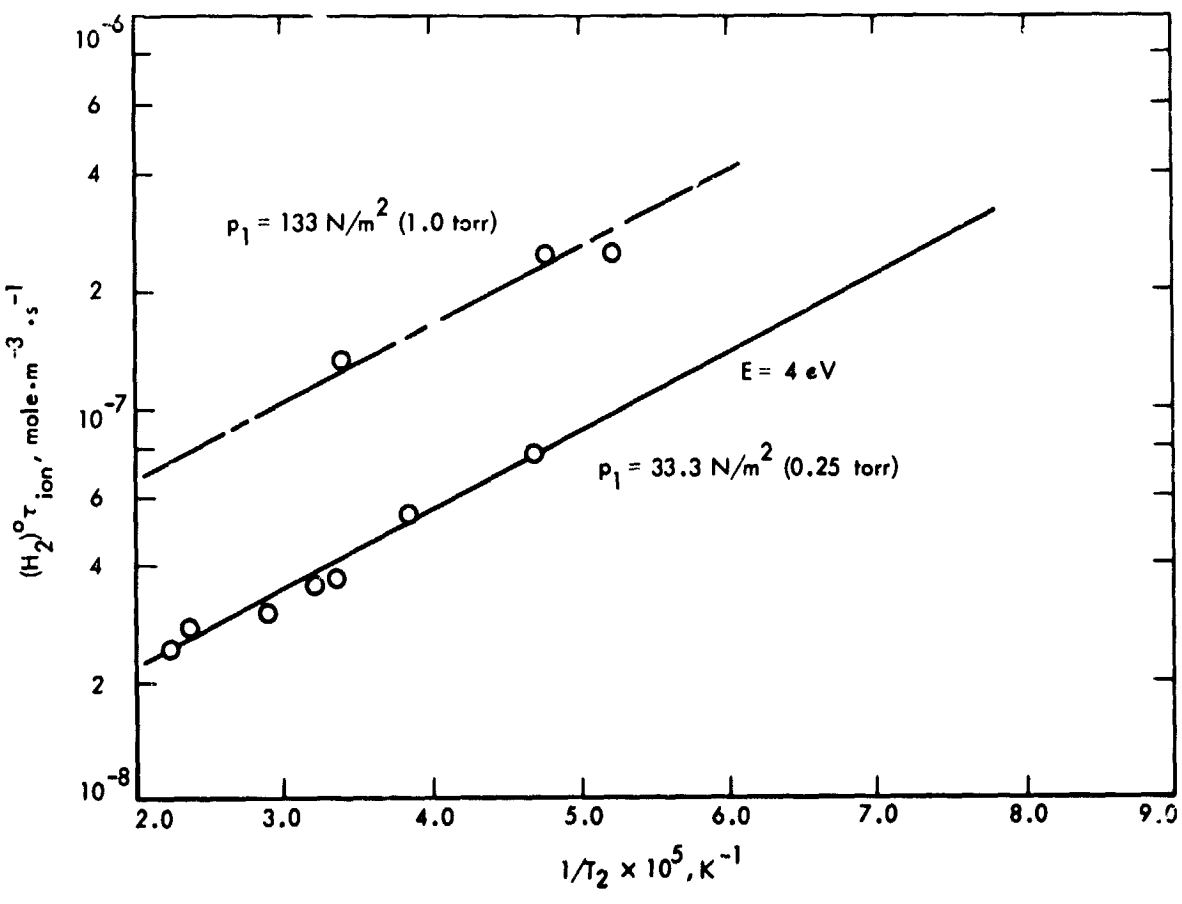

Figure 4. Normalized ionization time as a function of the reciprocal of shocked-gas temperatures

Conclusions

Time-resolved measurements of emission intensity of the H_β line and Cr line radiation have shown that a test slug free from driver gas impurities is formed in the JPL electric arc shock tube. Test times which allow nonequilibrium and steady-state measurements to be made were obtained for shock velocities up to 2.5×10^4 m/s.

Both the low value for the activation energy and the insensitivity of the ionization time to initial pressure indicate that the collisional ionization of hydrogen is not the dominant process for the intensity profiles. Although the activation energy for H_2 dissociation (4.5 eV) is close to the experimental activation energy, the decomposition time is expected to be 100 times faster than the measured ionization times. Comparison with ionization processes in other gases leads one to expect activation energies closer to the 13-eV ionization energy of hydrogen and τ_{ion} to be inversely proportional to initial concentration. However, experimental measurements of ionization rates of noble gases have been found to be sensitive to impurities in the part-per-million range. In the runs of this experiment the impurity level in the initial test gas was approximately 880 ppm. Therefore, the domination of measured intensity profiles by impurity ionization processes is a definite possibility.

Several modifications to the experimental technique are being made in order to determine the effect of impurity level on ionization time measurements. The pumping system is being modified so that a diffusion pump and liquid nitrogen cold trap will be used at each end of the shock tube. The test gas filling system will be changed to permit continuous flushing of test gas down the shock tube, thus minimizing the effects of absorption and desorption of gases on the shock tube wall. Finally, a test gas mixture made from ultra high purity grade gases and with an analysis of all impurities is being obtained.

The measurement of τ_{ion} as a function of U_s and p_1 will be repeated to determine the effect of the improved purity of the system. If these measurements indicate that impurities are no longer a problem and that the ionization times have not become larger than the available test time, an improved spectroscopic technique is planned. By making both absolute and relative continuum intensity measurements across the Balmer series limit, the electron concentration and electron temperature can be obtained as a function of time without the reliance on collisional equilibrium assumptions required of other spectroscopic techniques.

Reference

1. Menard, W. A., "A Higher Performance Electric-Arc-Driven Shock Tube," in *JPL Quarterly Technical Review*, Vol. 1, No. 1, pp. 17–28. Jet Propulsion Laboratory, Pasadena, Calif., Apr. 1971.

N72-17890

JPL Quarterly Technical Review Volume 1, Number 4 January 1972

On the Possibility of Earth Re-entry Simulation of Shallow Angle Jupiter Entry

A. D. McRonald

Environmental Sciences Division

Possible Earth re-entry simulation of shallow angle (3–30 deg) Jupiter entry has been investigated in terms of four parameters of the bow shock layer ahead of a blunt vehicle: peak (equilibrium) temperature, peak pressure, peak inward radiative flux, and time-integrated radiative flux. The comparison shows that simulation ranging from fair to good can be achieved, generally the easiest (lowest Earth re-entry speed) at steep Earth re-entry, in the Earth entry speed range of 15–22 km/s, for both the Jupiter "nominal" and "cool" atmospheres. Increasing Earth speed is required, generally, for increasing Jupiter entry angle, and for temperature, radiative flux, time-integrated flux and pressure, in that order. It appears that a meaningful simulation test could be done using a launch vehicle with the speed and payload capability of the Titan IIID/Centaur/BII.

Introduction

The possibility of simulating the major features of entry from near-parabolic inertial entry speed into the atmosphere of Jupiter by means of an Earth re-entry test is of considerable interest on two main accounts:

(1) As a "calibration" point for several aspects of Jupiter entry probe design, including:

   (a) Theories and models for the very high enthalpy hypersonic flow field with strong coupling of intense radiation, convection, and ablation.

   (b) Ablation materials response when subject to high radiative flux (of order of 100 kW/cm^2), large gasdynamic mass flux over the body, and large "inertia" forces due to violent deceleration.

(2) As a prior-to-launch validation of design of a prototype Jupiter entry capsule, including trajectory, aerodynamic stability, structural integrity, heat shield, communications, instrument performance, etc.

Analysis

Simplifying Assumptions

For this first analysis, various simplifying assumptions have been made, including:

(1) The shock layer is in thermochemical equilibrium, is uniform in composition, and is an isothermal parallel slab of uniform thickness (presupposes a fairly large blunt vehicle and fairly high gas density; good approximation near peak conditions during entry; facilitates temperature and radiative flux calculations).

(2) The shock layer thickness is constant during the entry (ignores change in body (nose) radius due to ablation and change in gas density ratio over the shock; facilitates radiative flux calculations).

(3) The shock layer pressure is $\rho_1(V_{rel})^2$, where ρ_1 is the undisturbed atmospheric density, and V_{rel} is the speed of the vehicle relative to the atmosphere.

(4) All other factors relating to the comparison of Jupiter and Earth entry, e.g., diffusion, chemical reaction, and ablation, are either similar in effect or minor.

Trajectories

The trajectories considered for Jupiter entry were for a ballistic coefficient[1] of 154 kg/m^2, an inertial entry speed of 61 km/s (slightly hyperbolic), entry angles of from 3 (near ballistic skip-out) to 30 deg, and a "downwind" equatorial entry (giving V_{rel} at entry in range 48–50 km/s). For Earth, similar entry at all entry angles, the same ballistic coefficient, and inertial entry speeds of 12, 14, 16, 18, 20, and 22 km/s were evaluated. A two-degree-of-freedom (motion in a plane) computer program was used to calculate approximate trajectories.

Radiative Flux

Data on the emergent radiative flux from the parallel, isothermal slab of hot gas of uniform thickness, as a function of slab pressure and temperature, have been published (Reference 1 for air, Reference 2 for the Jupiter nominal and cool atmospheres). The JPL thermochemistry program (Reference 3) was used to calculate shock layer temperature, pressure, and gas density ratio across the shock. The slab (shock layer) thickness δ was evaluated from the Lighthill formula:

---

[1] The value is one for which many prior trajectory calculations have been made by the author, and corresponds to a 45-deg cone of base radius 1 m and an average specific gravity of ½.

$$\delta = R\epsilon\left[1 - \sqrt{\frac{8\epsilon}{3}} + 2.6\epsilon\right]$$

where R is the vehicle nose radius, $\epsilon = \rho_1/\rho_2$, and ρ_2 is the shock layer density. For convenience of calculation, the δ values for Jupiter gas and air were taken as 5 cm and 3 cm, respectively; the body is sketched, and values of R, δ, and ρ_2/ρ_1 are given in Figure 1.

Results

The absolute levels of peak shock layer pressure, temperature, inward radiative flux, and integrated flux for the entry bodies considered are shown in Figures 2, 3, 4, and 5, respectively. From these, the Earth entry speed and angle to simulate a given Jupiter entry angle as regards the above four parameters can be calculated. Figures 6 and 7 show Earth entry conditions

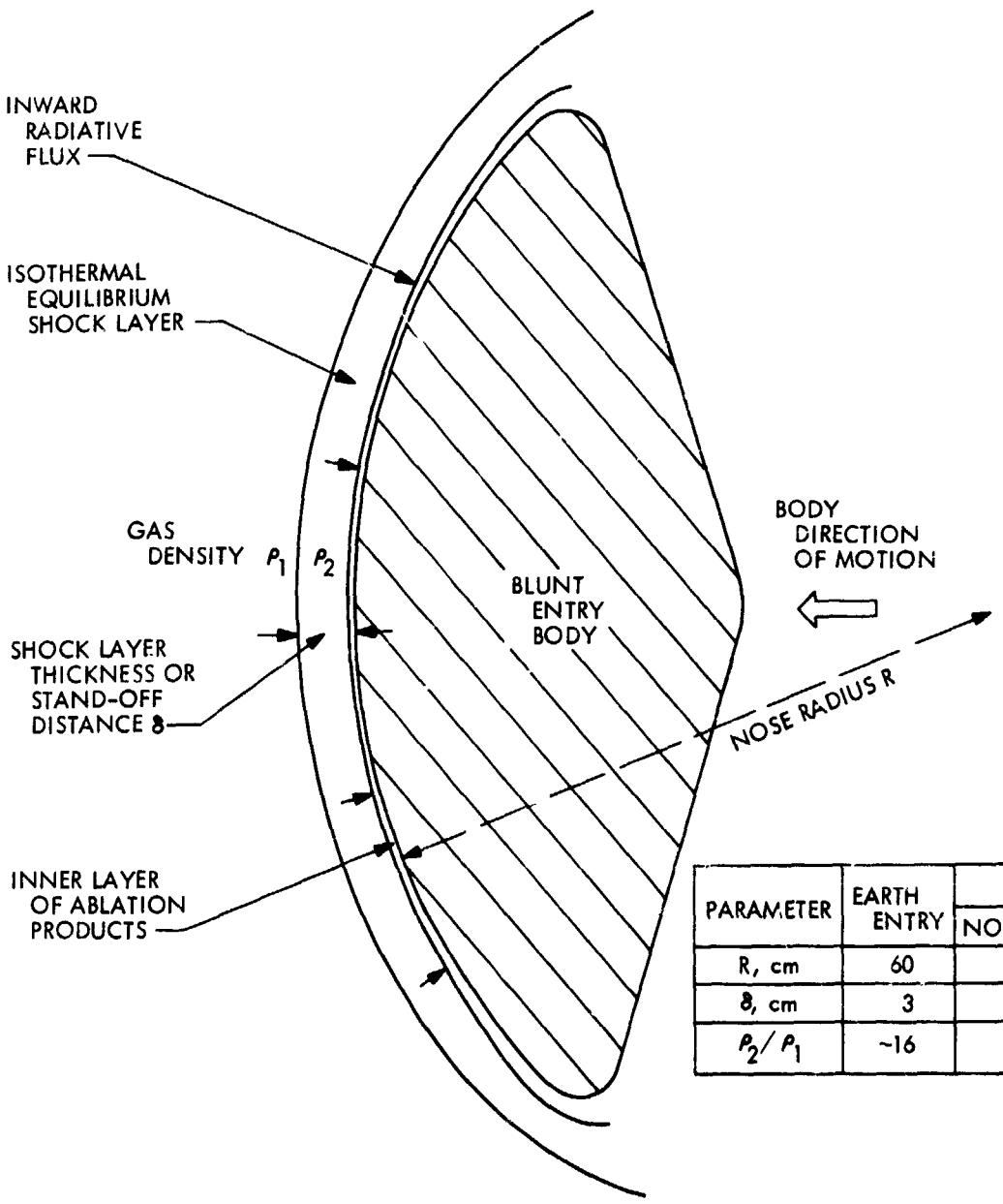

PARAMETER	EARTH ENTRY	JUPITER	
		NOMINAL	COOL
R, cm	60	74	67
δ, cm	3	5	5
ρ_2/ρ_1	~16	~11	~10

Figure 1. Type of blunt entry body considered in radiative flux calculations

to simulate 10-, 20-, and 30-deg Jupiter entry into the nominal and cool atmospheres, respectively. The 90-deg Earth entry speeds to simulate the various parameters for 10-, 20-, and 30-deg entry into the Jupiter nominal and cool atmospheres are shown in Table 1.

As a prelude to discussion of simulation, it is appropriate to comment on performance of available launch vehicles. The feasibility of an Earth entry test depends on launch-vehicle capability, which is outlined in Figure 8 (data from Reference 4).

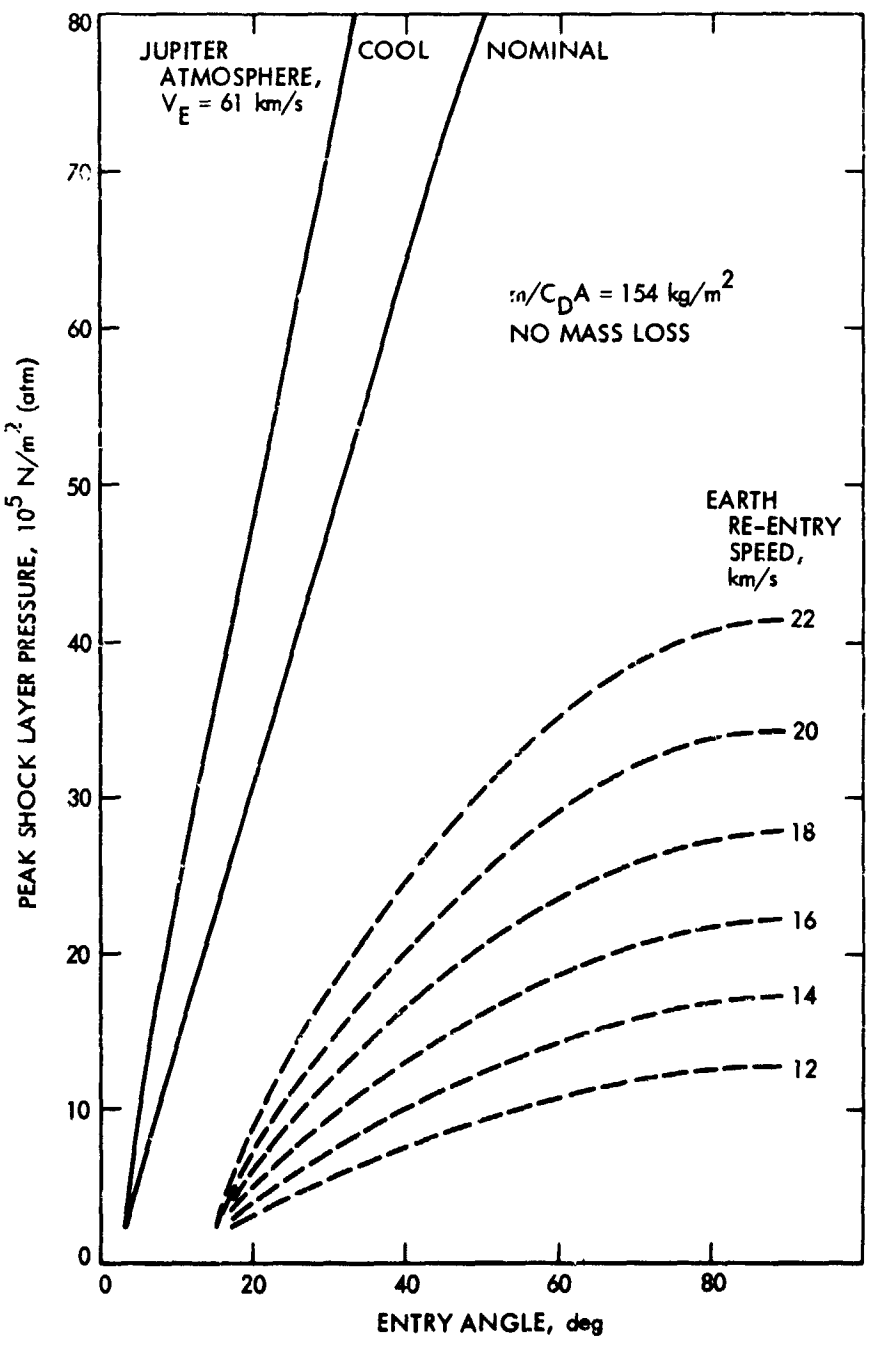

Figure 2. Peak shock layer pressure versus entry angle

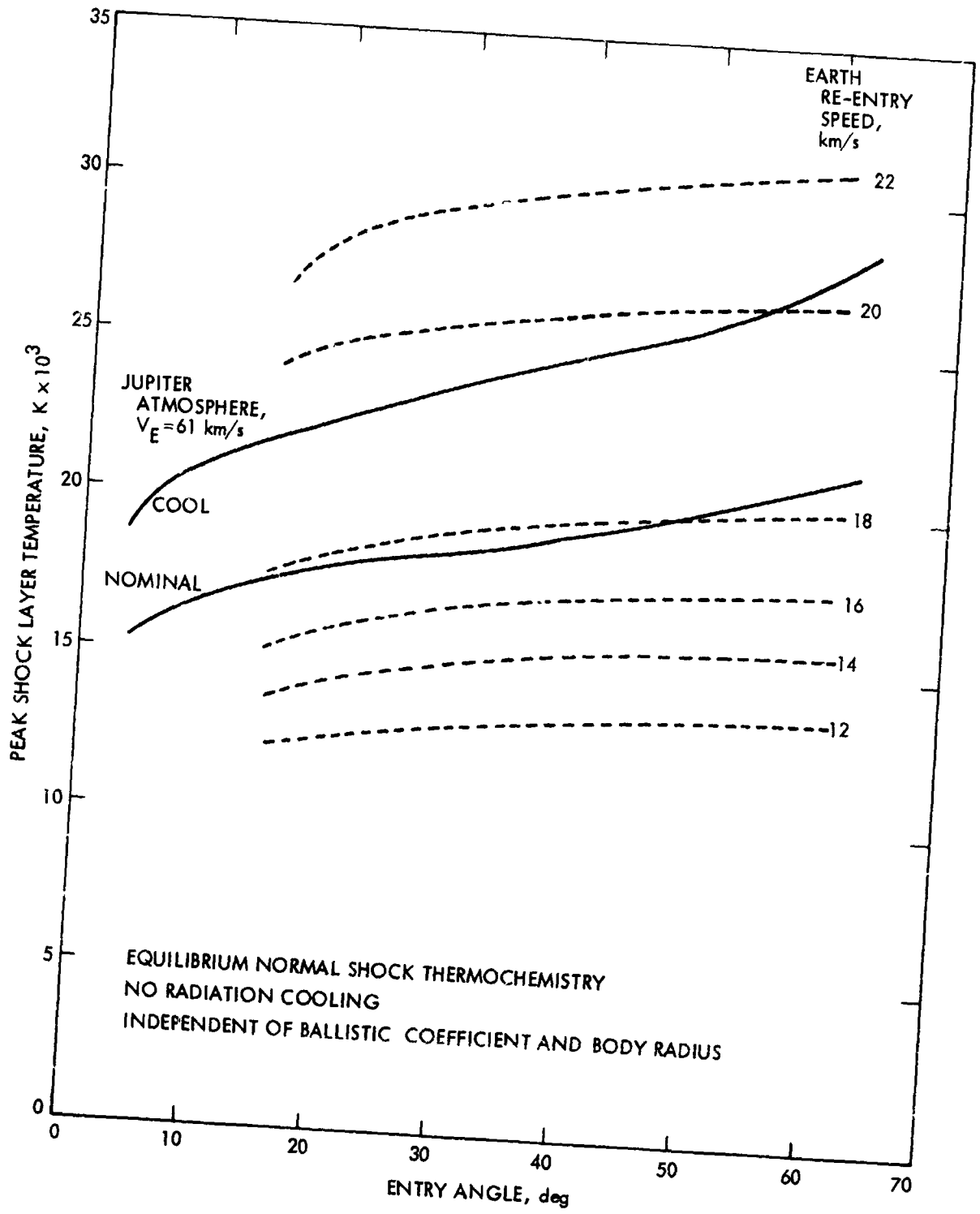

Figure 3. Peak shock layer temperature versus entry angle

Discussion

The comparison between Earth and Jupiter entry has been made for blunt bodies of comparable size (about R = 60-cm nose radius) and one value of ballistic coefficient m/C_DA (154 kg/m^2). The degree of simulation attainable will vary with the R and m/C_DA values of both the Jupiter and Earth vehicles.

The shock layer temperature is insensitive to R and m/C_DA. The pressure will vary about linearly with m/C_DA, which will in turn scale as R, if proportions are preserved. The radiative flux (per unit area, as calculated here) will vary as R for the low gas density part of a trajectory, but may

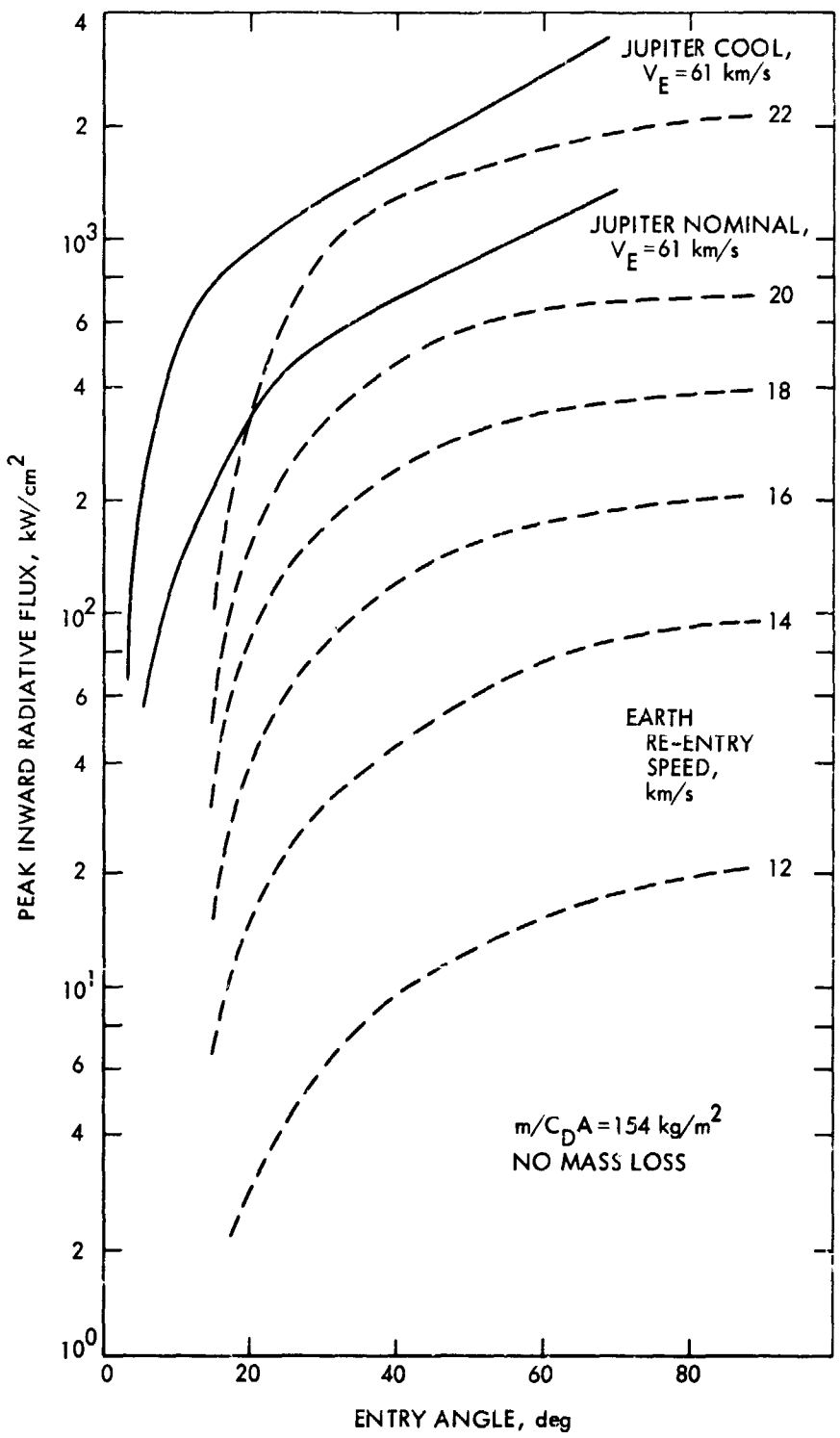

Figure 4. Peak inward radiative flux versus entry angle

approach constancy as increasing density brings the flux toward the black body limit.

As regards the Jupiter entry angle to be simulated, it is noted that the pressure is very sensitive to angle, the peak radiative flux quite sensitive (particularly at low angles), and the integrated flux and temperature not very sensitive (low flux at low angle being compensated by longer entry flight time).

The launch-vehicle payload capability is likely to impose serious restraints on Earth re-entry vehicle mass, and hence on R and m/C_DA. Similarly, entry speed and weight appear to be limited, for practical reasons of cost, to about

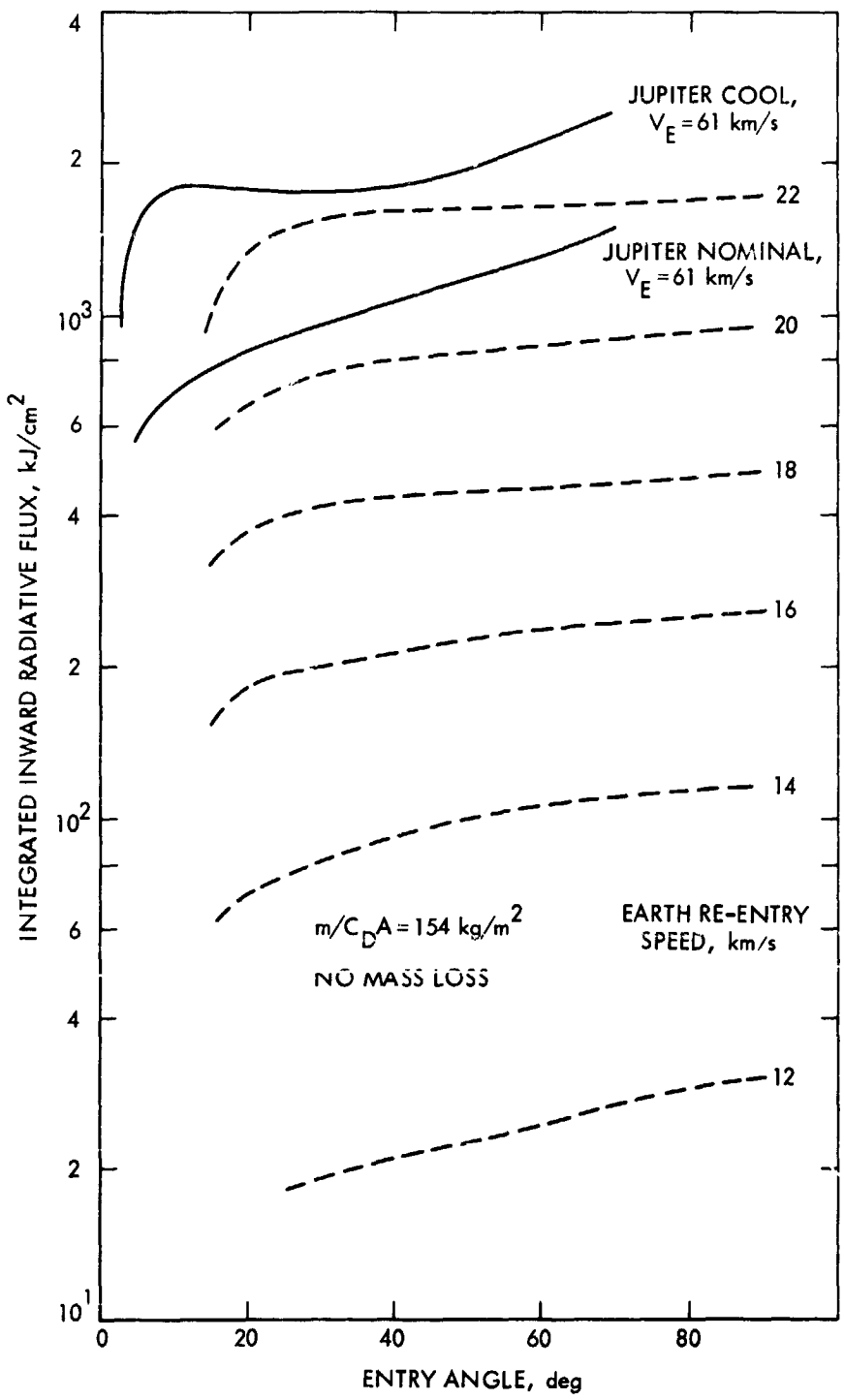

Figure 5. Time-integrated inward radiative flux versus entry angle

19 km/s and 50-kg payload, corresponding to a vehicle like the Titan IIID/Centaur/BII. It may then be difficult to construct an Earth re-entry vehicle with $R = 60$ cm and $m/C_DA = 154$ kg/m^2 as calculated here, subject to a 50-kg mass, and there is clearly a trade-off between mass and speed for best simulation. However, the conclusions below will be given in terms of an Earth vehicle of comparable size to the Jupiter vehicle.

Conclusions

The following conclusions can be drawn from Figures 6, 7, and 8, as regards Earth entry simulation of Jupiter entry.

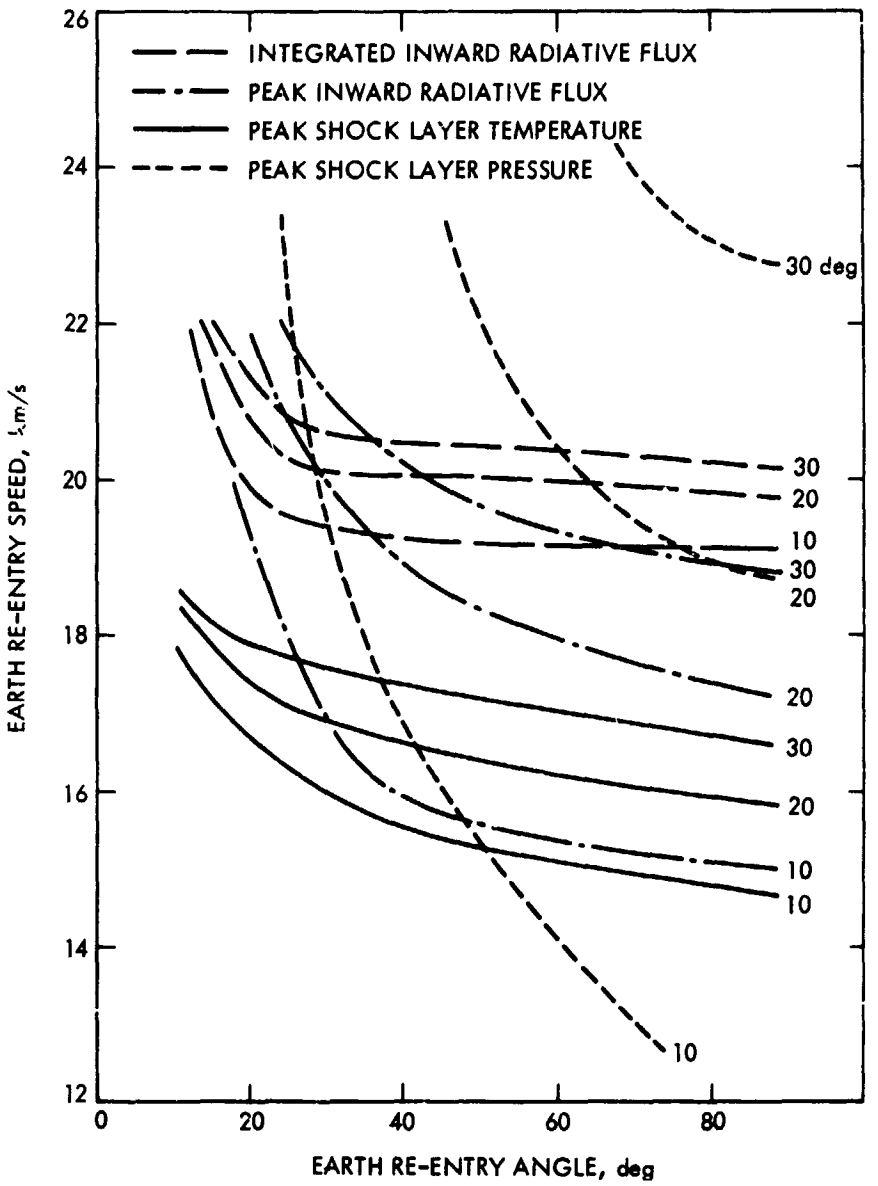

Figure 6. Simulation of 10-, 20-, and 30-deg Jupiter entry by Earth re-entry: Jupiter nominal atmosphere

(1) As the Jupiter entry becomes more shallow, less Earth entry speed is required for simulation of the four parameters.

(2) For a given simulation, less Earth entry speed is required at steep Earth entry than at shallow.

(3) Shock layer temperature is simulated most readily, requiring Earth entry speeds in the range 15 to 17 km/s for the Jupiter nominal, and 18 to 19 km/s for the cool atmosphere, at Jupiter entry angle of 10 to 30 deg.

(4) Inward radiative flux simulation can be achieved for 10–30-deg Jupiter entry into the nominal atmosphere (Earth entry speeds of 15 to 18.6 km/s), but only for about a 10-deg entry into the cool atmosphere (Earth entry speeds of 18.8 to 21.0 km/s for 10–30-deg entry).

(5) Time-integrated radiative flux can barely be simulated, requiring Earth entry speeds of 19.2 to 20.3 km/s for 10–30-deg Jupiter entry

Table 1. Earth re-entry speeds to simulate shallow Jupiter entry

Parameter	Earth entry speed at 90 deg, km/s					
	Nominal atmosphere			Cool atmosphere		
	10[a]	20[a]	30[a]	10[a]	20[a]	30[a]
Temperature	15.0	15.9	17.0	18.0	18.6	19.0
Pressure	12.4	19.3	23.0	18.0	24.0	–
Flux	15.1	17.4	18.6	18.8	20.2	21.0
Integrated flux	19.2	19.8	20.3	22.2	22.2	22.2

[a] Jupiter entry angle, degrees.

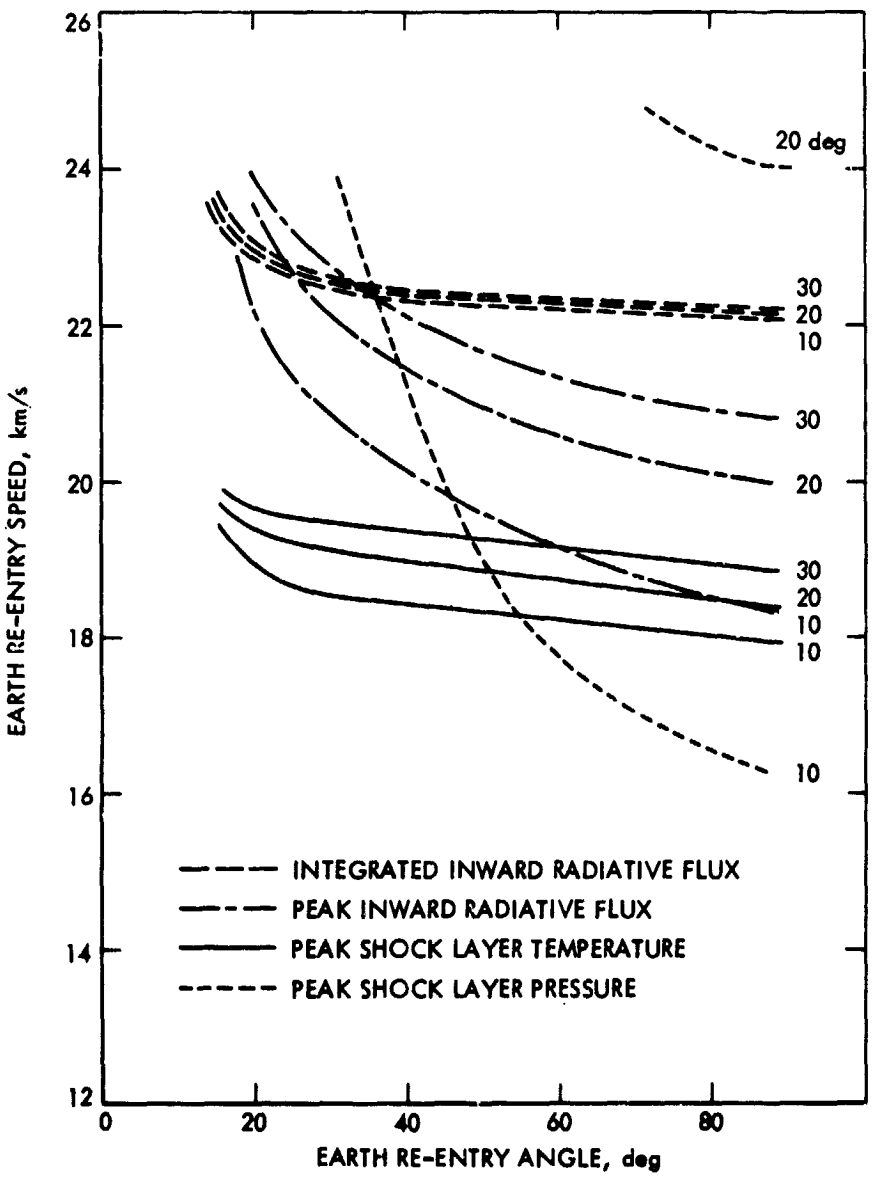

Figure 7. Simulation of 10-, 20-, and 30-deg Jupiter entry by Earth re-entry: Jupiter cool atmosphere

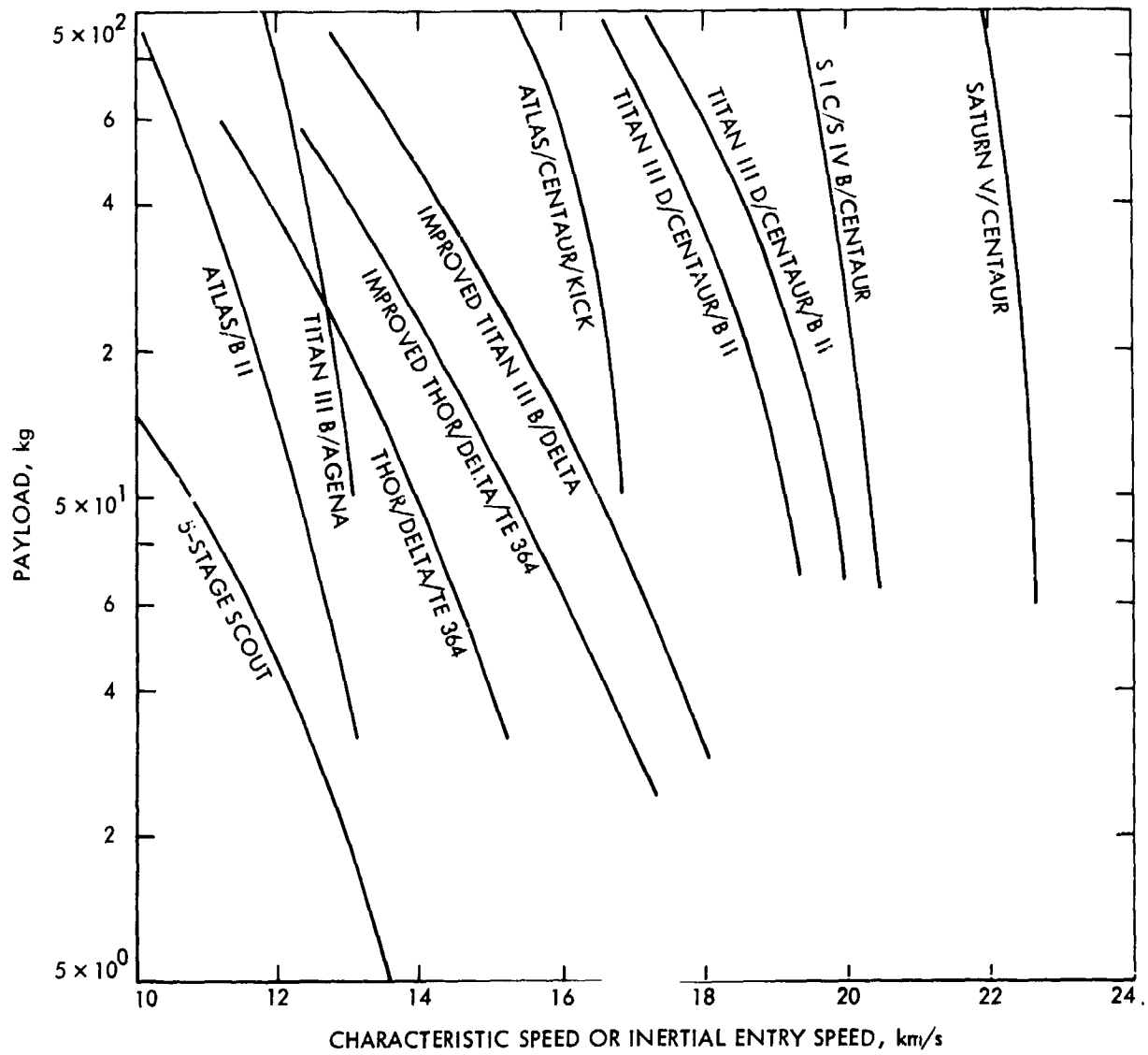

Figure 8. Performance of present and proposed launch vehicles

into thc nominal atmosphere, and about 22.2 km/s for similar entry into the cool atmosphere.

(6) Shock layer pressure can be simulated for 10–20-deg entry into the nominal atmosphere (Earth entry speeds of 12.4–19.3 km/s) and for only about 10-deg entry into the cool atmosphere (Earth entry of 18.0 km/s for 10 deg, 24.0 for 20-deg entry).

(7) Prospects of simulating two, three, or four of these parameters (temperature, pressure, flux, and integrated flux) for a specific case, by proper choice of ballistic coefficient, nose radius, and Earth entry angle and speed, are good for Jupiter entry in the range 10–20 deg for the nominal atmosphere, and 10–15 deg for the cool atmosphere.

(8) A meaningful Earth re-entry simulation of shallow Jupiter entry appears to be possible using a launch vehicle about the scale of the Titan IIID/Centaur/BII (19 km/s at 50 kg, 16.5 km/s at 500 kg).

References

1. Wilson, K. W., and Grief, R., *J. Quant. Spectrosc. Radiat. Transfer*, Vol. 8, p. 1062, 1968.

2. Stickford, G. H., Jr., "Total Radiative Intensity Calculations for 100% H_2 and 87% H_2-13% He," to be published in *J. Quant. Spectrosc. Radiat. Transfer.*

3. Horton, T. E., and Menard, W. A., *A Program for Computing Shock-Tube Gasdynamic Properties*, Technical Report 32-1350. Jet Propulsion Laboratory, Pasadena, Calif., Jan. 15, 1969.

4. *Launch Vehicle Estimating Factors*, NASA document, National Aeronautics and Space Administration, Washington, Jan. 1970.

N72-17891

JPL Quarterly Technical Review Volume 1, Number 4 January 1972

Measurement of the Power Spectral Density of Phase of the Hydrogen Maser

A. Sward

Telecommunications Division

Hydrogen masers are being developed by JPL to satisfy the needs of the Deep Space Network for improved frequency standards in order to achieve better timing accuracies, reduced doppler residuals, and lower phase noise in the tracking system. Performance data for the JPL hydrogen masers is given in two forms: time-domain performance, useful for analyzing time-keeping systems and doppler systems; and frequency-domain performance, useful for analyzing tracking systems. Particular attention is given to frequency-domain performance, as obtained from both time-domain measurements and direct measurements.

The power spectral density of phase for the JPL hydrogen masers (References 1, 2, and 3) has recently been measured and found to be in close correlation with that which was calculated using time-domain stability measurements. This has allowed the 3-dB bandwidth of the hydrogen maser to be calculated as well as the frequencies at which the various types of noise are predominant.

A plot of the measured standard deviation of the average fractional frequency departure versus averaging time for the hydrogen maser is shown in Figure 1. The flat region of the plot, which occurs for averaging times of 50 s and greater, is caused by a random noise called flicker-of-frequency noise, and is characterized in the power spectral density of phase by a f^{-3} slope. The portion of Figure 1 that varies approximately as $1/\tau$ for averaging times of less than 50 s is called flicker-of-phase noise. This noise would have a spectral density of phase varying as f^{-1}.

Before describing the equations that are used to convert from the time-stability plot to the power density spectrum of phase, it is important to define several terms. First, the term $\sigma^2(N,T,\tau)$ is a sample variance of N measurements of the time-varying frequency, $f(t)$, each of duration τ, spaced every T units of time. The units of $\sigma^2(N,T,\tau)$ are rad^2/s^2. The standard deviation of the average frequency departure is divided by ω_0 to obtain the average fractional frequency departure. The variance of frequency fluctuations for flicker of frequency exhibits a logarithmic divergence as the

number of measurements increases. It is thus necessary to fix the number of measurements in order to obtain meaningful data. A convenient measure, called the Allen variance, is obtained by fixing N at 2, and by modifying the usual sample-variance definition by the factor $N/(N-1)$. It can be shown that the optimum value (Reference 4) for N is, in fact, very close to 2. Normally, the mean sample variance for a large number of sample-variance measurements is taken in order to reduce the uncertainty for such a low number of measurements N.

In order to calculate the spectral density of phase, the following relationships are needed: For flicker-of-frequency noise (Reference 5),

$$S_\phi(f) = \frac{[\sigma^2(2,\tau,\tau)]}{(2\pi)^2 f^3 2 \ln 2} \tag{1}$$

where $S_\phi(f) \triangleq$ power spectral density of phase in rad^2/Hz. For flicker-of-phase noise (Reference 5),

$$S_\phi(f) = \frac{[\sigma^2(2,\tau,\tau)]}{(f)\{3[2 + \ln(\tau\omega_n)] - \ln 2\}} \tag{2}$$

where $\omega_n \triangleq$ noise bandwidth in rad/s. An important point should be noted here. In the time-domain plot, frequency stability varies as $1/\tau$ for white phase noise, whereas the stability varies as $\sqrt{\ln \tau}/\tau$ for flicker-of-phase noise.

White phase noise (f^0 behavior in the frequency domain) produces a $1/\tau$ behavior in the time-domain plot of σ versus τ, while flicker-of-phase noise (f^{-1} behavior in the frequency domain) produces a $\sqrt{\ln \tau}/\tau$ dependence (Reference 5). These two types of noise are difficult to distinguish in the time domain because of measurement dispersion. A direct measurement in the frequency domain is often more useful to determine which type of noise is present. Such measurements have, in fact, verified the existence of flicker-of-phase noise.

The time-domain plot of the average fractional frequency departure, $\sigma(2,\tau,\tau)/\omega_0$ versus averaging time τ for the hydrogen maser, is shown in Figure 1. The power spectral phase density calculated from Figure 1 is shown in Figure 2, with the measured values superimposed. Equating and solving Equations 1 and 2 results in a solution for crossover frequency between the two types of noise. This value is 1.59×10^{-2} Hz at a center frequency of $f_0 = 100$ MHz. Direct measurements at the device 100-MHz output have verified the validity of the spectral plot within 1.4 dB over the frequency band 4 to 100 Hz on each side of the carrier. In addition, at the 10- and 1-MHz outputs, obtained by frequency division of the 100-MHz signal, measurements have degradations of only about 1 dB in the power density spectrum. It was found that at the 1-MHz output, white phase noise became the predominant noise above 20 Hz from the carrier, which, if extrapolated back to the 100-MHz output, corresponds to a crossover frequency of about 200 kHz.

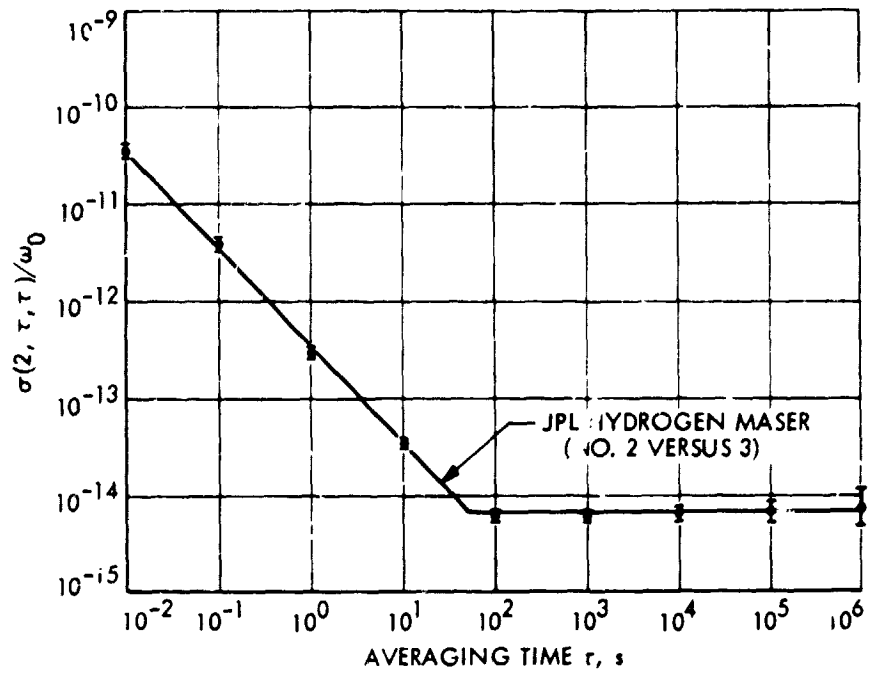

Figure 1. JPL hydrogen maser frequency stability

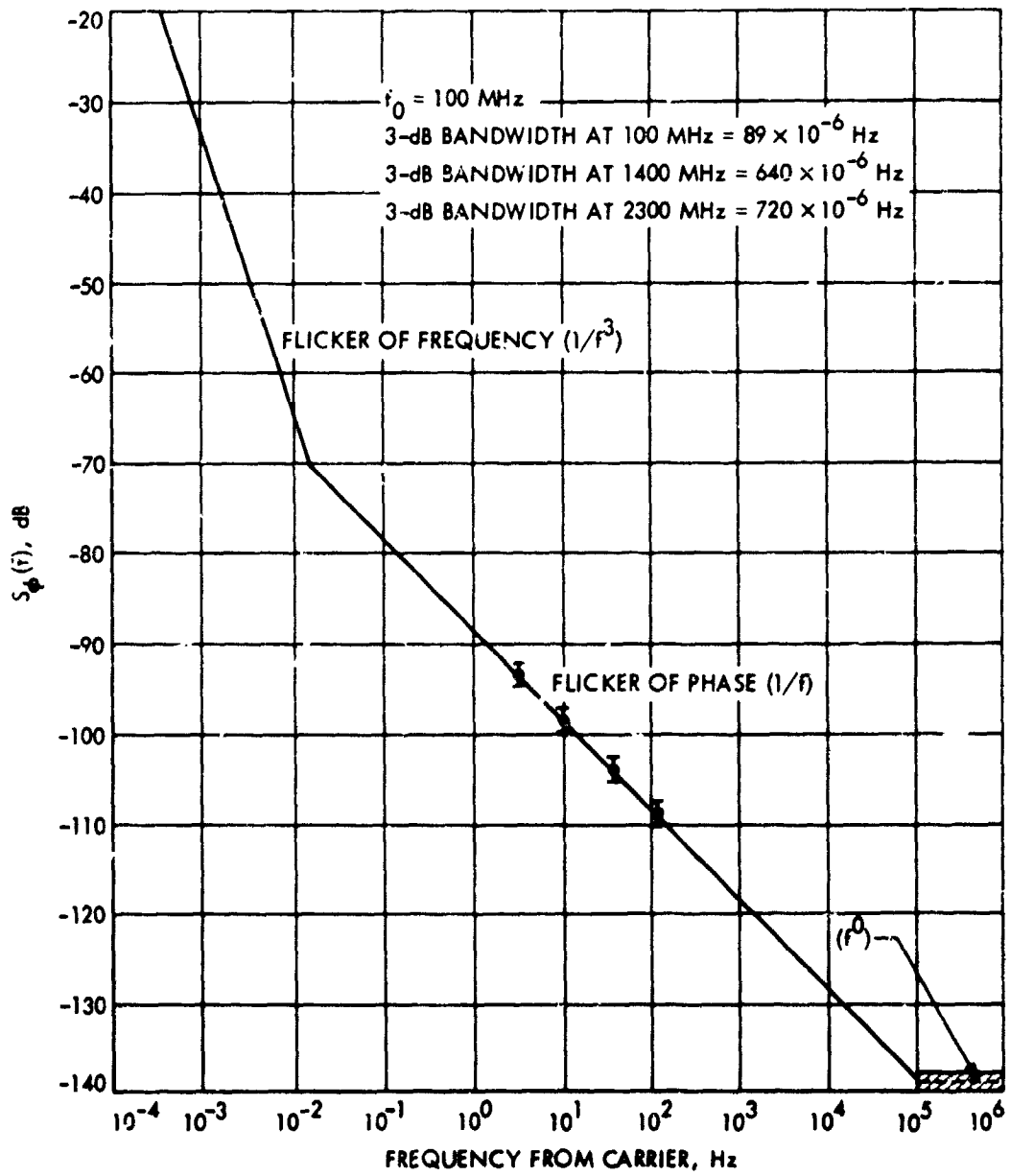

Figure 2. Power spectral density of phase for hydrogen maser

The 3-dB bandwidth of the hydrogen maser at its output frequency of 1420 MHz was calculated by extrapolation to be 6.4×10^{-4} Hz from the power spectral density plot.

References

1. Sward, A., "New Developments in the Hydrogen Maser Frequency Standard," in *The Deep Space Network Progress Report*, Technical Report 32-1526, Vol. II, pp. 72–74. Jet Propulsion Laboratory, Pasadena, Calif., Apr. 15, 1971.

2. Erpenbach, H., Finnie, C., and Petty, S., "Frequency Generation and Control: Atomic Hydrogen Frequency Standard," in *The Deep Space Network*, Space Programs Summary 37-58, Vol. II, pp. 52–55. Jet Propulsion Laboratory, Pasadena, Calif., July 31, 1969.

3. Sward, A., "Frequency Generation and Control: The Hydrogen Maser Frequency Standard," in *The Deep Space Network*, Space Programs Summary 37-59, Vol. II, pp. 40–43. Jet Propulsion Laboratory, Pasadena, Calif., Sept. 30, 1969.

4. Tausworthe, R. C., *Convergence of Oscillator Spectral Estimators for Counted Frequency Measurements*, to be published.

5. Allan, D., "Statistics of Atomic Frequency Standards," *Proc. IEEE*, Vol. 54, Feb. 1966.

N72-17892

JPL Quarterly Technical Review Volume 1, Number 4 January 1972

Reduction of Near-In Sidelobes Using Phase Reversal Aperture Rings

W. F. Williams

Telecommunications Division

Spacecraft antennas having high gain and extremely low sidelobes will be needed for communications satellites. Low sidelobe performance is needed to isolate beams of multibeam systems using the same carrier frequency (frequency re-use). Because of a limited allowable spectrum for transmission, frequency re-use may be necessary. A technique for reducing near-in lobes by cancellation is described. This technique takes a small portion of the radiation from the antenna aperture and generates the near-in lobes, which are are then fed out-of-phase relative to the main signal. Results of sample cases indicate that the first three lobes can be nearly eliminated at a 40% reduction in aperture efficiency.

Introduction

A current NASA-sponsored work program has as its objective the development of antenna techniques that may be useful in high-gain satellite antennas used for Earth communications. One of the most important characteristics of such future antennas will probably be extremely low sidelobes. This is because of the expected use of the same carrier frequency channel simultaneously on several different antenna beams, each carrying different information. To avoid interference, such beams should not overlap. However, interference also exists when the sidelobe of one such beam occurs within the main lobe of another. The power transmitted within this sidelobe, as dictated by its gain, will determine whether it is detected by an Earth station and cause interference.

Sidelobe size and structure are the result of the illumination function on the antenna aperture. Uniformly illuminated circular apertures result in first sidelobes of about −17 dB. When the illumination is reduced at the aperture edge (tapering), sidelobes are reduced. Interfering structures in front of an aperture (feeds and struts for a paraboloidal reflector) will change this distribution and also raise sidelobes. A typical reflector antenna with 10-dB taper and average blockage may have first sidelobes of about −20 dB. More extreme tapers can be used, and, with careful attention to blockage, sidelobe structure can be improved. But it is generally conceded to be doubtful that a

–30-dB sidelobe level could be reached by edge-taper schemes—probably a –26-dB number is more likely.

A required level of sidelobe reduction has not been established for any specific system as yet. However, there are indications (Reference 1) that the levels mentioned above may not be adequate and that means other than edge-taper might be needed to obtain even lower sidelobes.

The lobes of importance are only the first, second, and possibly the third, since beyond that point the lobes will be looking into regions of no interest for frequency re-use.

The following sections describe a technique for lowering near-in sidelobes, but at the expense of gain and an increase in the lobes that occur at greater angles from the main beam.

Sidelobe Cancelling

An approach to this problem is to construct a second antenna whose radiation pattern is similar to only the sidelobe structure of the main antenna. If this second antenna is then excited out-of-phase relative to the main unit and of proper magnitude, the sidelobes will be eliminated or greatly reduced. The example chosen for the cancelling antenna for discussion in this article is a selected ring or rings within a circular aperture.

Consider a circular aperture as the radiating source of the spacecraft antenna. It might be a circular paraboloid, or the face of a phased array, horn, or lens antenna. As a parabola or lens, the illumination would normally be tapered for 20-dB sidelobes; as an array, it could be uniform for 17-dB first sidelobes. Further, consider this aperture to be made up of a complete set of narrow adjacent concentric circular rings. Each ring may be assumed to be uniformly excited, the intensity being a function of its radius and the taper on the overall aperture. Each of these rings is then considered as a separate radiating aperture. The illumination on this sub-aperture is uniform around the periphery and zero throughout the rest of the area, which gives rise to a multilobed interference type of pattern—the larger the ring radius, the narrower these lobes will be. The sum of the patterns of all rings is the total pattern of the aperture. This suggests the way to reduce the inner sidelobes. A particular ring region will have its first interference lobe at the same (or near) position as the first lobe of the total antenna pattern. If this region of the aperture were then excited at 180-deg phase reversal, it would tend to cancel this first main lobe. Magnitude would be set by choosing the proper ring region and varying its width.

Sample Calculations

Figure 1 represents a coordinate system and the quantities that make up a circular aperture consisting of rings of equal width. A good approximation to a tapered illumination from a horn-type feed for either paraboloid or lens is

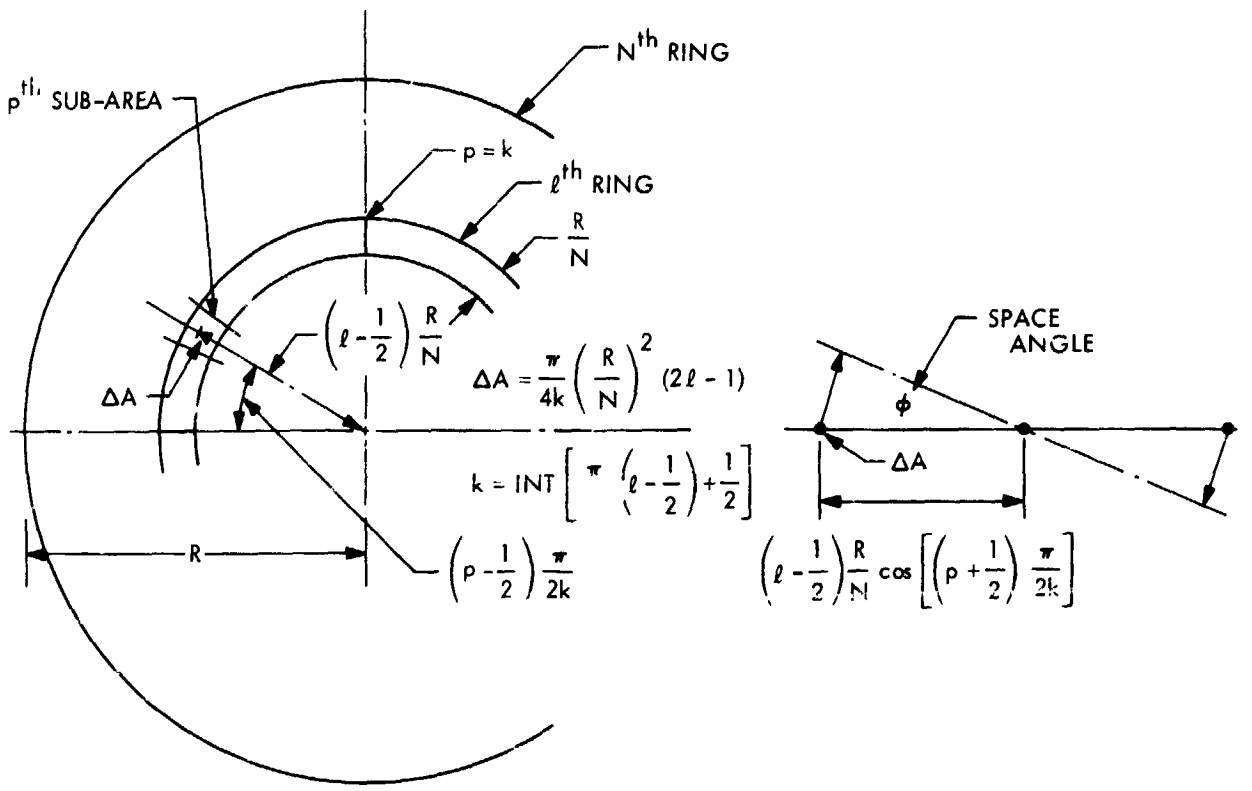

Figure 1. Aperture coordinate system

$$P(r) = \exp\left[-2a\left(\frac{r}{r_0}\right)^2\right] \text{watts/cm}^2 \qquad (1)$$

where r_0 is the aperture radius, and a defines the taper magnitude at the aperture edge. As a goes to zero, 100% efficient uniform illumination would be obtained.

When the aperture is made up of many rings, each ring can be considered as uniformly illuminated, at a value

$$\exp\left[-2a\left(\frac{\ell - \frac{1}{2}}{N}\right)^2\right] \text{watts/cm}^2 \qquad (2)$$

for the particular ring indexed by ℓ. The far-field pattern of such a ring can be considered as the sum of contributions from its smaller segments, ΔA, identically excited:

$$\sum_{p=1}^{k_\ell} \cos\left\{\frac{\left(\ell - \frac{1}{2}\right)}{N} (2\pi R\lambda \sin\phi) \cos\left[\left(p - \frac{1}{2}\right)\frac{\pi}{2k_\ell}\right]\right\}$$

where k_ℓ = integer value of

$$\left\{\frac{\pi}{2}\left(\ell - \frac{1}{2}\right) + \frac{1}{2}\right\}$$

k_ℓ is chosen in this manner so that the segments that make up the rings will be of nearly the same area throughout the aperture.

The total pattern is the sum of all rings,

$$E(\phi) = \sum_{\ell=1}^{N} \exp\left[-a\left(\frac{\ell - \frac{1}{2}}{N}\right)^2\right] \sqrt{\frac{2\left(\ell - \frac{1}{2}\right)}{k_\ell}}$$

$$\times \sum_{p=1}^{k_\ell} \cos\left\{\frac{\left(\ell - \frac{1}{2}\right)}{N} (2\pi R\lambda \sin\phi)\right.$$

$$\left. \times \cos\left[\left(p - \frac{1}{2}\right)\frac{\pi}{2k_\ell}\right]\right\}$$

To demonstrate the performance of such an antenna, a 50-wavelength aperture with 10-dB taper was assumed, and ring patterns were calculated for the outer half. The inner rings have broad patterns and are not useful in this cancelling technique. The total number of rings was set at 36; patterns of some of these are presented in Figure 2, which shows the relative spacings of their lobes. Boresight is at 0 deg. The total aperture pattern is then shown in Figure 3; the first, second, and third sidelobes are at 2.1, 3.25, and 4.4 deg. Observation indicates that ring 24 (⅔ of the distance to the edge) generates a lobe in such a position as to cancel the first sidelobe. However, it does not affect the second lobe, but increases the third lobe of the main pattern. Further, ring 30 cancels the second lobe, while ring 31 cancels the third, but does not aid in cancelling the first sidelobe. Selective

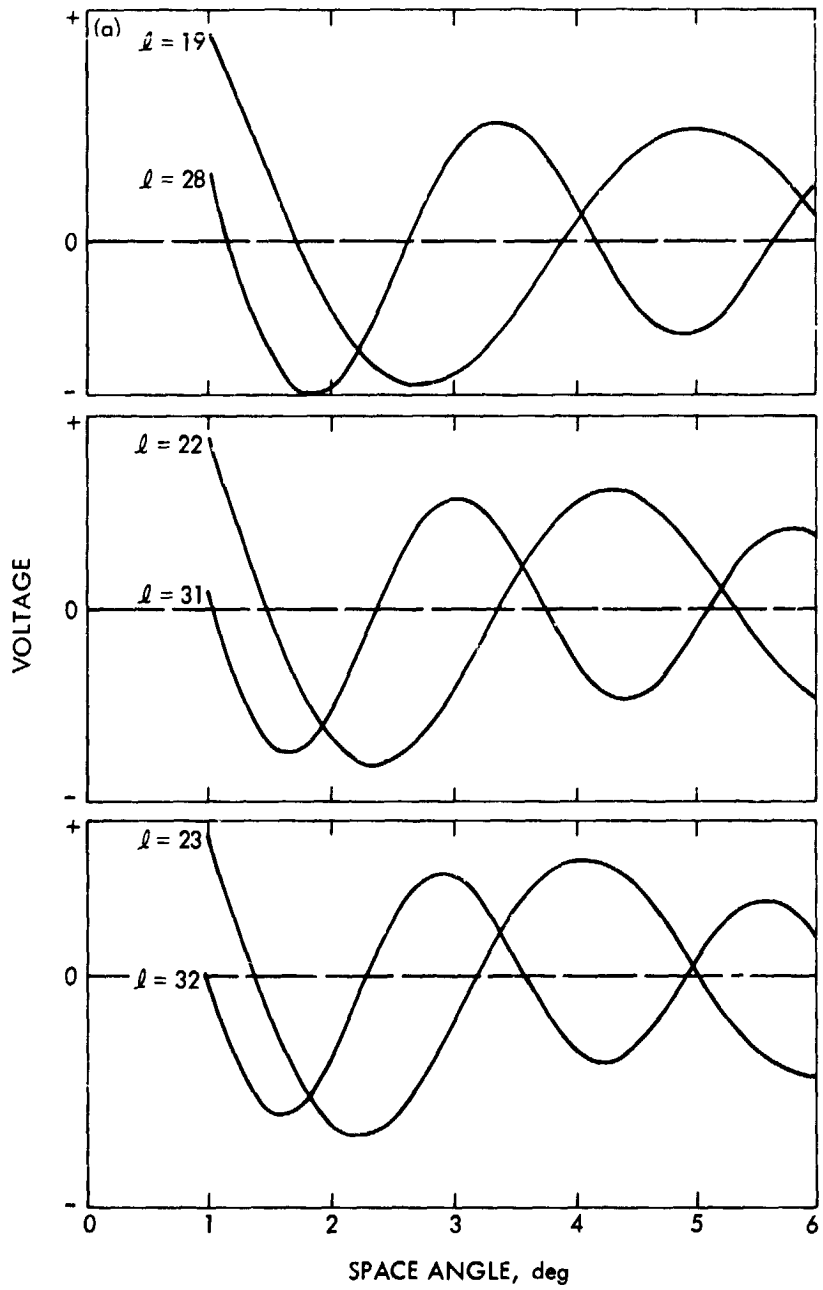

Figure 2. Ring radiation patterns

combinations must therefore be tried to obtain a proper combination to reduce the first three lobes. Such a result is indicated in Figure 4. The first three sidelobes of the main pattern are indicated (main lobe is not shown), as well as the contributions of four selected rings. The result of reversing the phase of the selected rings is near-cancellation of the sidelobes from 2 to 5 deg off boresight, with a lobe coming up beyond 5 deg. Figure 5 shows the resulting radiation pattern, to be compared with that shown in Figure 3. Sidelobe radiation lies below –37 dB out to about 5 deg, beyond which point the lobes increase well above the normal pattern, but still remain below –28 dB. Other similar combinations can be chosen with slight variations in the result.

Attempts to achieve significant sidelobe reduction using only a single ring did not succeed. Although the first lobe was reduced, other lobes increased.

The technique described could be easily implemented with a waveguide lens antenna by placing 180-deg phase shifters in selected ring areas about the lens center.

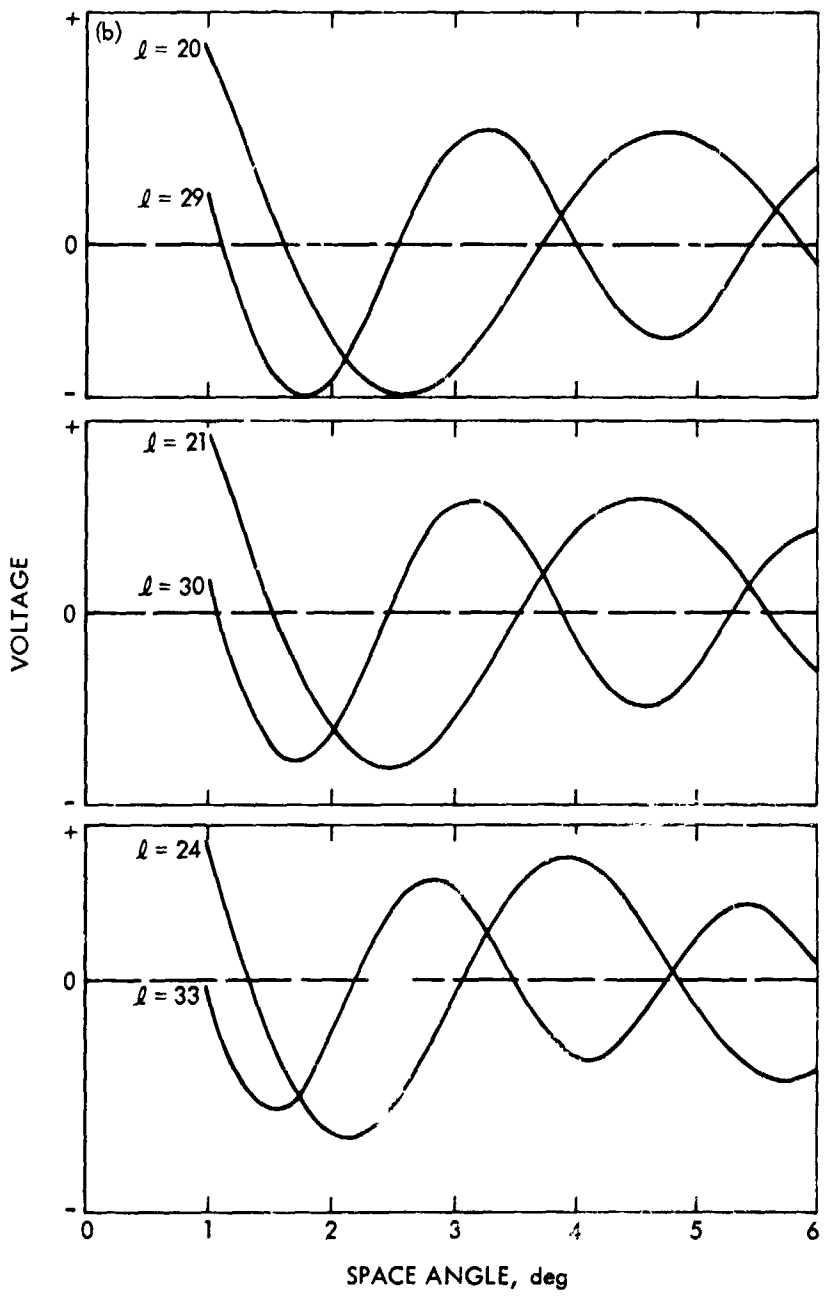

Figure 2. (contd)

Conclusion

Phase reversal of selective aperture zones can effectively cancel given sidelobes in the radiation pattern of a circular aperture far beyond the sidelobe reduction obtainable by edge-taper techniques. The technique necessarily reduces the on-axis antenna gain because of the reduced illumination efficiency. In the example given, this gain was reduced by about 2.2 dB in cancelling the first three lobes.

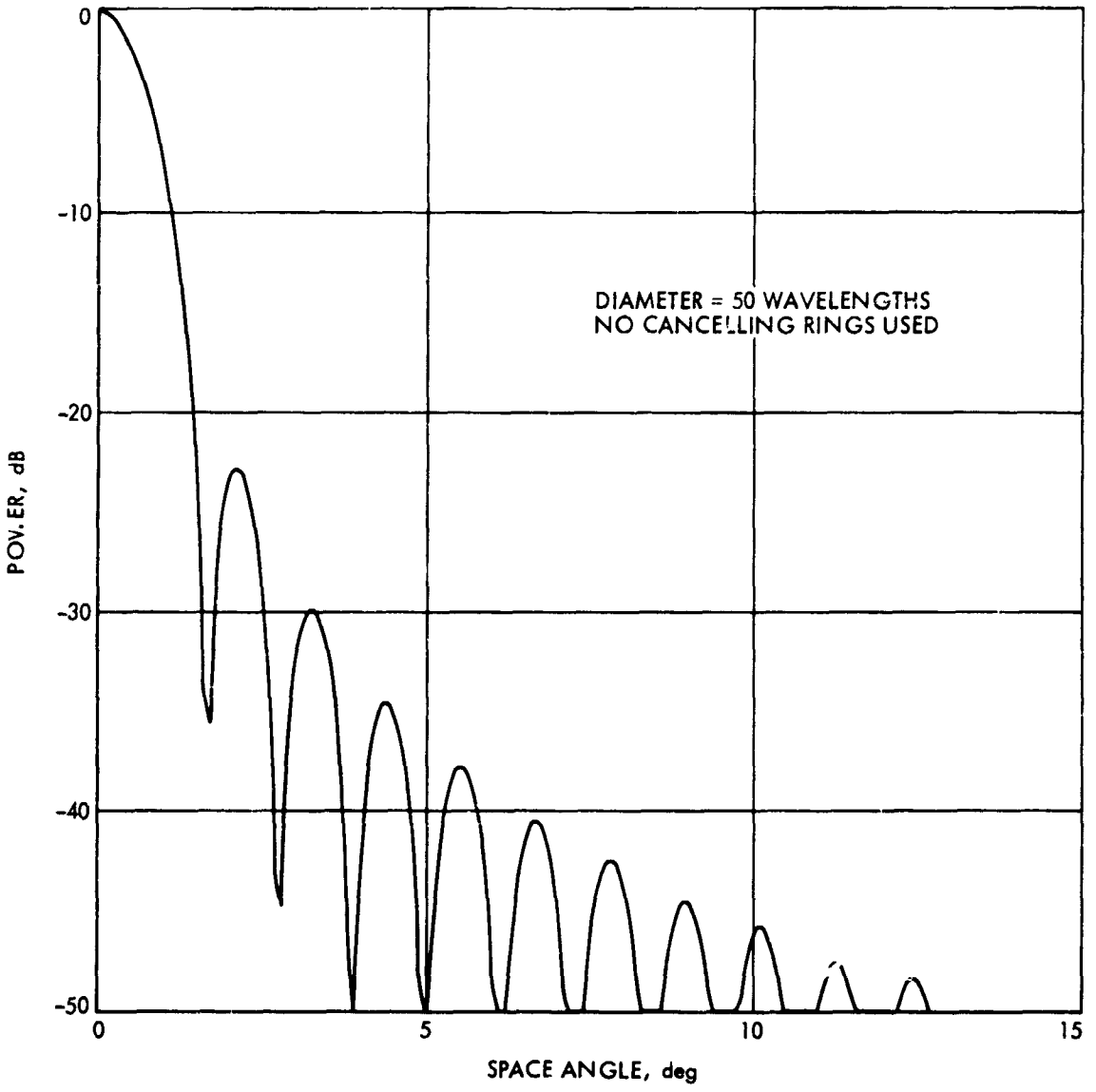

Figure 3. Pattern of circular aperture illuminated with 10-dB taper

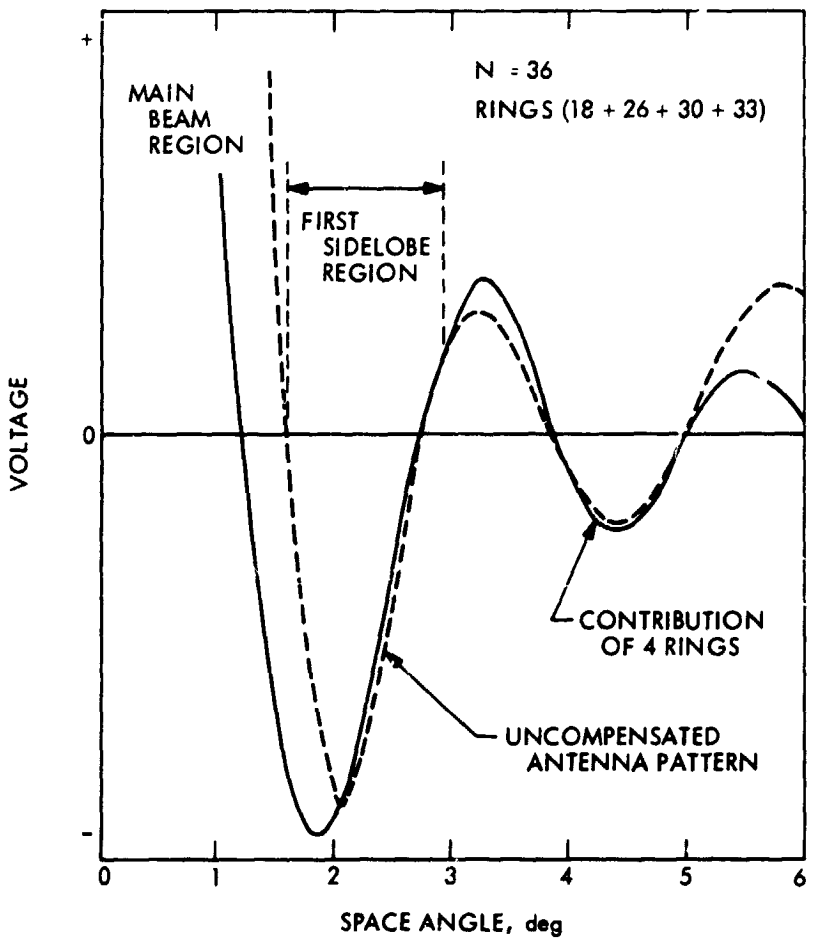

Figure 4. Illustration of the subtraction of the contributions from four rings

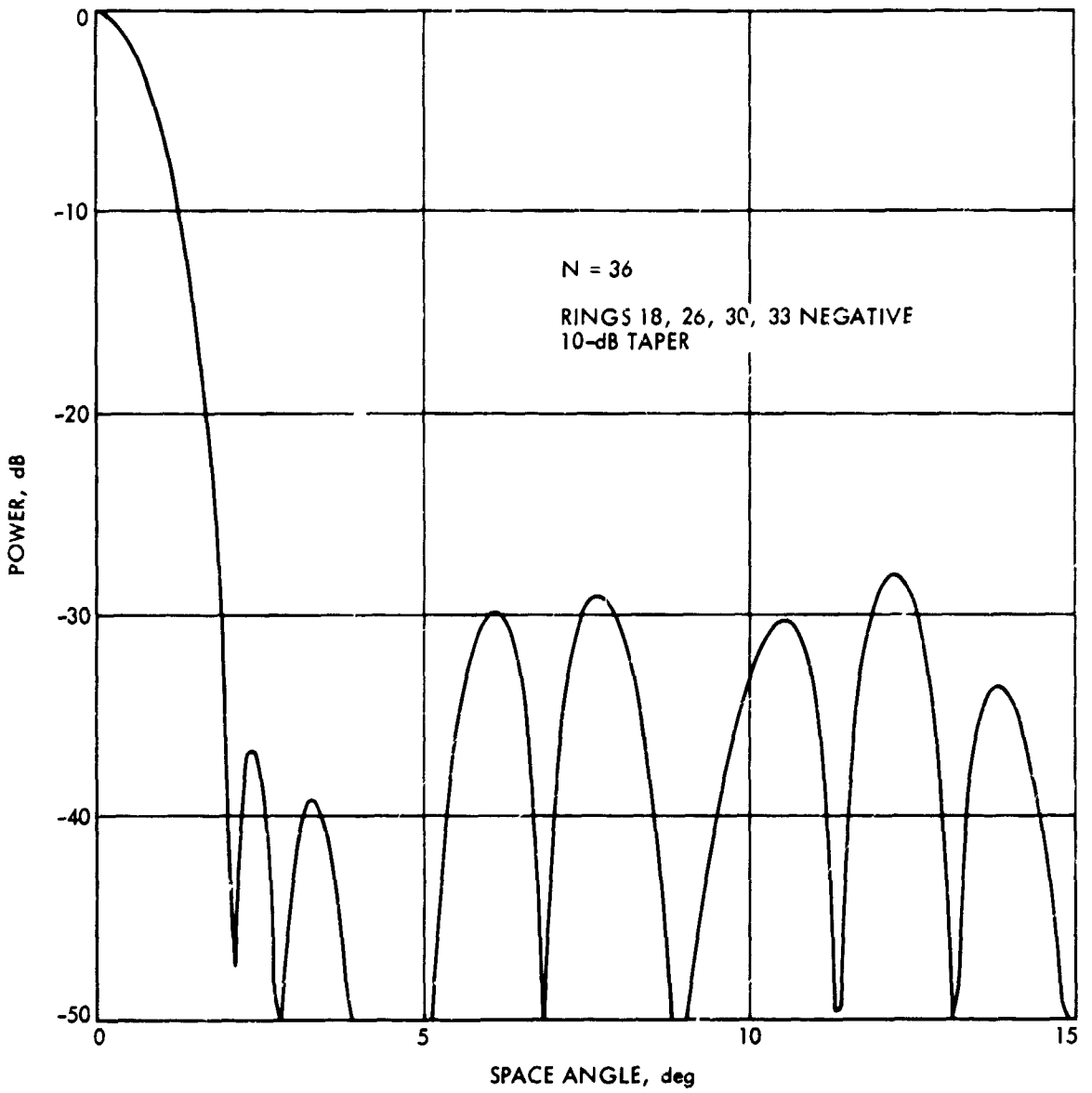

Figure 5. Radiation pattern resulting from sidelobe cancellation technique

Reference

1. Document IV/1057-E, CCIR XIIth Plenary Assembly, New Delhi, Nov. 19, 1969.

N72-17893

JPL Quarterly Technical Review Volume 1, Number 4 January 197.

Development of a 20-W Solid-State S-Band Power Amplifier

A. G. van der Capellen

Telecommunications Division

As an alternative to the use of traveling-wave-tube amplifiers in spacecraft with long-life mission requirements, JPL is developing a solid-state 20-W S-band power amplifier. Traveling-wave-tube amplifiers have limited reliability because of the relative short life of the cathode and the complexity of the power supply. A solid-state amplifier with an output of 20 W at 2295 MHz, a dc/RF efficiency of 38%, and a gain of 27 dB has been developed. This article describes the physical and electrical performance of the solid-state amplifier.

Introduction

A solid-state 2295-MHz prototype power amplifier is being developed in support of anticipated long-life missions such as the Outer Planet Grand Tour missions and the Space Station program. Traveling-wave-tube (TWT) amplifiers are not suitable because of their limited reliability and short life. Presently available microwave power transistors make solid-state power amplification at S-band feasible. The solid-state power amplifier is to be designed to operate continuously for 12 yr. Design goals for this amplifier are summarized in Table 1.

Circuit Description

All circuitry is housed in one module. Figure 1 is a block diagram of the power amplifier and Figure 2 shows the module. The amplifier consists of three driver stages. The first two stages employ MSC 3000 transistors and the third stage uses the MSC 3003. The final stage consists of four summed MSC 3005 transistors. All stages except the first operate Class C in common base configuration. The first stage is biased in Class A (common base). A single-stage amplifier is shown in Figure 3 and a schematic in Figure 4. Semilumped circuitry is employed in the amplifiers, consisting of two pairs of Johanson Type 6453 capacitors (in a back-to-back configuration) forming an L matching network. Interstage coupling is achieved by short pieces of

Table 1. Design goals for the 20-W solid-state S-band power amplifier

Electrical:	
RF power output	20 W
Frequency	2295 MHz
Efficiency	30% minimum (goal 40%)
Bandwidth	>20 MHz (1 dB)
Gain	28 dB
Spurious signal output	>70 dB below rated output
Input impedance	50 Ω nominal (VSWR to be determined)
Load impedance	50 Ω nominal (open or short circuit capability to be determined)
Environmental:	
Life (combined effect of radiation, aging, etc.)	12 yr (confidence = 0.95, power degradation < 1 dB)
Temperature	-40 to +65°C (power degradation to be determined)
Baseplate	35°C (average temperature for reliability calculations)
Physical (exclusive of thermal baseplate):	
Weight	1.3 kg
Size	12.5 × 22 × 4.5 cm

50-Ω microstrip lines on alumina substrates to facilitate testing. The power splitter and summer are identical in design and consist of 50-Ω, 3-dB hybrids, which provide a port-to-port isolation of approximately 30 dB and input-to-output insertion loss of 0.3 dB (for one splitter or summer). The final summing point is connected to a drop-in type circulator (0.3-dB insertion loss at 2.3 GHz), which serves as protection against inadvertent load removal. All amplifier stages are voltage-derated and operate off a dc supply voltage of 25 V.

Assuming thermal resistances for the transistors to be as stated by the manufacturer, i.e.,

MSC 3005 = 8.5°C/W

MSC 3003 = 17°C/W

MSC 3000 = 45°C/W

the highest calculated junction temperature occurs in the MSC 3003 driver. For an assumed baseplate temperature of 35°C, this transistor junction is calculated to operate at 96°C. This is within the goal of 100°C maximum

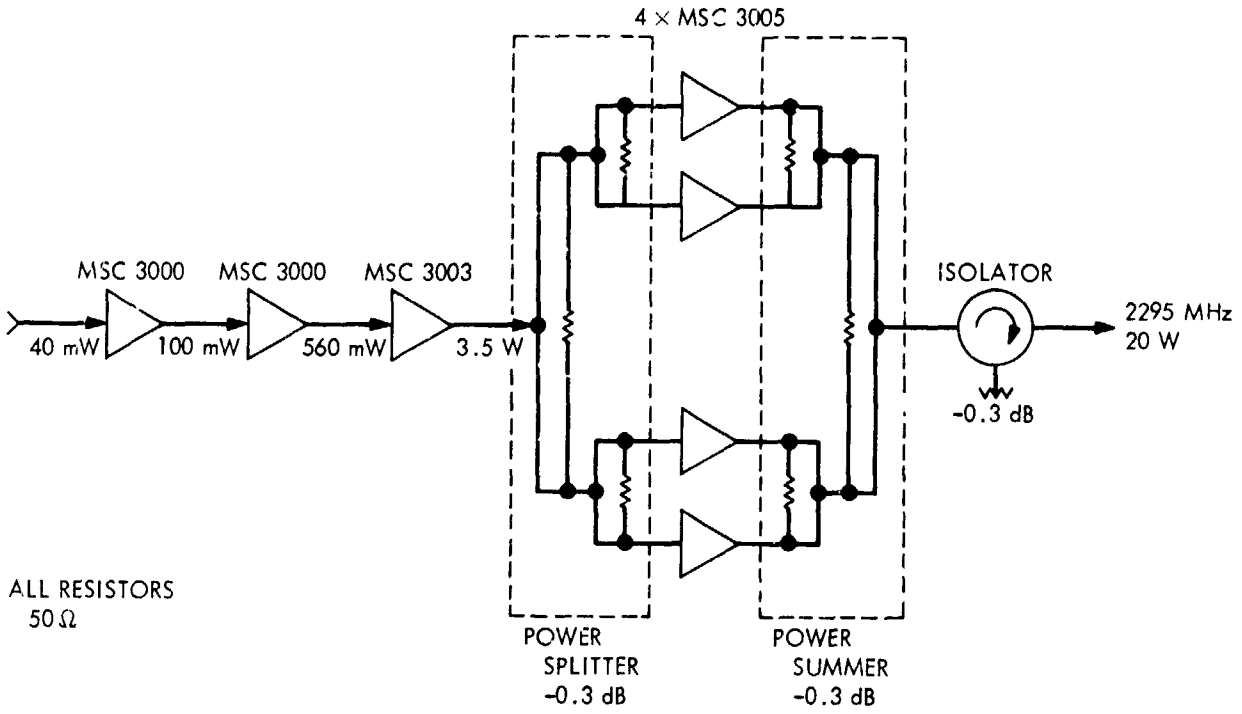

Figure 1. Block diagram of 20-W solid-state S-band power amplifier

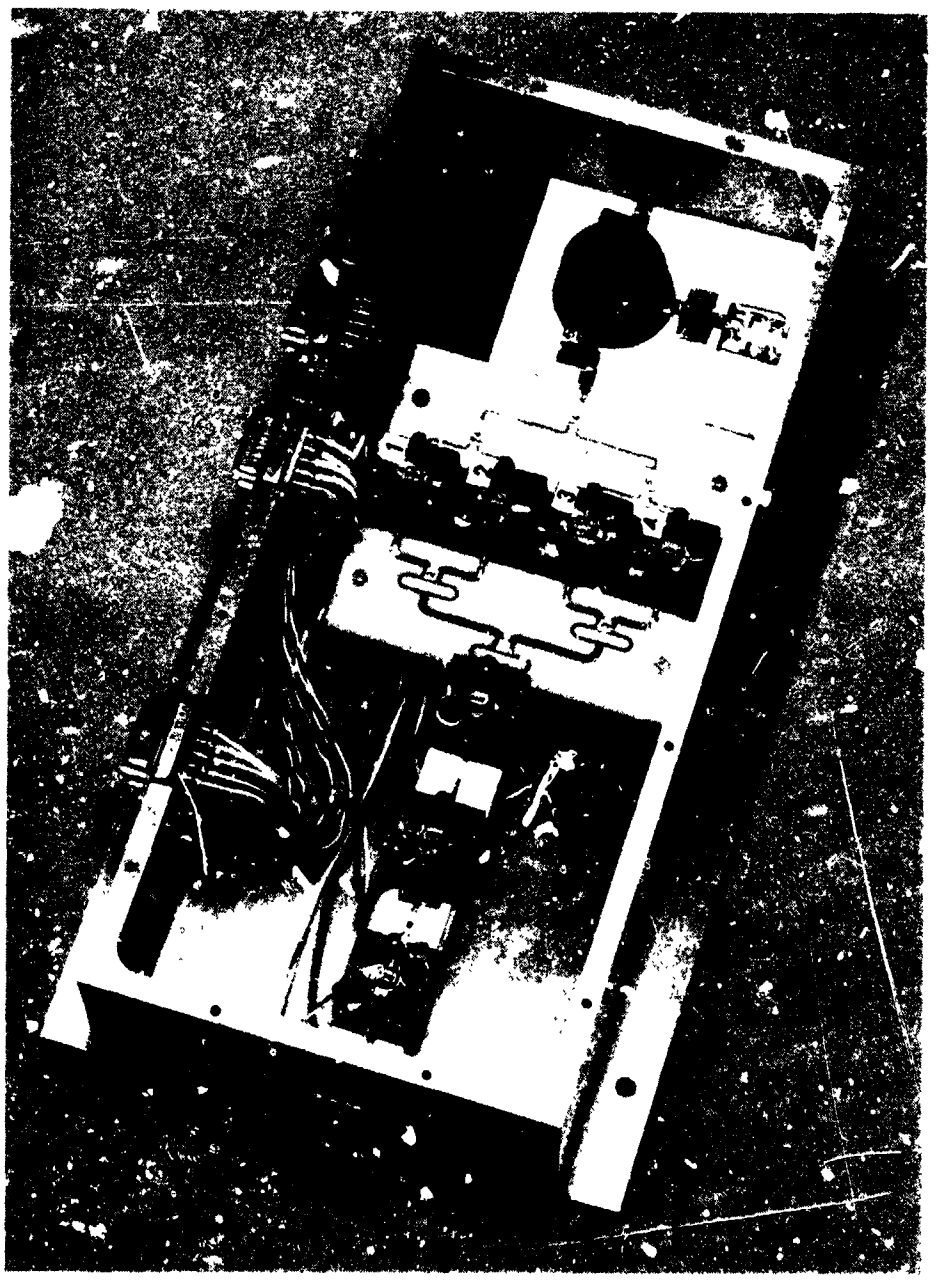

Figure 2. Breadboard of 20-W solid-state S-band power amplifier

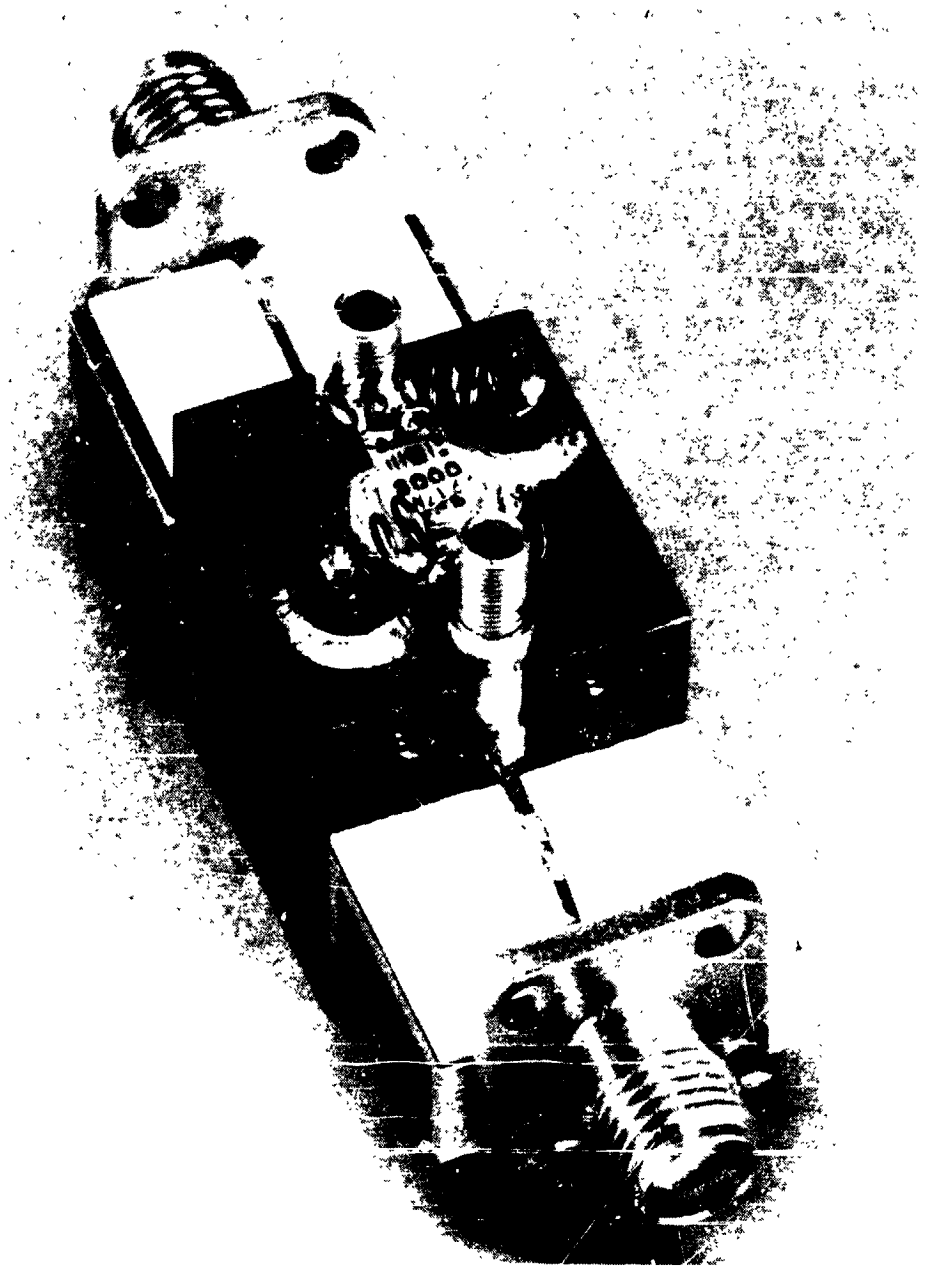

Figure 3. Single-stage amplifier breadboard

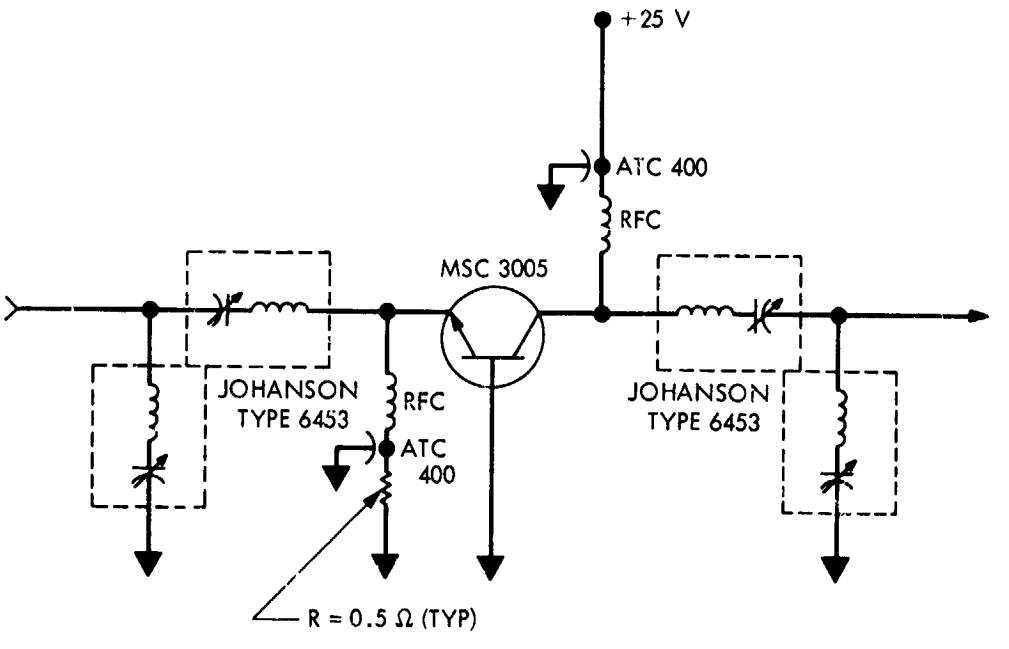

Figure 4. Single-stage amplifier schematic

Table 2. Performance data for single-stage amplifier MSC 3005[a]

Output power, W	Gain, dB	Efficiency, %	Supply voltage, V
6.8	9.3	42	25
6.4	9.0	50	25
5.0	5.6	54	25
5.0	4.8	55	25
8.0	7.3	45	28

[a] Frequency = 2295 MHz; bandwidth = 100 MHz (3 dB).

junction temperature set for this development. The MSC 3005 operates at a junction temperature of 86°C (under the same assumptions).

Development Status

The power amplifier breadboard shown in Figure 1 has been developed at JPL. An output of 20 W at 38% dc/RF efficiency and 27-dB gain has been achieved with a dc supply voltage of 25 V. Bandwidth is 35 MHz (3 dB), 25 MHz (1 dB). Data for the output stage (MSC 3005) are shown in Table 2.

Four MSC 3005 transistors were radiation-tested. Table 3 summarizes the dose values that the transistors were exposed to (including background radiation). The transistors were not operating during irradiation. They were mounted in test fixtures where they remained throughout all RF and radiation testing. This procedure was followed to avoid a shift in the data as a result of displacement of the transistor relative to the circuit. All four MSC 3005 transistors survived the radiation test without observable (resolution 0.2 to 0.5 dB) degradation.

RF breakdown tests have been conducted on the final stage. No breakdown of any kind was observed at pressures between 10.1 N/cm^2 and 4.0×10^{-7} N/cm^2 (760 torr and 3×10^{-5} torr). (Electron source was present.)

Table 3. Radiation dose values

Radiation type	Energy, MeV	Flux, particles/cm^2-s	Fluence, particles/cm^2	Background
Electrons	2	3×10^{10}	1.4×10^{13}	None
Neutrons	1.5	1.4×10^{10}	1.6×10^{13}	4.3×10^3 rad
Protons	140	1.2×10^8	$9 \pm 2 \times 10^{12}$	$10^9 - 10^{10}$ neutrons/cm^2 5×10^4 rad

Four MSC 3005 transistors in final stage configuration are presently under life test; 1200 h have been accumulated without failure. Baseplate temperature is held at 35°C.

Work has begun on the development of a microstrip version of the 20-W power amplifier with plans to achieve a wider bandwidth (200 MHz, 3 dB minimum). This amplifier will employ an RCA TA 7995, which has emitter ballasting for better reliability.

Future plans include a trade study between efficiency and other requirements such as bandwidth, life, and temperature. Radio frequency life testing will continue to gather more data. Also, failure mechanisms in microwave power transistors will be studied along with a transistor RF circuit model.

N72-17894

JPL Quarterly Technical Review Volume 1, Number 4 January 1972

A Markov Chain Technique for Determining the Acquisition Behavior of a Digital Tracking Loop

H. D. Chadwick

Telecommunications Division

Tracking loops have two characteristic modes of operation: acquisition and steady-state tracking. The steady-state behavior of such nonlinear tracking loops as the phase-locked loop has been the subject of considerable analysis. The acquisition behavior of a loop, the transition period between turning the loop on and the steady state, has resisted analysis for all but the simplest configurations. An iterative procedure is presented for determining the acquisition behavior of discrete or digital implementations of the tracking loop. The technique is based on the theory of Markov chains and provides the cumulative probability of acquisition in the loop as a function of time in the presence of noise and a given set of initial condition probabilities. A digital second-order tracking loop to be used in the Viking command receiver for continuous tracking of the command subcarrier phase has been analyzed using this technique, and the results agree closely with experimental data. Possible extensions of the technique include the analysis of continuous loops using discrete approximations.

Introduction

A digital second-order servo loop is to be used in the Viking command receiver for continuous tracking of the command subcarrier phase (Reference 1). An initial coarse estimate of the subcarrier phase is provided by a separate circuit, and the tracking loop is expected to begin tracking with an initial phase error as large as the maximum error of the coarse estimate and a phase error rate of change due to the doppler shift. The subcarrier loop should be able to acquire lock and eliminate this initial error, thus yielding a small steady-state average phase error. The behavior of this loop during this initial acquisition is studied in this article. The cumulative probability of acquisition as a function of time in the presence of noise has been calculated for the loop by a Markov chain approach.

Tracking Loop Model

The subcarrier tracking loop being analyzed is illustrated in Figure 1. It is a typical digital second-order loop which is complicated by the presence of

the limiter in the error signal path. Figure 2 shows the same loop reduced to its important details. The accumulate-and-dump circuit for the error signal accumulates the values of $2M$ phase samples and has the effect of only improving the signal-to-noise ratio per $2M$ samples. Otherwise it may be ignored for analytical purposes. The effect of using the sign bit of this accumulator is equivalent to that of a limiter circuit. The subcarrier waveform, which is sampled in the phase detector, is basically a square wave, with a small linear region in the vicinity of the zero point. This waveform is illustrated in Figure 3. The phase quantization level or "bump" size is determined by the phase detector and the phase estimate accumulator. Sampling in the phase detector can be performed twice per cycle with appropriate sign reversal circuitry. This circuitry can also be ignored in the analysis. The phase detector can thus be considered to provide a signal that is linearly related to the phase error over a small region close to zero and saturates to a constant level beyond the linear region. A new phase estimate is provided once every M subcarrier cycles (one data bit period).

Discrete State Space

Using the model described in the previous section, there are two state variables inherent to the tracking loop. These variables have been assigned and labeled x_1 and x_2 in Figure 2, where x_1 is the phase error signal and x_2 the loop accumulator output. The state space for the loop is thus two-dimensional and discrete because movement from one point to another can only take place in discrete jumps. The system is also discrete in time, and the movement in the state space is describable by difference equations.

In the absence of noise, because of the nonlinearity presented by the limiter, the state space must be analyzed in two regions: the region in which $x_1 > 0$ and the limiter output is positive, and the region in which $x_1 < 0$ and the limiter output is negative. In this noiseless case, the loop will follow a

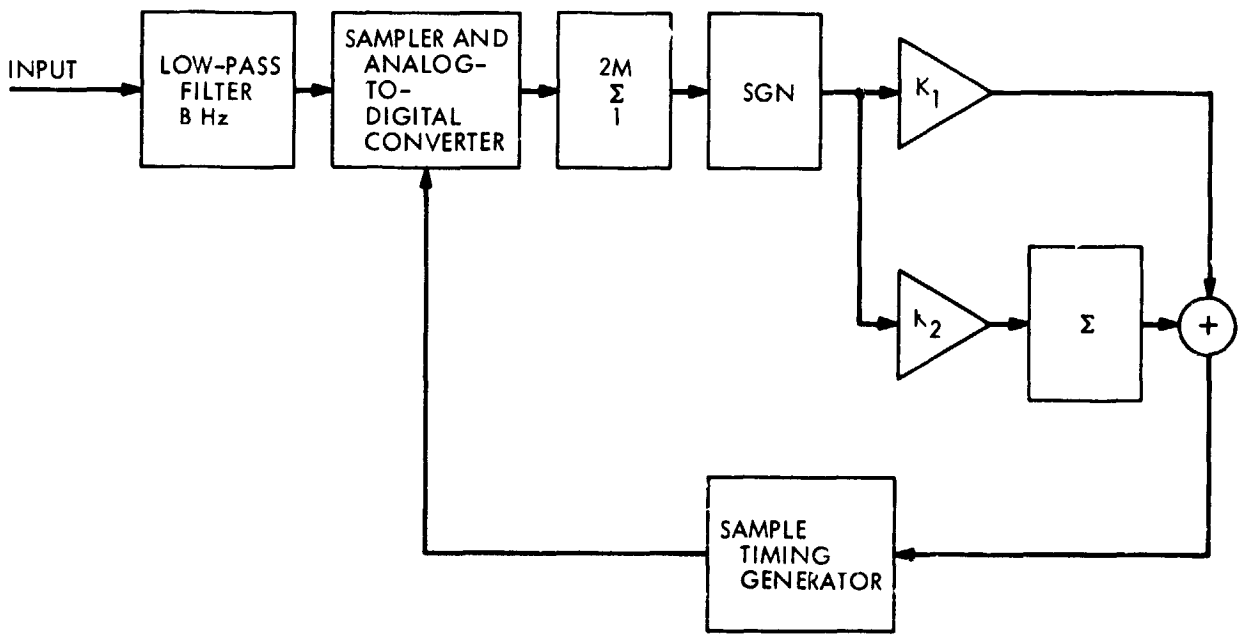

Figure 1. Subcarrier tracking loop

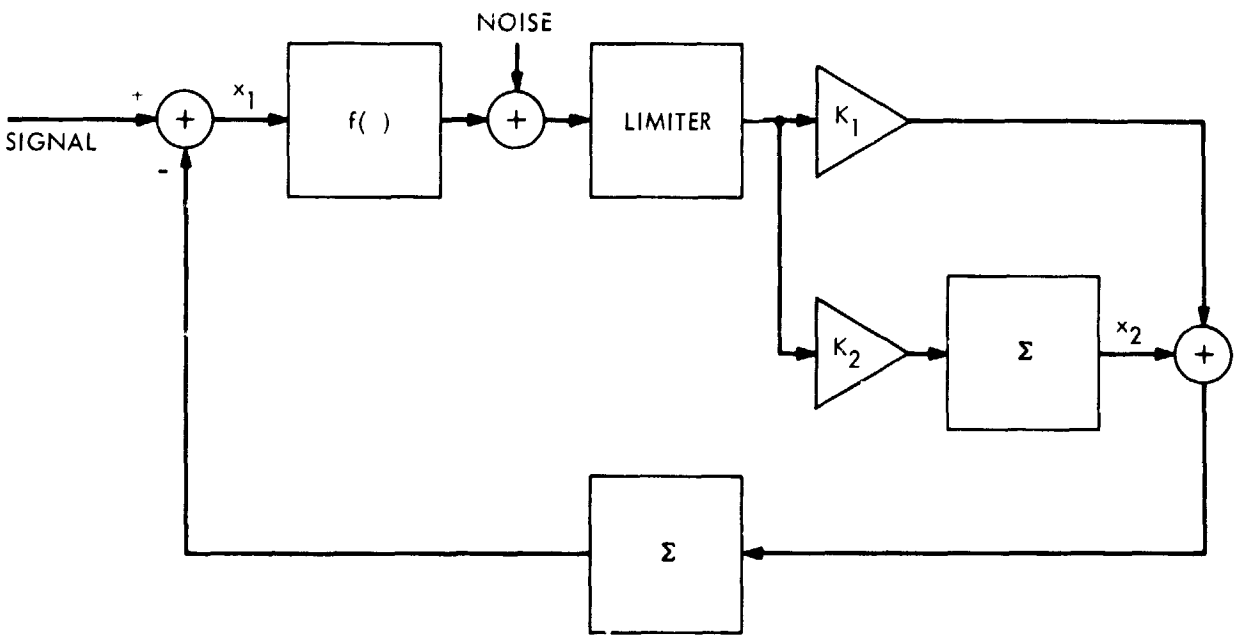

Figure 2. Equivalent subcarrier tracking loop

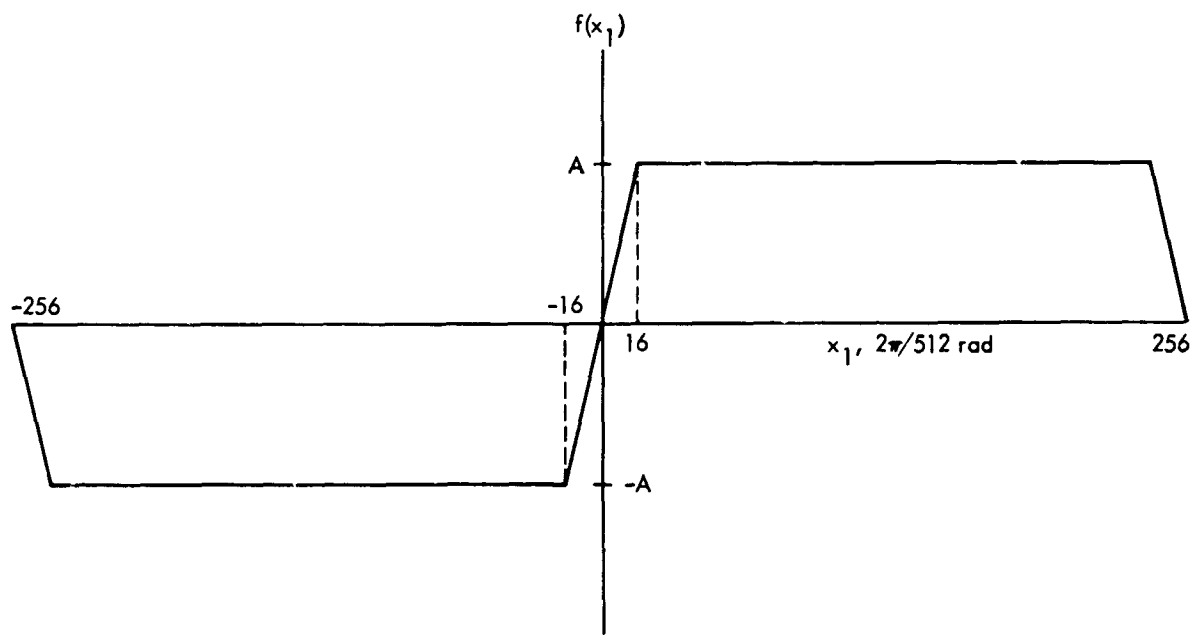

Figure 3. Phase detector characteristic

deterministic path from a point representing a given set of initial conditions to an equilibrium point.

When noise is present, however, the path becomes a random walk in the x_1,x_2 plane. At each point in the plane there are two possible subsequent points. One such point is the same as the noiseless deterministic point and will occur if the limiter input signal (phase error) plus noise has the same polarity as the signal only. The other point may be considered the wrong point and occurs if the noise biases the limiter input to a polarity opposite that of the phase error. Thus, for every possible origin point in the plane, there are two destination points, and the transition probabilities can be computed from the noise probability density and the phase error amplitude.

Transition Probability Matrix

The movement of the state of the tracking loop in the state plane can be considered as a random walk or Markov chain. If the transition probabilities from state to state are written in the transition probability matrix P, then, in matrix notation,

$$p_{n+1} = Pp_n \tag{1}$$

where p_n is the vector of state probabilities after n iterations of the loop. Given the initial state probabilities p_0, iterative application of Equation 1 will provide the state probabilities for any time thereafter. The boundary conditions for the state space are crucial to the application of this equation. In a steady-state analysis, it does not matter which subcarrier cycle the loop is presently tracking. For this purpose, the boundaries of the phase error variable at ±½ cycle from the origin may be made reflecting. This is equivalent to considering the phase error modulo 2π, which is common in phase-locked loop analyses. In this case a steady-state solution to the state probabilities can be obtained from the eigenvector equation

$$p = Pp \tag{2}$$

where p is the vector of steady-state probabilities. For acquisition, however, movement from one subcarrier cycle to another is considered failure to acquire and this probability is of interest. (This definition of acquisition without cycle slipping was a requirement of the Viking mission.) The boundary at $x_1 = \pm ½$ is, therefore, made absorbing, and the probability of reaching this boundary is called the probability of failure to acquire. With these boundary conditions, the steady-state probability vector is zero for all states except the boundary. The loop will eventually go out of lock with probability one. For the purposes of studying the acquisition behavior, a small region around the equilibrium point was defined as the lock region, and the cumulative probability of reaching this region was calculated as a function of the number of iterations of the Markov chain equation.

Determination of Transition Probabilities

Examination of the system diagram in Figure 2 shows that the difference equations for the transitions that can occur are:

$$E(x_2) = K_2 \text{ sgn } [f(x_1) + n] \tag{3}$$

$$E(x_1) = E(\theta) - x_2 - K_1 \text{ sgn } [f(x_1) + n] \tag{4}$$

where E is the forward difference operator, θ is the phase angle input, $E(\theta)$ is the change per time interval of the phase angle, and n is the sum of $2M$ gaussian noise samples. The function $f(\bullet)$ is the phase detector characteristic of Figure 3 multiplied by the accumulator gain of $2M$. When

$$f(x_1) + n > 0$$

the signum function is $+1$ and

$$E(x_2) = K_2 \tag{5}$$

$$E(x_1) = E(\theta) - x_2 - K_1 \tag{6}$$

The probability of this occurrence is

$$p^+(x_1, x_2) = \frac{1}{2}\left[1 + \text{erf}\left(\sqrt{R(x_1)/2}\right)\right] \tag{7}$$

where

$R(x_1)$ = phase accumulator output signal-to-noise ratio

$= f^2(x_1)/2MN_0B$

$N_0/2$ = two-sided noise spectral density

B = noise bandwidth

The probability of the complementary event that

$$f(x_1) + n < 0$$

and

$$E(x_2) = -K_2 \tag{8}$$

$$E(x_1) = E(\theta) - x_2 + K_1 \tag{9}$$

is

$$1 - p^+(x_1, x_2) = \frac{1}{2}\operatorname{erfc}\sqrt{R(x_1)/2} \tag{10}$$

These relations depend only on the values of x_1 and x_2 and the signal-to-noise ratio R. The transition matrix can therefore be calculated exactly for any specified signal-to-noise ratio.

Acquisition Behavior of the Viking Tracking Loop

A computer program was written to calculate by the above method the cumulative probability of acquisition for the Viking subcarrier tracking loop. The specific values used in the Viking loop analysis are as follows:

M = 16 cycles

1 phase increment = 1/512 cycles = $\pi/256$ rad

K_1 = 6 increments

K_2 = 1 increment

R = 4 dB in the saturated region of the phase characteristic

$E(\theta)$ = 6.5 increments/time unit

The linear region of the phase characteristic extends ±16 increments from the zero point. The initial condition state vector p_0 was calculated from the statistics of the coarse phase estimator by C. Tegnelia (see Figure 4). Because of the large size of the transition matrix (for the above numbers the matrix would be 262144 × 262144), the calculations were performed only in a reduced area of the state plane. The area used for computation was the region $-175 \leq x_1 \leq 75$, $-50 \leq x_2 \leq 50$ (25000 × 25000 transition matrix). The degree of approximation induced by using this reduced area is small due to the phase error rate and initial conditions that were used. The asymptotic

value of the probability of acquisition is biased low, however, because the reduced area causes the probability of absorption at the boundary to be high. This asymptotic value was determined to be high enough to provide a good lower bound for the Viking system.

The results of the calculation are shown in Figure 5, together with experimental values taken from simulation runs. The difference between the curve and the experimental values is probably due to a slight difference in the definition of acquisition between the two cases. The analytical results show that the probability of failure to acquire without cycle slipping within 75 bit periods is less than 10^{-5}, a figure which could not be determined experimentally in a reasonable amount of time. This result indicated that the proposed design would be adequate for the Viking mission.

Further Applications of the Technique

In the future this technique is expected to be used to determine the behavior of the tracking loop during the bit synchronization acquisition phase, which follows the subcarrier acquisition phase in the command

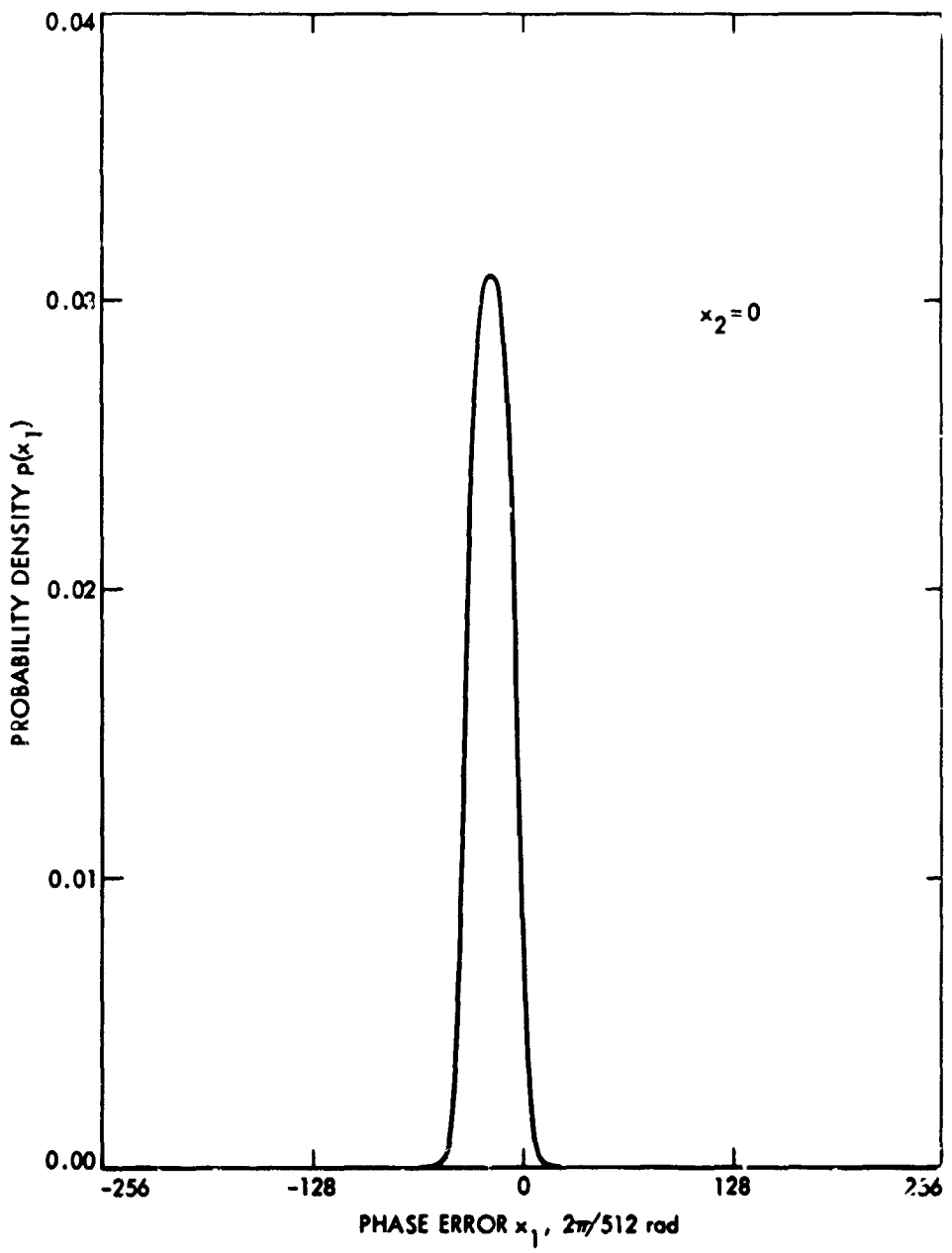

Figure 4. Experimentally determined initial condition state probabilities

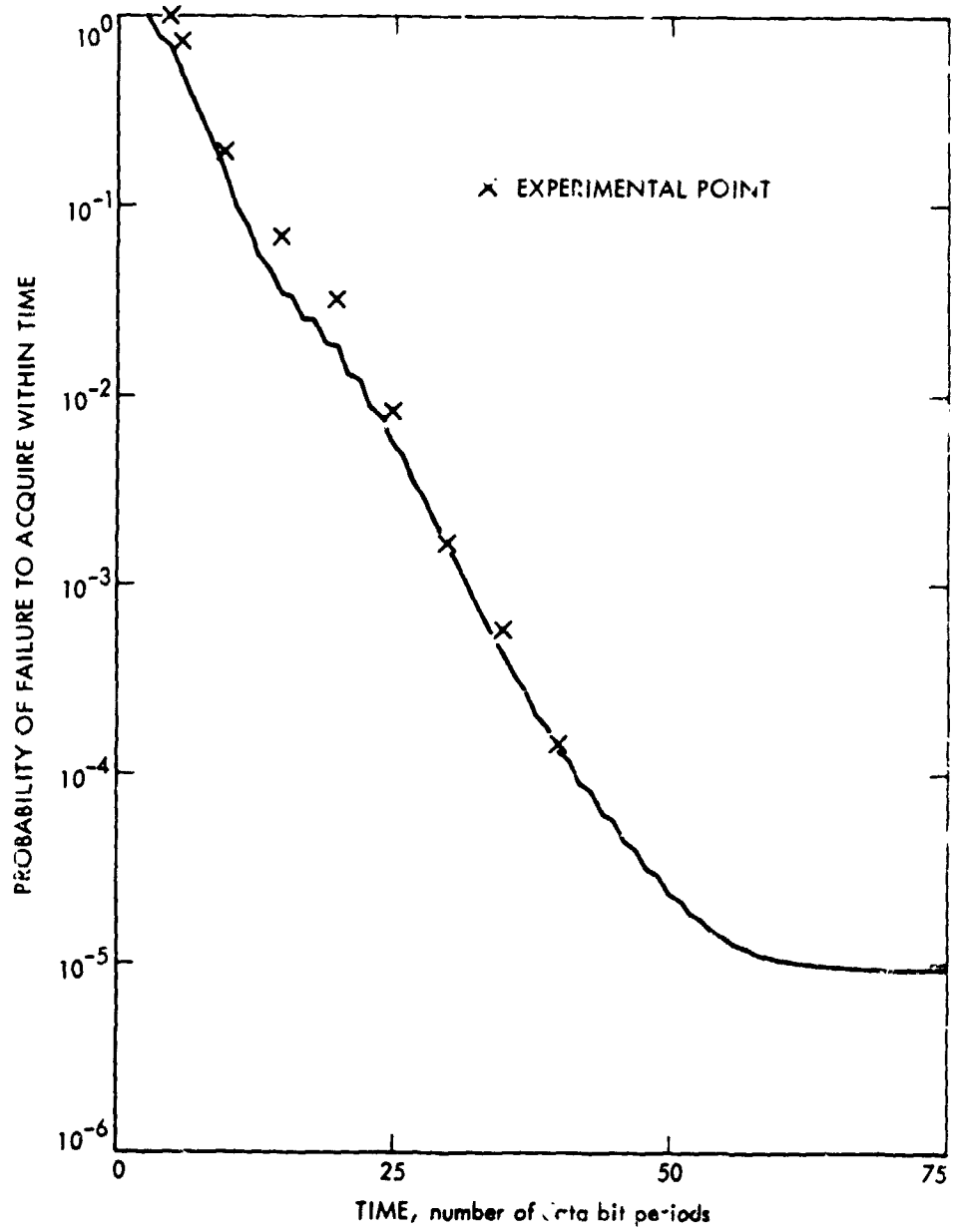

Figure 5. Acquisition probability of loop

receiver. In this case the state probability vector can be used to determine the probability density function of the phase error at the end of the bit synchronization phase, during which the effective signal-to-noise ratio in the loop is reduced.

The technique may also be used in the study of the acquisition behavior of other tracking loop systems. While the Markov chain transition matrix is inherently discrete in nature, it may be applicable to continuous systems with suitable quantized approximations, although the matrix dimensions may make this approach unfeasible.

Summary

A discrete Markov chain technique has been used to determine the acquisition probability as a function of time for a digital tracking loop. The technique has been applied to the Viking command receiver subcarrier tracking loop with results that agree very closely to the experimental results, and extend these results beyond those that can be achieved experimentally

in a reasonable time. The technique is applicable to a wide range of tracking loop problems.

Reference

1. Holmes, J., *Performance of the Second Order All-Digital Command System Subcarrier Timing Loop,* Interoffice Memo 331-71-117, Mar. 24, 1971 (JPL internal document).

N72-17895

JPL Quarterly Technical Review Volume 1, Number 4 January 1972

Bias and Spread in Extreme Value Theory Measurements of Probability of Error

J. G. Smith

Telecommunications Division

Performance tests of communication systems characterized by low bit rates and high data reliability requirements frequently utilize classical Extreme Value Theory (EVT) to avoid the excessive test times required by bit error rate (BER) tests. If the underlying noise is gaussian or perturbed gaussian, EVT will produce results either biased or with excessive spread, if an insufficient number of test samples are used. This article examines EVT to explain the cause of the bias and spread, gives experimental verification, and points out procedures that minimize these effects. Even under these conditions, however, EVT test results are not particularly more significant than BER tests.

Introduction

Classically, performance testing of a digital communication system consists of counting the numbers of wrong outputs of the system in response to a sequence of known inputs. This so-called bit error rate (BER) test procedure is known (Reference 1) to produce an estimator of the probability of error which converges to the right answer eventually regardless of the type of underlying noise; i.e., it is unbiased, consistent, and distribution-free. But, the lower the probability of error of the system, the longer the sequence length must be to generate a sufficient number of errors to construct meaningful confidence intervals; and the lower the data rate of the system, the longer the time required to generate this sufficient sequence.

As a time-saving alternate to BER testing of communication systems characterized by low bit rate and low probability of error, classical Extreme Value Theory (EVT) (References 1–9) has been utilized. Procedures based on classical EVT do not record the number of errors generated by the system, but rather examine the noisy data input to the decision element of the system, and attempt to measure probability of error from the statistics of the noisiest data, i.e., the extremes of the data. Classical EVT is known (Reference 2) to be asymptotically unbiased, consistent, and distribution-free for a broad class of noise. Unfortunately, the rate of convergence of the EVT

estimate to its asymptote is sensitive to the statistics of the underlying noise—and particularly slow when that noise is gaussian (References 6–9). Further, for a large class of noise, including gaussian noise, the estimator suffers either excessive bias or excessive spread for finite sequence length. These two features combine to render classical EVT of questionable advantage in a gaussian-noise type of environment for these communication systems.

This article documents the bias and spread of EVT in the given test environment and indicates how to minimize these effects. Specifically, for a given number of test samples, the effects of the number of extremes and the number of samples from which each extreme is drawn are examined.

Classical EVT

Suppose we have a set of n independent samples (data points) $x_1,\cdots,x_n$ of a random variable X with unknown distribution function

$$F_X(x) = \Pr[X < x]$$

and we want to estimate

$$\Pr[X \geq x_0] = 1 - F_X(x_0)$$

for fixed threshold x_0. The largest (the extreme) value, x, of this sample has a distribution function

$$\Phi_n(x) = \Pr[\text{all } X_i < x]$$

$$= \prod_{i=1}^{n} \Pr[X_i < x]$$

$$= (F_X)^n(x)$$

If the random variable X can take on all values of x (that is, it is not limited to some finite interval), and its distribution function $F_X(x)$ is asymptotically lower bounded by the exponential distribution, then for large enough n, $\Phi_n(x)$ has been shown to be of the asymptotic form (References 1 and 2)

$$\Phi_n(x) = \exp\left\{-\exp\left[-\alpha_n(x - u_n)\right]\right\}$$

where α_n and u_n are unknown parameters. Thus, the procedure followed in classical EVT is this: We take several (k) independent groups of data, each group of size n, and from each group we record the largest (the extreme) sample value. Then, using this block of extremes, we estimate α_n and u_n

[using, for example, a maximum-likelihood criterion, a minimum distance criterion, or possibly others (Reference 2)]. Then our estimate of probability of error becomes

$$p = 1 - F_X(x_0)$$

$$= 1 - (\Phi_n)^{1/n}(x_0)$$

$$= 1 - \left[\exp \left\{ -\exp \left[-\alpha_n (x_0 - u_n) \right] \right\} \right]^{1/n}$$

Note that the total number (m) of samples required for the test is $m = n \bullet k$. Unfortunately, if n is too small, the estimate turns out to be biased. We consider why for gaussian noise.

The Bias of EVT

We define a new random variable v_n (the so-called *reduced variate*) as a function of the underlying random variable X by

$$v_n(x) = -\log \left[n\left(1 - F_X(x)\right) \right]$$

This can be rewritten to obtain

$$F_X(x) = 1 - \exp\left(-v_n(x)\right)/n$$

$$\Phi_n(x) = (F_X)^n(x)$$

$$= \left(1 - \exp\left(-v_n(x)\right)/n\right)^n$$

$$\overrightarrow{n} \exp\left(-\exp\left[-v_n(x)\right]\right)$$

Thus, the extremes of X have a distribution function $\Phi_n(x)$, which asymptotically in n has the double-negative exponential form characteristic of classical EVT. Convergence to this asymptotic form will be fairly rapid, in terms of increasing n, whenever $v_n(x)$ is relatively insensitive to changes in n. Further, the development so far has left F_X unspecified (within the broad class mentioned earlier).

However, the distribution function is in terms of the reduced variate values $v_n(x)$, rather than the extreme values x themselves. Measured or recorded extreme values x must be converted to values $v_n(x)$ before statistics

can be computed. Because the relationship of $v_n(x)$ to x depends on the unknown functional nature of F_X, the characteristics of $\Phi_n(x)$ need to be further understood.

For example, if F_X were exponential, i.e.,

$$F_X(x) = 1 - \exp(-\alpha x)$$

then we could immediately solve for $v_n(x)$,

$$v_n(x) = \alpha(x - u_n)$$

where the only n-dependence appears in the parameter

$$u_n \triangleq (\log n)/\alpha$$

In such a case there would be a nice *linear* relationship between the extremes x and the values $v_n(x)$ of the reduced variate, so that

$$\Phi_n(x) = \exp\left(-\exp\left[-\alpha(x - u_n)\right]\right)$$

would hold for any reasonably large value of n.

But if the noise were gaussian (it suffices here to consider a zero-mean, unit-variance process), then

$$1 - F_X(x) = \frac{1}{\sqrt{2\pi}} \int_x^\infty \exp(-x^2/2)\, dx$$

which can be expanded asymptotically as (Reference 1)

$$1 - F_X(x) = \frac{\exp(-x^2/2)}{x\sqrt{2\pi}} \left(1 - R(x)\right)$$

where $R(x)$ is positive, small, and falls off as $1/x^2$. Defining

$$\epsilon \triangleq -\log\left(1 - R(x)\right)$$

$$\rho_n \triangleq \sqrt{2 \log n}$$

$$\ell_n \triangleq \log\sqrt{2\pi(\rho_n)^2}$$

and manipulating, we obtain a nonlinear relationship between x and $v_n(x)$:

$$v_n(x) = \rho_n(x-\rho_n) + (x-\rho_n)^2/2 + \log(x/\rho_n) + \ell_n + \epsilon$$

However, since $\log y \approx y - 1$ for $y \approx 1$, then for values of x near ρ_n, i.e., when $|x - \rho_n| << \rho_n$, we can neglect ϵ and the quadratic term and obtain

$$v_n(x) \approx \alpha_n(x - u_n)$$

where

$$\alpha_n \triangleq \rho_n + 1/\rho_n$$

$$u_n \triangleq \rho_n - \ell_n/\alpha_n$$

Thus, for all x near ρ_n, we have

$$\Phi_n(x) \approx \exp\left(-\exp\left[-\alpha_n(x - u_n)\right]\right)$$

Classical EVT thus draws a "best" linear fit to the log-log empirical distribution function. If we assume we have a sufficient number of extremes so that the data "clusters" well around the empirical distribution function, and at least a moderate sample size per extreme, then classical EVT also draws a "best" linear fit through $v_n(x)$. The classical EVT estimate of probability of error is a function only of the ordinate of the linear curve at threshold (i.e., at x_0). Thus, for classical EVT to yield accurate results, we require a large enough n that $v_n(x)$ is reasonably linear near threshold; i.e., we require n such that

$$|x - \rho_n| << \rho_n$$

for all x near threshold x_0, or, in particular, we might require

$$|x_0 - \rho_n| \ll \rho_n$$

For example, if $x_0 = 4$ (i.e., $x_0 = 4\sigma$ with $\sigma = 1$), and we require $x_0 \cong \rho_n$, then

$$n = \exp\,[(x_0)^2/2] \approx 3000$$

Thus, we see the need for some minimal sample size n per extreme to guarantee dominance of the linear portion of $v_n(x)$. For gaussian noise of mean m and variance σ^2, α_n is scaled by $1/\sigma$, u_n is scaled by σ and shifted up by m, and the criterion for dominance of the linear term near threshold becomes

$$\left|\frac{x_0 - m}{\sigma} - \rho_n\right| \ll \rho_n$$

Furthermore, since $\partial^2 v_n(x)/\partial x^2$ is positive for all x greater than 1, classical EVT places a linear curve through an upward-curved function [assuming we have enough extremes that the data clusters around the curve $v_n(x)$]. We should point out that if the threshold x_0 exceeds u_n, then the linear curve must cross threshold at a *lower* value than $v_n(x)$, because most of the recorded extremes used in making the best linear fit lie near u_n, and probably none exceed x_0. If we have a large number of extremes exceeding threshold, our value of n is probably sufficiently large to permit classical bit error testing. Thus, we can assume $u_n < x_0$.

Recall now that the true probability of error p is

$$p = 1 - \exp\left(-\exp\,[-v_n(x_0)]\right)^{1/n}$$

while the classical EVT probability of error p' is

$$p' = 1 - \left(\exp\left\{-\exp\,[-\alpha_n(x_0 - u_n)]\right\}\right)^{1/n}$$

Thus, since

$$\alpha_n(x_0 - u_n) < v_n(x_0)$$

then $p' > p$; that is, classical EVT estimates an *excess* probability of error, and thus the bias $b \triangleq p - p'$ is negative. Clearly, the magnitude of the bias will decrease as n is increased, since $v_n(x)$ becomes increasingly linear as n is increased.

The Spread of EVT

Given a set of independent data $\{x_1,\cdots,x_k\}$, ordered so that

$$x_1 \leqslant x_2 \leqslant \cdots \leqslant x_k$$

with some distribution function $\Phi_n(x)$, we note that the fraction of points with value no greater than x_i (for any $i - 1,\cdots,k$) is i/k. Thus, we could define an empirical distribution function $e^*_{nk}(x)$ by

$$e^*_{nk}(x) \triangleq \sum_{i=1}^{k} \frac{i}{k} \mathcal{U}(x - x_i)$$

for then, in the limit, as k gets large, $e^*_{nk}(x)$ would converge to $\Phi_n(x)$, as demanded by the law of large numbers.

To avoid problems with log-log functions of the $e^*_{nk}(x)$ defined above, however, it is conventional to modify the definition somewhat to

$$e_{nk}(x) \triangleq \sum_{i=1}^{k} \frac{i}{1+k} \mathcal{U}(x - x_i)$$

Again, there is ultimate convergence of $e_{nk}(x)$ to $\Phi_n(x)$.

We may then define the *reduced empirical variate* $u_{nk}(x)$ by

$$u_{nk}(x) \triangleq -\log\,[-\log e_{nk}(x)]$$

so that if

$$\Phi_n(x) \underset{n}{\rightarrow} \exp\left(-\exp\,[-v_n(x)]\right)$$

(which it does for moderate n), then $u_{nk}(x)$ also converges to $v_n(x)$. This provides a qualitative measure of the number of extremes needed. We require a sufficient number that the reduced empirical variate $u_{nk}(x)$ clusters well around the reduced variate $v_n(x)$. If k is too low, then the "best" linear fit of the data will not necessarily "fit" well, no matter how linear $v_n(x)$ may be. That is, an insufficient number of extremes will cause excessive *spread* of the parameter estimates in any sequence of tests.

Figure 1 shows the reduced variate $v_n(x)$, the reduced empirical variate $u_{nk}(x)$, and the linear curve $\alpha_n(x - u_n)$ for a sample of 30 extremes, each drawn from a block size of 100, with threshold $x_0 = 4$.

Experimental Evidence

We have pointed out that the number k of extremes used must be large enough so that the reduced empirical variate clusters near the reduced variate, and that the sample size n from which each extreme is drawn must be large enough to minimize the bias (effect of nonlinearity). For a given total test size m, we must ask what apportioning values of n and k give a best tradeoff between bias (n too low) and spread (k too low). Figures 2 and 3 compare the effects of various values of n and k as a function of test size m. These results were obtained from examination of independent samples from a gaussian source with known statistics, and a threshold x_0 of 4 sigma points. Figure 3 summarizes the results at m = 3000, 12000, 30000, and 60000, for k = 10, 20, 30, 50, and 100. As k increases, the spread decreases but moves upward, reflecting the increased bias due to decreasing n.

As a reasonable compromise between the effects of bias and spread, a k of 30 (30 extremes/total test) was selected for this threshold of 4σ, and EVT was compared with BER using the same gaussian source. The performance curves are shown in Figure 4. The five solid EVT performance curves include the 90% quantiles, the first sigma points, and the average. The two dashed BER performance curves are the 90% confidence curve and the

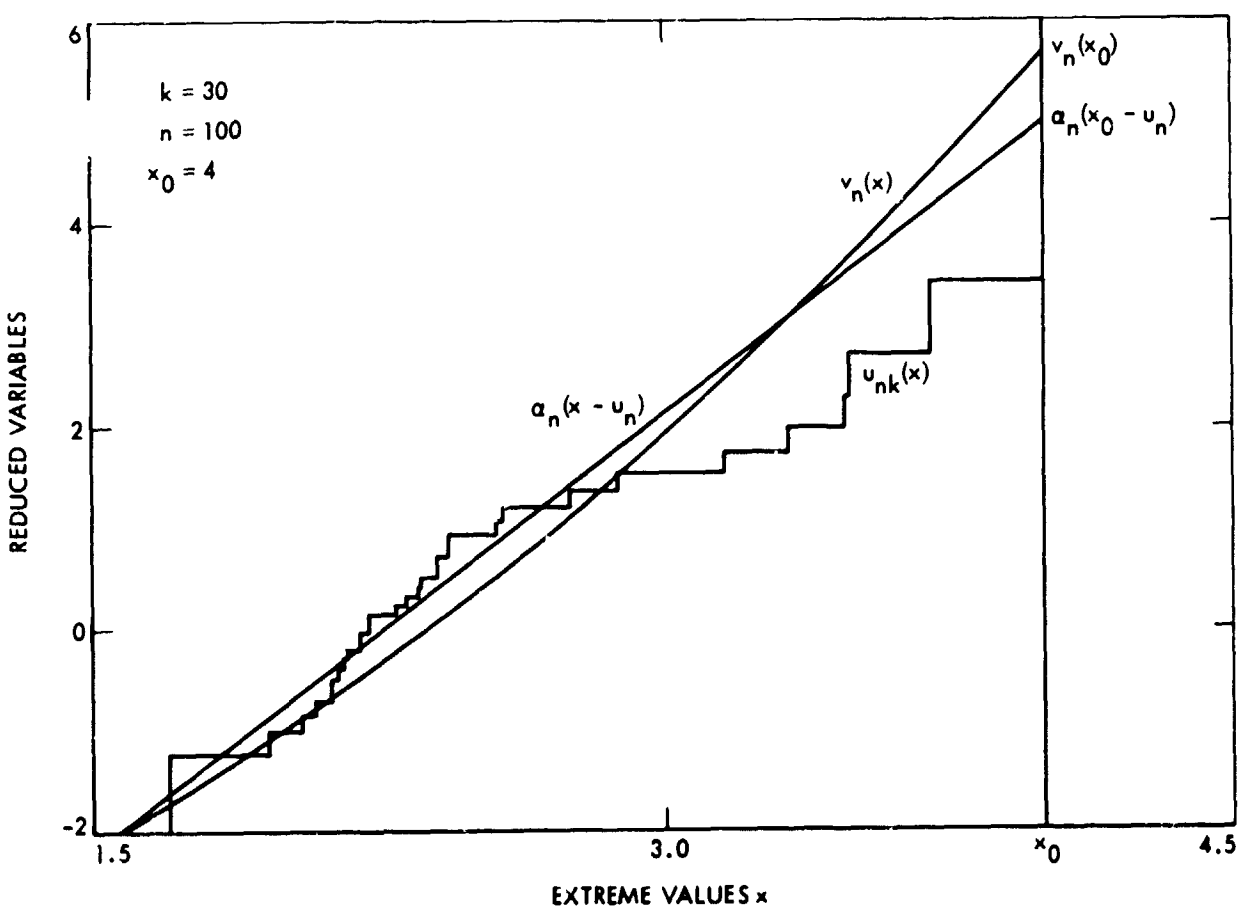

Figure 1. Typical reduced variables

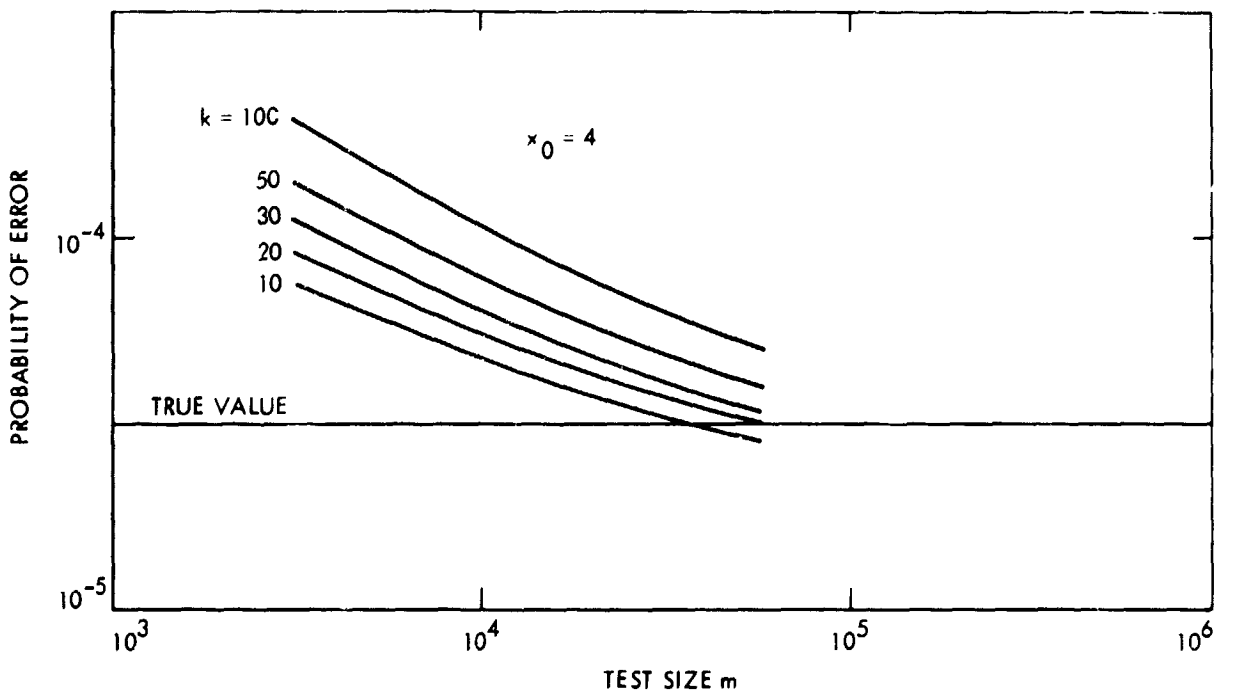

Figure 2. EVT average performance as a function of group number for gaussian noise

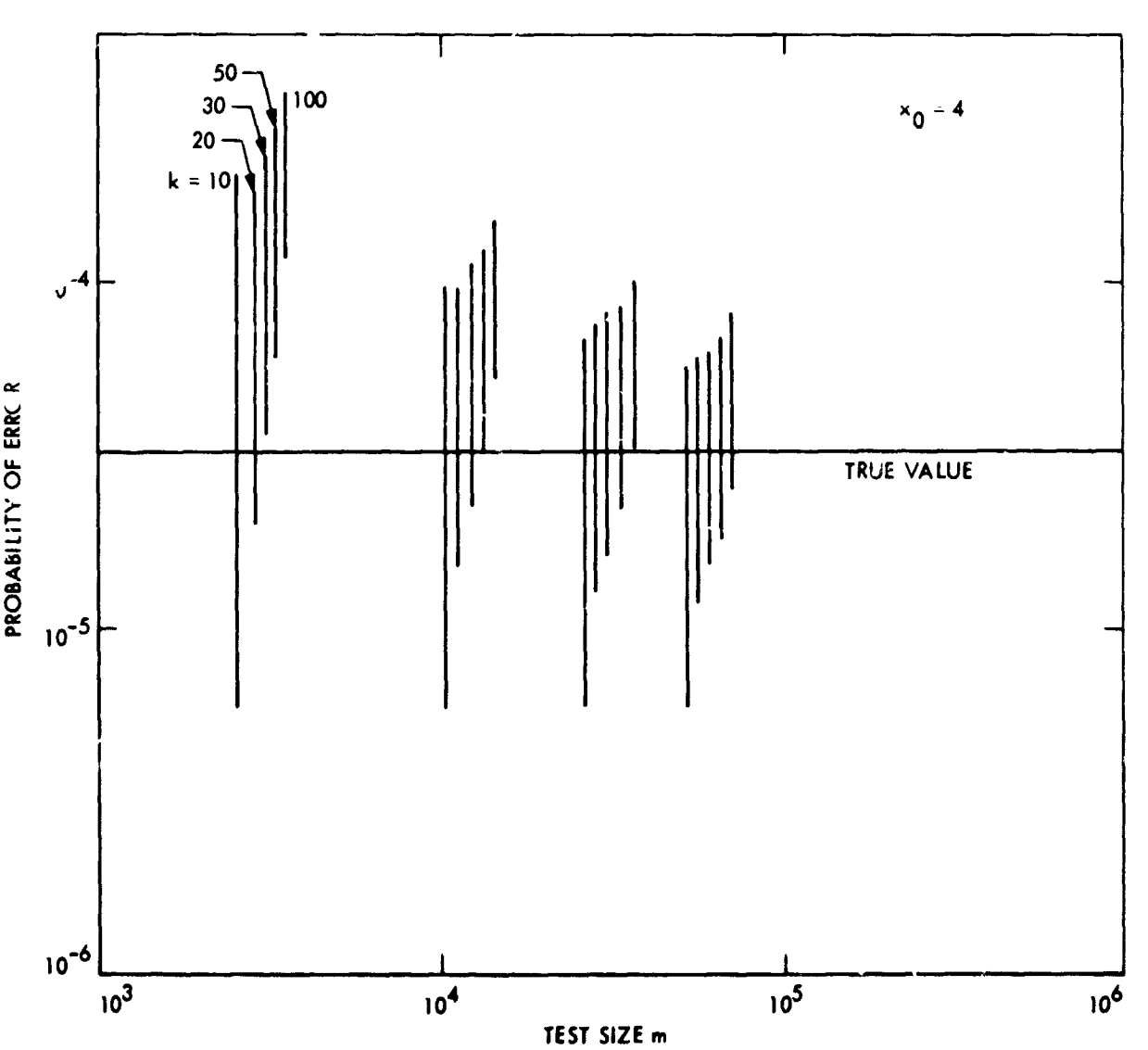

Figure 3. EVT 90% spread as a function of group number for gaussian noise

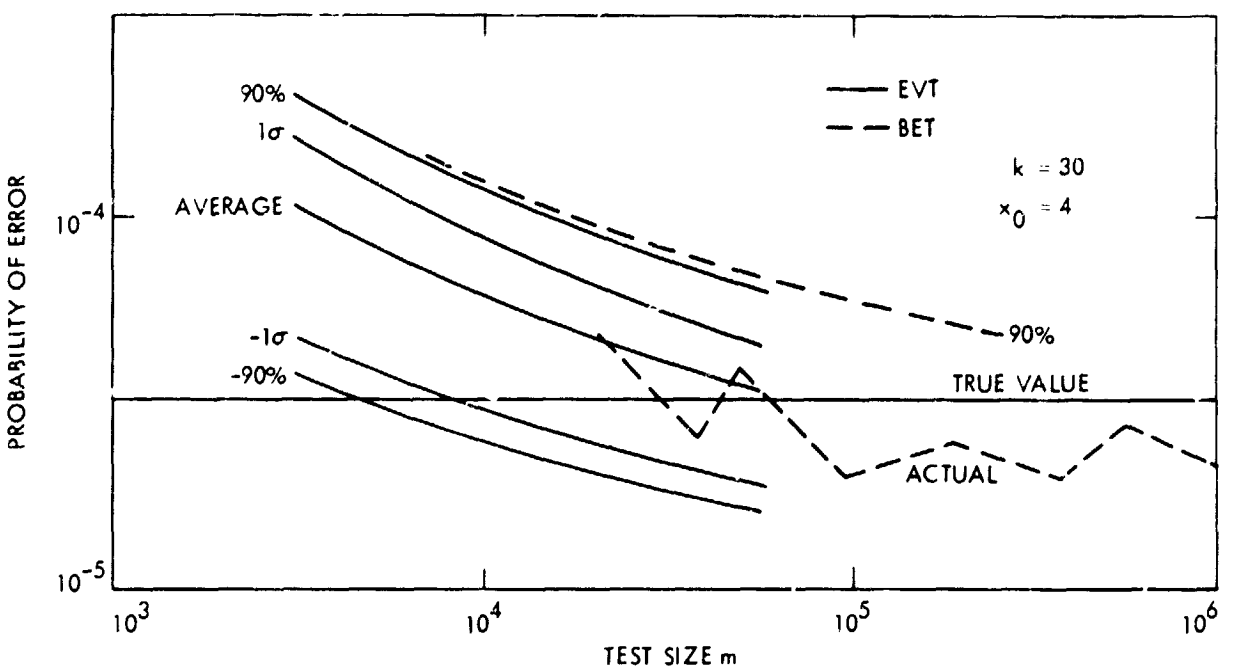

Figure 4. Comparison of BET and EVT for gaussian noise

actual bit error count. Clearly, EVT holds no distinct edge over BER for this data source. Comparable tests at other threshold values also bear out this conclusion.

For noise with density function of the form

$$f(x) = \alpha \cdot \exp\left(-\left|\frac{x}{\tau}\right|^r\right)$$

for $r > 1$, analysis again reveals a nonlinear form of $v_n(x)$ and a negative bias. Experiments have shown the same tradeoffs between spread and bias, and comparable performance.

Summary

We have shown that bias and spread impose conflicting requirements in the use of EVT for testing digital communication systems, have indicated how to minimize the effects of these factors, and have compared EVT with BER testing of a gaussian source. It seems apparent that under the best of conditions EVT does not perform significantly better than BER.

References

1. Cramer, H., *Mathematical Methods of Statistics*. Princeton University Press, Princeton, N. J., 1946.

2. Gumbel, E. J., *Statistics of Extremes*. Columbia University Press, New York, 1958.

3. Epstein, B., "Elements of the Theory of Extreme Values," *Technometrics*, Vol. 2, No. 1, pp. 27-41, Feb. 1960.

4. Posner, E. C., *The Application of Extreme-Value Theory to Error Probability Estimation in the Ranger Block III Command Detector*, Technical Report 32-705. Jet Propulsion Laboratory, Pasadena, Calif., Jan. 15, 1965.

5. Ashlock, J. C., and Lurie, S. M., *On the Application of Extreme-Value Statistics to Command Oriented Problems*, Technical Report 32-1025. Jet Propulsion Laboratory, Pasadena, Calif., Oct. 15, 1966.

6. Fisher, R. A., and Tippett, L. H. C., "Limiting Forms of the Frequency Distribution of the Largest or Smallest Member of a Sample," *Cambridge Philosophical Society Proceedings*, Vol. 24, Part 2, pp. 180–190, 1928.

7. Tippett, L. H. C., "On the Extreme Individuals and the Range of Samples Taken From a Normal Population," *Biometrika*, Vol. 17, pp. 364–387, 1925.

8. Dronkers, J. J., "Approximate Formulae for the Statistical Distribution of Extreme Values," *Biometrika*, Vol. 45, pp. 447–490, 1958.

9. Anderson, C. L., *Generalized Asymptotes for Extreme Value Distributions*, PhD dissertation. Southern Methodist University, Texas, 1969.

JPL Quarterly Technical Review Volume 1, Number 4 January 1972

On the Selection of an Optimum Design Point for Phase-Coherent Receivers Employing Band-Pass Limiters

M. K. Simon

Telecommunications Division

In the design of phase-coherent receivers employing band-pass limiters, it is customary to specify system performance relative to its value at a fixed design point. For a given design point, an optimum tradeoff can be found between the power allocated to the carrier and the sideband signals. This article describes an attempt to further improve the performance of such coherent carrier systems by optimizing the design point based upon a given practical optimizing criterion. The single-channel system is treated in detail and a brief discussion is given on how to extend the technique to a two-channel system.

introduction

Over the years a great deal of interest has been demonstrated relative to the problem of optimum power allocation in single-channel command, and one- and two-channel telemetry coherent carrier systems for spacecraft applications (References 1–4). One fact in common to all of the solutions that have been suggested is that the *system design point* [i.e., the carrier tracking loop signal-to-noise ratio (SNR) at "threshold"] has been *arbitrarily* fixed while the other system parameters are varied to achieve the optimum tradeoffs. To date, very little consideration has been given to the question of what is the optimum design point based upon a given practical optimization criterion.

To answer this question, the problem must be posed in such a way that the relation between an actual operating point and the design point is clearly placed in evidence, thereby resulting in a solution of significant importance to the practicing engineer. This article suggests a method for doing so. The technique involved makes use of the up-to-date phase-locked loop and band-pass limiter theories recently contributed in References 5 and 6.

Statement of the Problem

There are two parts to the optimum power allocation problem associated with the design of a phase-coherent receiver employing a band-pass limiter. The first part (which is that most commonly considered in the literature) is to fix either the system error probability or total transmitter energy-to-noise ratio and minimize the other quantity by varying the system modulation indices. This approach can be applied to either single- or two-channel systems and implicitly assumes that the system design point is held fixed during the optimization.

The second part of the problem considers, in effect, the locus of these minima as the design point is varied, and this information is used to select an optimum design point. This part of the optimum power allocation problem has, to the author's knowledge, not been considered and is the principal motivation behind this article.

System Model

A functional diagram of a phase-coherent receiver preceded by a band-pass limiter (BPL) is illustrated in Figure 1. The input signal (point 1) is characterized by a carrier biphase modulated by a unit power digital data modulation. The loop phase detector, loop filter, and voltage-controlled oscillator (VCO) comprise a phase-locked loop (PLL) whose purpose it is to establish from the amplified, band-pass limited input signal a coherent reference for demodulating the data. In computing the error probability performance of the data detector, several possibilities exist depending on how the data signal is demodulated off the carrier. Specifically, the following three cases are of interest.

(1) The input IF filter passes the total modulation which is subsequently transferred to the data detector directly from the PLL phase detector

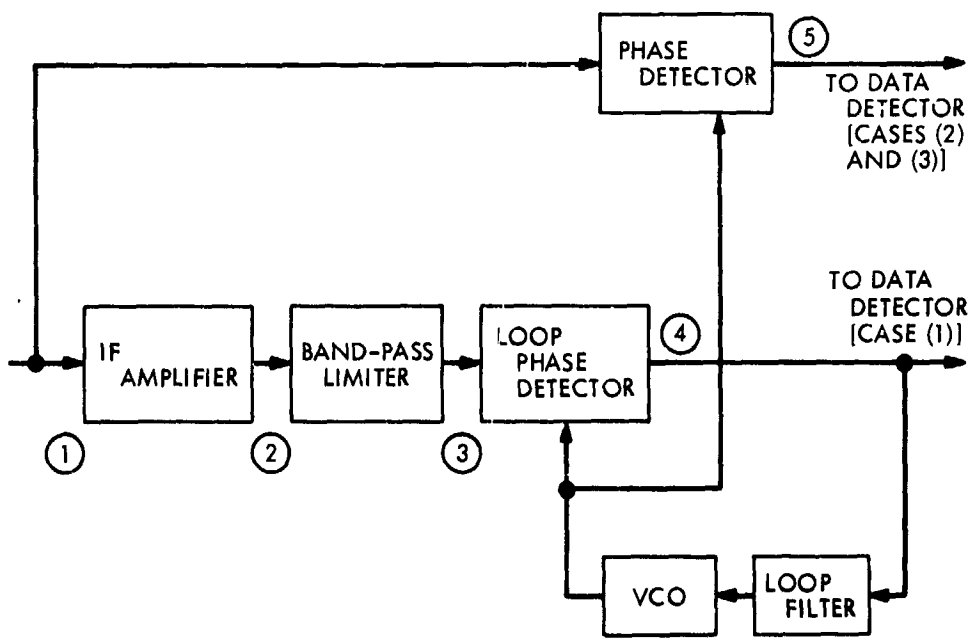

Figure 1. A phase-coherent receiver employing a band-pass limiter

output (point 4 in Figure 1). This situation is typical of present and past command transponders used in deep-space applications.

(2) The input IF filter passes the total modulation; however, the modulated carrier is tapped off prior to entering the band-pass filter and is demodulated by the PLL reference in a separate phase detector (point 5). The output of this phase detector represents the modulation to be recovered by the data detector. This case is typical of present-day methods for recovery of ranging data and is of interest in future command applications.

(3) The input IF filter completely filters out the modulation, with the modulation being recovered as in case (2). This situation would correspond to the case where the data modulation is placed on a subcarrier whose frequency is outside the IF bandwidth. This case is typical of phase-coherent reception of telemetry data.

In cases (1) and (2), the BPL suppression factor, and hence the effective loop SNR, is a function of the *total* power-to-noise ratio in the input bandwidth. In case (3), the BPL loss is increased [relative to case (2)] because it is now only a function of the carrier component of the total power-to-noise ratio in the input bandwidth. Hence, with all other parameters unchanged, the effective loop SNR is reduced and the noisy reference loss increased. This effect produces a minor degradation in case (3) relative to case (2).

Regardless of which case is applicable, an important parameter to consider is the design point loop bandwidth-symbol time product. Ordinarily, for command applications $\delta_0 = 1/(W_{L0}T)$ is sufficiently small (e.g., $<$ 0.5) such that the phase error can be assumed to vary rapidly over a symbol interval T. In many low-to-medium rate telemetry systems, this assumption still remains valid. Hence, to a good approximation, the data detector error probability P_E is for all three cases described by

$$P_E = \frac{1}{2}\operatorname{erfc}\left[(R_d)^{1/2}\,\overline{\cos\phi}\right] \tag{1}$$

where

$$\left.\begin{aligned} R_d &= \frac{S_d T}{N_{0d}} \\ \overline{\cos\phi} &\triangleq E\{\cos\phi\} \end{aligned}\right\} \tag{2}$$

The parameters S_d and N_{0d} are the data signal and noise powers, respectively; both depend upon which of the three cases is being considered. The validity of the gaussian noise model is justified as follows. In cases (2) and (3), the noise affecting the data detection process is clearly gaussian because it

has not been transmitted through the BPL. In case (1), the noise entering the matched filter detector (i.e., the phase detector output at point 4 in Figure 1) is not gaussian, but, for small input signal-to-noise ratio, is approximately zero mean. However, because the effective bandwidth of this noise is much wider than $1/T$, the integrate and dump action of the matched filter acts as a narrow-band filter and the output statistic is approximately gaussian.

Optimization of Performance as a Function of Design Point

In designing phase-coherent receivers preceded by band-pass limiters, it is convenient to characterize loop performance at a given operating point relative to its value at a fixed design point. In the past, it has been customary to choose this design point to correspond to a carrier SNR in the design point loop bandwidth $\Upsilon_0 = 2P_{c0}/(N_0 W_{L0})$ of 3 dB, i.e., so-called "loop threshold." More recently, it has become apparent that the threshold effect exhibited by the loop is a more complicated phenomenon than can be expressed entirely in terms of a given carrier SNR. Hence, the original motivation behind choosing $\Upsilon_0 = 2$ is, strictly speaking, no longer valid. Rather, one should allow Υ_0 to be chosen as that value that results in optimum receiver performance. Our first step, then, is to divide the power between carrier and sideband to minimize the total energy-to-noise ratio, PT/N_0, at the transmitter for a fixed error probability, P_E, in the data channel and a fixed ratio of data rate, $1/T$, to design point loop bandwidth, W_{L0}. This procedure enables the design engineer to constrain, *a priori*, the minimum acceptable signal-to-noise ratio in the design point bandwidth, $x_{\min}$; this minimum is based upon tracking performance considerations and, once established, allows the engineer to seek the optimum power split subject to that constraint. If the minimum total transmitted energy-to-noise ratio occurs at a value of $x = 2P_c/N_0 W_{L0}$ less than $x_{\min}$, the system designer selects the value of PT/N_0 at $x_{\min}$. As we shall see shortly, this additional constraint determines an optimum design point.

For a given P_E, a fixed design point Υ_0, and specified values of the ratio of loop filter time constants, τ_2/τ_1, loop damping factor at the design point, r_0, input IF filter bandwidth, W_i, and δ_0, one can find an infinite set of paired coordinate values (x, R_d). For each pair of values, the ratio of the total energy per bit to noise density may be found from[1]

$$\frac{PT}{N_0} = R'_d + \frac{x}{2\delta_0} \tag{3}$$

For any of the three cases being considered, a plot of PT/N_0 versus x exhibits a minimum. As an example, consider a command application wherein the

[1] For case (1), $R'_d = R_d \Gamma_p$; whereas for cases (2) and (3), $R'_d = R_d$. The parameter Γ_p is the limiter performance factor defined in Reference 6. Also, any symbol or subcarrier synchronization and demodulation losses that might be present have been neglected.

command data is obtained by demodulating the BPL input with the PLL reference signal [case (2)]. Plotted in Figure 2 is PT/N_0 in dB versus x in dB for $P_E = 10^{-5}$ and parameter values $\tau_2/\tau_1 = 0.002$, $r_0 = 2$, $\Upsilon_0 = 2$, $W_i = 9$ kHz, $W_{L0} = 18$ Hz, $1/T = 4$ bps. The minimum value of PT/N_0 is observed to occur at $x = 5.8$ dB, which is greater than Υ_0. If Υ_0 is now increased in value (all other parameters held fixed), one finds that the minimum PT/N_0 together with the value of x at which it occurs both continue to decrease. Thus, it appears, at least at first glance, that continued improvement in performance (in the sense of minimum PT/N_0) can be had simply by raising the design point indefinitely. Of course, this cannot be true in practice, and hence some additional constraint must be placed on the problem to counteract this anomaly.

One practical consideration is that the value of x chosen for the final system design must be greater than some minimum value $x_{\min}$. Where $x_{\min}$ is related to the design point by $x_{\min} = K_0\Upsilon_0$, and where Υ_0 increases, a point is eventually reached at which the value of x at the minimum of PT/N_0 becomes equal to $x_{\min}$. From that point on, the value of PT/N_0 at $x = x_{\min}$ is selected as the best operating condition. Figure 3 illustrates a plot of $(PT/N_0)_{\min}$ versus Υ_0 for case (2) and the same parameters as those used in arriving at Figure 2.[2] Also assumed in Figure 3 is that $x_{\min}$ is chosen at the design point itself (i.e., $K_0 = 1$). The physical significance of such a choice is that the operating point loop bandwidth can never fall below its value at the design point, i.e., W_{L0}. One notes from Figure 3 that an improvement of 0.41 dB can be obtained by allowing the design point, Υ_0, to be increased from its previously chosen value of 3 dB (i.e., 0 dB in $2B_{L0}$) to 5.8 dB, the point at which the minimum value of $(PT/N_0)_{\min}$ is achieved.

---

[2] The results for case (1), where the data signal is derived directly from the phase detector output, are negligibly different from those of case (2). The difference is strictly due to the effect of the BPL loss on R_d because the noisy reference loss (approximately 0.2 dB) is the same for both. Hence, Figure 3 can also be thought to apply to case (1).

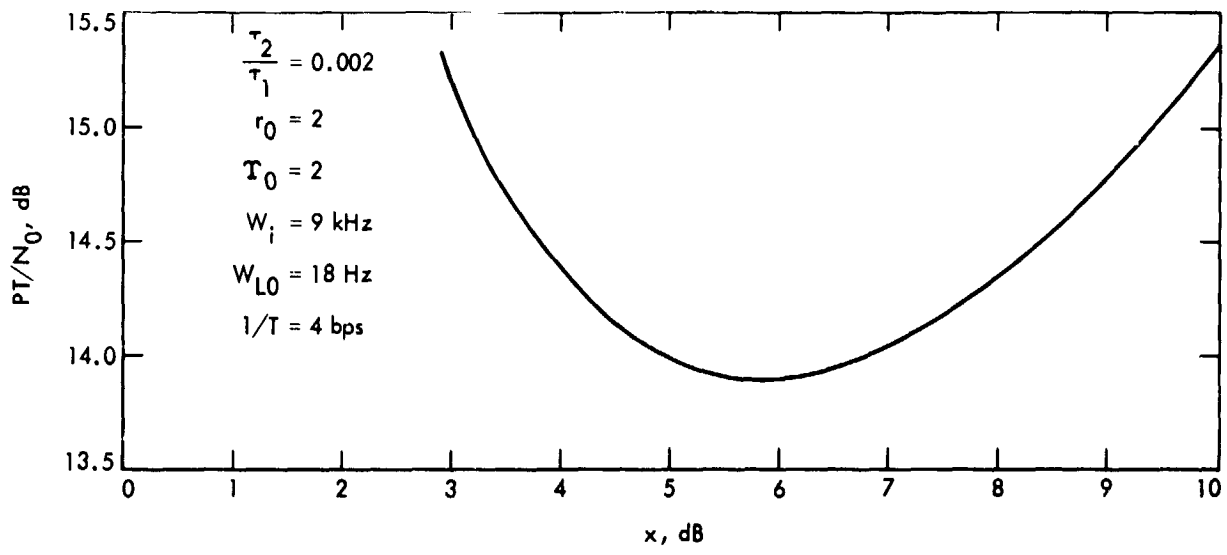

Figure 2. Total power-to-noise ratio versus carrier signal-to-noise ratio in the design point loop bandwidth for a fixed design point: parameters are typical of command application

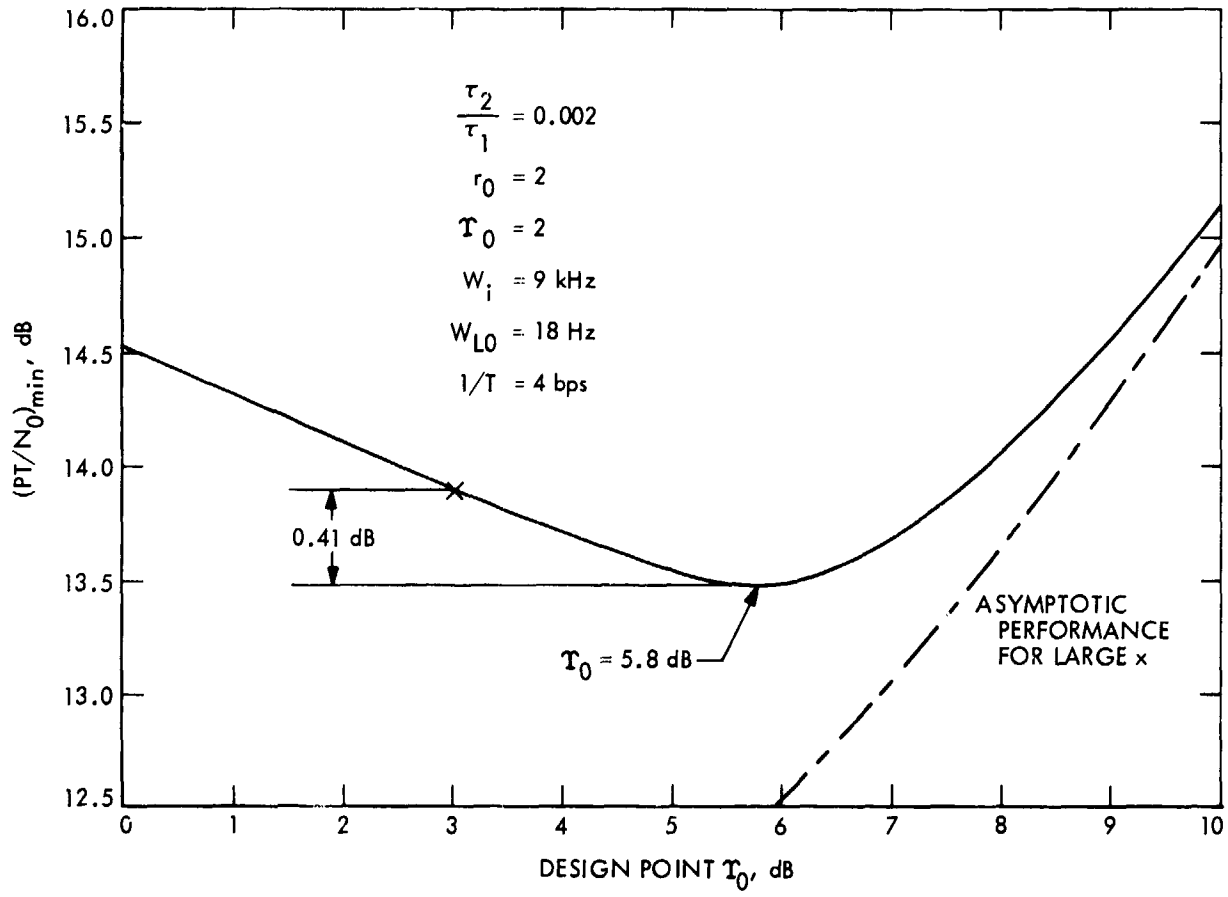

Figure 3. Minimum total power-to-noise ratio as a function of design point: parameters are typical of command application—case (2)

Assuming case (3), i.e., the single-data channel is on a subcarrier that is outside the bandwidth of the input IF amplifier, Figures 4 and 5 illustrate the choice of an optimum design point for two sets of parameters typical of telemetry systems for $P_E = 10^{-3}$. In both Figures 4 and 5, $\tau_2/\tau_1 = 0.002$, $r_0 = 2$, $W_i = 4$ kHz, $1/T = 8⅓$ bps; in Figure 4, $W_{L0} = 12$ Hz; in Figure 5, $W_{L0} = 48$ Hz.

Indicated by dashed lines on Figures 3, 4, and 5 is the asymptotic behavior of Equation 3 as x becomes large, corresponding to the case where the noisy reference due to the RF carrier becomes negligible. This asymptote satisfies the equation

$$\frac{PT}{N_0} = \left[\text{erfc}^{-1}\,(2P_E)\right]^2 + \frac{K_0 \Upsilon_0}{2\delta_0} \tag{4}$$

Application to Two-Channel Systems

This article is concluded with a brief discussion on how the optimization technique presented here might be applied in a two-channel system. Of particular interest in deep-space applications is the situation where both channels are used for the transmission of telemetry information, e.g., the

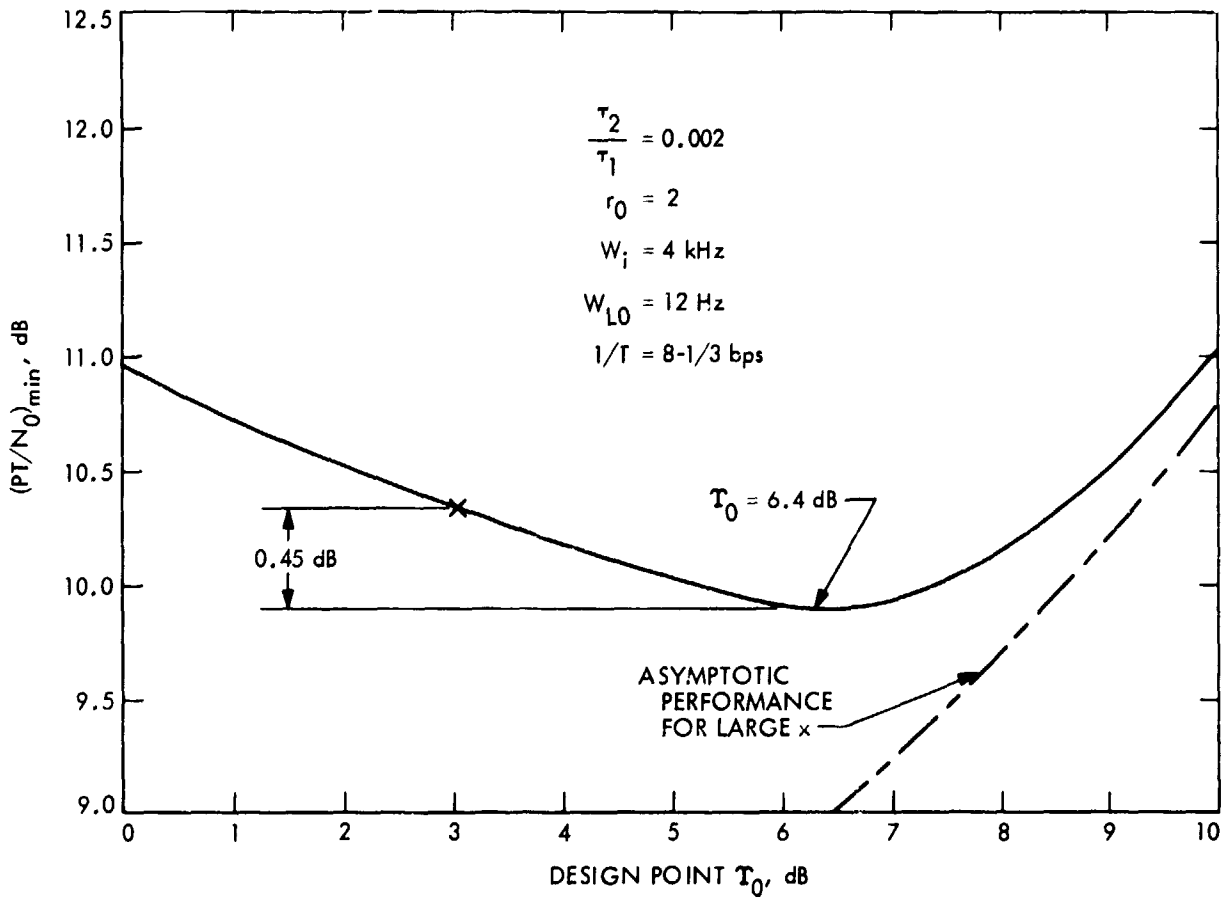

Figure 4. Minimum total power-to-noise ratio as a function of design point: parameters are typical of telemetry application—case (1)

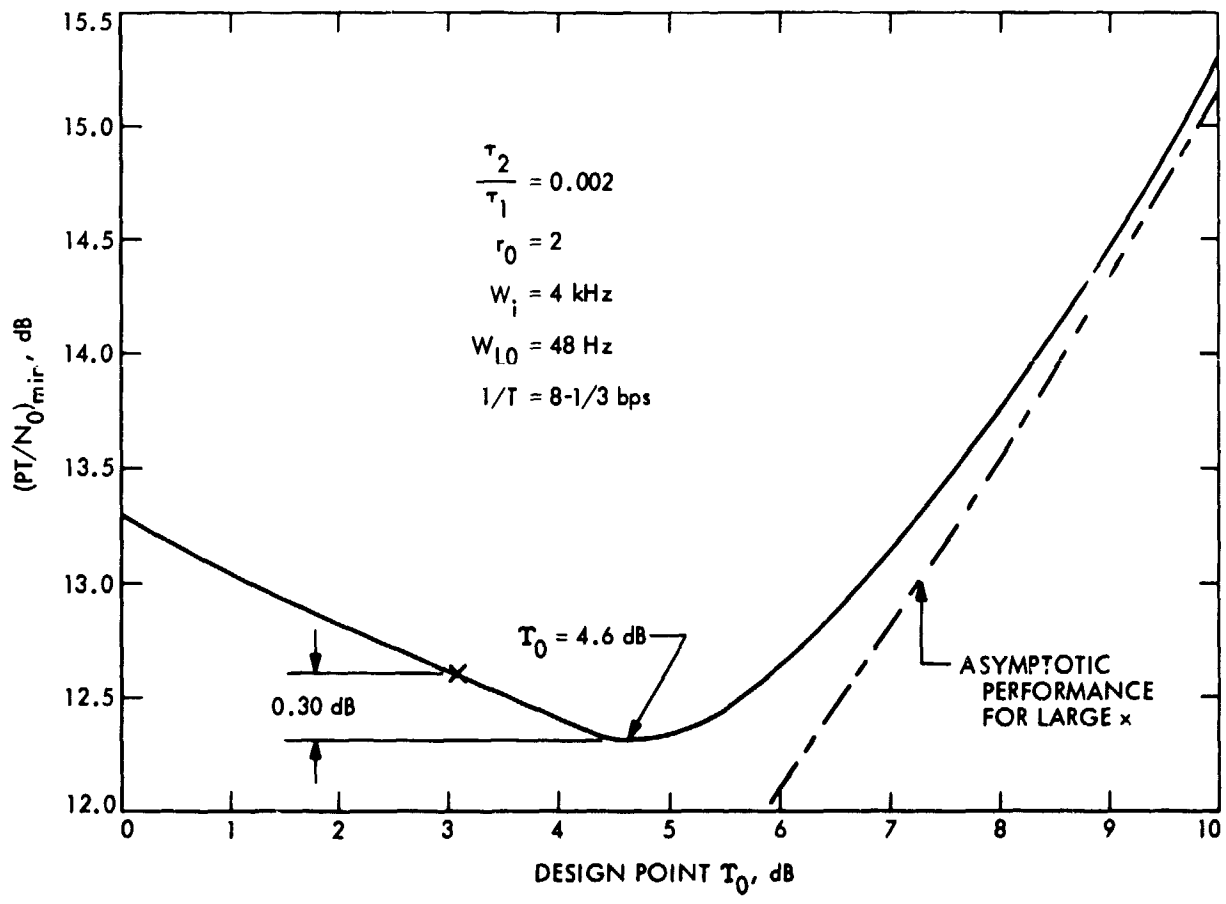

Figure 5. Minimum total power-to-noise ratio as a function of design point: parameters are typical of telemetry application—case (2)

science and engineering channels in the Mariner Mars 1969 mission. Assuming that the two-channel telemetry model is classified as case (3), the optimization equation analogous to Equation 3 is given by

$$\frac{PT_1}{N_0} = R_{d1} + \left(\frac{T_1}{T_2}\right) R_{d2} + \frac{x}{2\delta_{01}} + \frac{R_{d1} R_{d2} \left(\frac{T_1}{T_2}\right)}{\frac{x}{2\delta_{01}}} \tag{5}$$

where the subscripts 1 and 2 now refer to channels 1 and 2, respectively. For given error probabilities in the two channels, i.e., P_{E1} and P_{E2}, and fixed parameter values for τ_2/τ_1, r_0, T_1, T_2, W_i, W_{LO}, Ω_0, and Υ_0, a plot of PT_1/N_0 versus x once again exhibits a minimum. If, as before, Υ_0 alone is now allowed to vary subject to the constraint $x > x_{\min}$, then, as in the single-channel case, there exists an optimum design point in the sense of minimum PT_1/N_0. The practical significance of this optimum design point depends upon the specific parameter values that characterize the system. The asymptotic behavior of Equation 5 for large x satisfies an equation similar to Equation 4, namely,

$$\frac{PT_1}{N_0} = \left[\text{erfc}^{-1}\,(2P_{E1})\right]^2 + \left(\frac{T_1}{T_2}\right)\left[\text{erfc}^{-1}\,(2P_{E2})\right]^2 + \frac{K_0 \Upsilon_0}{2\delta_{01}} + \frac{\left[\text{erfc}^{-1}\,(2P_{E1})\right]^2 \left[\text{erfc}^{-1}\,(2P_{E2})\right]^2 \left(\frac{T_1}{T_2}\right)}{\frac{K_0 \Upsilon_0}{2\delta_{01}}} \tag{6}$$

Acknowledgment

The author is indebted to James C. Springett of the Jet Propulsion Laboratory for suggesting the problem and for many useful discussions relative to its formulation.

References

1. Lindsey, W. C., "Optimal Design of One-Way and Two-Way Coherent Communication Links," *IEEE Trans. Communication Technology*, Vol. COM-13, pp. 418–431, Aug. 1966.

2. Lindsey, W. C., "Determination of Modulation Indices and Design of Two-Channel Coherent Communication Systems," *IEEE Trans. Communication Technology*, Vol. COM-14, pp. 229–237, Apr. 1967.

3. Lindsey, W. C., "Design of Block-Coded Communication Systems," *IEEE Trans. Communication Technology*, Vol. COM-15, pp. 525–534, Aug. 1967.

4. Lindsey, W. C., "Performance of Phase-Coherent Receivers Preceded by Bandpass Limiters," *IEEE Trans. Communication Technology*, Vol. COM-16, pp. 245–251, Apr. 1968.

5. Lindsey, W. C., "Nonlinear Analysis of Generalized Tracking Systems," *Proc. IEEE*, Vol. 57, No. 10, pp. 1705–1722, Oct. 1969.

6. Springett, J. C., and Simon, M. K., "An Analysis of the Phase Coherent/Incoherent Output of the Bandpass Limiter," *IEEE Trans. Communication Technology*, Vol. COM-19, No. 1, pp. 42–49, Feb. 1971.

N72-17897

JPL Quarterly Technical Review Volume 1, Number 4 January 1972

Jupiter Trapped Radiation Belts

A. J. Beck

Project Engineering Division

Previously developed models for trapped electron radiation belts and trapped proton radiation belts in the Jovian magnetosphere are described. The spatial distribution of flux and the *L*-shell dependence of the characteristic energy are displayed for both models. Based on these models, the fluence accumulated by a Jupiter flyby spacecraft is given in terms of the equivalent 3-MeV fluence for electrons and the equivalent 20-MeV proton fluence for protons. Finally, some impacts of these fluences on outer-planet missions are described.

Introduction

The observed synchrotron radiation from Jupiter implies the existence of relativistic electrons trapped in the Jupiter magnetosphere (Reference 1). Although no direct observational data exists to confirm the existence of a trapped proton belt, both trapping theory and analogy with the Earth's radiation belts suggest that Jupiter should have an energetic trapped proton belt as well. Based on the existing models for the trapped radiation (References 1, 2, and 3), the number density flux and energy of the particles are expected to be quite large compared to the Earth's radiation belt. Consequently, the radiation belts may have a strong impact on the design of spacecraft which fly by or orbit Jupiter, and on the missions which are designed to investigate Jupiter or investigate the outer planets using Jupiter for gravity assist.

On July 13–15, 1971, a Jupiter Radiation Belt Workshop was conducted at JPL. The workshop brought together scientists and engineers from JPL, NASA, various universities, and industry with the goal of establishing models from which particle flux and fluence distributions of both electrons and protons could be derived in forms suitable for use as space vehicle design criteria. The workshop produced four models of Jupiter trapped radiation belt: a nominal electron model, an upper limit electron model, a nominal proton model, and an upper limit proton model. These models are referred to as the workshop models. Divine (Reference 2) has described models from which the early design requirements for the Thermoelectric Outer-Planets

Spacecraft were derived. These models are referred to as the preworkshop models.

Trapped Radiation Belt Electron Models

Electron models are based on the observed synchrotron radiation from Jupiter. Understanding the synchrotron radiation requires a knowledge of the magnetic field strength, which is taken as 10 gauss in the equatorial plane at a distance of one planetary radius (R_J) from the center of the planet. In addition, in order to structure a spatial distribution in the model, radial diffusion of solar wind electrons from the magnetosheath and conservation of the first invariant (the magnetic moment μ) are assumed. As a consequence of these assumptions, the characteristic energy E_0 and the differential flux ϕ of the electrons both vary as L^{-3}, where L is the magnetic shell parameter.

Assuming a value for the magnetic field strength, the characteristic energy of the electrons in the synchrotron region at $L = 2$ can be estimated from the conservation of the magnetic moment. To make this estimate, the value of the magnetic moment at $L = 2$ is set equal to the magnetic moment of solar wind particles outside of the magnetosheath. This process leads to a value for the electron characteristic energy which is of the same order of magnitude as that required for electrons producing the observed synchrotron emission (Reference 1). Although this general agreement provides some support for the assumed conservation of the magnetic moment, the electron flux (2×10^7 electrons/cm^2-s) and the characteristic energy (6 MeV) for the nominal electron model have been derived at $L = 2$ from the observed synchrotron emission.

Because of the estimated uncertainties in the magnetic field strength, synchrotron beaming, and unfolding of the synchrotron data, the upper limit model has both the electron flux and the electron energy larger than the corresponding nominal model values by a factor of three.

Figure 1 shows models for the distribution of the electron flux in the equatorial plane of Jupiter's magnetosphere. The dashed lines are preworkshop models (Reference 2), and the solid lines are workshop flux models. The horizontal axis is the L-shell parameter, while the vertical axis is the flux of omnidirectional electrons having energy greater than zero for the model. However, fluxes of electrons having energy much less than the characteristic energy may also be present, as, for example, in a thermal plasma. All the models are constant for $L < 2$, but for $L > 2$, the fluxes are proportional to L^{-4}, L^{-3}, L^{-3}, and L^{-2} for the four lines, starting from the bottom. Although this figure does not show the latitude dependence, the flux models are assumed to be latitude dependent, having an e-folding value of about 30 deg (Reference 3).

The variation of the characteristic energy is shown in Figure 2 for the electron models. These electrons have been assumed to have a differential energy spectrum, given by

$$\frac{d\phi}{dE} = \phi_0 \left[E/(E_0)^2\right] e^{-E/E_0}$$

where E_0 is the local characteristic energy. The horizontal axis represents the magnetic shell parameter, as evaluated either in or away from the magnetic equatorial plane, and the vertical axis represents the local characteristic kinetic energy of the electrons. The dashed lines represent the preworkshop upper limit model, and the solid lines represent the workshop models. All models' energies are flat for $L \leq 2$, but for $L > 2$, the energies are proportional to L^{-3}, L^{-3}, and L^{-1} for the three lines, starting from the bottom.

Trapped Radiation Belt Proton Model

The workshop proton models are theoretical in nature. Furthermore, no observational data exists to confirm the existence of a Jupiter trapped proton radiation belt nor to limit the concentration of protons below the limit imposed by the maximum concentration that the magnetic field can contain.

In the absence of any observational data, the same physical processes which trap and accelerate electrons are assumed in formulating the nominal proton model. Thus, the nominal proton model assumes many of the features of the nominal electron model. It is assumed that the equatorial magnetic field strength at 1 R_J is 10 gauss, that radial diffusion transports protons from the magnetosheath, that the first adiabatic invariant is conserved, and that there are no losses, except those which occur at small L values. The number density of protons at $L = 2$ is set equal to the corresponding electron number density, and the proton energy at $L = 2$ is set equal to 10 times the corresponding electron energy. It is assumed that the protons are able to diffuse past the satellites of Jupiter without loss.

An upper limit model was also proposed. The proton flux is limited at intermediate L values ($L \cong 10$) by ion-cyclotron wave instabilities. In addition, a 10-gauss equatorial magnetic field, radial diffusion, conservation of the first invariant, and losses only at small L values are assumed. The assumption of the conservation of the first invariant again leads to the characteristic energy varying as L^{-3}.

Figure 3 shows models for the distribution of the proton flux in the equatorial plane of Jupiter's magnetosphere. The dashed lines are preworkshop models (Reference 2), while the solid lines are workshop proton flux models. The horizontal axis is the L-shell parameter, while the vertical axis is the flux of omnidirectional protons having energy greater than zero for the model. However, fluxes of protons having energy much less than the characteristic energy may also be present, as, for example, in a thermal plasma. The preworkshop flux models (Reference 2) are flat out to $L = 2$ (nominal) and to $L = 12.6$ (upper limit); beyond these limits they are proportional to $L^{-5.5}$ and L^{-6}, respectively. The workshop fluxes are

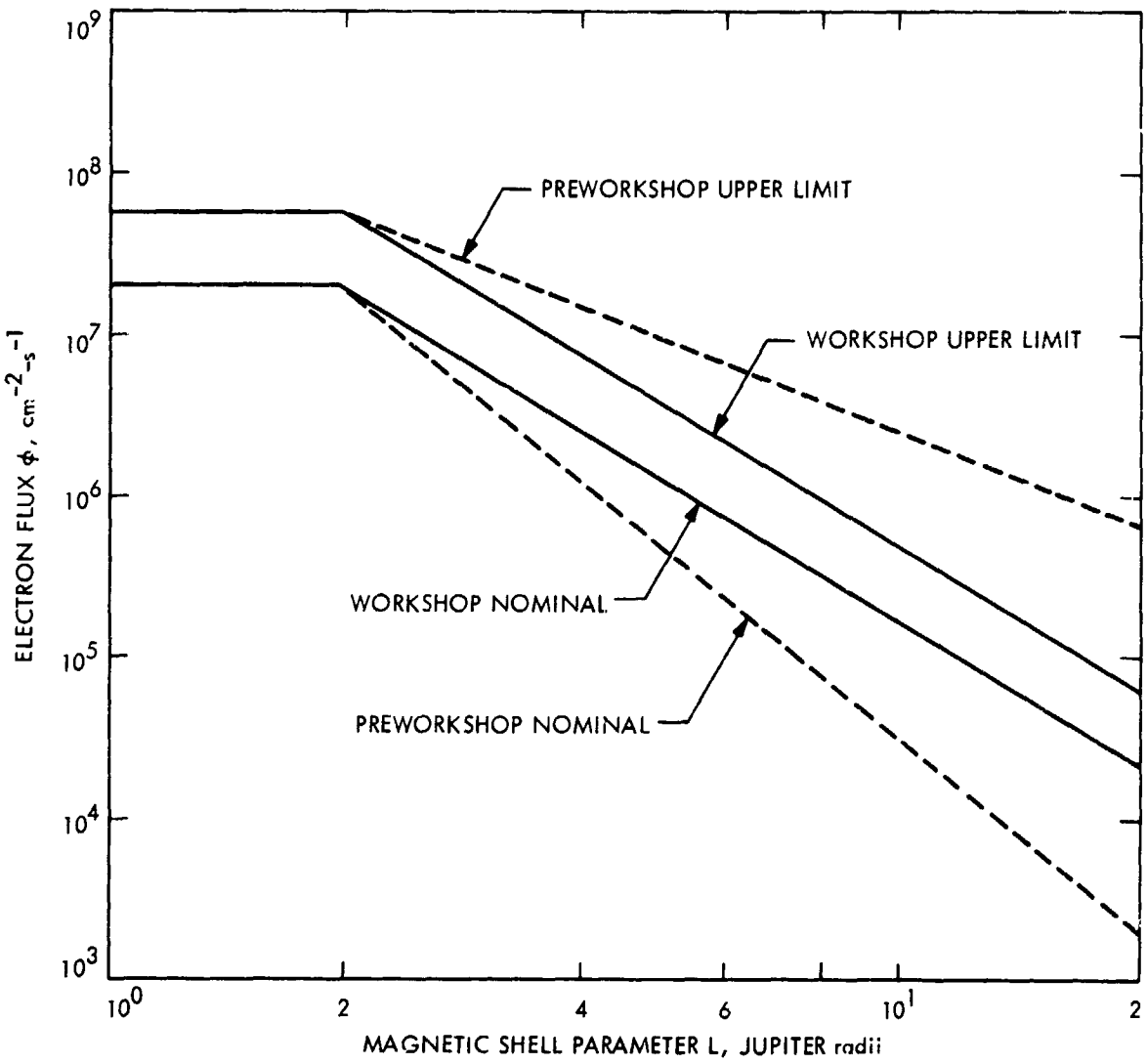

Figure 1. Jupiter electron models in the equatorial plane

proportional to L^{-3} for all $L > 1$. The nearly three orders of magnitude difference between the workshop models reflects the uncertainty in this environmental description. Although this figure does not show the latitude dependence, the flux models are assumed to be latitude dependent, having an *e*-folding value of about 30 deg (Reference 3).

The variation of the characteristic energy E_0 with L is shown in Figure 4 for the proton models. The protons have been assumed to have a differential energy spectrum, given by

$$\frac{d\phi}{dE} = \phi_0 \, [E/(E_0)^2] \, e^{-E/E_0}$$

where E_0 is the local characteristic energy. The horizontal axis represents the magnetic shell parameter, as evaluated either in or away from the magnetic equatorial plane, and the vertical axis represents the local characteristic kinetic energy of the protons. The dashed lines represent the

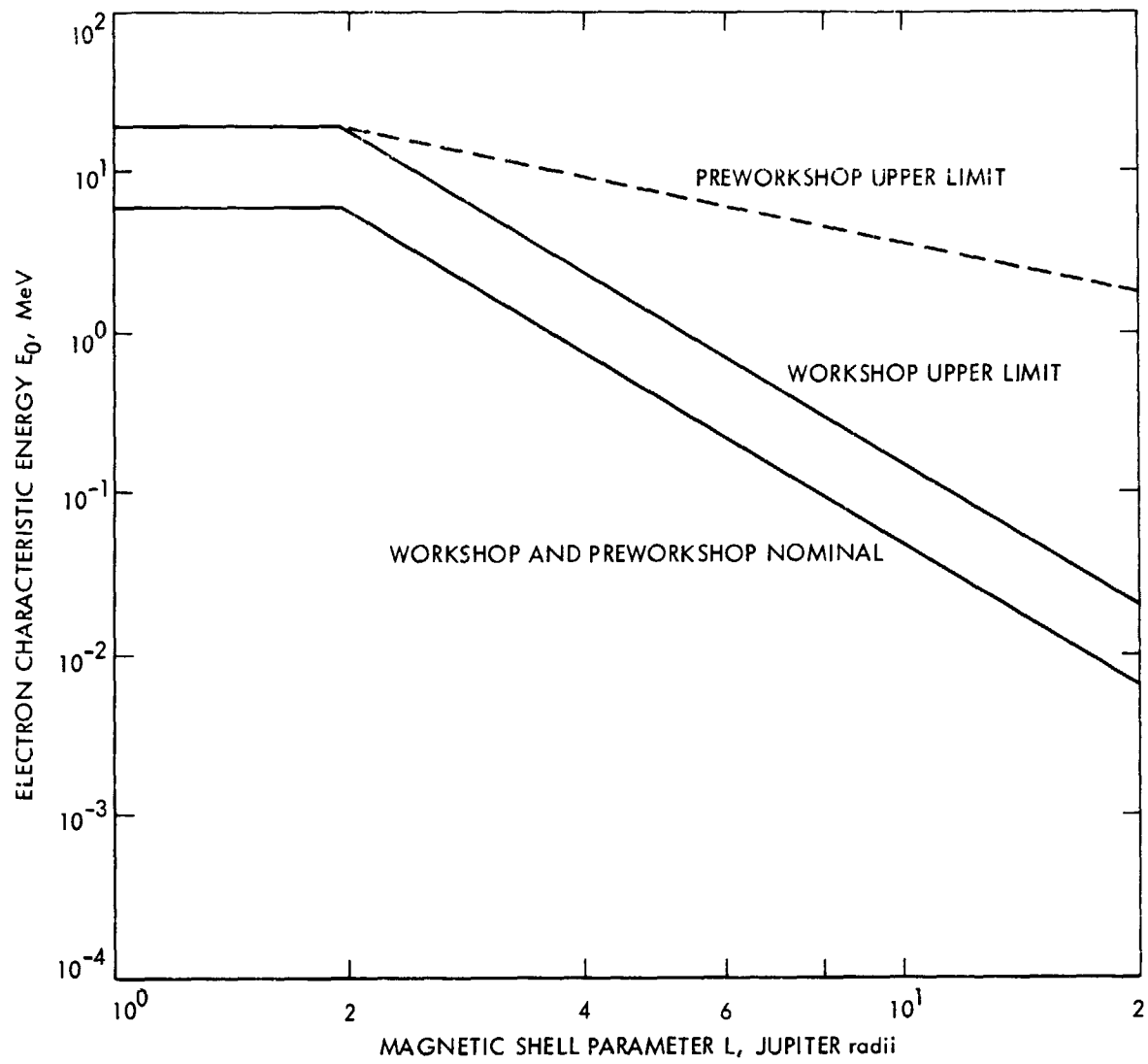

Figure 2. Jupiter trapped electron characteristic energy

preworkshop upper limit model; note that the upper limit preworkshop model energy is independent of L. The solid lines represent the workshop models. All diagonal lines represent energies proportional to L^{-3}, as required by any theory (e.g., L-shell diffusion) in which the particle magnetic moment is conserved during acceleration.

Electron and Proton Fluences for Jupiter Flyby Missions

The electron fluences and the proton fluences have been computed, using Jupiter radiation workshop models, for Jupiter flyby missions. In presenting the results, the fluence is given in terms of the equivalent 3-MeV electron fluence for electrons and the equivalent 20-MeV fluence for protons. The equivalent fluence Φ_c (Reference 4) is defined by

$$\Phi_c = \frac{\int_0^\infty D(E) \frac{d\Phi(E)\, dE}{dE}}{D(E_0)}$$

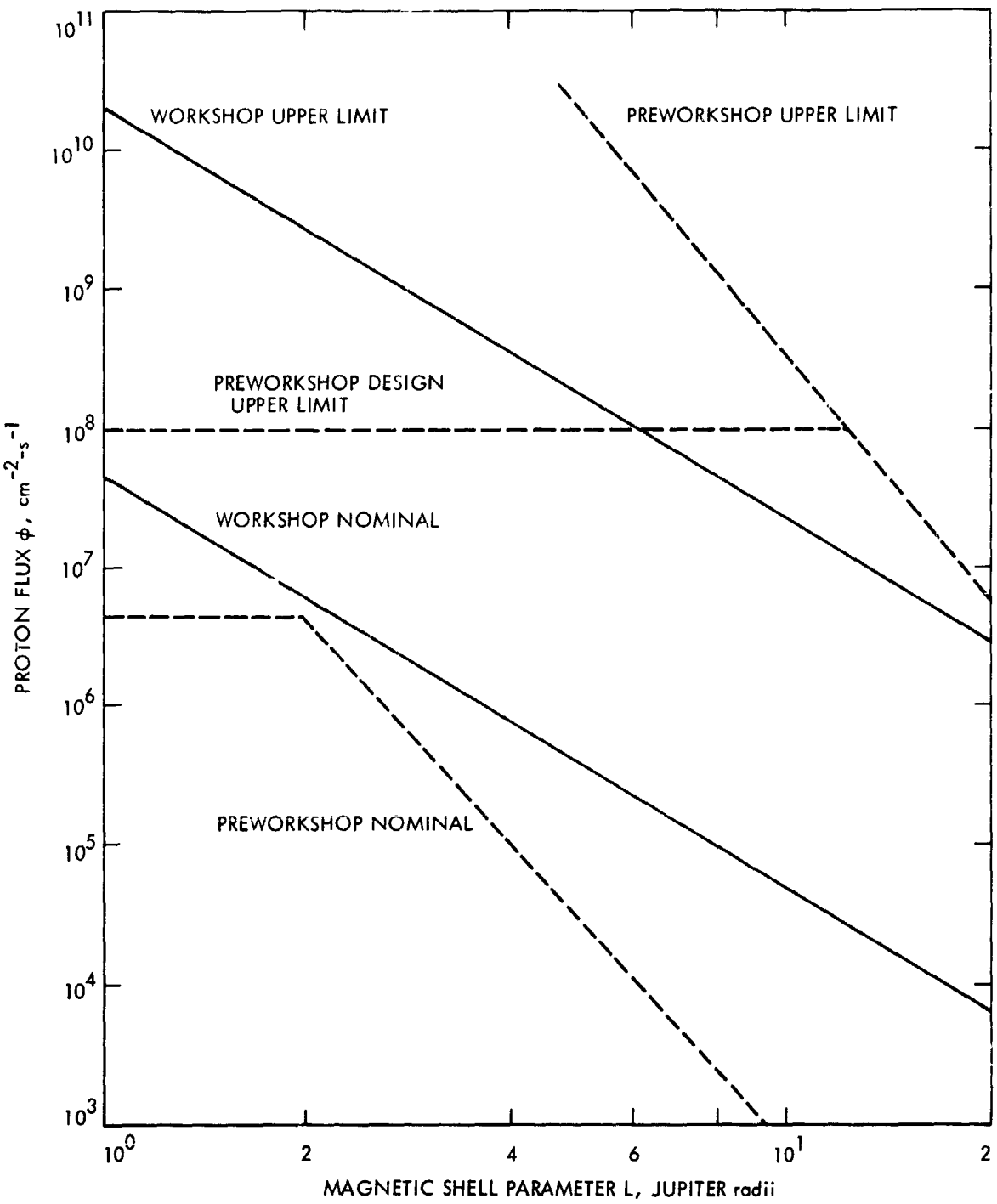

Figure 3. Jupiter proton models in the equatorial plane

where Φ_c is the equivalent fluence of particles at the reference energy E_c, $d\Phi(E)/dE$ is the differential energy fluence spectra, and $D(E)$ is the function which gives the radiation damage produced by particles of energy E.

The electron fluence accumulated during flyby missions past Jupiter is shown in Figure 5. The horizontal axis represents the altitude of closest approach of an equatorial flyby spacecraft, and the vertical axis represents the fluence (particles per unit area) of relativistic electrons, equivalent to 3 MeV according to the displacement damage they produce in silicon semiconductors. The dashed lines are based on the upper limit workshop electron model, for zero shielding (uppermost curve) and for 1.0-g/cm^2 shielding (e.g., 150 mils aluminum). The solid curves are based on the

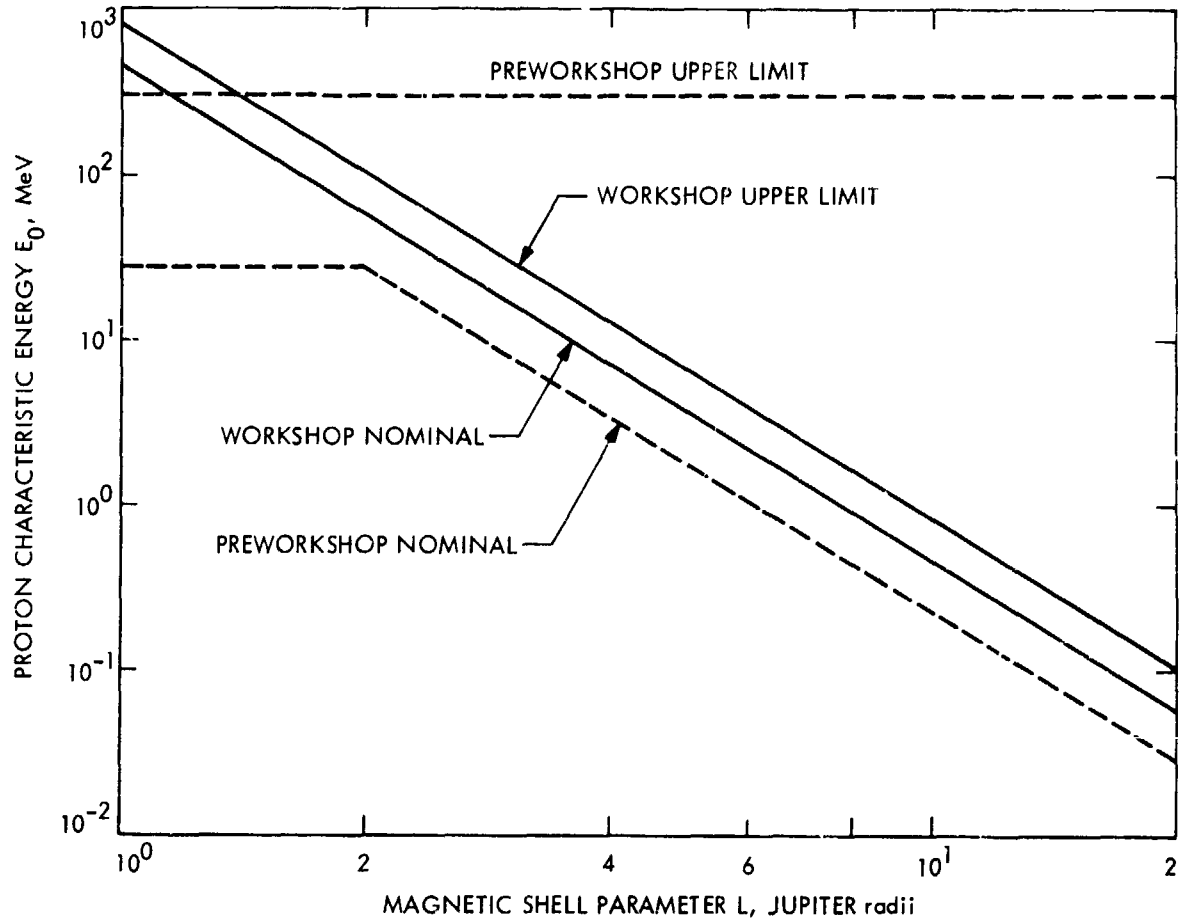

Figure 4. Jupiter trapped proton characteristic energy

nominal workshop electron model for the same two cases. The variation of the flyby turning angle (between 60 and 140 deg) and inclination (within ±10 deg) yields reductions in the fluence less than a factor of two. A considerable range of electron fluence exists for each of the outer-planet flyby missions corresponding to the possible missions between the minimum and maximum closest approach distances. The minimum and maximum altitudes of closest approach for the Jupiter–Saturn–Pluto 1977 (JSP 77) and Jupiter–Uranus–Neptune 1979 (JUN 79) missions are shown by vertical lines. For these missions the fluence is less than 2×10^{11} electrons/cm^2.

The proton fluence accumulated during the flyby of Jupiter is a sensitive function of both the closest approach distance and the amount of shielding available. Figure 6 shows the proton fluence for a range of closest approach altitudes. The horizontal axis represents the altitude of closest approach of an equatorial flyby spacecraft, and the vertical axis represents the fluence (particles per unit area) of energetic protons, equivalent to 20 MeV according to the displacement damage they produce in silicon semiconductors. The dashed lines are based on the upper limit workshop proton model, for zero shielding (uppermost curve) and for 1.0-g/cm^2 shielding (e.g., 150 mils aluminum). The solid lines are based on the nominal workshop proton model for the same two cases. The variation of the flyby turning angle (between 60 and 140 deg) and inclination (within ±10 deg) yields reductions in the fluence less than a factor of two. The radiation effects data for some

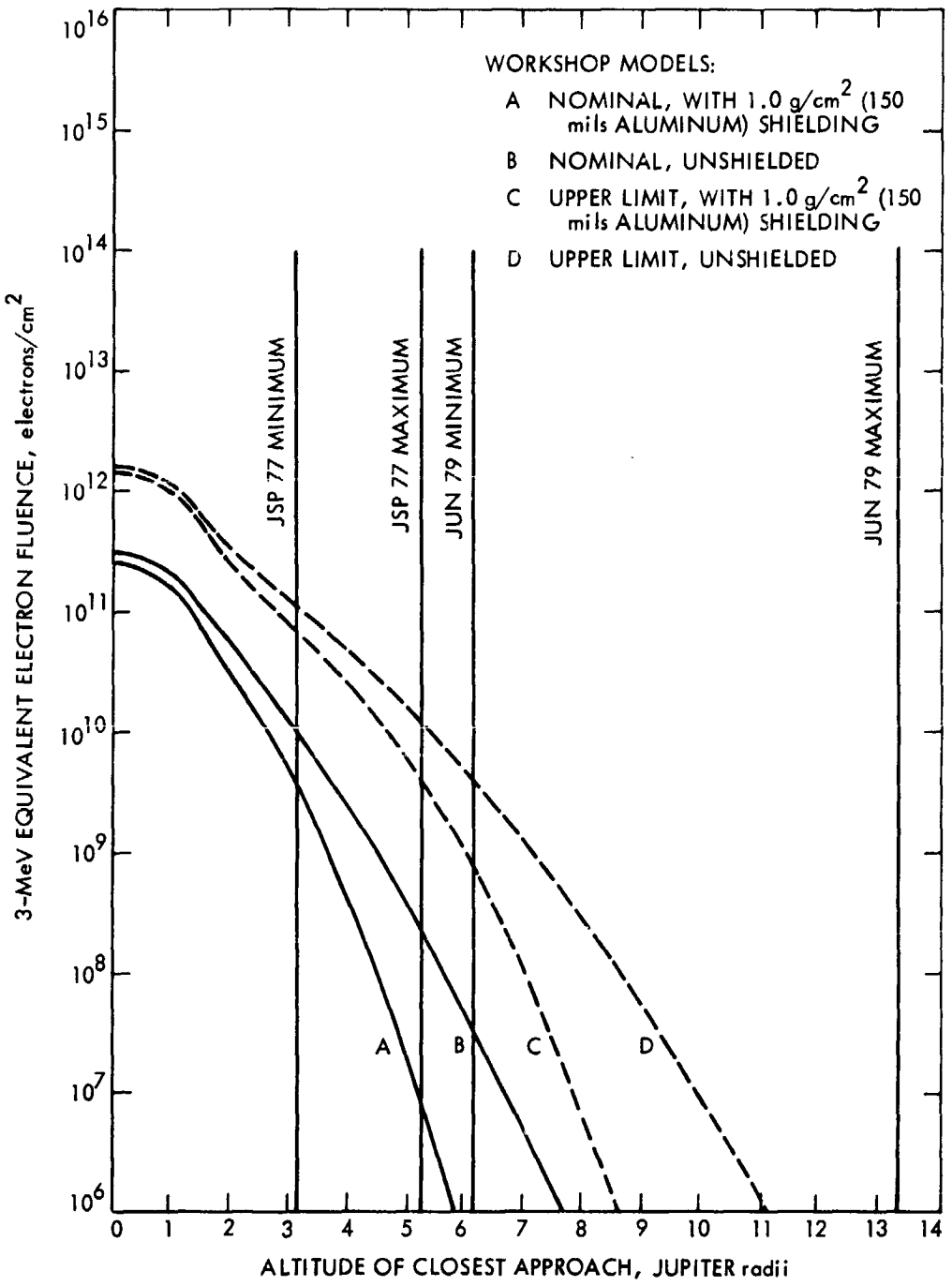

Figure 5. Equatorial flyby electron fluences (shielded and unshielded)

piece-parts show that the threshold for damage is a fluence approximately 3 $\times 10^9$ protons/cm^2 (Reference 4). By selecting radiation-resistant parts and employing design techniques to reduce the sensitivity of electronic assemblies, it may be possible to increase the threshold fluence by two to three orders of magnitude.

Conclusions

Models for the electron radiation belt and the postulated proton radiation belt at Jupiter have been described. These models resulted from the Jupiter Radiation Belt Workshop that was held at JPL during July 13–15, 1971. Proceedings for the workshop are expected to be published in the near future. In the interim, the models described here represent what the group

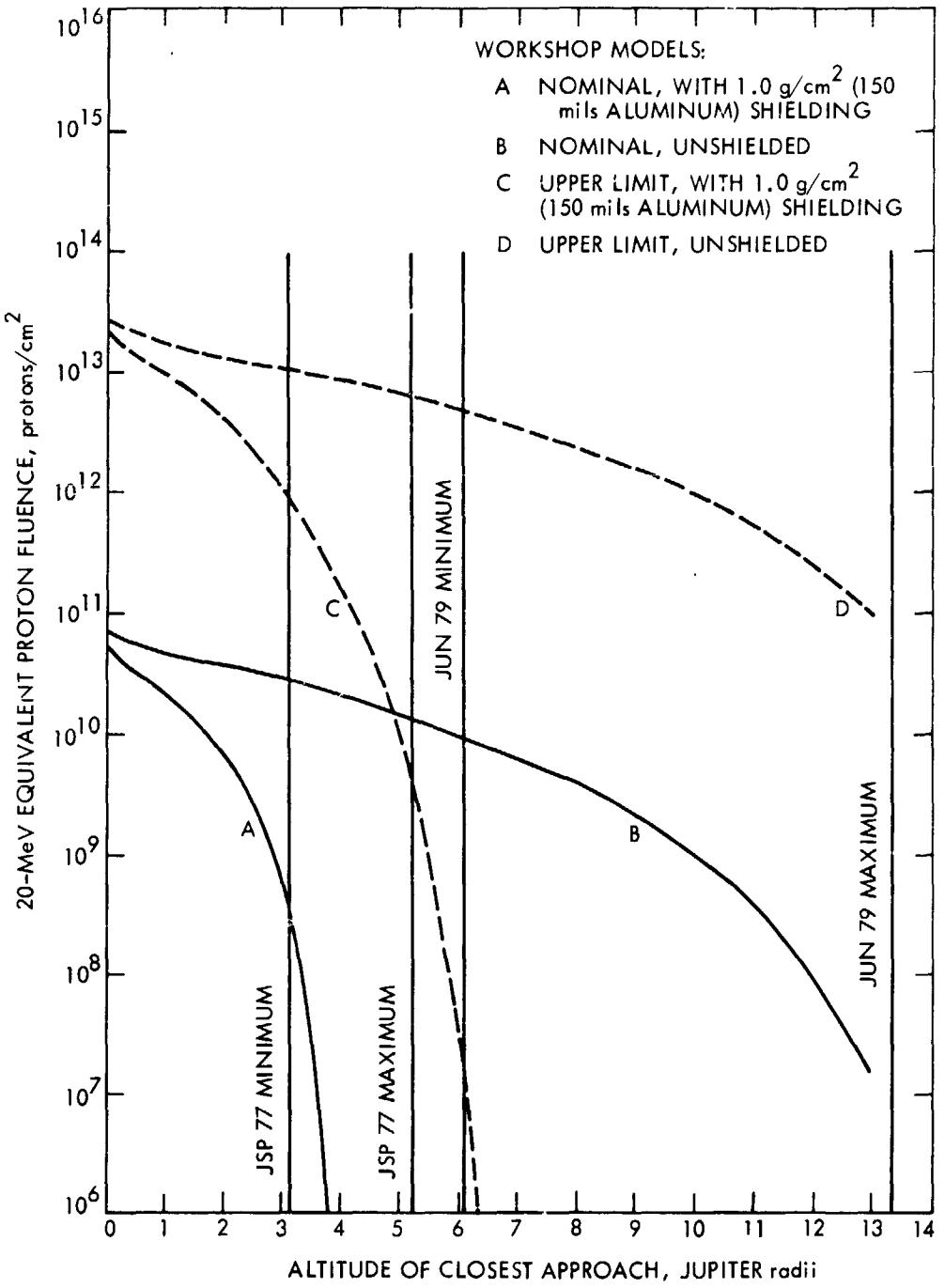

Figure 6. Equatorial flyby proton fluences (shielded and unshielded)

considered to be the best available description of the Jupiter radiation belts available at that time for the purpose of determining space vehicle radiation design requirements. The group, however, recognized the need to examine specific features of the models to insure internal consistency with the basic assumptions. For example, the effects of relativistic corrections on the assumed constancy of the first adiabatic invariant should be carefully examined. In addition, the spatial distribution for the flux models will require modification. Consequently, the models of Jupiter's radiation belts are still evolving. Yet, any revisions which may be required are not expected to affect the basic conclusions that are drawn here.

The Jupiter radiation belts, as described by these models, generally present a greater hazard to spacecraft than the Earth's radiation belts do. The most important reasons are that the Jupiter belts are much more extensive and that the particle energy at L values between 1 and 2 are generally larger than the energy of particles in the Earth's radiation belts. In addition, the proton flux is larger at the small L values. However, a considerable uncertainty exists in the electron flux as well as in the proton flux. A measure of this uncertainty for the proton flux can be readily seen by the nearly three-orders-of-magnitude difference between the nominal and upper limit flux models in Figure 3.

The electron and proton fluences are shown in Figures 5 and 6 for flyby missions in the equatorial plane having various closest approach altitudes. Comparing the fluences received for closest approach distances near the planet with the fluences that damage electronic parts (as given, for example, in Reference 4) shows that the proton fluence is generally more damaging than the electron fluence. Consequently, from a spacecraft design viewpoint, the proton model is more significant.

Figures 5 and 6 also show the relative effectiveness of radiation shielding. Radiation shielding clearly becomes more effective as the altitude of closest approach increases. This increased effectiveness results from the softening of the radiation because of the L^{-3} spatial dependence of the characteristic energy. A spacecraft probably has a minimum inherent self-shielding of the electronic parts, ranging from 0.66 g/cm^2 (100 mils of aluminum) to 1 g/cm^2 (150 mils of aluminum). When this inherent self-shielding is considered, the fluence reaching the electronic parts is so small for closest approach altitudes greater than 4 R_J for the nominal proton model and about 6 R_J for the upper limit proton model that the protons are no longer a significant design problem. However, there could still be some effects on science instruments.

For the electrons, radiation effects data (Reference 4) generally indicate, with the possible exclusion of some part types, that parts can be selected which can tolerate electron fluences somewhat in excess of 10^{11} electrons/cm^2. Consequently, considering the spacecraft self-shielding and by selecting and screening parts, the spacecraft can be made insensitive to the radiation fluences described by the nominal models for closest approach distances well inside of 4 R_J. The corresponding distance for the upper limit models is well within 6 R_J.

References

1. Warwick, J. W., *Particles and Fields Near Jupiter*, Report CR-1685. National Aeronautics and Space Administration, Washington, 1970.

2. Divine, N., "Jupiter Radiation Belt Engineering Model," paper presented at the National Symposium on Natural and Man-Made Radiation in Space, Las Vegas, Nevada, March 1–5, 1971.

3. Anon., *The Planet Jupiter (1970)*, NASA Space Vehicle Design Criteria Monograph, NASA SP-8069. National Aeronautics and Space Administration, Washington, 1971.

4. Barengoltz, J. B., "Jupiter Radiation Test Levels and Their Expected Impact on an Encounter Mission," paper presented at the National Symposium on Natural and Man-Made Radiation in Space, Las Vegas, Nevada, March 1–5, 1971.

N72-17898

JPL Quarterly Technical Review Volume 1, Number 4 January 1972

Nozzle Exhaust Plume Backscatter Experiment Using the JPL Molsink Facility

W. Simon

Propulsion Division

The flow field of gases and scattered particulates in the forward direction from a rocket nozzle is not presently predictable on a quantitative basis. Qualitative tests have been made with water injected through the nozzle wall and the droplet trajectories observed photographically. These tests were conducted for nozzles where the boundary layer is a significant portion of the flow. The tests indicated that both gases and particulate matter will be found in the region outside of the plume boundaries that can be calculated using current analytical techniques. A test program is being conducted in the JPL Molsink facility to measure the distribution of exhaust gases from small nozzles using an electron beam/photomultiplier system and a matrix of quartz crystal microbalances. Analysis of data from these tests, using nitrogen, will result in a better understanding of the backscattering flow field. Calibration tests of the Molsink, using simulated hydrazine exhaust product gas mixtures, have also been conducted, and future tests with small hydrazine thrusters are being considered. The test program and results of the pumping calibration tests with hydrazine (simulated hydrazine exhaust products) are reported.

Introduction

The interaction of plumes with spacecraft components can cause problems in such diverse areas as flight mechanics, materials and structures, communications, and scientific experiments. The possible problems are aggravated if a large percentage of the plume is composed of nozzle boundary layer gases. Because these have a lower velocity than the nozzle core gases, they have a higher potential of expansion and will cause a backscattering, or forward flow, of the exhaust gases. Although analytical methods, such as the method of characteristics, are available to predict plume characteristics for nozzles with negligible boundary layers, no equivalent methods are available for those with large boundary layers. Because the latter type of nozzles are typical of those used aboard unmanned spacecraft today, an experimental and analytical program to predict the nature of these plumes has been undertaken.

The JPL Molsink is being used to study the plume characteristics of small thruster nozzles. To obtain accurate measurements of the plume gas flow distribution, a number of special systems have been built and evaluated for use in the Molsink. An electron beam/photomultiplier system is used to map plume densities, and quartz crystal microbalance systems are used to detect the mass flux at a number of locations along the wall of the chamber. In addition, a gas supply system was designed, which can be adapted to a variety of test nozzles. These systems and some interim results of the test program are described in the following sections. To obtain a qualitative measure of the dispersal of small liquid droplets from a nozzle, a simple water injection test was conducted. Water was injected through a static pressure hole near the nozzle exit plane. Figure 1 is a photograph taken at a vacuum of 133.3 N/m^2 (1 torr).[1] The nozzle exit plane is in the center of the photo and the flow is downward. It is significant to note that even under the conditions of a finite back pressure, the photograph indicates that some of the water droplets are "backscattered," that is, they flow upward, forward of the exit plane of the nozzle.

Facility and Test Apparatus

The Molsink is an ultra-high-vacuum facility which consists of three concentric chambers. The inner-most chamber is a sphere approximately 3.048 m (10 ft) in diameter, maintained at a temperature between 15 and 20 K with gaseous helium. The walls are wedge-shaped, resembling an anechoic chamber, with a total surface area of approximately 185.8 m^2 (2000 ft^2). The chamber walls are also coated with titanium, which acts as "getter" material to trap helium and hydrogen that are not cryopumped by the 15-K surfaces. The titanium coating can be renewed while the chamber is evacuated. Recent tests, described in a later section, have shown that by coating the walls with carbon dioxide, the amount of hydrogen that can be pumped is greatly increased over that which can be pumped by the gettering action of the titanium alone.

The test gases are supplied from gas cylinders, located on a platform above the Molsink, into the nozzle plenum chamber, which is a 3.8-cm (1.5-in.) diameter tube penetrating through the top of the Molsink. It can be raised or lowered to change the location of the nozzle in the Molsink by about 15.24 cm (6 in.). The plenum chamber is instrumented to record both plenum temperature and pressure immediately above the nozzle throat. Heating elements control the temperature of the test gases.

A variety of small nozzles is available, with area ratios as low as 15:1 and as high as 240:1. Wall half-angles of these conical nozzles are 15, 25, and 40 deg. The throat diameter of most of the nozzles is 0.254 cm (0.100 in.) (see Reference 1). Pressure taps are located at the throat and exit plane as well as at the midpoint.

---

[1] Values in customary units are included in parentheses after values in SI (International System) units if the customary units were used in the measurements or calculations.

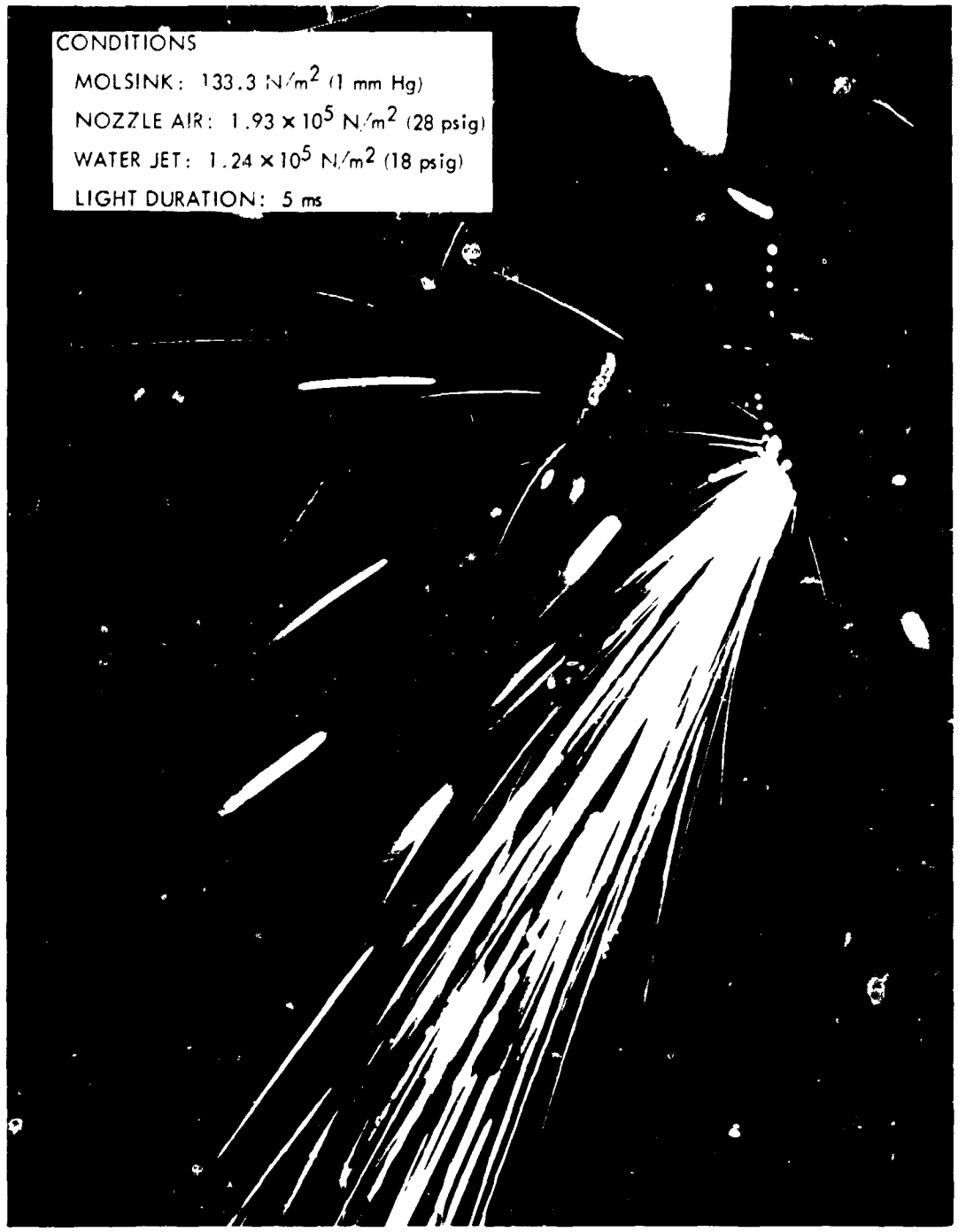

Figure 1. Nozzle water injection test

An electron beam/photomultiplier system measures the densities using the molecular fluorescence technique. A thin collimated beam of electrons at 10 to 20 kV is projected into a gas, resulting in an illuminated path, the intensity and spectral characteristics of which can be related to gas density. The fluorescence is measured with a photomultiplier. Its output, normalized by the electron beam current, is calibrated against known gas densities. For nitrogen a pressure range of 6.67×10^{-4} to 1.33×10^{1} N/m^2 (5×10^{-6} to 10^{-1} torr) can be measured. At the low density limit of operation, there is insufficient light intensity, while at the high density limit quenching collisions suppress light intensity. In terms of Mach number, the lower limit means that, for a nozzle using nitrogen and operating at a nozzle plenum pressure of 6.89×10^{3} N/m^2 (1 psia), densities in the region where the Mach

number is approximately 18 can be measured. Orientation of the electron beam/photomultiplier system is schematically shown in Figure 2. Motors, which are not shown in the figure, drive the system: one moves the electron beam and photomultiplier assembly relative to the test nozzle, and another moves the photomultiplier relative to the electron beam gun so that the density along the beam path can be measured. Potentiometers continuously record the position of these parts of the system. Mounted along the wall of the Molsink chamber are a series of quartz crystal microbalances (QCM), which are capable of detecting mass fluxes on the order of a monolayer or less. The key element of the QCM systems is a piezoelectric crystal which changes resonant frequency when mass is added to its surface. For a given temperature, the relationship between frequency and mass deposition is linear. By pairing quartz crystals the temperature effect is eliminated. The QCM is capable of detecting a cumulative buildup of mass, and it can detect discernible particles impinging and adhering on the crystals. Figure 3 is a schematic of the chamber, showing the relative location of the test nozzle, the electron beam and photomultiplier, and the quartz crystals mounted along the chamber wall. Mounted on the bottom door of the chamber is the electron beam apparatus used to sublimate the titanium which is deposited on the chamber wall surfaces. More detailed information about the chamber can be found in References 2, 3, and 4.

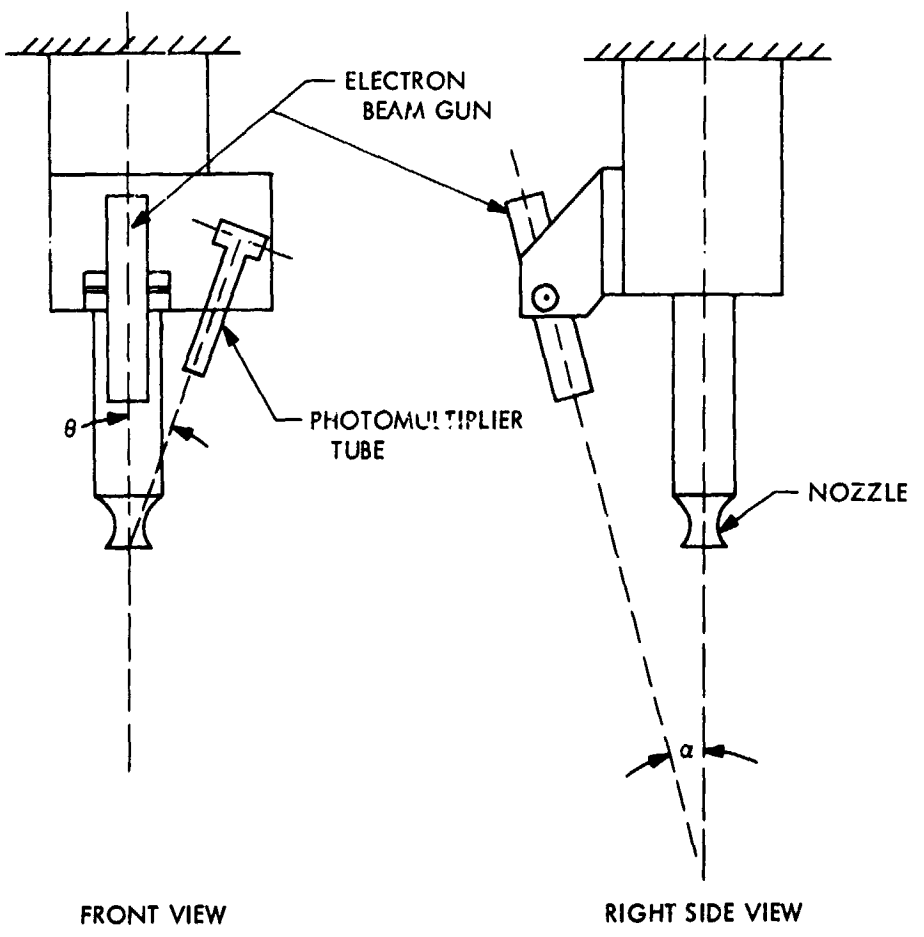

Figure 2. Electron beam/photomultiplier angles

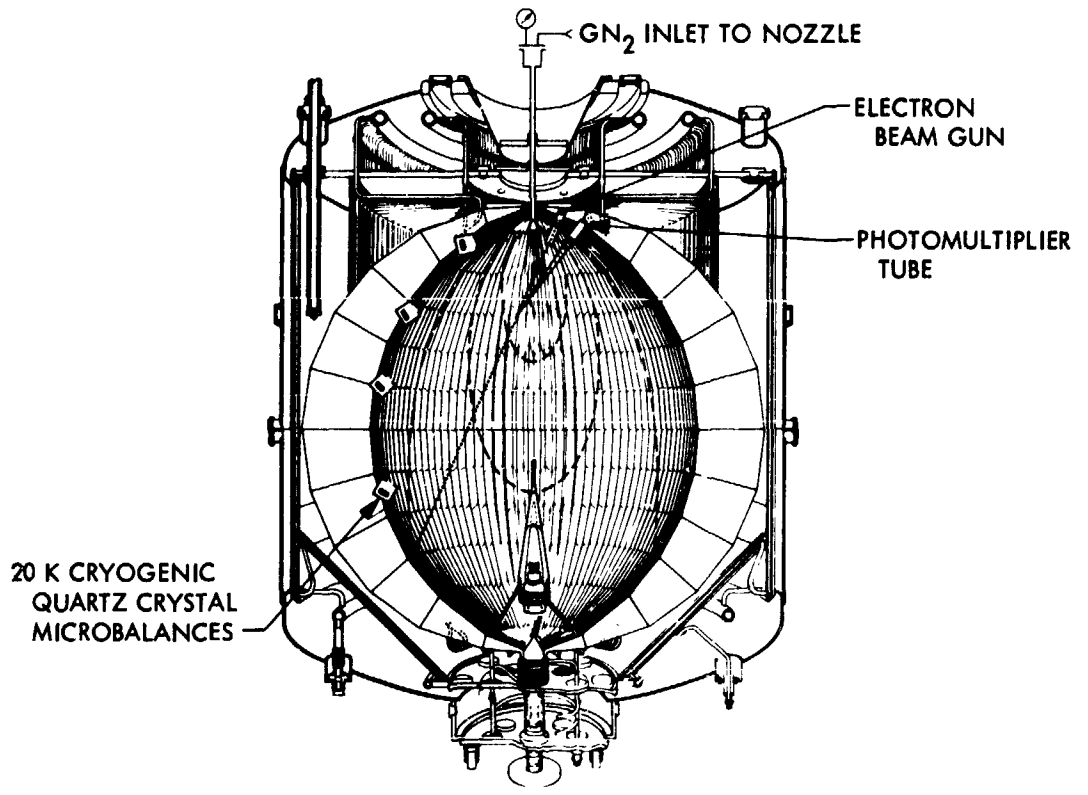

Figure 3. Molsink

Hydrogen Pumping Capacity

Molsink pumping capacity tests were conducted to determine its capability for plume tests of hydrazine thrusters in the 0.222- to 0.444-N (0.05- to 0.10-lb) range. The exhaust products from these engines contain hydrogen, ammonia, and nitrogen. The nitrogen and ammonia are easily cryopumped by the 15-K walls of the Molsink. Previous calibration tests, using nitrogen, have indicated that the Molsink pressure could be maintained at 1.33×10^{-3} N/m^2 (10^{-5} torr) with flow rates as high as 3 g/s. Hydrogen is more difficult to cryopump because 5-K walls are required to condense the hydrogen. To maintain the walls at this temperature, liquid helium would have to be circulated through the wall, which is expensive. Some hydrogen will be absorbed by the titanium, which is on the Molsink wall, but calculations indicate that the amount of hydrogen that can be pumped by the walls is inadequate.

Pumping of hydrogen by carbon dioxide cryodeposits has been reported in Reference 5. This method consists of injecting carbon dioxide gas into a vacuum chamber whose walls have been cooled to about 20 K or less. The carbon dioxide forms a porous frost on the walls and removes the hydrogen by sorption pumping. Therefore, calibration tests of the Molsink using hydrogen/nitrogen mixtures were conducted. Hydrazine exhaust products contain hydrogen, nitrogen, and ammonia, but it was decided to substitute nitrogen for the ammonia to simplify the tests. A mixture of 53% hydrogen and 47% nitrogen, by volume, was used. This percentage of hydrogen is typical in the exhaust products of small hydrazine monopropellant thrusters.

Carbon dioxide gas was injected through the test nozzle at a flow rate of 0.2 g/s for 24 min to coat the walls of the Molsink. After the frost coating had been allowed to stabilize on the walls, the hydrogen/nitrogen mixture was injected through the test nozzle at a flow rate of approximately 0.1 g/s as shown in Figure 4. The results of the tests are shown in Figure 5, which indicates that a pressure in the 1.33×10^{-2}-N/m^2 (10^{-4}-torr) range was maintained for approximately 4½ min. The pressure in the Molsink prior to the test gas injection was 6.67×10^{-4} N/m^2 (5×10^{-6} torr). The pressure rose to 2.67×10^{-2} N/m^2 (2×10^{-4} torr) within 0.3 min after the test gas was injected. This pressure was maintained for 4½ min, after which the pressure rose rapidly (an order of magnitude per minute) and the gas flow into the chamber was terminated. The tests have indicated that the use of carbon dioxide frost is an inexpensive and convenient method for pumping hydrazine exhaust products in the Molsink. The hydrogen/nitrogen gas flow rates used during the tests were those equivalent to a 0.222-N (0.05-lbf) thruster. Future Molsink calibration tests are planned to determine the pumping capacity, using carbon dioxide frost, and test gas flow rates equivalent to 0.444-N (0.10-lbf) thrusters. In addition, cyclic test sequences will be used to see if by renewing the carbon dioxide frost coating before it is saturated the Molsink pressure can be prevented from rising above the

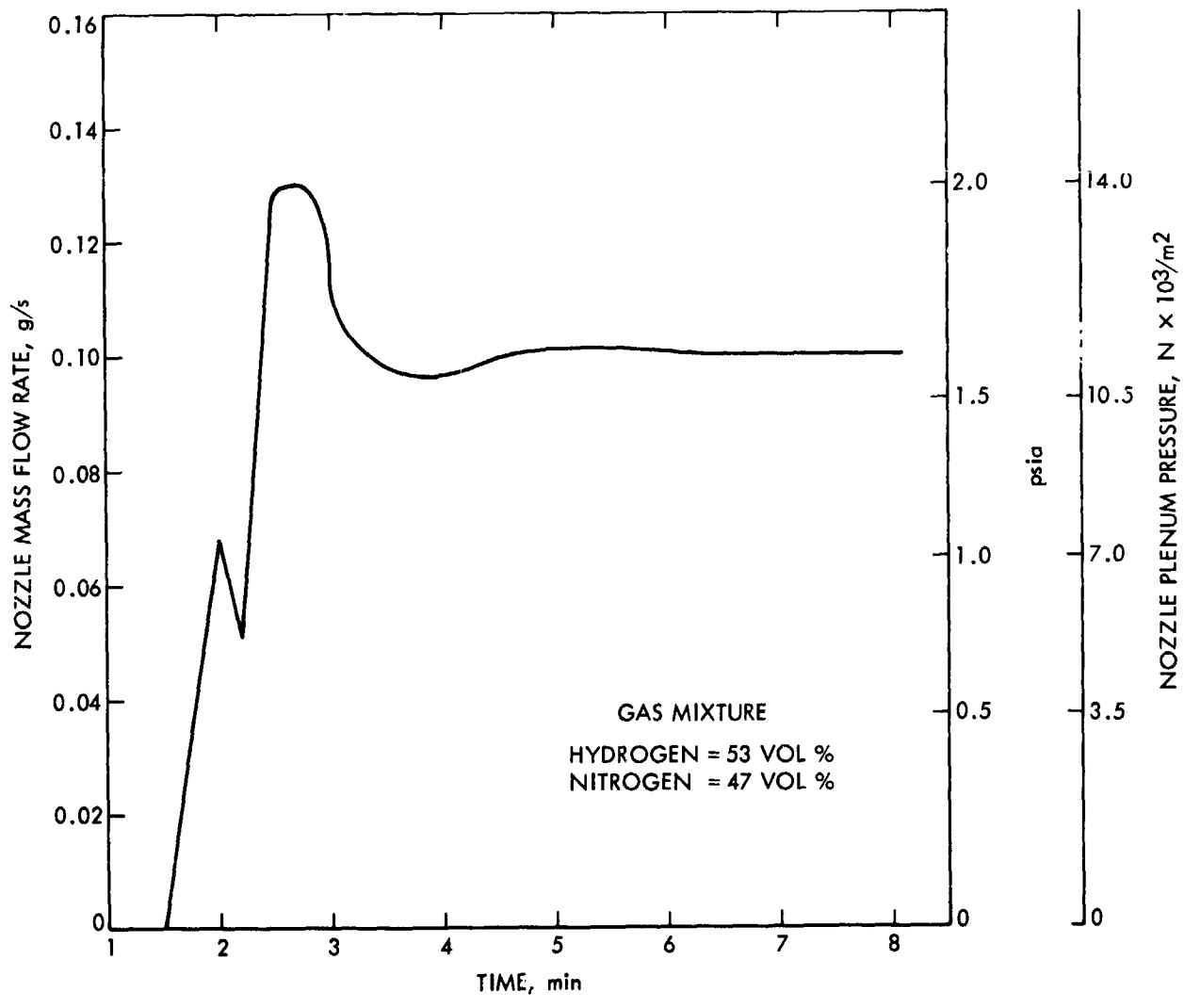

Figure 4. Molsink hydrogen/nitrogen gas mixture injection parameters

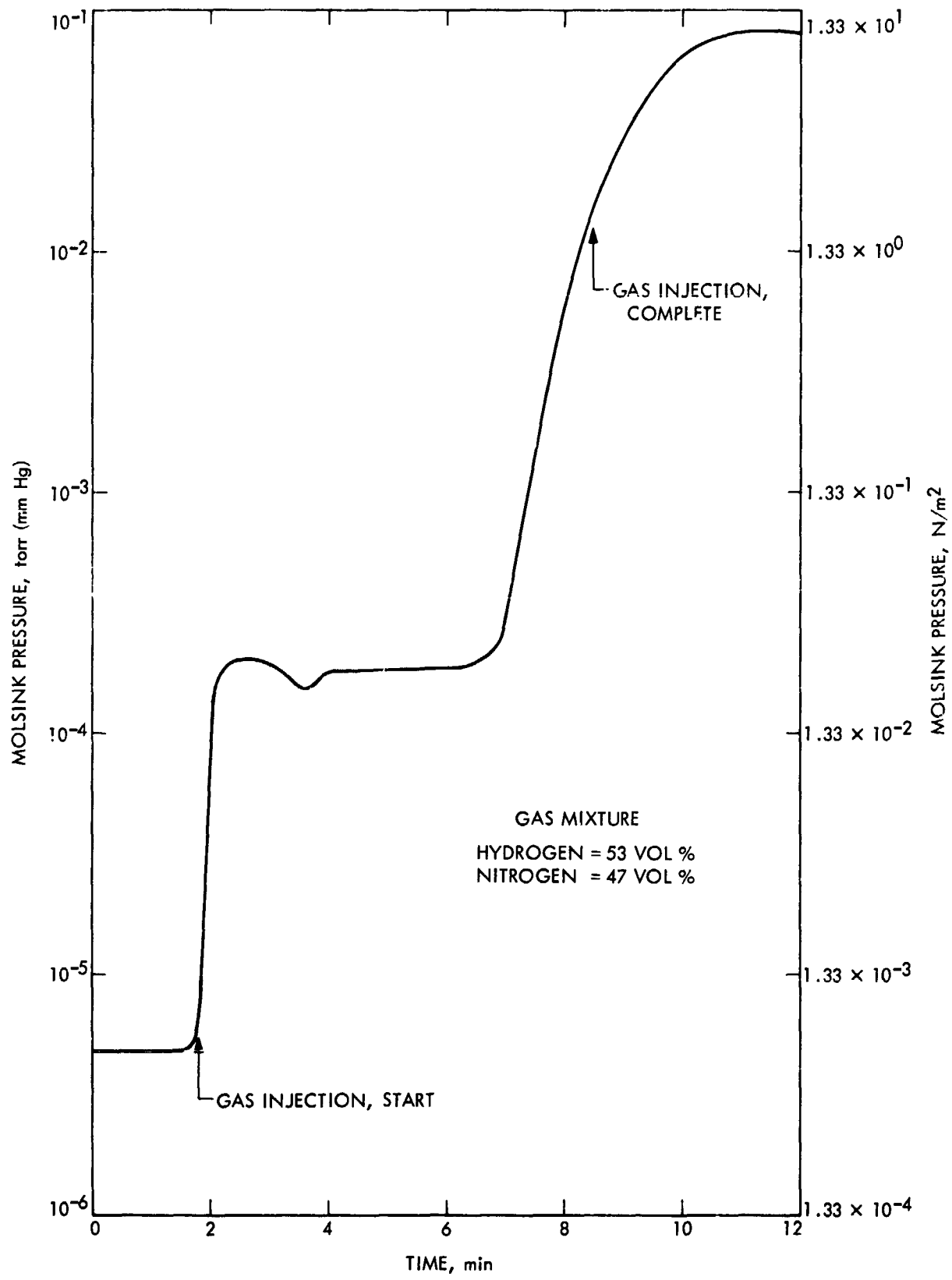

Figure 5. Molsink pressure history of hydrogen/nitrogen mixture injection

value established when the test gas is initially injected. The amount of carbon dioxide injected will also be varied to determine the relationship between the frost coating thickness and mass, the chamber pressure, and the amount of hydrogen pumped.

Future Test Plans

Tests are continuing in the Molsink using the electron beam and quartz crystal systems. The data from these tests will be used to help establish an analytical model that can be used to predict the plume characteristics of small thrusters where the boundary layer is an important influencing factor.

References

1. Herrera, G., "Thrust and Plume Measurements Taken on Miniature Nozzles in a Vacuum Chamber," in *Supporting Research and Advanced Development*, Space Programs Summary 37-62, Vol. III, pp. 214–216. Jet Propulsion Laboratory, Pasadena, Calif., Apr. 30, 1970.

2. Stephens, J. B., "Spacecraft Mechanism Testing in the Molsink Facility," paper presented at 4th Aerospace Symposium, University of Santa Clara, May 22–23, 1969.

3. Stephens, J. B., "Molecular Sink," *Research/Development*, July 1967.

4. Stephens, J. B., "Space Molecular Sink Simulator Facility Design," *J. Spacecraft Rockets*, June 1966.

5. Tempelmeyer, K. E., Dawbarn, R., and Young, R. L., "Sorption Pumping of Hydrogen by Carbon Dioxide Cryodeposits," *J. Vacuum Sci. Technol.*, Vol. 8, No. 4, 1971.

N72-17899

JPL Quarterly Technical Review Volume 1, Number 4 January 1972

New Polymer Systems: Chain Extension by Dianhydrides

R. A. Rhein and J. D. Ingham

Propulsion Division

New highly stable polymers are required for materials applications on future long-term planetary missions. This article presents the results of a systematic investigation on the use of anhydrides to prepare stable elastomeric materials using mild reaction conditions. The three anhydrides investigated were found to provide effective chain extension of hydroxy-terminated poly(alkylene oxides) and poly(butadienes). These were tetrahydrofuran tetracarboxylic dianhydride, pyromellitic dianhydride, and benzophenone tetracarboxylic dianhydride. The most effective catalyst investigated was ferric acetylacetonate, which resulted in chain extension at 333 K (60°C). A novel feature of these anhydride reactants is that they are difunctional as anhydrides, but tetrafunctional if conditions are selected that lead to reaction of all carboxyl groups. Therefore, chain extension can be effected and then followed by crosslinking via the residual carboxyl groups.

Introduction

The objective of this work is the development of stable elastomeric systems for solid-propellant binders applicable to long-term planetary missions. Achieving this objective requires dimensional and mechanical stability as well as insensitivity to radiation. Such elastomers should evolve a minimum of volatile products. These new elastomers should be useful in other applications. Previous work has shown that anhydrides can be used to chain-extend hydroxy-terminated prepolymers (Reference 1 and related unpublished JPL work); however, chain extension was limited and reaction conditions were relatively severe. The work reported here was conducted to obtain higher molecular weights and determine the effects of different catalysts, diols, and dianhydrides.

Diols included poly(propylene oxide) (PPO), poly(ethylene oxide) (PEO), and poly(butadienes). For a polymer of increased stability, saturated hydrocarbon prepolymers will be more extensively tested in future work. Anhydrides included tetrahydrofuran tetracarboxylic dianhydride

(THFTDA), pyromellitic dianhydride (PMDA), and extension can be illustrated by

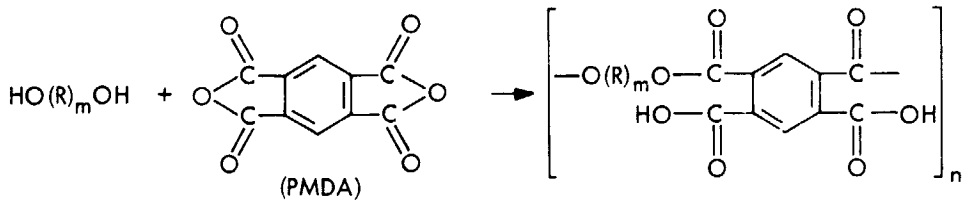

where R is a monomeric unit in the prepolymer, extension can be illustrated by where R is a monomeric unit in the prepolymer, m is the prepolymer degree of polymerization, and n is the degree of polymerization of the extended prepolymer.

Results and Discussion

For most of the experiments, poly(propylene oxide) of mol wt 2000 and hydroxyl of 1.0 eq/kg (Union Carbide, Lot 439430) was used as the diol. Approximate intrinsic viscosities $[\eta]$ were calculated from the expression

$$\eta_{sp}/C = [\eta] + 0.39 [\eta]^2 C$$

from measurements at one concentration C in benzene or dimethylformamide at 303 K (30°C). This relationship is strictly valid only for PPO–toluene diisocyanate (TDI) polymers (Reference 2), but is used here for comparison of anhydride polymers with the values obtained for PPO–TDI, as an approximation of the degree of chain extension. For the extension of prepolymers, the dianhydride and low molecular weight polymer were stirred at 448–468 K (175–195°C) to dissolve the anhydride; the catalyst (if any) was added, and the solution was cured in a vacuum oven at the desired temperature.

Since imidazole had been found to be a catalyst for the reaction of alcohols with PMDA for hydroxyl analytical methods (Reference 3), it was tested as a catalyst for the reaction of PPO with PMDA. The desired catalytic effect was found to be negligible. At a mole ratio of PMDA to PPO (AN/OH) of 1.0 and a curing temperature of 373 K (100°C), the values of $[\eta]$ were 1.6 and 1.5 m^3/kg in the presence (21-h cure) and absence (24-h cure) of imidazole, respectively. The catalyst concentration was 0.2 mole per mole of PMDA. There are two functions of a catalyst in systems of this type. Not only should it increase the rate of the desired chain-extension reaction, but it is also desirable that it increase this rate relative to side-reaction rates. Therefore, although imidazole was found to increase the chain-extension rate at times shorter than 24 h, the final molecular weight for longer cure times was no higher when it was present, indicating that side-reaction rates were also catalyzed. When short-reaction times are desired, as for analytical

methods, imidazole is an effective catalyst for anhydride–hydroxyl reaction. Further work showed that imidazole, pyrole, and pyridine did not give higher values of $[\eta]$ than no catalyst for cure times from 14 to 134 h at 333 K (60°C) with a mole ratio of PMDA to PPO of 1.05. The intrinsic viscosities were always 1.1 (±0.3) kg/m^3 under these conditions.

However, the presence of ferric acetylacetonate (FeAA) resulted in an intrinsic viscosity ~2.4 m^3/kg in 66 h at 333 K (60°C). The ratio of FeAA/anhydride was 0.2; thus, the catalyst concentration was higher and the effect less than for isocyanate–hydroxyl reactions. In an experiment in which the FeAA to anhydride or diisocyanate ratio was 0.002, the extended anhydride and isocyanate polymers had $[\eta]$ = 1.8 and 8.8 m^3/kg, respectively. However, the reactant ratio was probably more nearly optimum for the urethane polymer, accounting for part of the larger increase in molecular weight.

Figure 1 indicates the effect on $[\eta]$ when PPO was chain-extended with several different anhydrides in the absence of catalyst at 333 K (60°C). THFTDA resulted in the highest molecular weights and was as effective as TDI under these conditions. Inspection of the results in Figure 1 indicates that the rate of chain extension may depend on the solubility parameters of anhydride and diol.

From Figure 2, it can be seen that the anhydride–hydroxyl mole ratio is in the vicinity of 1.05 for maximum chain extension. The value appears to be relatively critical and somewhat less than the value of 1.10 generally used for NCO/OH ratios. Figure 2 also shows that FeAA is a much more effective catalyst for anhydride extension than CuAA or NiAA, which is also true for the isocyanate reaction.

Some experiments were also carried out at higher temperatures, for which gelation times were measured. Results are indicated in Figure 3. Because of esterification following anhydride ring opening, it appears that a crosslinked network can be formed and gelation may occur in 150 h at 373 K (100°C). The apparent upward curvature at lower temperatures is probably real, but, even if it is not, the relative rate of anhydride opening would be approximately six times faster than esterification at 333 K (60°C), indicating that negligible esterification would take place under normal low-temperature curing conditions for this system.

Table 1 shows some results obtained for chain extension and crosslinking of poly(ethylene oxide), poly(butadienes), and a reduced saturated poly(butadiene). The higher temperature, 463 K (190°C), was used to dissolve the anhydride in the prepolymer. For these prepolymers, considerable chain extension and some crosslinking took place during the dissolution, as indicated by high initial intrinsic viscosities and gel formation within 10 min at 463 K in some cases.

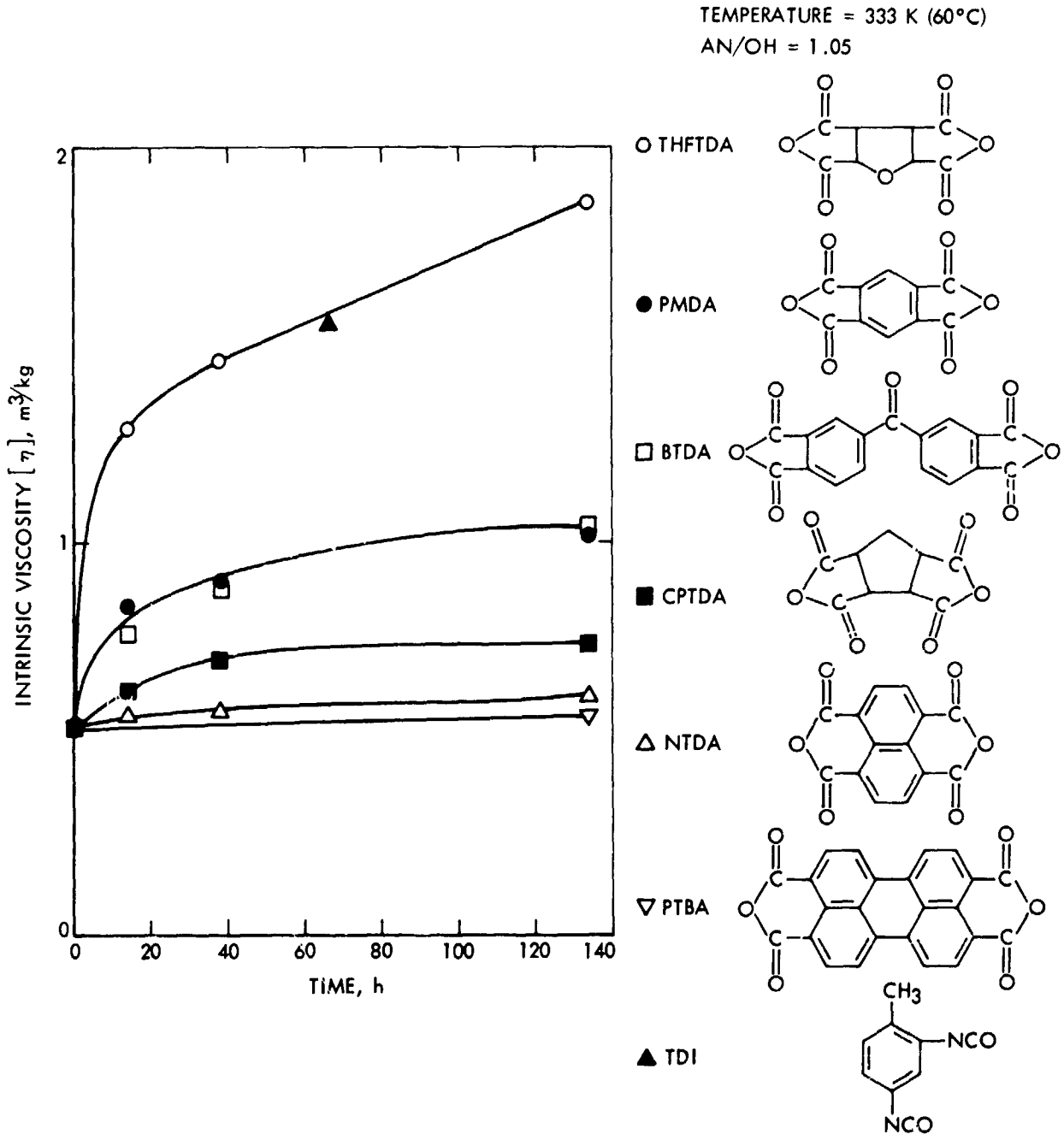

Figure 1. Solution viscosity of anhydride chain-extended poly(propylene oxide)

Conclusions and Recommendations

It has been found that THFTDA readily chain-extends PPO to high molecular weights in the presence of FeAA catalyst at 343 K (70°C) or lower. The reaction with hydrocarbon prepolymers appears to take place at higher rates, even in the absence of a catalyst.

Further work, particularly with saturated hydrocarbon prepolymers, should be conducted to define the minimum dissolution temperature and to determine which dianhydride will produce maximum chain extension and minimum esterification at moderate temperatures. Crosslinking of the carboxyl groups formed on ring opening should be investigated further, especially to form crosslinks at temperatures below 373 K (100°C). Trifunctional hydroxyl compounds, as well as metallic salts or oxides, should be tested. The former would be analogous to triols in urethane system, whereas the latter should provide salt crosslinks that would react with some of the free carboxyl groups and may tend to increase chemical stability.

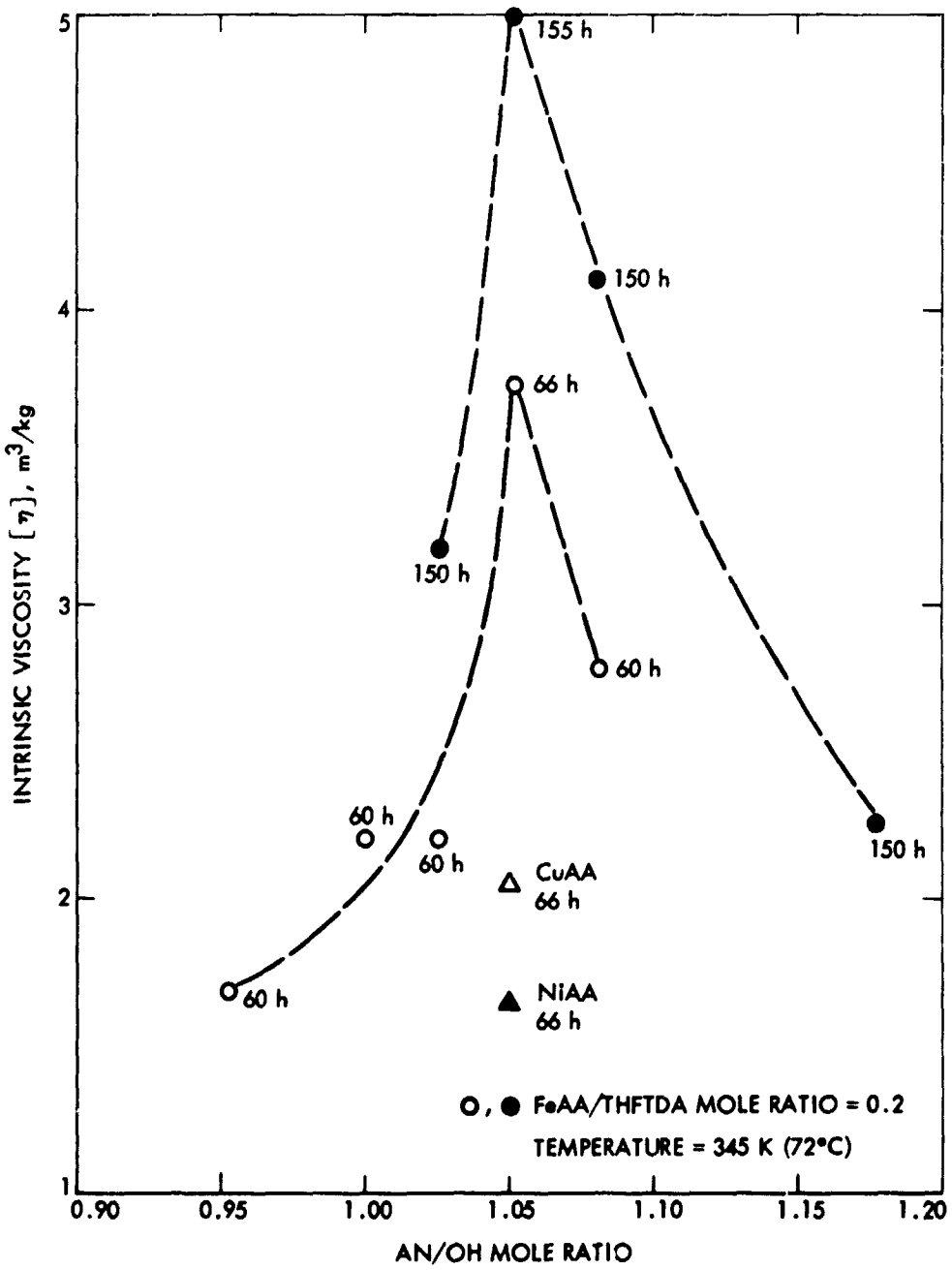

Figure 2. Solution viscosity of anhydride-poly(propylene oxide) versus anhydride to hydroxyl mole ratio

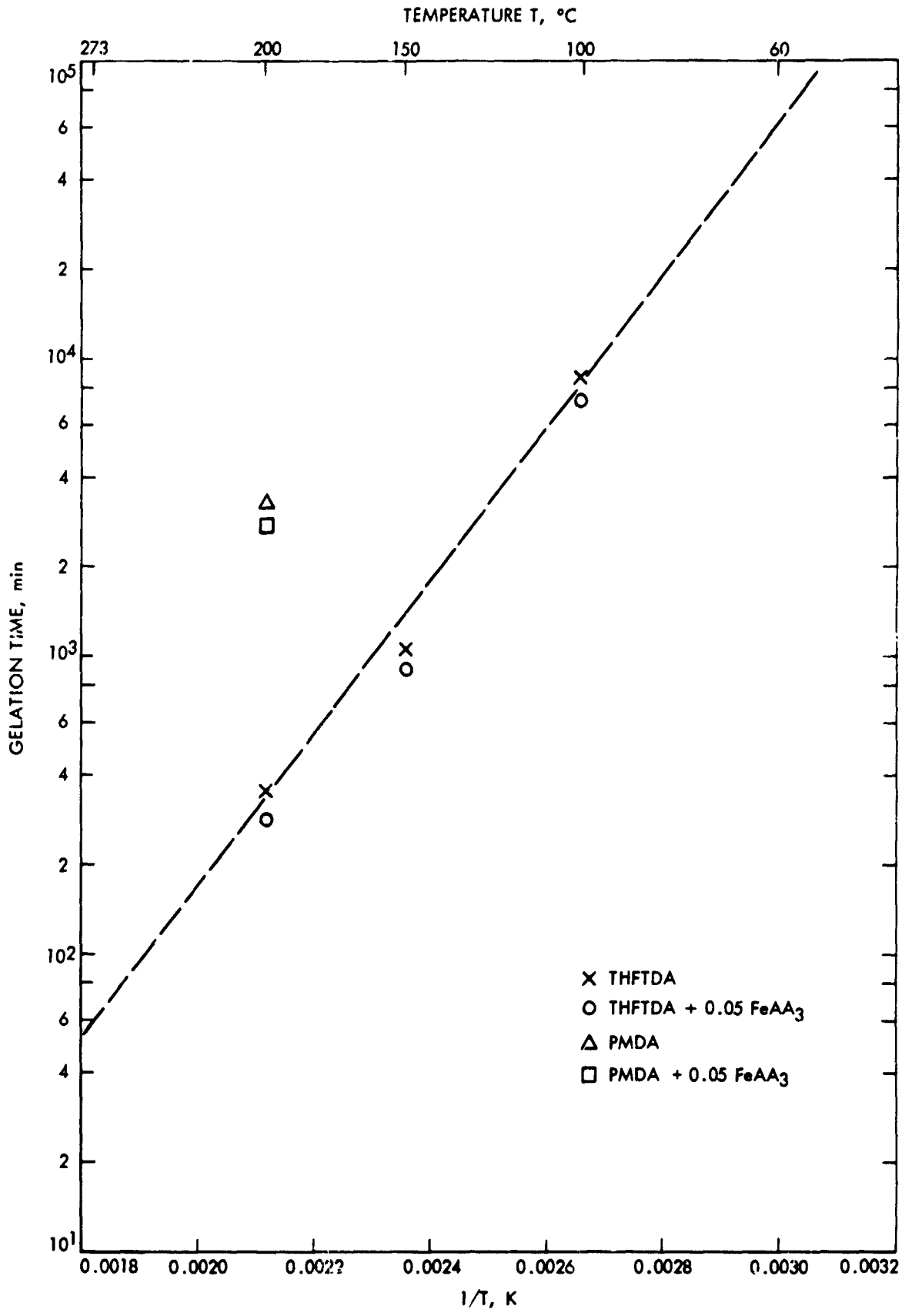

Figure 3. Gelation time versus temperature for anhydride-poly(propylene oxide) polymers

References

1. Ingham, J. D., "Saturated Hydrocarbon Prepolymers," in *Supporting Research and Advanced Development*, Space Programs Summary 37-52, Vol. III, pp. 97–98. Jet Propulsion Laboratory, Pasadena, Calif., Aug. 31, 1968.

Table 1. Prepolymer chain extension with THFTDA

Prepolymer	Time, min	Temperature, K (°C)	Mole ratio AN/OH	Initial $[\eta]$,[a] m^3/kg	Final $[\eta]$,[a] m^3/kg
Poly(ethylene oxide)[b]	3960 (66 h)	345 (72)	1.05[c]	0.8	1.6
Telagen-S[d]	10	463 (190)	1.05	0.8	2.3
Telagen-S[d]	60	463 (190)	1.16[c]	–	Gel
Telagen-S[d]	1080 (18 h)	345 (72)	1.05	–	Gel
Hycar HTB[e]	10	463 (190)	1.00[c]	0.6	6.4
Butarez HTS[f]	10	463 (190)	1.05	1.5	3.0
Butarez HTS[f]	18	345 (72)	1.05	–	Gel
Poly-BD, CN-15[g]	10	463 (190)	1.05	–	Gel
Poly-BD, R-45M[g]	10	463 (190)	1.05	–	Gel
Poly-BD, R-15M[g]	10	463 (190)	1.05	–	Gel
Poly-BD, R-45HT[g]	10	463 (190)	1.05	–	Gel
Poly-BD, CS-15[g]	10	463 (190)	1.05	–	Gel

[a] Viscosities obtained by single-point measurements using $\eta_{sp}/C = [\eta] + 0.4\,[\eta]^2C$.
[b] A. G. Fluka, mol wt 2000.
[c] Contained FeAA/anhydride mole ratio = 0.05.
[d] Saturated poly(butadiene) α,ω-diol, GT and R, Lot 242 AM 148AH, hydroxyl 0.91 eq/kg.
[e] Poly(butadiene) α,ω-diol, B. F. Goodrich, Lot V-74, hydroxyl 0.38 eq/kg.
[f] Poly(butadiene) α,ω-diol, Phillips Petroleum, Lot 4760, hydroxyl 0.51 eq/kg.
[g] Hydroxy-terminated poly(butadienes), ARCO Chemical (all hydroxyl values from supplier's data):

CN-15, Lot 003061, hydroxyl 0.58 eq/kg
R-45M, Lot 008281, hydroxyl 0.70 eq/kg
R-15M, Lot 710291, hydroxyl 0.65 eq/kg
R-45HT, Lot 006041, hydroxyl 0.84 eq/kg
CS-15, Lot 912211, hydroxyl 0.62 eq/kg

2. Moacanin, J., "Diisocyanate-Linked Polymers. I. Dilute Solution Properties of Toluene Diisocyanate-Extended Polypropylene Glycol," *J. Appl. Polym. Sci.*, Vol. I, No. 3, pp. 272–282, 1959.

3. Kingston, H. M., Garey, J. J., and Hellwig, W. B., "Imidazole Catalysis of Organic Hydroxyl Group Determination by Reaction with Pyromellitic Dianhydride in Dimethylformamide," *Anal. Chem.*, Vol. 41, pp. 86–89, 1969.

N72-17900

JPL Quarterly Technical Review Volume 1, Number 4 January 1972

Mariner Venus–Mercury 1973 Midcourse Velocity Requirements and Delivery Accuracy

E. L. McKinley

Mission Analysis Division

The Mariner Venus–Mercury 1973 Mission represents the first attempt to navigate a single spacecraft to more than one planet. The primary mission consists of encounters with Venus and Mercury (a second encounter with Mercury is also possible). In this study, the expected navigation sequences are simulated with a Monte Carlo computer program for the purpose of determining midcourse correction velocity requirements and delivery accuracies. These simulations provide the sensitivity of the velocity requirements and delivery accuracies to the error sources affecting the navigation process. The orbit determination capability at the final pre-Venus maneuver is shown to be the dominant contributor to the velocity requirements for the primary mission. Similarly, the orbit determination capability at the final pre-Mercury maneuver is shown to be the dominant contributor to the delivery accuracy at Mercury.

Introduction

In the 1970's, several opportunities exist for using the gravitational field during a planetary encounter to assist a spacecraft in attaining still another planetary encounter. (Missions of this type are made possible by the particular geometrical alignments of the planets.) One such opportunity occurs in the 1973–1974 time period and involves the planets Earth, Venus, and Mercury. Known as the Mariner Venus–Mercury 1973 mission, the primary mission consists of encounters with Venus and Mercury (with scientific emphasis on Mercury) where the encounter with Venus is designed to provide departure conditions necessary to achieve the Mercury encounter. (For a given Earth launch date and Mercury arrival date, arrival conditions at Venus are fixed.) Although not presently a part of the Mariner Venus–Mercury 1973 mission, a second Mercury encounter may be possible. This is made possible by a second fortuitous circumstance, namely, that the period of the post-Mercury heliocentric trajectory is approximately twice the orbital period of Mercury. Therefore, for appropriately selected aim

points at the first Mercury encounter (Mercury I), a second encounter (Mercury II) will occur approximately 176 days later.[1]

The essential elements of the mission described above are given by Figure 1, which shows a heliocentric plane view for a typical Mariner Venus–Mercury 1973 trajectory. Also shown is an edge view of the ecliptic plane illustrating the motion of the spacecraft out of the ecliptic plane. Additional detail on the mission design is given by References 1, 2, and 3.

This article describes results of a Mariner Venus–Mercury 1973 navigation study directed toward answering the following questions:

(1) What midcourse maneuvers are required to accomplish the primary mission, and to accomplish an extended mission consisting of a second encounter with Mercury?

(2) What are the corresponding maneuver magnitudes?

(3) How well can the delivery to the target planets be accomplished?

(4) What is the relative importance to the midcourse maneuver magnitudes of the various error sources which contribute to the overall navigation errors?

The answers to these questions depend upon the actual spacecraft and mission designs, and certain of the results described here are subject to minor changes as the design continues. However, unless there are considerable changes in certain areas affecting the navigation process, the characteristics of the navigation and maneuver strategy given below are a good representation of what can be expected during the Mariner Venus–Mercury 1973 mission.[2]

Maneuvers Required

The Mariner Venus–Mercury 1973 mission is one of the more ambitious interplanetary space flights which has been undertaken. This is particularly true of the navigation phase. Table 1 presents a typical Mariner Venus–Mercury 1973 mission sequence for which the maneuver magnitudes, delivery capability, and error sensitivities have been determined. The rationale, described below, for selecting this maneuver sequence is based upon experience from previous Mariner missions.

The mission begins with the injection of the spacecraft by an Atlas/Centaur launch vehicle. The predicted trajectory dispersions resulting from

---

[1] Aim points selected for Mercury I based on obtaining good return from the scientific experiments do not preclude Mercury II; indeed, little compromise is required for certain launch/arrival dates (Reference 1).

[2] The Mission Analysis Division at the Jet Propulsion Laboratory is currently studying many of the error sources contributing to the navigation accuracy. Some of this effort is reported in Reference 4.

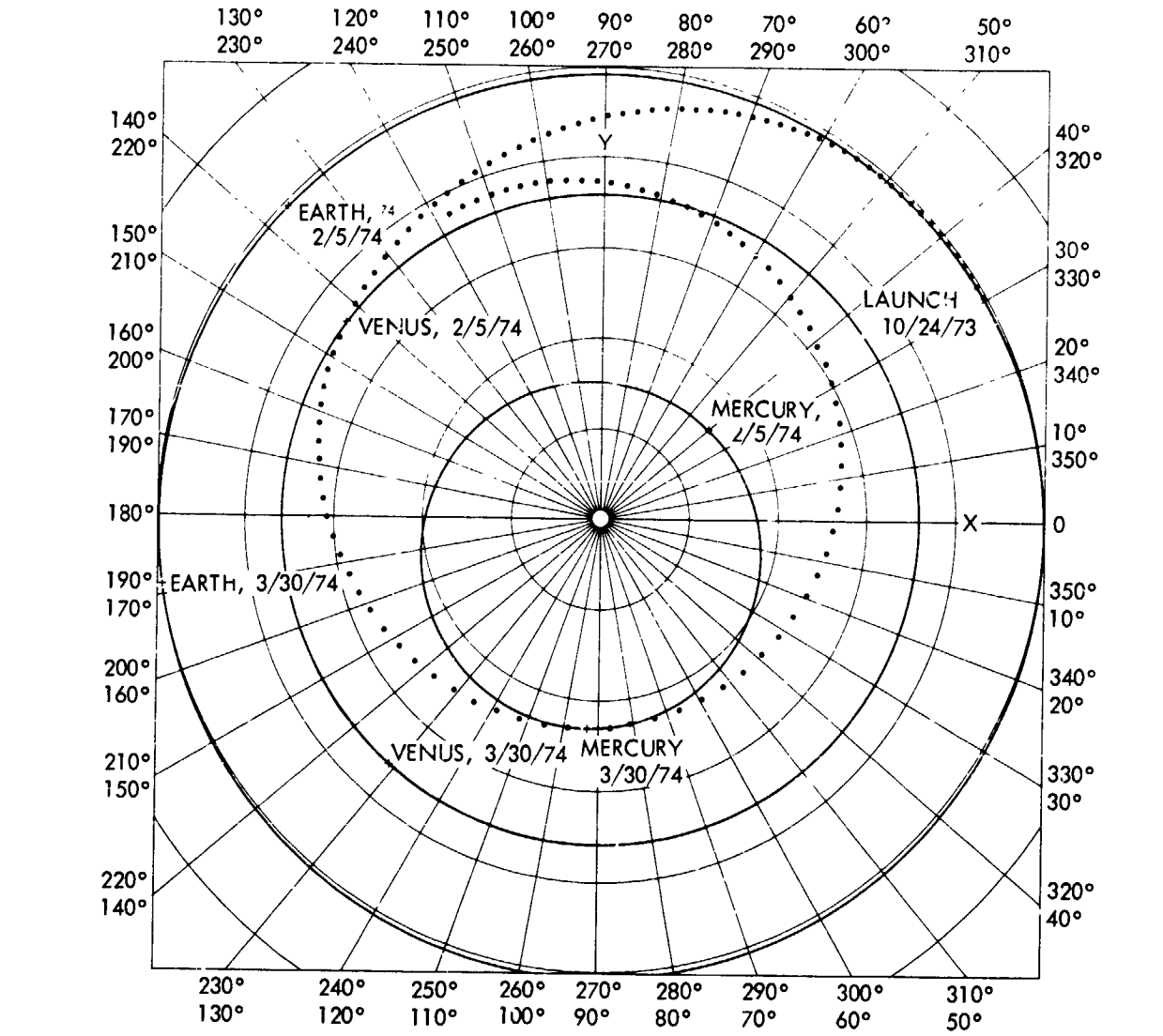

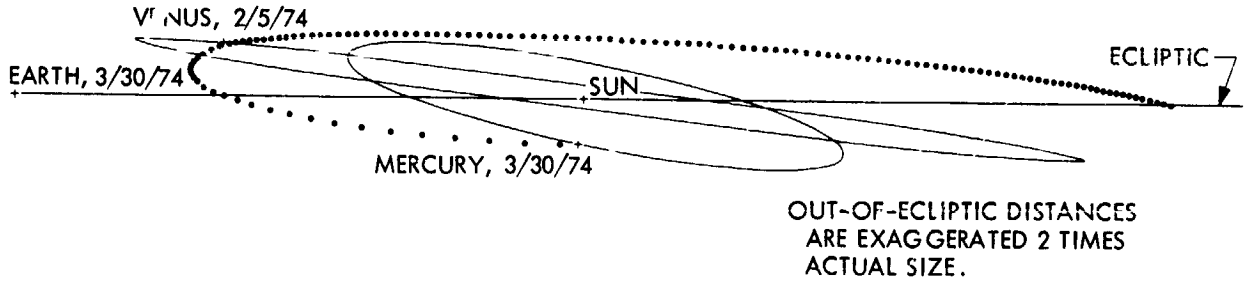

Figure 1. Heliocentric plane view for Mariner Venus–Mercury 1973 trajectory (dots are at approximately two-day intervals)

this injection are fairly large (0.99 probability of falling within an ellipse in the B-plane, Figure 2, of Venus with a semi-major axis slightly in excess of 6×10^4 km), resulting in a virtually certain requirement for at least one midcourse correction. In order to minimize the magnitude of the first maneuver, it is performed as soon after injection as is practicable, the only limitation normally being the time required to obtain a good estimate of the post-injection orbit from tracking data.

The orbit determination dispersion at the time of the first maneuver and the maneuver execution errors resulting from the first maneuver typically

Table 1. Typical event sequence for the Mariner Venus–Mercury 1973 mission[a]

Event	Time (nominal)
Primary mission:	
Launch	Oct 24, 1973
First midcourse (launch +10 days)	Nov 03, 1973
Second midcourse (Venus encounter - 3 days)	Feb 02, 1974
Venus encounter	Feb 05, 1974
Third midcourse (Venus encounter + 3 days)	Feb 08, 1974
Fourth midcourse (Venus encounter + 20 days)	Feb 24, 1974
Mercury I encounter	Mar 30, 1974
End of primar mission (Mercury I encounter + 15 days)	Apr 14, 1974
Extended mission:	
Fifth midcourse (Mercury I encounter + 37 days)	May 06, 1974
Sixth midcourse (Mercury I encounter + 149 days)	Aug 26, 1974
Mercury II encounter (Mercury I encounter + 176 days)	Sep 22, 1974

[a] For this study, an Earth launch/Mercury I arrival of Oct 24, 1973/Mar 30, 1974 was used. This trajectory is quite representative, and other launch/arrival combinations will not appreciably alter the findings of the study.

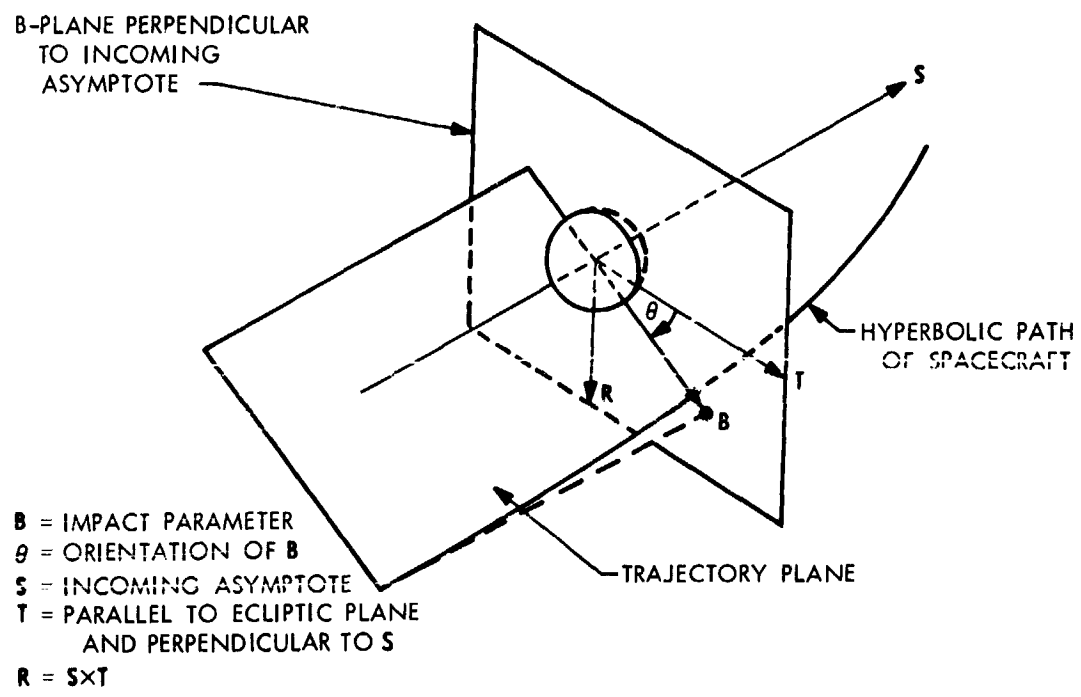

Figure 2. Encounter R–S–T coordinate system

combine to give a three-sigma dispersion ellipse of several hundred kilometers. On past single-planet Mariner missions, potential errors of this size have been acceptable; however, Figure 3 shows the effect on delivery to Mercury of a 1-km spherical error at Venus. Consequently, a second midcourse correction is virtually certain to be required.

To minimize the contribution of the maneuver execution errors on the delivery accuracy at Venus, the second maneuver is scheduled just a few days before Venus Encounter. Consequently, the uncertainty in the orbit estimate used to target the maneuver determines the delivery capability to

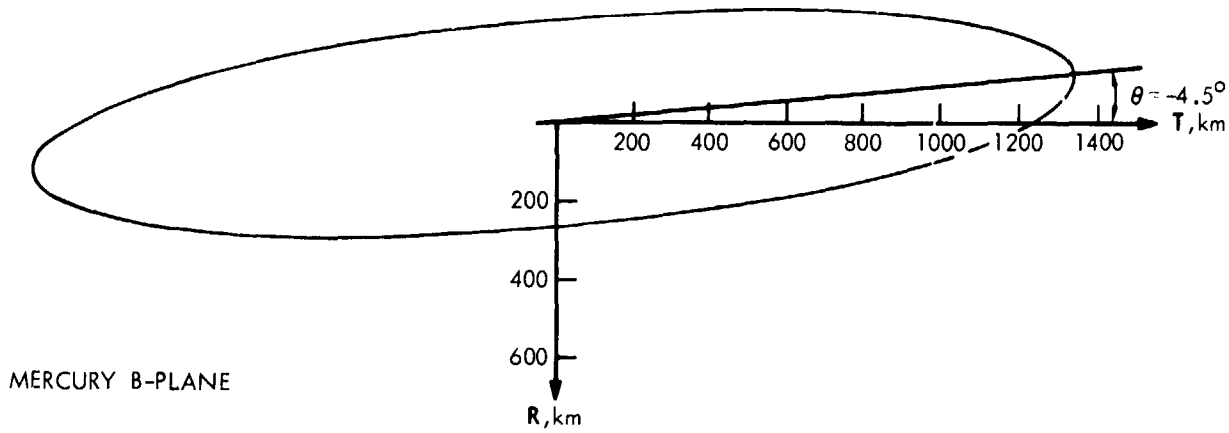

Figure 3. Contour of the B-plane miss at Mercury resulting from a 1-km spherical miss at Venus for the Mariner Venus–Mercury 1973 mission

Venus. Because of the error magnification at Mercury shown in Figure 3, the size of the second maneuver orbit determination uncertainty (while small by current standards) will make still another maneuver necessary following Venus encounter. Indeed, the Venus-to-Mercury navigation problem is practically a duplication of the Earth-to-Venus navigation problem. Likewise, if the mission is extended to include a second Mercury encounter, the above arguments would apply to the Mercury-to-Mercury navigation problem with the following exception: because of a thermal constraint, the spacecraft is precluded from performing midcourse corrections at distances closer to the Sun than 0.58 AU. The timing of maneuvers 4, 5, and 6 satisfies this constraint.

Maneuver Magnitudes

A Monte Carlo computer simulation of the mission navigation sequence described above was used to determine the maneuver magnitudes. The program assumes a linear relationship between perturbations in velocity and in encounter parameters, the appropriate matrices being obtained by integrating the variational forms of the equations of motion about the nominal trajectory. Orbit determination characteristics are described by covariance matrices of encounter parameters. Other inputs to the program include pointing accuracies, propulsion system impulse accuracies, and a covariance matrix of Atlas/Centaur injection errors.

Table 2 gives the results of the Monte Carlo simulation. Included are the average velocity requirements for the primary and extended missions, the standard deviations, and, most importantly, the velocity needed, in the presence of expected navigation errors, to give a 0.995 probability that the velocity required is less than the indicated value. The velocity requirements for the 0.995 probability level were derived from the cumulative distributions calculated by the Monte Carlo program. The cumulative distributions for the primary and extended missions are shown in Figures 4 and 5, respectively.

The velocity requirements given by Table 2 for the primary mission are well within the total capability of the spacecraft. This capability will vary between approximately 90 and 140 m/s depending upon the final spacecraft

Table 2. Nominal midcourse correction velocity requirements for the Mariner Venus–Mercury 1973 mission

Parameter	Maneuver						All maneuvers	
	First[a]	Second[b]	Third[c]	Fourth[d]	Fifth[e]	Sixth[f]	Primary	Extended
Mean velocity, m/s	4.8	3.8	17.1	0.6	12.9	1.5	26.3	40.7
Standard deviation (σ), m/s	2.5	2.5	11.9	0.4	10.0	1.8	13.1	17.3
Mean + 3σ, m/s	12.3	11.3	52.8	2.0	42.9	6.9	65.6	92.6
0.995 Probability that velocity shown will not be exceeded, m/s	13.4	14.0	55.1	2.2	46.1	10.0	66.5	97.5

[a] Injection + 10 days.
[b] Venus encounter – 3 days.
[c] Venus encounter – 3 days.
[d] Venus encounter + 20 days.
[e] Mercury I encounter + 37 days.
[f] Mercury I encounter + 149 days.

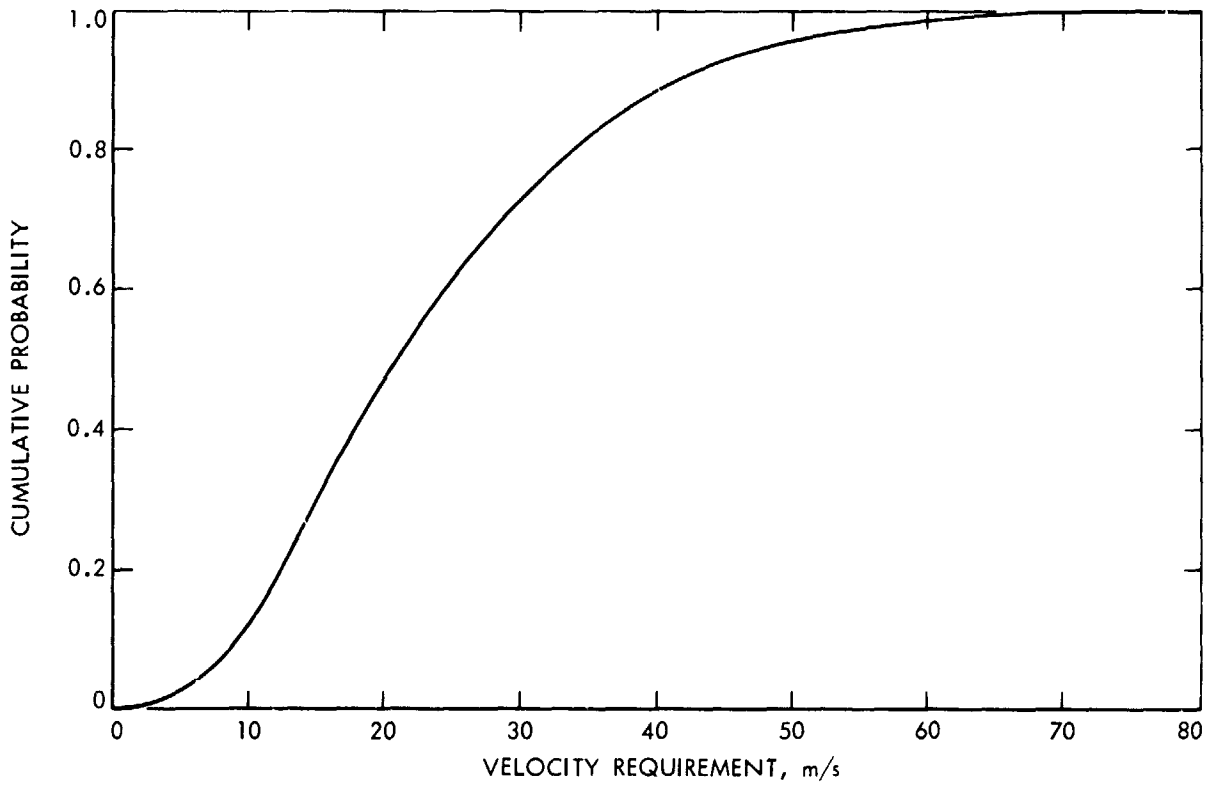

Figure 4. Cumulative distribution for the Mariner Venus–Mercury 1973 midcourse velocity requirements of the primary mission

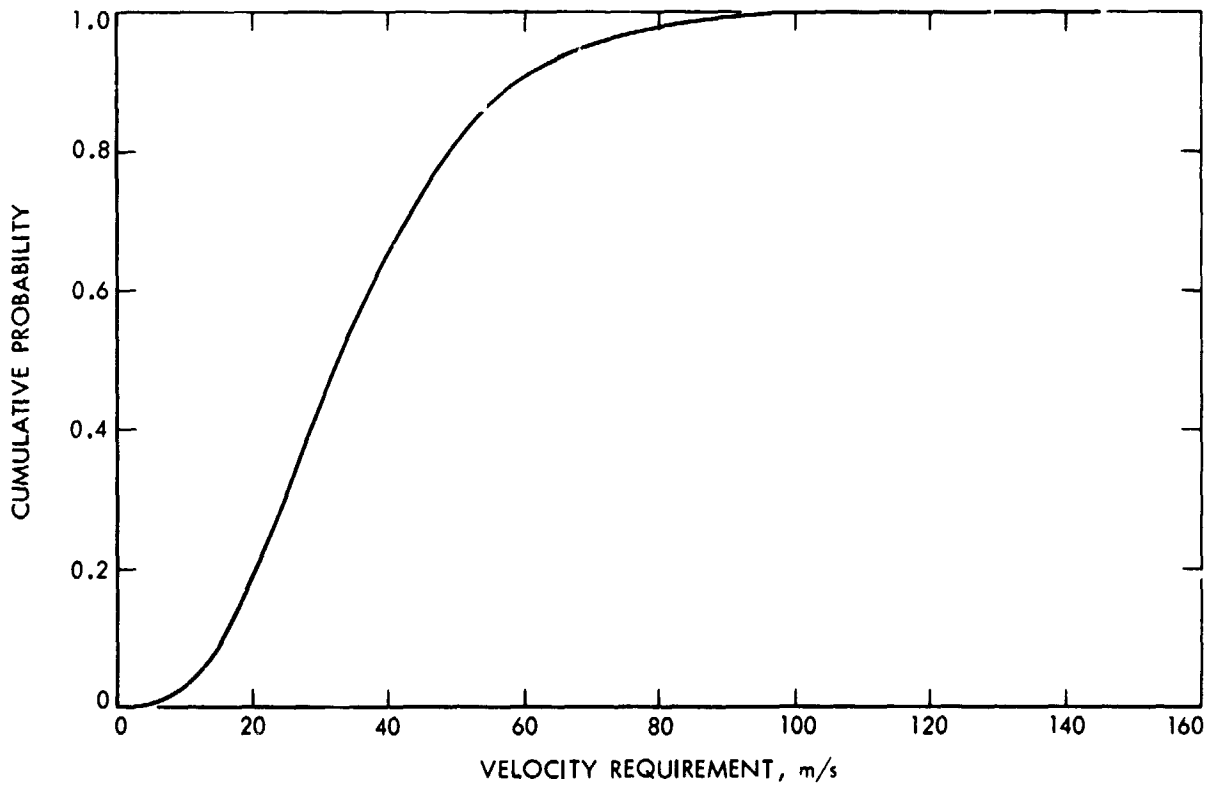

Figure 5. Cumulative distribution for the Mariner Venus–Mercury 1973 midcourse velocity requirements of the extended mission

mass.[3] On the other hand, again depending on the final spacecraft mass, the capability to accomplish the extended mission will range from marginal to relatively certain (subject, as always, to selecting a Mercury return aim point at Mercury I).

Finally, as the discussion of "Maneuvers Required" suggested, the accurate navigation to the intermediate encounter (Venus for the primary mission and Mercury I for the extended mission) is crucial if reasonable velocity requirements are to be maintained. This is clearly evident from comparison of the post-encounter velocity requirements, maneuvers 3 and 5, with the primary and extended mission velocity requirements. This conclusion will be reinforced in the section below dealing with navigation sensitivities to the contributing error sources.

Delivery Accuracy

The purpose of the Mariner Venus–Mercury 1973 mission is to perform certain scientific investigations near the target planet. This intent gives rise to the definition of a guidance success zone at the target planet(s), the implication being that if the spacecraft passes through this zone the scientific investigations can be performed satisfactorily. In the case of Mariner Venus–Mercury 1973, the guidance success zone at Venus is a small region about that point for which Mercury encounter would be achieved without further corrections.

The guidance success zone for Mercury I is shown by Figure 6. The boundary is labeled with the names of the instrument(s) determining the particular segment of the boundary. Two zones are shown with relative "worth" values as indicated. Also shown is a typical three-sigma delivery dispersion ellipse, describing the delivery capability after performing four maneuvers. Clearly, there is a significant probability of passing within the 90% value guidance success zone. This is confirmed by Table 3, which shows the probability of guidance success following the indicated number of maneuvers. It should also be noted that the probability is nearly unity for passing through the 50% science value zone.

Currently, no guidance success zone has been defined for Mercury II. Consequently, a probability of guidance success at Mercury II cannot be calculated at this time.

Sensitivity Analysis

In this section the sensitivities of the velocity requirements and delivery capability to the various error sources are presented. Information of this

---

[3] Variations in spacecraft mass alone are not responsible for the relatively large range of 90–140 m/s in maneuver capability. Rather, because of costs involved in calibrating the blowdown propulsion subsystem, the calibrations will be made with propellant tanks approximately two-thirds full and full. Then, for a given spacecraft dry mass, the tanks (at launch) will be loaded to full or two-thirds capacity in order to stay within the launch vehicle payload capability.

Table 3. Nominal Mariner Venus-Mercury 1973 probabilities of guidance success

Number of Maneuvers	Probability of guidance success	
	At Venus	At Mercury I (90% value zone)
1	0.28	~0
2	~1	$<3 \times 10^{-4}$
3	Not applicable	0.05
4	Not applicable	0.91

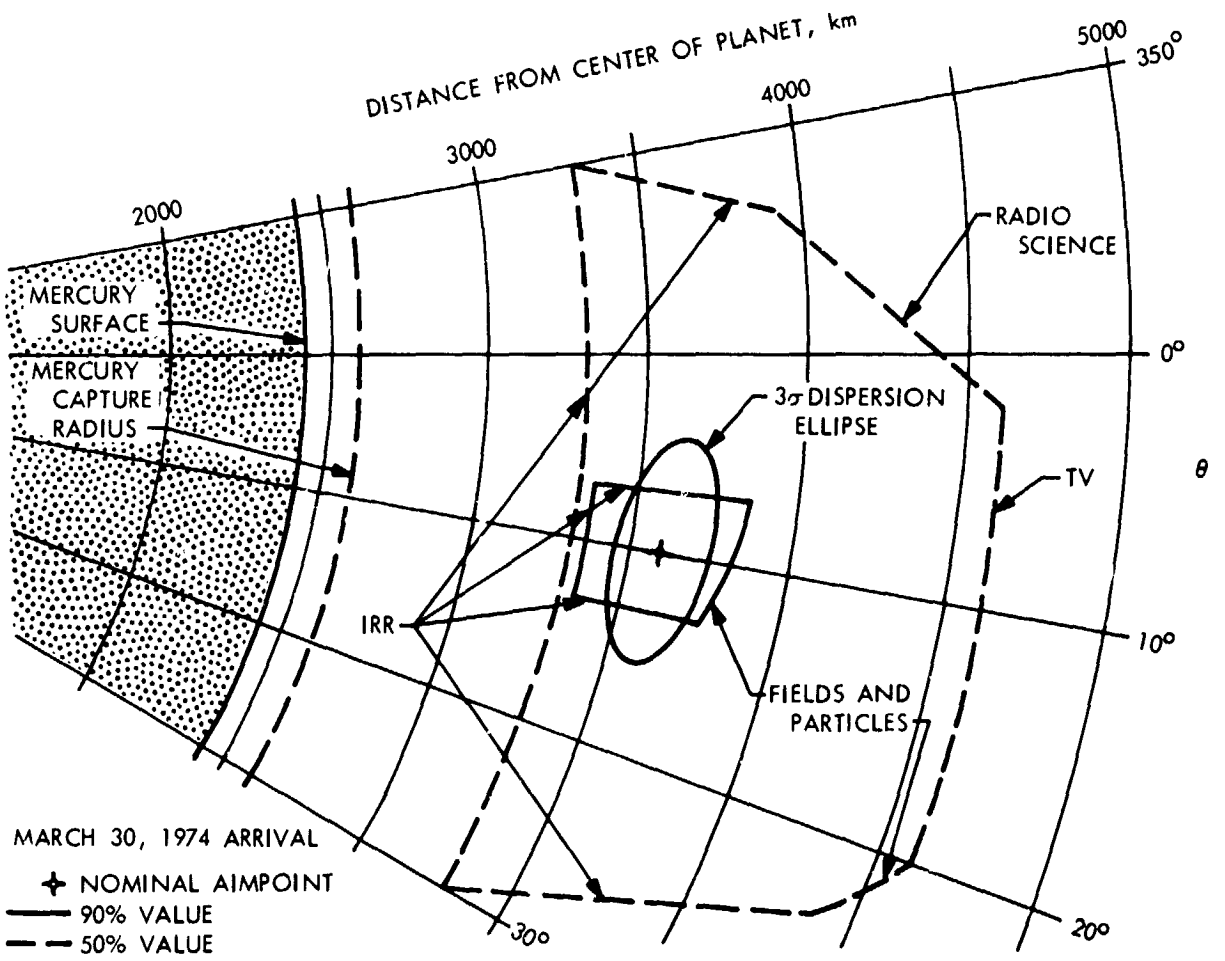

Figure 6. Mariner Venus–Mercury 1973 Mercury aiming zones

type will help in developing an understanding of the interplay among the various navigation elements by showing the effects of changes in element capability on the overall navigation capability.

To establish these sensitivities, the Monte Carlo simulation was performed for separate increases of 20% in the expected error of each of the

follow[illegible]major contributors to the total navigation capability: orbit determination at each maneuver time, maneuver thrust vector pointing, and maneuver impulse control. The pointing and impulse control describe the execution error sources.

The results of the sensitivity study are given by Table 4, where the change in the mean value of the velocity requirement for each maneuver and for both the primary and extended mission are shown for each of the indicated changes. Inspection of this table shows the following:

(1) As expected, changes in the orbit determination capability at or following a maneuver epoch do not affect the velocity requirements at or preceding that maneuver.

(2) The velocity requirements are most sensitive to the orbit determination capability just preceding a planetary encounter (orbit determination at maneuvers 2 and 4). This reflects the fact that the final delivery accuracy is dominated by the orbit determination capability.[4] Consequently, it is principally the orbit determination errors that experience the magnification effects shown by Figure 2.

(3) For virtually the same reason as just stated, the delivery accuracy to Mercury I is most sensitive to the orbit determination capability at the time of the fourth maneuver.

(4) The velocity requirements and delivery accuracy are relatively insensitive to pointing and impulse errors. This, too, reflects the comments given for (2) above, since the pointing error and most of the impulse error are proportional to the maneuver velocity increment.

Conclusions

The Mariner Venus–Mercury 1973 spacecraft design provides adequate midcourse velocity correction capability for the primary mission. Depending upon the eventual propellant loading (see Footnote 3), the midcourse velocity correction capability for the extended mission will be either marginal or adequate.

The mission velocity requirements are most sensitive to the delivery accuracy to encounters with the intermediate targets, Venus in the case of the primary mission, and Mercury I in the case of the extended mission. Furthermore, these delivery accuracies are currently limited by the present orbit determination capability; however, the orbit determination capability is adequate for mission success.

---

[4] This is the result of (1) performing multiple maneuvers between encounters, thereby reducing the contribution of execution errors that are proportional to the maneuver size; and (2) performing the final pre-encounter maneuver as close as possible to that encounter in order to reduce the contribution of execution errors that are independent of the maneuver size.

Table 4. Change in velocity and delivery requirements for a 20% increase in error sources

Parameter	Nominal, m/s	Error sources[a]						
		Pointing	Impulse	Orbit determination at maneuver				
				One	Two	Three	Four	Five
Change from nominal in the mean velocity requirement, m/s:								
First maneuver	4.8	0.0	0.0	0.0	0.0	0.0	0.0	0.0
Second maneuver	3.8	0.2	0.0	0.5	0.0	0.0	0.0	0.0
Third maneuver	17.1	0.4	0.2	0.3	2.7	0.0	0.0	0.0
Fourth maneuver	0.6	0.1	0.1	0.0	0.1	0.1	0.0	0.0
Primary mission	26.3	0.7	0.3	0.8	2.8	0.1	0.0	0.0
Fifth maneuver	12.9	0.8	0.5	0.4	0.3	0.6	2.5	0.0
Sixth maneuver	1.5	0.2	0.3	0.1	0.1	0.1	0.3	0.1
Extended mission	40.7	1.7	1.1	1.3	3.2	0.8	2.8	0.1
Change from nominal in Mercury 1 probability of guidance success	0.906	-0.009	-0.002	0.0	-0.007	-0.002	-0.063	–

[a] Error source perturbed by +20% from nominal.

For the primary mission, the probability of requiring at least four maneuvers in order to accomplish an accurate Mercury encounter is approximately 0.95. With four maneuvers, the delivery accuracy to Mercury I can be rated as good, since the probability of passing through the guidance success zone for the 90% value level is approximately 0.91.

References

1. Bourke, R. D., and Beerer, J. G., "Mariner Mission to Venus and Mercury in 1973," *Astronaut. Aeronaut.*, pp. 52–59, Jan. 1971.

2. Sturms, F. M., Jr., *Trajectory Analysis of an Earth–Venus–Mercury Mission in 1973*, Technical Report 32-1062. Jet Propulsion Laboratory, Pasadena, Calif., Jan. 1, 1967.

3. *Mariner Venus/Mercury 1973 Study*, Technical Memorandum 33-434. Jet Propulsion Laboratory, Pasadena, California, Aug. 1, 1969.

4. Ondrasik, V. J., and Rourke, K. H., "Applications of Quasi-VLBI Tracking Data Types to the Zero Declination and Process Noise Problems," paper presented at the Astrodynamics Specialists Conference, Fort Lauderdale, Florida, August 17–19, 1971.

N72-17901

JPL Quarterly Technical Review Volume 1, Number 4 January 1972

Application of New Radio Tracking Data Types to Critical Spacecraft Navigation Problems

V. J. Ondrasik and K. H. Rourke

Mission Analysis Division

This article is concerned with newly envisioned Earth-based radio tracking data types involving simultaneous or near-simultaneous spacecraft tracking from widely separated tracking stations. These data types are conventional tracking instrumentation analogs of the very long baseline interferometry (VLBI) of radio astronomy—hence the name quasi-VLBI. Quasi-VLBI promises to help alleviate two particularly troublesome problems encountered in interplanetary orbit determination: the zero declination and process noise problems. This article motivates quasi-VLBI with a preliminary analysis using simplified tracking data models. The results of accuracy analysis studies are then presented for a representative mission, Viking 1975. The results indicate that, contingent on projected, not overly optimistic future tracking system accuracy, quasi-VLBI can be expected to significantly improve navigation performance over that expected of conventional tracking data types.

Introduction

Two particularly troublesome problems that occur in determining the orbit of an interplanetary spacecraft are the zero declination and process noise problems. The process noise problem refers to the difficulties encountered in determining the orbit of a spacecraft that is subject to random nongravitational acceleration uncertainties. The acceleration uncertainties, although often negligible in their direct effect on the physical orbit of a spacecraft, can severely limit the capability of actually solving for the orbit on the basis of conventional tracking data types. The zero declination problem is a more familiar difficulty, i.e., the magnification of declination errors at low spacecraft declinations.

In pursuit of new techniques for alleviating the low declination and process noise problems, the advantages offered by very long baseline interferometry (VLBI) data are being investigated. It was determined that the VLBI data does, in concept, provide at least a partial solution to both the low declination and process noise problems. Furthermore, it was discovered that the information needed for the solution of these two problems may be

obtained by using sufficiently high quality doppler and range data taken simultaneously, or near simultaneously, from widely separated tracking stations, without having to resort to the special data taking and reduction procedures required by VLBI. The data quality requirements are well within anticipated capabilities which will be associated with the 1-m ranging machines, hydrogen masers, and improved transmission media (i.e., troposphere, ionosphere, space plasma) calibrations.

As will be shown later the use of the simultaneous and near-simultaneous data can be expected to reduce declination errors that are produced by low declination geometries by a factor of 2–4, and to reduce errors in the estimate of the spacecraft state (i.e., position and velocity) produced by unmodelable accelerations by two orders of magnitude. Because of the similarities between VLBI data and simultaneous or near-simultaneous doppler and range data, the latter type of data is often called quasi very long baseline interferometry data (QVLBI).

Simultaneous and Near-Simultaneous Data

Conventional methods of radio interplanetary navigation rely almost entirely on the use of the "two-way" coherent doppler and range data types. Two-way doppler and range are obtained by a tracking station that continuously transmits to a spacecraft which, in turn, receives and retransmits to the transmitting station. Transmitted and received signals are compared to obtain measurements of the spacecraft's range rate and range with respect to the tracking station. Practical considerations prohibit two-way measurements being made by separate stations. Nontransmitting stations are, however, free to receive the signal that is being transmitted by the spacecraft. This procedure, in principle, provides a measurement of the round-trip distance, and its rate of change, between the two tracking stations and the spacecraft. Measurements obtained in this way via the separate stations are referred to as "three-way" data types. The schematic configurations associated with two-way and three-way tracking are illustrated in Figure 1. (Three-way range has not as yet been used as an explicit data type, yet is equivalent to interstation timing techniques that have been used for lunar spacecraft tracking. See Reference 1.)

The three-way tracking data suffers from practical difficulties that have heretofore restricted their use from interplanetary applications. The three-way measurements are by necessity based on frequency and clock standards remote from the transmitting station. The conventional rubidium frequency standards, although suitably stable for two-way measurements over moderate round-trip communication distances, introduce doppler measurement errors that preclude the usefulness of the three-way tracking data. The new generation hydrogen frequency standards to be installed in the Deep Space Network do, however, provide the degree of improvement required to make three-way tracking data an attractive interplanetary navigation data type.

The effective use of three-way range is still hampered by the requirement of precise interstation clock synchronization to enable the accurate

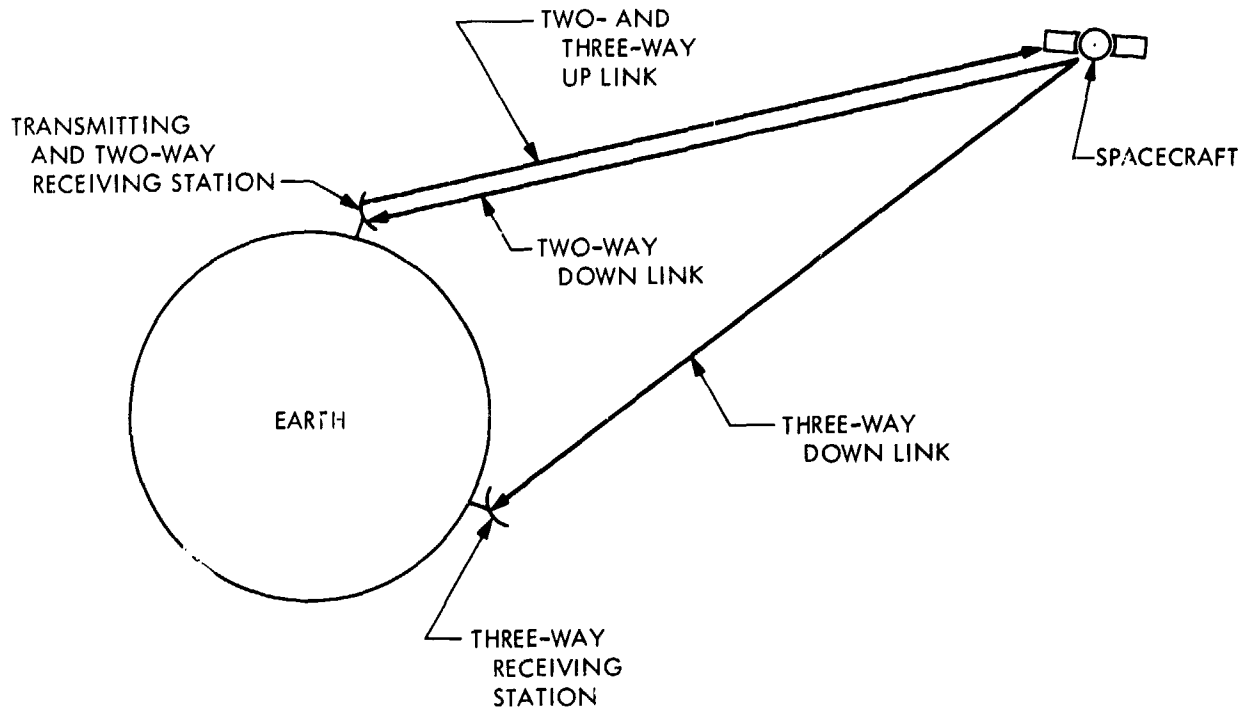

Figure 1. Transmitting and receiving configuration for two-way and three-way data

measurement of the round-trip signal delay. Current microsecond-level timing accuracies would introduce excessive three-way range measurement errors on the order of 300 m. The clock synchronization problem can be circumvented by replacing the simultaneous two-way and three-way range measurements with near-simultaneous two-way range measurements between the two tracking stations, one just before and one just after an interstation handover. In this case the clock discrepancy only introduces errors into each measurement epoch specification. This synchronization error produces negligible errors, given today's timing accuracies. This technique is limited somewhat by uncertainties present in the motion of the spacecraft between the near-simultaneous measurements. For example, if the topocentric range rate of spacecraft is known to only 1 mm/s and the near-simultaneous measurements are separated by 15 min, then the motion uncertainty introduces an error of

$$1 \text{ mm/s} \times 900 \text{ s} = 0.9 \text{ m}$$

Analytical Representations of the Doppler and Range Observables

An insight into how QVLBI techniques help to resolve the low declination and process noise problems may be obtained by performing a simple analysis based upon analytical representations of the doppler (or, equivalently, range rate) and range observables. These representations developed by Hamilton and Melbourne (Reference 2) are based upon the following approximations of the topocentric range, from a tracking station to a distant spacecraft:

$$\rho(t) = r(t) + z_s \sin \delta(t) - r_s \cos \delta(t) \cos [\omega t + \phi + \lambda - \alpha(t)] \qquad (1)$$

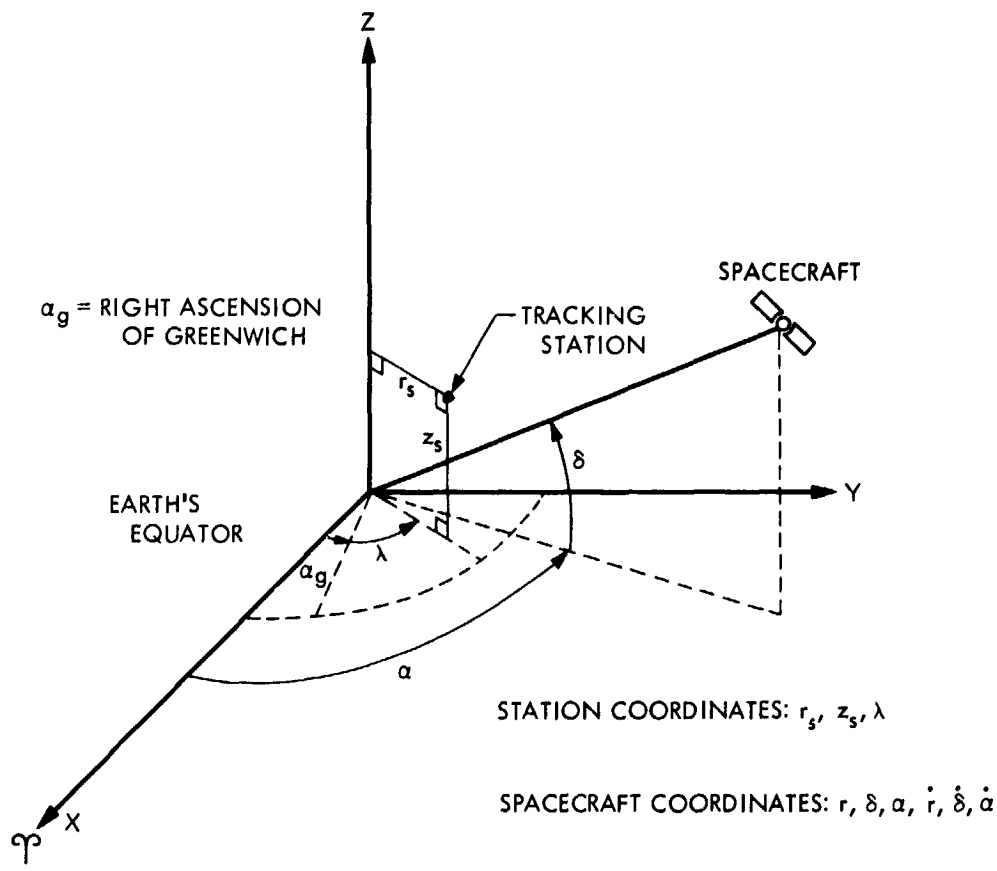

Figure 2. Spacecraft and station coordinates

where (see Figure 2)

ρ = topocentric range

r = geocentric range

δ = declination

α = right ascension

r_s = distance of tracking station from the Earth's spin axis

z_s = distance of tracking station from the Earth's equator

λ = longitude of tracking station

ω = Earth's rotation rate

ϕ = a phase angle that depends on the choice of epoch

t = time past epoch

As schematically illustrated in Figure 3, this equation shows that the observables are composed of a diurnal sinusoidal motion, provided by the Earth's spin, superimposed upon the slowly varying geocentric motion. The term produced by the Earth's spin is a strong source of angular data and usually provides a good estimate of δ and α within a few days. The slowly varying term contains information on all the spacecraft state variables, but by itself can seldom provide complete estimates. This is because of

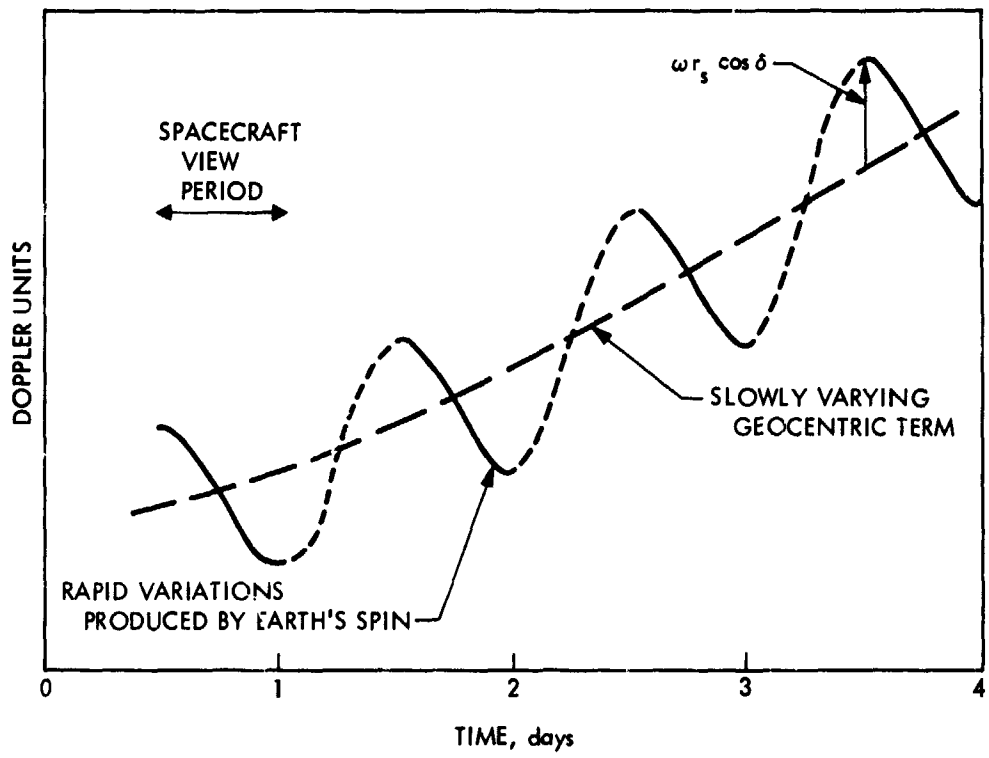

Figure 3. Schematic illustration of the doppler observable

difficulties associated with separating the geocentric motion effects produced by specific variations in the state variables.

A convenient approximation to the doppler observable, which may be used to examine the declination and right ascension information contained in a single pass of doppler data, is shown in Equation 2, and is obtained by assuming that δ and α are constant:

$$\dot{\rho}(t) = \dot{r}(t) + \omega r_s \cos \delta_0 \sin (\omega t + \phi + \lambda - \alpha_0) \tag{2}$$

where

$$\dot{a} = da/dt$$

$$a_0 = a(t=0)$$

The Low Declination Problem

As mentioned above, when conventional data is used, the determination of the declination is made principally through the amplitude of the sinusoidal term. The amplitude b may be written as

$$b = r_s \cos \delta \tag{3}$$

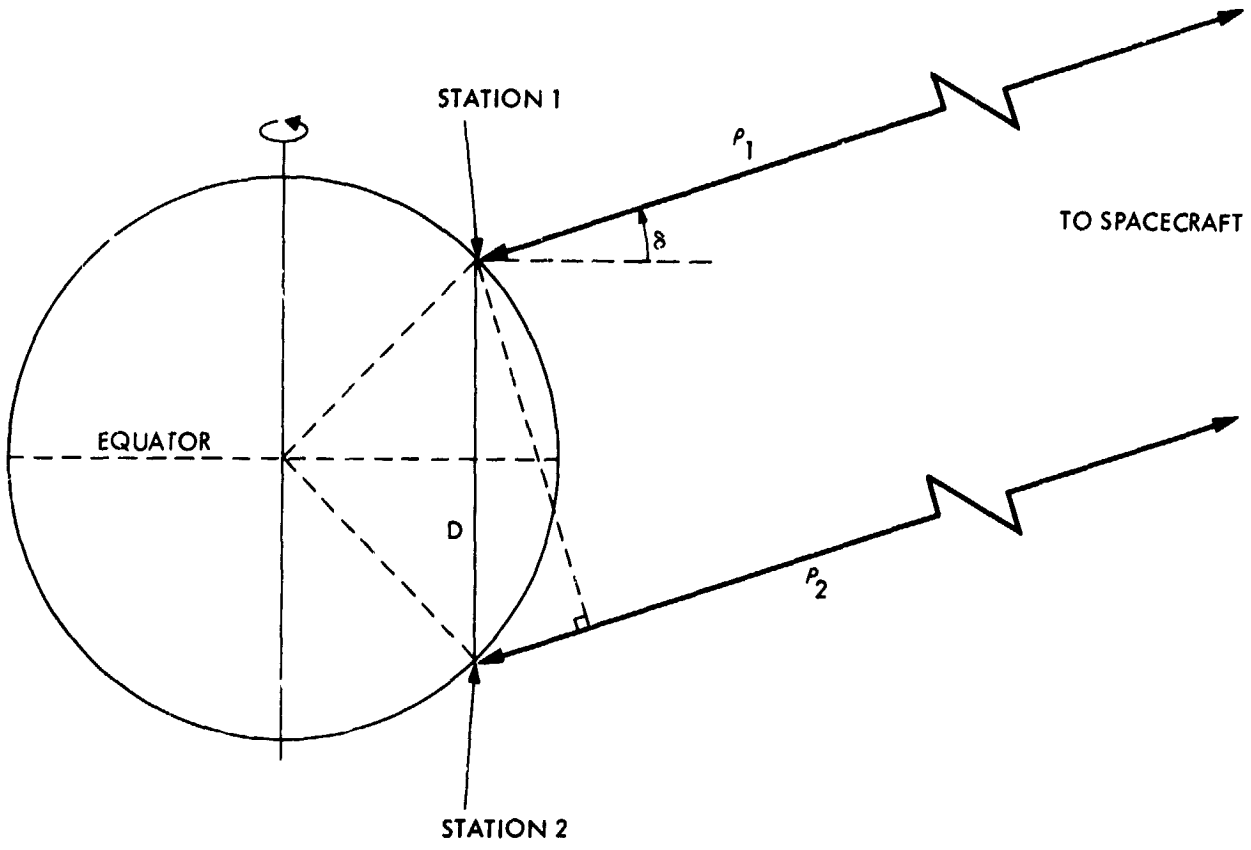

Figure 4. Simultaneous ranging from two stations

Since the data taken during a tracking pass may be thought of as providing a measure of b, the orbit determination filter will attempt to leave it unchanged. Therefore, an error in r_s, Δr_s, will produce a compensating error in the declination, $\Delta\delta$, which for data arcs of a few days may be approximated by the following equation:

$$\Delta\delta = \frac{\cos\delta}{\sin\delta}\,\frac{\Delta r_s}{r_s} \tag{4}$$

The most notable feature of this equation is that there is a singularity at $\delta = 0$. Although this singularity does not occur in the actual orbit determination procedure, there is almost always a substantial magnification of declination errors, as δ approaches zero.

An insight into how QVLBI-type data avoids the low declination problem may be easily obtained by considering the situation depicted in Figure 4, where two stations are making simultaneous range measurements at local spacecraft meridian crossing. Assume that the stations share the same longitude and have equal but opposite latitudes. From this figure it is easily seen that the difference between the two range measurements is related to the baseline D and the spacecraft declination through the following equation:

$$\rho_2 - \rho_1 = D \sin \delta \tag{5}$$

Clearly, range-type errors, $\Delta\rho$, whether they are the result of actual measurement errors or station location errors, will give declination errors of the approximate amount

$$\Delta\delta = \frac{1}{\cos \delta} \frac{\Delta\rho}{D} \tag{6}$$

This equation, unlike Equation 4, is well behaved at low declination and illustrates that, given data of sufficient quality, simultaneous (differenced or nondifferenced) range data from widely separated tracking stations provides a superior determination of the declination than does the conventional range and doppler data.

The Process Noise Problem

This section describes how random accelerations actually affect orbit determination solutions, and provides the motivation for the use of QVLBI data types as a countermeasure to the process noise problem.

This discussion is concerned with the short-term process noise effects and their influence on a single day's pass of conventional doppler data. The short-term effects of process noise on the orbit determination of a distant spacecraft can be illustrated with the aid of the Hamilton/Melbourne doppler data representation as shown in Equation 2.

Consider particular corrections $\Delta\dot{r}$, $\Delta\alpha$, and $\Delta\delta$ to the spacecraft geocentric range rate, right ascension, and declination, respectively. They produce the following range-rate (doppler) residual signature:

$$\Delta\dot{\rho} = \Delta\dot{r} - (r_s\, \omega \sin \delta \sin \omega t)\Delta\delta + (r_s\, \omega \cos \delta \cos \omega t)\Delta\delta, \qquad -\pi/2 \leqslant \omega t \leqslant \pi/2 \tag{7}$$

over the day's pass of data. Normally, $\Delta\dot{r}$, $\Delta\delta$, and $\Delta\alpha$ are considered to be constant over one day (as well as δ, the nominal spacecraft declination). The effect of particular error sources can be expressed in terms of their corresponding doppler residuals. Assume that $\Delta\dot{r}$ is not constant but perturbed by random accelerations. The perturbation produces the strongest effect on $\Delta\alpha$ and $\Delta\delta$ determinations if

$$\Delta\dot{r} \sim \Delta\dot{r}_0 + a \sin \omega t + b \cos \omega t$$

i.e., if the error residual is sinusoidal with a one-day period. For example, a radially acting acceleration of 10^{-12} km/s^2 (typical for a ballistic spacecraft) varying as

$$(10^{-12}\ \text{km/s}^2) \times \cos \omega t$$

produces an effect indistinguishable from a $\Delta\delta$ perturbation on the order of $(10^{-12})/r_s\omega^2$, nearly 0.04 second of arc. The resulting position error for a spacecraft at 2 AU from the Earth is 60 km. The actual net movement of the spacecraft is zero; its maximum perturbed displacement is 0.2 m. Thus, conventional doppler tracking data can be expected to be very sensitive to uncertainties in the geocentric radial motion of the spacecraft. Uncertainties in the $\Delta\alpha$ and $\Delta\delta$ directions caused by process noise can be shown to be negligible for a single pass of doppler data.

The influence of process noise on $\Delta\dot{r}$ estimation errors is comparable in magnitude to the corresponding errors in $r_s\omega\Delta\alpha$ and $r_s\omega\Delta\delta$. The direct effects of the $\Delta\dot{r}$ errors are not significant; e.g., a large (with respect to typical acceleration uncertainties) 10-mm/s $\Delta\dot{r}$ error produces only a 10-km range error in 10 days. However, given purely ballistic motion, considerable information concerning the dynamical state of the spacecraft is available from the variation of $\Delta\dot{r}$ over several days. Thus, process noise sensitivities similar to those occurring for a single pass of data can be expected over the longer data arcs. This phenomenon is particulary evident for orbit determination data processing methods that ignore the effects of random acceleration uncertainties. This point is developed in considerable detail in Reference 3.

Differenced Tracking Data as a Countermeasure for the Process Noise Problem

The preceding section serves as an introduction to the use of differenced simultaneous or near-simultaneous tracking data from two widely separated tracking stations as a countermeasure to the process noise problem. The differencing of the data types is effective because it eliminates the troublesome geocentric corruptions common to both tracking stations, yet preserves the "topocentric" information arising from the two stations' rotation. Consider, then, the range-rate residuals observed from two separated tracking stations:

$$\left.\begin{aligned} \Delta\dot{\rho}_1(t) &= \Delta\dot{r}(t) + b_1 \sin \omega t + c_1 \cos \omega t \\ \Delta\dot{\rho}_2(t) &= \Delta\dot{r}(t) + b_2 \sin \omega t + c_2 \cos \omega t \end{aligned}\right\} \tag{8}$$

The parameters b_1, b_2, c_1, c_2 are linear expressions in the $\Delta\alpha$ and $\Delta\delta$ corrections, their explicit form depending on the particular time reference used in the above representations. Two-way doppler residuals obtained at

Station 1 can be expressed as $2\Delta\dot{\rho}_1$. Three-way doppler residuals available at Station 3 are of the form $\Delta\dot{\rho}_1 + \Delta\dot{\rho}_2 - c\Delta f/f$, where the $c\Delta f/f$ term arises from the frequency standard discrepancy Δf between Stations 1 and 2. The difference of two-way doppler from Station 1 and three-way doppler from Station 2 is represented as

$$\Delta\dot{\rho}_1 - \Delta\dot{\rho}_2 + \frac{c\Delta f}{f} = \frac{c\Delta f}{f} + (b_1 - b_2)\sin\omega t + (c_1 - c_2)\cos\omega t \qquad (9)$$

over the stations' view period overlap $\psi_2 < \omega t < \psi_1$. The geocentric range-rate terms subtract out and are replaced by a "velocity bias" $c\Delta f/f$ arising from the relative station-to-station frequency standard bias $\Delta f/f$ (c = speed of light). Thus, in the presence of large unmodelable random accelerations, the differenced doppler allows separation of $\Delta\delta$ and $\Delta\alpha$ determination, through $b_1 - b_2$ and $c_1 - c_2$, from a corrupted $\Delta\dot{r}$ determination. The technique is hindered, however, by the introduction of a velocity bias uncertainty in the place of the geocentric range-rate uncertainty. Clearly, the differenced doppler data can be effective in circumventing process noise effects only as long as the uncertainties arising from frequency standard instability are significantly less than the process noise uncertainties expected in the conventional doppler data.

In the section on *The Low Declination Problem*, the use of simultaneous or near-simultaneous range measurements was discussed with regard to determining spacecraft right ascension and declination angles. Since these measurements allow short arc solutions of equatorial angles, they exhibit the same advantages of reduced sensitivity to short-term process noise effects as does the differenced doppler data. In contrast to doppler measurements, however, the range measurements permit declination solutions at low spacecraft declination.

This discussion is not intended to imply that the use of differenced two-way and three-way doppler or differenced range data is necessarily an efficient use of the data received at both stations from the spacecraft. The differenced data is effective in allowing separation of topocentric and geocentric tracking information—even in the case of a spacecraft experiencing large random accelerations. Ultimately, maximum information is extracted if concurrent two-way and three-way data are processed together with a suitably designed orbit determination filter that takes advantage of the known random acceleration characteristics. The differenced data provides, nevertheless, a simple conceptualization for preliminary analysis, as well as a straightforward and probably adequate approximation to an "optimal" treatment of concurrent two-way and three-way data.

Example Mission

In the preceding section and in the section on *The Low Declination Problem*, simplified representations of the range and doppler data were used

to illustrate how QVLBI data may help resolve the low declination and process noise problems. However, to quantitatively describe the utility of the QVLBI data, detailed accuracy analyses are required. Such a study was performed for the Viking Mission B trajectory described in Table 1, using data taken during the tracking pattern shown in Figure 5. The study consisted primarily of performing conventional weighted least-squares batch filter solutions to examine the effects that data noise, station location errors, and process noise have on the estimates of the spacecraft state at epoch. For comparative purposes, parallel solutions were made with the data-taking strategies described in Table 2.

These data strategies include: (1) a conventional single-station strategy using nominal accuracy range-rate data, with ranging data weighted at 100 m; (2) single-station range and range-rate tracking with tight, 3-m range weight specification; (3) single-station range rate with 3-m simultaneous range measurements; and (4) differenced simultaneous range rate and range, QVLBI data, augmented with loosely weighted conventional range and range-rate measurements.

The above-mentioned data weights are data accuracy specifications provided to the orbit determination filter, and should be distinguished from expected measurement precision. For instance, range data of a given quality may be assigned different weights, depending on how well the spacecraft/tracking system environment can be modeled.

The results of this study are summarized in Figure 6, which shows the standard deviations in δ, α, $\dot{\delta}$, and $\dot{\alpha}$ produced by data noise, and errors in these same quantities produced by the indicated station location errors and process noise. The standard deviation and errors of each component are then root-sum-squared to obtain the consider standard deviation σ_c, which is also

Table 1. Description of Viking Mission B trajectory

Coordinate	Value at encounter[a] - 30 days	Value at encounter[a] - 9 days
r, km	0.3300×10^9	0.3489×10^9
δ, deg	11.44	6.853
α, deg	153.8	165.8
$\dot{r}$, km/s	0.1142×10^{-2}	0.8390×10
$\dot{\delta}$, rad/s	-0.3952×10^{-7}	-0.4441×10^{-7}
$\dot{\alpha}$, rad/s	0.1109×10^{-6}	0.1112×10^{-6}

[a] Encounter = 23:45:00, August 6, 1976.

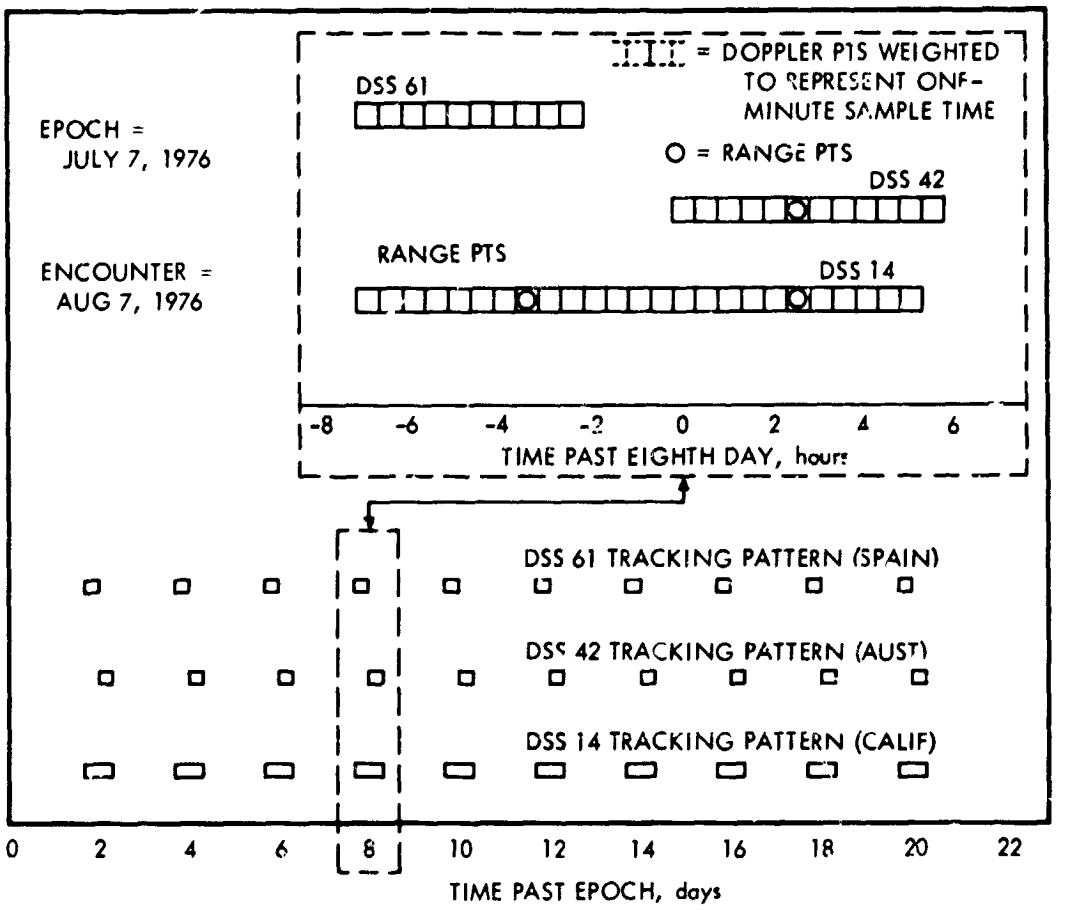

Figure 5. Tracking pattern

shown. The corresponding r_0 and $\dot{r}_0$ errors are not shown because they are always less than errors in the δ and α directions.

Figure 6 vividly illustrates some of the problems associated with determining the orbit of a spacecraft at low declinations using conventional doppler and range (σ_p = 100 m) data. Of particular note is the inability to solve for $\dot{\delta}$, and the sensitivity of δ to errors in station locations as shown by the 500-km declination direction error. The solution is improved by approximately 30% if the weight on the range data taken at a single station is changed to 3 m. A dramatic improvement in the solution is provided by the addition of simultaneous 3-m weighted range points from Australia. Simultaneous range data reduces the station location error sensitivity by factors of three or five over the two single-station data sets and increases the ability to solve for $\dot{\delta}$ by a factor of two over the conventional solution.

Although the simultaneous range data dramatically reduces the solution errors produced by station location errors, the requirement of tight range weights substantially increases the importance of process noise as an error source. Process noise sensitivities for the various data sets are shown in Figure 6. The analysis technique used to evaluate the process noise effects is that developed by Curkendall in Reference 3. The technique enables evaluation of suboptimal, weighted least-squares data filter performance for particular process noise environments. The process noise is modeled with adequate generality as a three-axis, exponentially time-correlated stationary stochastic process. The effect of a range of noise correlation times is shown

Table 2. Data strategies

Data set	Description	Data weights and contributing stations							
		Range		Doppler		Differenced range		Differenced doppler	
		Station	Weight, m	Station	Weight, mm/s	Station	Weight, m	Station	Weight, mm/s
1	Conventional (loose range)	14	100	14	1				
2	Conventional (tight range)	14	3	14	1				
3	Simultaneous range	14, 42	3	14	1				
4	QVLBI	14	10000	42[a]	100	14, 42	3	14, 42, 62	1

[a] One point per pass.

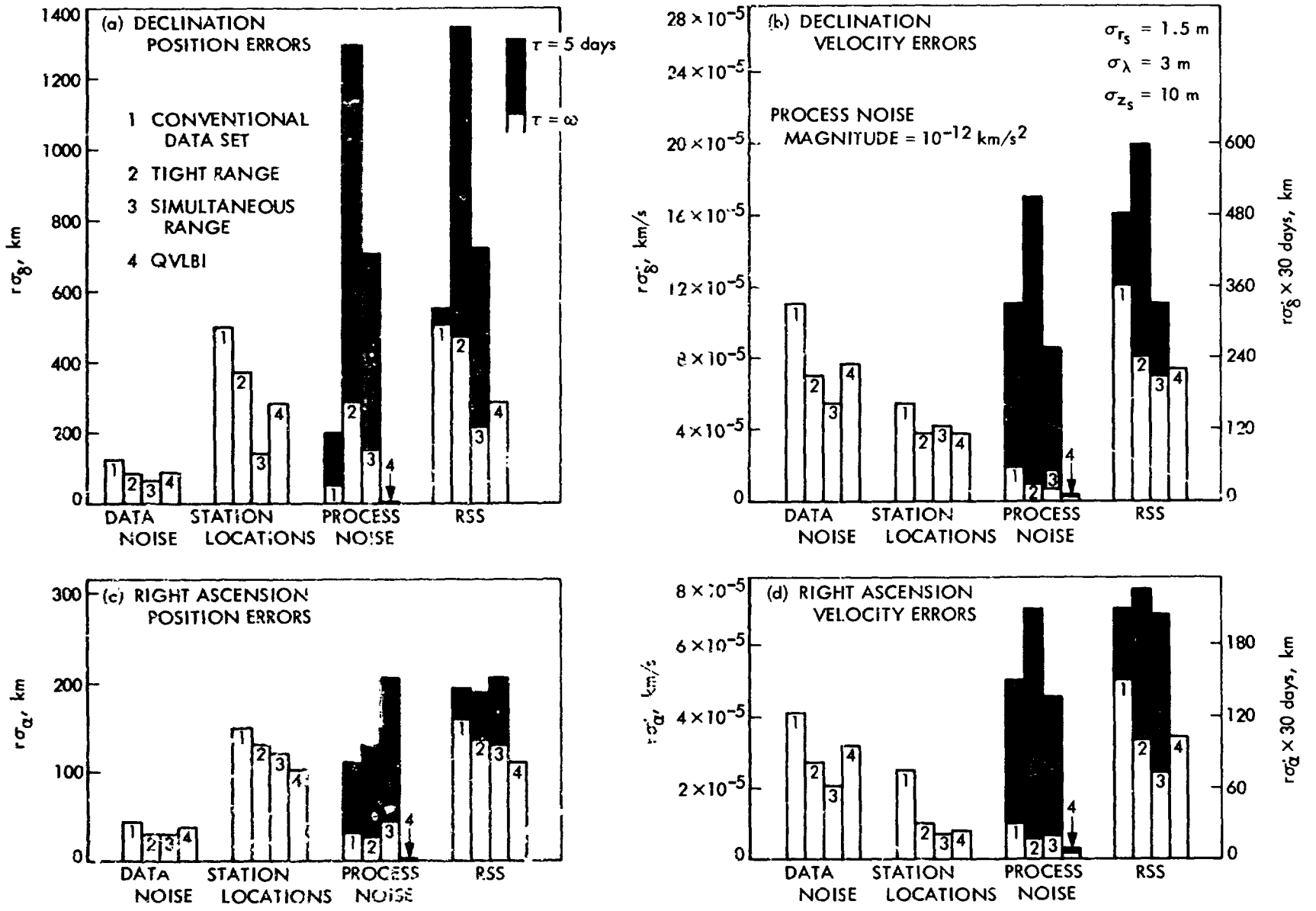

Figure 6. Position and velocity errors resulting from the use of conventional, simultaneous range, and QVLBI data

with the bar shading—the lower level corresponding to a relatively optimistic bias noise assumption (infinite correlation time), the upper level corresponding to a pessimistic, rapidly varying noise assumption (5-day correlation time). Although the noise magnitude is given as 10^{-12} km/s^2, the results are completely general inasmuch as the process noise errors are scalable with respect to the noise magnitude.

Data set 4 includes, in place of the precise simultaneous range (and range rate) measurements, precise *differenced* simultaneous range and range measurements. Thus, although some available geocentric information is deleted, the process noise sensitivity should be reduced. The actual results are remarkable. Process noise declination errors are reduced from 1000-km levels to 3 and 2 km for $\tau = \infty$ and $\tau = 5$, respectively. Similar reductions are observed for declination velocity as well as for the right ascension direction errors. The geocentric range and range-rate accuracies are commensurate with the data set 4 conventional data type accuracies.

A criticism of the above analysis is that the nondifferenced data is treated unfairly, in that an attempt to account for process noise through more modern filtering techniques can be expected to result in significant reductions in process noise sensitivity. Nevertheless, the importance of simultaneous range measurement for improving declination solutions cannot be minimized, given that proper precautions are taken against process noise sensitivity—either in the form of explicit data differencing or "optimal" processing. "Optimal" processing, by recovering some geocentric information, can be expected to outperform suboptimally processed differenced data, although probably marginally, and at the expense of some sensitivity to the process noise assumptions used in the filter design.

QVLBI Error Sources

Although QVLBI data in certain circumstances is inherently superior to conventional data, its practicable superiority depends heavily upon the quality of the data.

The crucial accuracies affecting the feasibility of effective simultaneous doppler and range measurements lie in the media and instrumentation error categories. The primary limitation to simultaneous doppler measurements lies in the three-way doppler sensitivity to local oscillator stability. As mentioned previously, feasible application of three-way doppler measurements requires hydrogen maser frequency standards. Adequate estimates of simultaneous range accuracies are difficult to obtain at this time since meter-level ranging accuracies have heretofore been considered unnecessary. Thus, current specifications are expected to be overly pessimistic with regard to differenced range applications. Table 3 presents media calibration and instrumentation accuracies for both simultaneous and near-simultaneous QVLBI techniques. In light of the uncertainty regarding the actual possible accuracies, several values are quoted for each error source, including expected present capability, and upper and lower values for projected future capability. The future quotations include earliest availability dates.

Table 3. Differenced range measurement errors

Error source	Present capability, m		Present configuration	Projected capability, m				Projected configuration
				Upper value		Lower value		
	Simultaneous	Near simultaneous		Simultaneous	Near simultaneous	Simultaneous	Near simultaneous	
Charged particles	1[a,b]	1	Faraday rotation	0.2	0.5	0.1	0.1	S-X down link, 1976
Troposphere	1[a,c,d]	1	Constant model	0.5	0.5	0.1	0.1	Historical data improved mapping, 1973
Signal arrival time/ground delay	10[e]	10[e]	*Mariner* Mars 1971 planetary systems	10	10	1	1	
Clock sync	1000[e]	1	3 μs	1	1	0.1	0.1	Star source VLBI, 1976
Clock rate at 1 AU	3[f]	3	Rb standard $\sim 10^{-11}$	0.3	0.3	0.1	0.1	H standard, 1973
Transponder delay instability	0.1	1	*Mariner* Mars 1971	0.2	1	0.1	0.1	

[a] Reference 4.
[b] Reference 6.
[c] Reference 7.
[d] Reference 8.
[e] Reference 5.
[f] Reference 9.

The projected accuracies are illustrated in Figure 4. (The future capabilities are drawn from Reference 4 that addresses several specific quasi-VLBI configurations.) These values indicate that meaningful demonstrations of differenced range techniques can be conducted at present, and that the future goal of 1-m level differenced range measurements is indeed a plausible one. Nevertheless, the advantages of differenced range techniques will become clearer with a more detailed analysis and with experimental verification of (1) range instrument capabilities in the 3-m domain, and (2) sub-meter charged particle and troposphere calibration capability.

References

1. Martin, W., Borncamp, F., and Brummer, E., "A Method for Precision Measurement of Synchronization Errors in Tracking Station Clocks," AGARD Conference Proceedings Number Twenty-Eight, Technivision Series, Slough, England, Jan. 1970.

2. Hamilton, T. W., and Melbourne, W. G., "Information Content of a Single Pass of Doppler Data from a Distant Spacecraft," in *The Deep Space Network*, Space Programs Summary 37-39, Vol. III, pp. 18–23. Jet Propulsion Laboratory, Pasadena, Calif., May 31, 1966.

3. Curkendall, D. W., "Problems in Estimation Theory With Applications to Orbit Determination," Doctoral Dissertation, University of California, Los Angeles, 1971.

4. Mulhall, B. D., et al., *Tracking System Analytic Calibration Activities for the Mariner Mars 1969 Mission*, Technical Report 32-1499. Jet Propulsion Laboratory, Pasadena, Calif., Nov. 15, 1970.

5. Hamilton, T. W., *Error Sources for VLBI-Like Spacecraft Measurements*, IOM 71-37 (JPL internal document).

6. Ondrasik, V. J., Mulhall, B. D., and Mottinger, N. A., "A Cursory Examination of the Effect of Space Plasma on Mariner V and Pioneer IX Navigation With Implications for Mariner Mars 1971 TSAC," in *The Deep Space Network*, Space Programs Summary 37-60, Vol. II, pp. 89–94. Jet Propulsion Laboratory, Pasadena, Calif., Nov. 30, 1969.

7. Ondrasik, V. J., and Thuleen, K. L., "Variations in the Zenith Tropospheric Range Effect Computed From Radiosonde Balloon Data," in *The Deep Space Network*, Space Programs Summary 37-65, Vol. II, pp. 25–35. Jet Propulsion Laboratory, Pasadena, Calif., Sept. 30, 1970.

8. Miller, L. F., Ondrasik, V. J., and Chao, C. C., "A Cursory Examination of the Sensitivity of the Tropospheric Range and Doppler Effects to the Shape of the Refractivity Profile," in *The Deep Space Network Progress Report*, Technical Report 32-1526, Vol. I, pp. 22–30. Jet Propulsion Laboratory, Pasadena, Calif., Feb. 15, 1971.

9. Levine, M. W., and Vessot, R. F., "Hydrogen-Maser Time and Frequency Standard at Agassiz Observatory," *Radio Science*, Vol. 5, No. 10, pp. 1287–1292, Oct. 1970.

Bibliography of Current Reporting

Author Index With Abstracts

ALLEY, C. O.

A01 Preliminary Results of Laser Ranging to a Reflector on the Lunar Surface

J. D. Mulholland, C. O. Alley (University of Maryland), P. L. Bender (Joint Institute for Laboratory Astrophysics), D. G. Currie (University of Maryland), R. H. Dicke (Princeton University), J. E. Faller (Wesleyan University), W. M. Kaula (University of California, Los Angeles), G. J. F. MacDonald (University of California, Santa Barbara), H. H. Plotkin (Goddard Space Flight Center), and D. T. Wilkinson (Princeton University)

Space Research XI, pp. 97–104, Akademie-Verlag, Berlin, 1971

For abstract, see Mulholland, J. D.

AUSMAN, N. E., JR.

A02 Simulation of Mariner Mars 1971 Spacecraft

N. E. Ausman, Jr., N. K. Simon, and C. F. Rodriguez

JPL Quarterly Technical Review, Vol. 1, No. 3, pp. 67–78, October 1971

In preparation for the Mariner Mars 1971 mission, operations personnel took part in an extensive training program during which the primary source of spacecraft data was a computer program simulating the spacecraft. The objectives of a simulation model for training purposes differ from objectives appropriate to a design or analysis model. Model subsystems were designed to provide realis-tic telemetry data reflecting changes due both to commands and environmental parameters affecting the spacecraft at various times during the mission.

The spacecraft is modeled along two separate functional lines. Boolean operations are concentrated in the spacecraft logic model, which determines the spacecraft state or mode, while mathematical operations or algorithms are executed in computational subsystem models. Although logic parameters are interrogated as a part of each computational pass, actual logic model processing occurs only when a change-of-state input is generated by the operations organization. This article discusses the program design, some of the special characteristics of each of the modeled subsystems, and how the model was used in support of mission operations training.

BASSET, R. S.

B01 DSN Progress Report for September–October 1971: DSN Telemetry System Tests

W. J. Kinder and R. S. Basset

Technical Report 32-1526, Vol. VI, pp. 10–12, December 15, 1971

For abstract, see Kinder, W. J.

BATELAAN, P. D.

B02 DSN Progress Report for September–October 1971: Waveguide Voltage Reflection Calibrations of the MXK Cone (Modification 1)

P. D. Batelaan

Technical Report 32-1526, Vol. VI, pp. 123–124, December 15, 1971

A listing of reflection coefficients for the multiple-frequency X- and K-band (MXK) cone (Modification 1), at both X- and K-band frequencies, is presented. Included is a short discussion of the measurement technique and results. These measurements were made on the ground at JPL and the Goldstone Deep Space Communication Complex during the final assembly stages of the updated cone.

BEER, R.

B03 Absorption by Venus in the 3–4-Micron Region

R. Beer, R. H. Norton, and J. V. Martonchik (University of Texas)

Astrophys. J., Vol. 168, No. 3, Pt. 2, pp. L121–L124, September 15, 1971

The continuum absorption by Venus in the 3–4-μ region has been determined from a detailed comparison of high-resolution spectra of Venus and the Sun. The resultant ratio shows a major depression centered near 2580 cm^{-1} and a less well-defined dip near 3050 cm^{-1}. The possibility that these may be due to bicarbonates in the upper clouds of Venus is discussed.

B04 Astronomical Infrared Spectroscopy With a Connes-Type Interferometer: II. Mars, 2500–3500 cm^{-1}

R. Beer, R. H. Norton, and J. V. Martonchik (University of Texas)

Icarus: Int. J. Sol. Sys., Vol. 15, No. 1, pp. 1–10, August 1971

New spectra of Mars in the 3- to 4-μm region at significantly higher resolution than previously available were obtained near the 1969 opposition. No features positively identifiable as being due to the Martian atmosphere could be detected. The existence of an albedo drop, probably due to surface water of hydration, is confirmed.

BENDER, P. L.

B05 Preliminary Results of Laser Ranging to a Reflector on the Lunar Surface

J. D. Mulholland, C. O. Alley (University of Maryland), P. L. Bender (Joint Institute for Laboratory Astrophysics), D. G. Currie (University of Maryland), R. H. Dicke (Princeton University), J. E. Faller (Wesleyan University), W. M. Kaula (University of California, Los Angeles), G. J. F. MacDonald (University of California, Santa Barbara), H. H. Plotkin (Goddard Space Flight Center), and D. T. Wilkinson (Princeton University)

Space Research XI, pp. 97–104, Akademie-Verlag, Berlin, 1971

For abstract, see Mulholland, J. D.

BERGSTRALH, J. T.

B06 Recomputation of the Absorption Strengths of the Methane $3\nu_3$ J-Manifolds at 9050 cm^{-1}

J. T. Bergstralh (McDonald Observatory) and J. S. Margolis

J. Quant. Spectrosc. Radiat. Transfer, Vol. 11, No. 8, pp. 1285–1287, August 1971

Absorption intensities of the *R*-branch *J*-manifolds ($0 \leq J \leq 7$) of the $3\nu_3$ methane band have been computed using half-widths measured for the individual components of the *J*-manifolds. The effects of small pressure shifts of the lines are included. The results yield a value for the rotational temperature in agreement with the laboratory temperature and are very close to the results obtained assuming no *J* dependence of the half-widths.

BERMAN, P. A.

B07 Effects of Storage Temperatures on Silicon Solar Cell Contacts

P. A. Berman and R. K. Yasui

Technical Report 32-1541, October 15, 1971

Solar cells having various contact systems and configurations were investigated to determine the effect of storage temperature and duration on cell electrical and mechanical characteristics. Cells having *n* diffused into *p*-base silicon, *p* diffused into *n*-base silicon, and *p* diffused into *n*-base lithium-containing silicon were studied. Contact systems of silver–titanium, silver–titanium with solder coating, silver–titanium with palladium, and electroless nickel were investigated. Also included in the study were submodules similar to those used in past JPL flight projects.

The results showed that electrical and mechanical degradations previously observed in high-humidity, high-temperature environments were the result of the combined environments and not due to the temperature component alone. Solder-coated silver–titanium contacts can be adversely affected by prolonged exposure to 150°C temperature soak and to –196°C liquid nitrogen exposure. The lithium-containing cells exhibited good electrical and mechanical contact stability with respect to the other cells tested at 150°C. The addition of palladium to the silver–titanium system presented no apparent advantage for the 150°C temperature soak, except in the case of relative top contact strength, where stability (but not absolute pull strength) was superior to that for the other cell types.

B08 Supporting Data Package for TR 32-1541, Effects of Storage Temperatures on Silicon Solar Cell Contacts

P. A. Berman and R. K. Yasui

Technical Memorandum 33-497, October 15, 1971

This data package is a companion document to JPL Technical Report 32-1541 and contains a series of summary curves for cells having various contact systems, depicting the effects of temperature exposure as a function of time on the electrical and mechanical characteristics. Each curve represents the results obtained from a minimum of 32 and a maximum of 1104 individual data inputs and includes the 95% confidence limits associated with each time-temperature combination for which measurements were obtained. The curves are useful for detailed analysis and comparison of the behavior of the contact systems as a function of the environmental conditions studied.

BERWIN, R.

B09 DSN Progress Report for July–August 1971: Superconducting Magnet for a Ku-Band Maser

R. Berwin, E. Wiebe, and P. Dachel

Technical Report 32-1526, Vol. V, pp. 109–114,
October 15, 1971

A superconducting magnet to provide a uniform magnetic field of up to 8000 G in a 1.14-cm gap for the 15.3-GHz (Ku band) traveling wave maser is described. The magnet operates in a persistent mode in the vacuum environment of a closed-cycle helium refrigerator (4.5 K). The features of a superconducting switch, which has both leads connected to 4.5 K heat stations and thereby does not receive heat generated by the magnet charging leads, is described.

BREMNER, D. S.

B10 DSN Progress Report for July–August 1971: DSS Communications Equipment Subsystem Simulation Center High-Speed Data Assembly

D. S. Bremner

Technical Report 32-1526, Vol. V, pp. 132-135,
October 15, 1971

The 1971–1972 era required expansion of the Simulation Center High-Speed Data Assembly involving extensive modifications. An

increase in the number of channels was necessary to provide simultaneous data handling configurations. New data sets were installed to double the data rate as required by the DSN-GCF High-Speed Data System.

CAMERON, R. E.

C01 Farthest South Soil Microbial and Ecological Investigations

R. E. Cameron, G. H. Lacy, F. A. Morelli, and
J. B. Marsh (University of California, Davis)

Antarctic J. U.S., Vol. VI, No. 4, pp. 105–106,
July–August 1971

In austral summer 1970–1971, soil samples were collected aseptically from the surface to the depth of hard permafrost or bedrock at sites near Mount Howe, Antarctica. Environmental measurements were made for soil and microclimatic characteristics. Air samples were also taken with liquid, semisolid, and high volume dry membrane-type air samplers. Soil properties determined by methods used for desert soil and other geologic material are given. Soil and air temperatures taken at one site are also given.

CAMPBELL, J. K.

C02 A Method of Orbit Determination Using Overlapping Television Pictures

J. K. Campbell

J. Spacecraft Rockets, Vol. 8, No. 8, pp. 867–872,
August 1971

A method that utilizes the Mariner Mars 1969 television pictures has been developed to aid in the post-encounter determination of the TV viewing directions. A weighted least-squares estimation scheme is used, based on observation of common Mars surface features in overlapping TV pictures. Estimates were also obtained for the encounter orbits of Mariners 6 and 7, and also for the orientation of the Mars spin axis; however, the estimated solutions for the spacecraft orbits and for the spin axis did not result in a reduction of the *a priori* uncertainties in these parameters. Good results were obtained for the estimated corrections and the *a posteriori* uncertainties of the nominal TV viewing directions

CANNON, W. A.

C03 Lunar Fines and Terrestrial Rock Powders: Relative Surface Areas and Heats of Adsorption

F. P. Fanale, D. B. Nash, and W. A. Cannon

J. Geophys. Res., Vol. 76, No. 26, pp. 6459–6461, September 10, 1971

For abstract, see Fanale, F. P.

CARTWRIGHT, D. C.

C04 Differential and Integral Cross Sections for the Electron-Impact Excitation of the $a^1\Delta_g$ and $b^1\Sigma_g^+$ States of O_2

S. Trajmar, D. C. Cartwright (The Aerospace Corporation), and W. Williams

Phys. Rev., Pt. A: Gen. Phys., Vol. 4, No. 4, pp. 1482–1492, October 1971

For abstract, see Trajmar, S.

CHAO, C. C.

C05 DSN Progress Report for September–October 1971: Tropospheric Range Effect Due to Simulated Inhomogeneities by Ray Tracing

C. C. Chao

Technical Report 32-1526, Vol. VI, pp. 57–66, December 15, 1971

A simple ray trace method is developed to study the effect in range correction of a radio wave passing through the troposphere with inhomogeneities. Inhomogeneities were simulated from previous observations. The uncertainties in range correction due to the unmodeled horizontal gradient in refractivity are mostly less than 1% for elevation higher than 5 deg. The average uncertainty due to local inhomogeneities, based on nine simulated cases, is below 1-m in one-way range correction for elevation angles greater than 5 deg.

C06 DSN Progress Report for September–October 1971: New Tropospheric Range Corrections With Seasonal Adjustment

C. C. Chao

Technical Report 32-1526, Vol. VI, pp. 67–82,
December 15, 1971

A study of two years' radiosonde balloon measurements shows that most of the significant seasonal fluctuations in refractivity profiles are due to the variation of the water content in the troposphere. At each of the six weather stations, the long-term seasonal variation in refractivity profile repeats quite well through the two-year span. Based on the two years' data, a new tropospheric range calibration method using monthly mean parameters at each station was developed.

The uncertainty of range correction with the new model over one pass is estimated to be 0.30–0.35 m for a 10-deg minimum elevation angle and 0.40–0.50 m for a 6-deg minimum elevation angle. This is below the required accuracy for tropospheric calibration of both the Mariner Mars 1971 and Viking 1975 missions.

CHELSON, P. O.

C07 Reliability Computation Using Fault Tree Analysis

P. O. Chelson

Technical Report 32-1542, December 1, 1971

A method is presented for calculating event probabilities from an arbitrary fault tree. The method includes an analytical derivation of the system equation and is not a simulation program. Systems that incorporate standby redundancy can be handled with the method. Conditional probabilities are used for computing fault trees where the same basic failure appears in more than one fault path.

C08 Reliability Computation From Reliability Block Diagrams

P. O. Chelson

Technical Report 32-1543, December 1, 1971

A method and a computer program are presented to calculate probability of system success from an arbitrary reliability block diagram. The class of reliability block diagrams that can be handled include any active/standby combination of redundancy, and the computations include the effects of dormancy and switching in any standby redundancy. The mechanics of the program are based on an extension of the probability tree method for computing system probabilities.

C09 Program Listing for Fault Tree Analysis of JPL Technical Report 32-1542

P. O. Chelson

Technical Memorandum 33-512, December 1, 1971

This memorandum presents the computer program listing for the fault tree analysis of Technical Report 32-1542, *Reliability Computation Using Fault Tree Analysis,* Jet Propulsion Laboratory, Pasadena, Calif., Dec. 1, 1971. The program is written in FORTRAN V and is currently running on a UNIVAC 1108.

C10 Program Listing for the Reliability Block Diagram Computation Program of JPL Technical Report 32-1543

P. O. Chelson and R. E. Eckstein

Technical Memorandum 33-513, December 1, 1971

This memorandum presents the computer program listing for the reliability block diagram computation program described in Technical Report 32-1543, *Reliability Computation From Reliability Block Diagrams,* Jet Propulsion Laboratory, Pasadena, Calif., Dec. 1, 1971. The program is written in FORTRAN V and is currently running on a UNIVAC 1108. Each subroutine contains a description of its function.

CHEN, C. J.

C11 Transition Probabilities for Ar I

C. J. Chen

J. Opt. Soc. Am., Vol. 61, No. 9, pp. 1267–1268, September 1971

Interest in the spectra of the rare gases has been renewed in connection with laser kinetic studies and other endeavors. Because the rare gases show large departures from L–S and jl coupling, intermediate-coupling schemes are required to calculate the transition probabilities of those gases. This article reports the results of calculations for some Ar I arrays of special current interest. The parameters adopted for the various configurations, together with the final transition probabilities, are included.

CHOI, S. D.

C12 High-Power Microstrip RF Switch

S. D. Choi

JPL Quarterly Technical Review, Vol. 1, No. 3, pp. 110–124, October 1971

A microstrip-type single-pole double-throw (SPDT) switch whose RF and bias portions contain only a metallized alumina substrate and two PIN diodes has been developed. It is superior to electromechanical and currently used circulator-type switches in many aspects of flight-qualified switch characteristics, such as power drain, weight, volume, magnetic cleanliness, cost, and reliability. A technique developed to eliminate the dc blocking capacitors needed for biasing the diodes is described. These capacitors are extra components and could lower the reliability significantly.

An SPDT switch fabricated on a 5.08- × 5.08- × 0.127-cm (2- × 2- × 0.050-in.) substrate has demonstrated an RF power-handling capability greater than 50 W at S-band. The insertion loss is less than 0.25 dB and the input-to-off port isolation is greater than 36 dB over a bandwidth larger than 30 MHz. The input voltage standing-wave ratio is lower than 1.07 over the same bandwidth. Theoretical development of the switch characteristics and experimental results, which are in good agreement with theory, are presented in this article.

CLAUSS, R. C.

C13 DSN Progress Report for July–August 1971: Tracking and Data Acquisition Elements Research: Low Noise Receivers: Microwave Maser Development

R. C. Clauss and R. Quinn

Technical Report 32-1526, Vol. V, pp. 102–108, October 15, 1971

A traveling-wave maser, tunable from 14.3 to 16.3 GHz, has been completed and is ready for installation on the 64-m antenna at Goldstone Deep Space Communication Complex. The maser can provide more than 30 dB net gain at any frequency within its tuning range; an equivalent input noise temperature of 8.5 K has been measured in the laboratory. The maser is a ruby-loaded comb structure (*C*-axis orientation 90 deg) which operates in a closed-cycle helium refrigerator. The 8000-G magnetic field required for maser operation is supplied by a superconducting magnet. The entire package weight is 70 kg, and the unit is capable of operation in any position.

C14 DSN Progress Report for September–October 1971: Microwave Maser Development

R. C. Clauss and H. F. Reilly, Jr.

Technical Report 32-1526, Vol. VI, pp. 118–122,
December 15, 1971

A traveling-wave maser operating at 15.3 GHz has been used to test the noise temperature contribution of various waveguide components. An assembled system, consisting of the maser, a directional coupler, a waveguide switch, a polarizer, and a feed horn, measured 23-K total system operating noise temperature. Previously measured X-band data are shown for comparison. The maser was installed on the 64-m antenna at the Goldstone Deep Space Communication Complex. Maximum changes of 2.2-deg signal phase and 0.25-dB signal amplitude were observed during antenna motion tests for maser phase and gain stability. The excellent stability performance is attributed to the use of a superconducting maser magnet.

COYNER, J. V., JR.

C15 Radial Rib Antenna Surface Deviation Analysis Program

J. V. Coyner, Jr.

Technical Memorandum 33-518, December 15, 1971

As described in this memorandum, a digital computer program has been developed that analyzes any radial rib antenna that has ribs radiating from a center hub. The program has the capability to calculate the antenna surface contour (reversed pillowing effect), calculate the optimum rib shape that minimizes the RMS surface error, calculate the actual RMS surface error, compensate for rib deflection due to mesh tension and catenary cable tension, and determine the pattern from which the mesh gores are cut.

CURRIE, D. G.

C16 Preliminary Results of Laser Ranging to a Reflector on the Lunar Surface

J. D. Mulholland, C. O. Alley (University of Maryland),
P. L. Bender (Joint Institute for Laboratory Astrophysics),
D. G. Currie (University of Maryland),
R. H. Dicke (Princeton University), J. E. Faller (Wesleyan University), W. M. Kaula (University of California, Los Angeles), G. J. F. MacDonald (University of California, Santa Barbara), H. H. Plotkin (Goddard Space Flight Center), and D. T. Wilkinson (Princeton University)

Space Research XI, pp. 97–104, Akademie-Verlag, Berlin, 1971

For abstract, see Mulholland, J. D.

DACHEL, P.

D01 DSN Progress Report for July–August 1971: Superconducting Magnet for a Ku-Band Maser

R. Berwin, E. Wiebe, and P. Dachel

Technical Report 32-1526, Vol. V, pp. 109–114, October 15, 1971

For abstract, see Berwin, R.

DALLAS, S. S.

D02 DSN Progress Report for July–August 1971: A Comparison of Cowell's Method and a Variation-of-Parameters Method for the Computation of Precision Satellite Orbits

S. S. Dallas and E. A. Rinderle

Technical Report 32-1526, Vol. V, pp. 74–78, October 15, 1971

A precision special perturbations program that uses either Cowell's method or a variation-of-parameters method to compute an elliptical orbit is analyzed to determine which mode is more efficient when computing satellite orbits. The results obtained indicate that the variation-of-parameters mode is significantly more efficient if the numerical integrator being used is optimized in that mode by varying the integration order and local error control and by using either a predictor or predictor-corrector algorithm.

DAVIS, E. K.

D03 DSN Progress Report for July–August 1971: Viking Mission Support

E. K. Davis

Technical Report 32-1526, Vol. V, pp. 24–28, October 15, 1971

Since the redirection of the Viking Project in January 1970, the DSN interface organization has been heavily involved with project organizational elements in advanced planning, exchanges of technical information, identification of requirements, capabilities, prob-

lems, and their resolution. This article is a general summary of the accomplishments in these areas of long-range planning including pertinent open questions to be resolved in the detailed planning phase.

DICKE, R. H.

D04 Preliminary Results of Laser Ranging to a Reflector on the Lunar Surface

J. D. Mulholland, C. O. Alley (University of Maryland), P. L. Bender (Joint Institute for Laboratory Astrophysics), D. G. Currie (University of Maryland), R. H. Dicke (Princeton University), J. E. Faller (Wesleyan University), W. M. Kaula (University of California, Los Angeles), G. J. F. MacDonald (University of California, Santa Barbara), H. H. Plotkin (Goddard Space Flight Center), and D. T. Wilkinson (Princeton University)

Space Research XI, pp. 97–104, Akademie-Verlag, Berlin, 1971

For abstract, see Mulholland, J. D.

DON, J. P.

D05 Application of Hybrid Propulsion Systems to Planetary Missions

J. P. Don and R. L. Phen

Technical Memorandum 33-483, November 1, 1971

The feasibility and application of hybrid rocket propulsion to outer-planet orbiter missions are assessed in this study, and guidelines regarding future development are provided. A Jupiter orbiter mission was selected for evaluation because it is the earliest planetary mission that may require advanced chemical propulsion. Mission and spacecraft characteristics that affect the selection and design of propulsion subsystems are presented. Alternative propulsion subsystems, including space-storable bipropellant liquids, a solid/monopropellant vernier, and a hybrid, are compared on the basis of performance, reliability, and cost. The comparisons that assess performance, reliability, and cost independently do not yield a conclusive evaluation of each alternative propulsion subsystem's competitive position. This handicap was overcome by comparing the alternative propulsion subsystems with a cost-effectiveness model that combines the above three variables into a single parameter. The results indicate that the hybrid and space-storable bipropellant mechanizations are competitive.

DUMAS, L. N.

D06 Temperature Control of the Mariner Mars 1971 Spacecraft

L. N. Dumas

Technical Memorandum 33-515, January 1, 1972

The Mariner Mars 1971 orbiter mission was a part of the ongoing program of unmanned planetary exploration. The spacecraft design was based on that of Mariner Mars 1969, with changes as necessary to achieve mission objectives. The temperature control design for Mariner Mars 1971 is described in this memorandum, with emphasis on those areas in which significant changes were implemented. Developmental tasks are summarized and discussed, and initial flight data are presented.

ECKSTEIN, R. E.

E01 Program Listing for the Reliability Block Diagram Computation Program of JPL Technical Report 32-1543

P. O. Chelson and R. E. Eckstein

Technical Memorandum 33-513, December 1, 1971

For abstract, see Chelson, P. O.

EISENMAN, A.

E02 The Characterization of Facsimile Camera Systems for Lunar and Planetary Surface Exploration

A. Eisenman

JPL Quarterly Technical Review, Vol. 1, No. 3, pp. 1–16, October 1971

For imagery of lunar and planetary surfaces from stationary or stopped remotely controlled vehicles, facsimile camera systems offer unique advantages: better geometric fidelity than television systems, more picture elements per frame, ability to take single frame panoramic pictures, a very high contrast ratio within a picture, a choice of one or more narrow-band spectral responses over a wide possible range, image transmission over a low bit-rate communications channel without storage, very low power, small size, low weight, and ruggedizability to meet space flight requirements. Systems of this kind are under development for the 1975 Viking Martian lander, and have been used by the Soviets on Lunas and Lunokhod. JPL has recently completed laboratory and field evaluation of an existing facsimile camera system. The results

of this test program are presented. The applicability of facsimile cameras to lunar and planetary rovers is demonstrated.

ESTABROOK, F. B.

E03 Hamiltonian Cosmology

F. B. Estabrook and H. D. Wahlquist

Phys. Lett., Vol. 35A, No. 6, pp. 453–454, July 12, 1971

In this article, a simple polynomial Hamiltonian is given for type VIII and IX vacuum cosmologies. This Hamiltonian also describes solutions with time-like homogeneous 3-surfaces and thus suggests quantized versions that involve fluctuations of 3-space signature and topology.

FALLER, J. E.

F01 Preliminary Results of Laser Ranging to a Reflector on the Lunar Surface

J. D. Mulholland, C. O. Alley (University of Maryland), P. L. Bender (Joint Institute for Laboratory Astrophysics), D. G. Currie (University of Maryland), R. H. Dicke (Princeton University), J. E. Faller (Wesleyan University), W. M. Kaula (University of California, Los Angeles), G. J. F. MacDonald (University of California, Santa Barbara), H. H. Plotkin (Goddard Space Flight Center), and D. T. Wilkinson (Princeton University)

Space Research XI, pp. 97–104, Akademie-Verlag, Berlin, 1971

For abstract, see Mulholland, J. D.

FANALE, F. P.

F02 Lunar Fines and Terrestrial Rock Powders: Relative Surface Areas and Heats of Adsorption

F. P. Fanale, D. B. Nash, and W. A. Cannon

J. Geophys. Res., Vol. 76, No. 26, pp. 6459–6461, September 10, 1971

Surface area measurements by Kr adsorption (BET method) indicate that Apollo 11 lunar fines and ground terrestrial mafic rock powders have similar effective surface areas that are a factor of 10–100 higher than their geometrical or surficial surface areas. There is no evidence that a significant increase in surface rough-

ness for lunar fines has resulted from their peculiar history of exposure on the moon's surface. Low apparent heats of adsorption for Kr adsorption on lunar fine material are consistent with the presence of glassy or glass-coated particles.

FANSELOW, J. L.

F03 DSN Progress Report for July–August 1971: The Goldstone Interferometer for Earth Physics

J. L. Fanselow, P. F. MacDoran, J. B. Thomas, J. G. Williams, C. Finnie, T. Sato, L. Skjerve (Philco-Ford Corporation), and D. Spitzmesser

Technical Report 32-1526, Vol. V, pp. 45–57, October 15, 1971

The first in a series of very long baseline interferometry feasibility demonstrations for applications to Earth Physics was conducted on January 29, 1971. In this demonstration two Goldstone tracking stations, the 26-m Echo station and the 64-m Mars station, were equipped with JPL hydrogen maser frequency systems and operated in electrically independent, although coordinated, observing modes. S-band (2.3 GHz) radio signals from 14 celestial radio sources were recorded at each station on digital magnetic tape. Later, these tapes were brought together for computer cross-correlation to produce an interferometric observable. Using the interferometer fringe frequency, a measurement of the two equatorial baseline components was made. The discrepancy between these measurements and the inter-station geodetic survey was less than 30 cm in each of these two components.

FINNIE, C.

F04 DSN Progress Report for July–August 1971: The Goldstone Interferometer for Earth Physics

J. L. Fanselow, P. F. MacDoran, J. B. Thomas, J. G. Williams, C. Finnie, T. Sato, L. Skjerve (Philco-Ford Corporation), and D. Spitzmesser

Technical Report 32-1526, Vol. V, pp. 45–57, October 15, 1971

For abstract, see Fanselow, J. L.

FLEISCHER, G. E.

F05 Flexible Spacecraft Control System Design Procedures Utilizing Hybrid Coordinates

P. W. Likins, E. L. Marsh, and G. E. Fleischer

Technical Memorandum 33-493, September 15, 1971

For abstract, see Likins, P. W.

FLETCHER, B. C.

F06 An Eclectic Integrated Circuit Reliability Model

B. C. Fletcher

Technical Memorandum 33-514, January 1, 1972

With the advent of solid-state physics and the subsequent integrated device technology, the task of assessing device reliability has become increasingly more difficult. One problem is that the parameters of integrated circuits and large-scale-integration devices are readily accessible only from the periphery, resulting in a lack of data needed for precise model definitions and constraints. Another problem is that existing modeling techniques can not, in general, be considered viable since there is no direct input for basic materials and process changes that tend to be inherent in technological change. Other problems witn existing n.odels originate from the assumptions forming the basis of present model derivations.

This memorandum presents an interim report on research relating to the development of an integrated circuit reliability model. Because of the complexities stated briefly above and described more fully in the memorandum, defects, modes, mechanisms (where possible), frequency of mechanism occurrence (where possible), manufacturing/processing impact on failure, time dependency of mechanisms, screening influences (supplie and user), and device application had to be considered in the modeling rationale that is proposed.

FLIEGEL, H. F.

F07 DSN Progress Report for July–August 1971: A Worldwide Organization to Secure Earth-Related Parameters for Deep Space Missions

H. F. Fliegel

Technical Report 32-1526, Vol. V, pp. 66–73,
October 15, 1971

A global express service to obtain timing and polar motion parameters for deep space mission support has been organized through the Bureau International de l'Heure. The results are incorporated into a daily operation. This article outlines what the new sources of data are, what procedures are used to reduce the data, and what software is available to the user.

GALLILY, I.

G01 On the Drag Experienced by a Spheroidal, Small Particle in Gravitational and Electrostatic Fields

I. Gallily

J. Colloid Interface Sci., Vol. 36, No. 3, pp. 325–339,
July 1971

The behavior of a suspended, rigid particle in a creeping motion depends generally on translation, rotation, and coupling tensors, which are geometric properties of the body. Previously, these second-rank tensors have been calculated only for a few simple forms. In this article, the drag on a spheroidal particle that moves in a creeping motion and performs simultaneously random rotations is calculated by a new method of averaging for cases of both gravitational and electrostatic fields. Appropriate expressions are written for the mobilities, which are computed subsequently for a range of spheroid sizes, axial ratios, and electrostatic field intensities.

GEORGEVIC, R. M.

G02 Mathematical Model of the Solar Radiation Force and Torques Acting on the Components of a Spacecraft

R. M. Georgevic

Technical Memorandum 33-494, October 1, 1971

Solar radiation pressure exerts a mechanical force upon the surface of a spacecraft that intercepts the stream of photons coming from the Sun. For high-precision spacecraft attitude control and orbit determination, it is necessary to generate a precise mathematical model of the solar radiation force and the moment of that force; such a model must be more accurate than the currently used "flat surface" model, based on the radiation force on the effective cross-sectional area of the irradiated body.

In this memorandum, the general expressions for the solar radiation force and torques are derived in the vectorial form for any given reflecting surface, provided that the reflecting characteristics of the surface, as well as the value of the solar constant, are known. An appropriate choice of a spacecraft-fixed frame of reference leads to relatively simple expressions for the solar radiation forces and torques in terms of the functions of the Sun–spacecraft–Earth angle.

The advantage of such a model over the standard flat-surface model is obvious, and it is very easy to find the expressions for the error of the standard model for any given reflecting surface. Another advantage of the model is that it can be used for the effects of the air drag, solar wind, etc.

GERBER, W.

G03 Quenching of Solid-Propellant Rockets by Water Injection

L. D. Strand and W. Gerber (Lockheed Aircraft Service Co.)

J. Spacecraft Rockets, Vol. 8, No. 9, pp. 992–996, September 1971

For abstract, see Strand, L. D.

GOODWIN, P. S.

G04 DSN Progress Report for July–August 1971: Helios Mission Support

P. S. Goodwin

Technical Report 32-1526, Vol. V, pp. 17-21, October 15, 1971

Project Helios is the first NASA international deep space project, although there have been prior NASA international sub-orbital and Earth-orbiting cooperative space projects. Helios is a joint undertaking by the Federal Republic of West Germany and the United States of America, who divide the project responsibilities. Two unmanned scientific satellites are planned for heliocentric orbits: the first to be launched in mid-1974, and the second in late-1975. Prior volumes of this series describe the history and objectives of this program, the contemplated spacecraft configuration, and its telecommunications and telemetry systems. This article deals with the spacecraft's command system, its requirements, and conceptual block diagrams.

G05 DSN Progress Report for September–October 1971: Helios Mission Support

P. S. Goodwin

Technical Report 32-1526, Vol. VI, pp. 25–32,
December 15, 1971

Project Helios, a joint endeavor between the United States and West Germany, will place two unmanned spacecraft into heliocentric orbits whose perihelion distance will come closer to the Sun than any previous or presently planned free-world deep space undertaking. The first spacecraft is expected to be launched in mid-1974 and the second in late-1975. Prior volumes of this series describe the history and objectives of this project, the contemplated spacecraft configuration, and the spacecraft's radio system. This article deals with the capabilities of the telecommunications link between the spacecraft and the DSN.

GORDON, H. J.

G06 Analysis of Mariner VII Pre-encounter Anomaly

H. J. Gordon, S. K. Wong, and V. J. Ondrasik

J. Spacecraft Rockets, Vol. 8, No. 9, pp. 931–937,
September 1971

The loss of signal at 127 h before the Mariner VII (Mariner 7) closest approach to Mars and the subsequent changes in the spacecraft and its trajectory are described. Real-time orbit determination activity and postencounter analysis are discussed. Great difficulty was experienced in processing tracking data influenced by an unknown nongravitational force that could not be properly modeled. Results of simulations using known perturbations are presented. It is concluded that the battery case ruptured and vented into the interior of the spacecraft. This rupture caused corona discharges, and escaping gas produced the translational forces.

GROTCH, S. L.

G07 Computer Techniques for Identifying Low Resolution Mass Spectra

S. L. Grotch

Anal. Chem., Vol. 43, No. 11, pp. 1362–1370,
September 1971

A number of computer programs have been developed for identifying low resolution mass spectra through search of an extensive library file. One set of programs used as a disagreement criterion the sum of the absolute values of the differences in peak height levels when peak height was encoded to 2, 8, or 10^4 levels at each nominal mass. Another program employed the maximum coincidence of the top N peaks. The programs were tested using 125 unknowns and the recognition performances were compared. The maximum coincidence criterion was significantly poorer in recognition performance than the other techniques which increased in reliability as the number of levels increased. However, even the two-level system attained very high reliability. Since computer requirements and economic costs are likely to be minimal for this case, it might suffice for many applications.

HADEK, V.

H01 Electrical Properties of 7,7′,8,8′-Tetracyanoquinodimethane Salts of Ionene Polymers and Their Model Compounds

V. Hadek, H. Noguchi, and A. Rembaum

Macromolecules, Vol. 4, No. 4, pp. 494–499,
July–August 1971

Electrically conducting polymeric salts were prepared by the reaction of ionene polymers with LiTCNQ in the presence or absence of neutral TCNQ (tetracyanoquinodimethane). The specific resistivity, the activation energy for conductivity, and the Seebeck coefficient were determined as a function of the number of CH_2 groups between positively charged nitrogens. The wide variations of electrical properties could not be correlated with the length of the polymethylene chain in the polymer. X-ray analysis of single crystals of model compounds revealed that the electrical properties depend mainly on crystal geometry.

HANSON, R. J.

H02 A Numerical Method for Solving Fredholm Integral Equations of the First Kind Using Singular Values

R. J. Hanson

SIAM J. Numer. Anal., Vol. 8, No. 3, pp. 616–622, September 1971

The integral equation in question is approximated by simple numerical quadrature formulas plus collocation. Each row of the resulting matrix equation for the unknown function values is weighted by the reciprocal of the standard deviation of the known function. A singular-value decomposition is used to obtain a solution for the resulting linear system. By avoiding the use of the smallest singular values, an approximate solution is calculated that frequently solves the problem "close enough" and removes a great deal of the oscillations in the solution that are inherently present due to the ill-posed nature of the problem. Test cases and computational results are presented.

HARPER, L.

H03 DSN Progress Report for July–August 1971: Contributions to a Mathematical Theory of Complexity

L. Harper (University of California, Riverside) and
J. E. Savage (Brown University)

Technical Report 32-1526, Vol. V, pp. 91–98, October 15, 1971

This article is another in a series that attempts to define precisely and investigate the "computational complexity" of a general class of problems which includes many problems that occur in the DSN control center. Specific DSN control center questions that a theory of computational complexity will help define and answer include the problem of the optimum mix of core, disk, and drum storage in the control center, and the intelligent allocation of computational resources to flight projects of differing complexity in such a way that simultaneous real-time computing commitments can be made. This article shows that there exists such a theory which is capable of providing important information about the true complexity of several classes of non-trivial problems.

H04 DSN Progress Report for July–August 1971: Some Results on the Matrix Multiplication Problem

L. Harper (University of California, Riverside) and
J. E. Savage (Brown University)

Technical Report 32-1526, Vol. V, pp. 99–101, October 15, 1971

Three results on the multiplication of two $n \times n$ matrices are presented. They contribute to our understanding of the complexity of matrix multiplication, and so of code decoding, tracking accu-

racy computation, antenna structural analysis and other DSN computational tasks.

HARTLEY, R. B.

H05 DSN Progress Report for July–August 1971: Apollo Mission Support

R. B. Hartley

Technical Report 32-1526, Vol. V, pp. 29–41,
October 15, 1971

The support provided by the DSN to the Manned Space Flight Network during the Apollo 15 mission is described. Support was provided from four 26-m (85-ft) DSN stations, the Goldstone 64-m (210-ft) antenna, the Ground Communications Facility, and the Space Flight Operations Facility. Premission and mission activities are discussed and a brief mission description is included.

HARTOP, R. W.

H06 DSN Progress Report for September–October 1971: Operational Time Sync Microwave Subsystem

R. W. Hartop

Technical Report 32-1526, Vol. VI, pp. 165–167,
December 15, 1971

The prototype Operational Time Sync Microwave Subsystem has been redesigned to accommodate the change in operational frequency and to increase its power-handling capability. The completed system has been successfully tested to 115 kW continuous wave at 7150 MHz and is expected to operate at 150 kW continuous wave, the design goal. A description of the subsystem is presented.

HEER, E.

H07 Maximum Dynamic Response and Proof Testing

J.-N. Yang and E. Heer (NASA Headquarters)

J. Eng. Mech. Div., Proc. ASCE, Vol. 97, No. EM4,
pp. 1307–1313, August 1971

For abstract, see Yang, J.-N.

HERMANN, A. M.

H08 Electrical Conductivity of Elastomeric TCNQ Complexes Under Mechanical Stress

A. M. Hermann (Tulane University), S. P. S. Yen, A. Rembaum, and R. F. Landel

J. Polym. Sci., Pt. B: Polym. Lett., Vol. 9, No. 8, pp. 627–633, August 1971

A significant amount of research has been made in the area of macroscopically inhomogeneous filled rubbers; however, no study of a homogeneous rubbery semiconductor under mechanical stress has been reported previously. This article gives a preliminary report of a study on the electrical conductivity of rubbery polymers complexed with tetracyanoquinodimethane (TCNQ). Measurements on a rubbery polymer mixed intimately with LiTCNQ are also discussed. The carbon-filled rubbers previously investigated had decreased conductivities under load; the rubbery polymeric-TCNQ polymers have either unchanged conductivities or, in some cases, increased conductivities in the stretched state. This increase in conductivities may be suggestive of stress-induced orientation.

HINTZ, G. R.

H09 A Viking Satellite Orbit Trim Strategy

G. R. Hintz

JPL Quarterly Technical Review, Vol. 1, No. 3, pp. 133–142, October 1971

The Viking Project places a number of interesting and stringent requirements on the control of the satellite orbit to obtain reconnaissance and to prepare for lander release. To satisfy these requirements, different orbit trim maneuver strategies have been developed for two typical Viking missions. This article describes one of these strategies. In addition, a summary of recent numerical results is included to show that this strategy satisfies the mission requirements which have been identified.

HOFMANN, A. H.

H10 DSN Progress Report for July–August 1971: Pioneer F and G Mission Support Area

A. H. Hofmann

Technical Report 32-1526, Vol. V, pp. 136–140,
October 15, 1971

With the advent of the third-generation computer systems and the increased complexity of interplanetary missions, the area required to support mission operations has exceeded available facilities within the SFOF. Consequently, the Pioneer F Jupiter flyby mission support area will be located in the new Systems Development Laboratory, Building 264, at JPL. The mission support area, its relationship with the SFOF and other DSN facilities, and some anticipated operational problems caused by its remote location from the SFOF are described in this article.

HOLMES, J. K.

H11 A Note on Some Efficient Estimates of the Noise Variance for First-Order Reed–Muller Codes

J. K. Holmes

IEEE Trans. Inform. Theor., Vol. IT-17, No. 5, pp. 628–630,
September 1971

The maximum-likelihood estimate based on order statistics for both a single-sample and an M-sample estimate are derived for the first-order Reed–Muller code sent over a zero-mean white Gaussian noise channel. The estimation method is subject to an equipment-complexity constraint. The constraint imposed requires that the estimates be obtained from successive comparisons of the correlations in a serial system, without the use of arithmetic operations. The maximum-likelihood estimates obtained here are compared to other such estimates and also the unrestricted maximum-likelihood estimate.

HUNTRESS, W. T., JR.

H12 Ion Cyclotron Resonance Power Absorption: Collision Frequencies for CO_2^+, N_2^+, and H_3^+ Ions in Their Parent Gases

W. T. Huntress, Jr.

J. Chem. Phys., Vol. 55, No. 5, pp. 2146–2155,
September 1, 1971

The complete solution for the equation of motion of an ion in the ICR cell is shown to give results for the instantaneous power absorption in excellent agreement with experiment at all pressures. The instantaneous power absorption at resonance initially increases linearly with time, and at high pressures levels off to a

constant value at saturation where the energy gained by ions from the RF electric field is equal to the energy dissipated in collisions. An expression is also derived for the average kinetic energy of an ion at saturation in the steady-state limit. Pulsed ICR techniques are used to obtain the instantaneous power absorption curves for N_2^+, CO_2^+, and H_3^+ ions in their parent gases as a function of pressure, from which are calculated the momentum transfer rate constants k, and the dependence of the rate constants on ion kinetic energy. At 293°K,

$$k(N_2^+) = k(CO_2^+)$$

$$= 0.67 \times 10^{-9} \text{ cm}^3\text{-molecule}^{-1}\text{-sec}^{-1}$$

$$k(H_3^+) = 1.09 \times 10^{-9} \text{ cm}^3\text{-molecule}^{-1}\text{-sec}^{-1}$$

For N_2^+ ions in N_2 and CO_2^+ ions in CO_2, the rate constants are both significantly greater than that predicted by polarization theory and both rate constants increase significantly with increasing ion kinetic energy. This behavior is most likely a consequence of long-range resonant charge transfer outside the orbiting impact parameter.

JACKSON, E. B.

J01 DSN Progress Report for July–August 1971: DSN Research and Technology Support

E. B. Jackson

Technical Report 32-1526, Vol. V, pp. 120–121, October 15, 1971

The major current activities of the Development Support Group, at both the Venus Deep Space Station and the Microwave Test Facility, are presented and accomplishments and progress for each are described. Activities include pulsar observations, planetary radar (including a general relativity experiment), 100-kW clock synchronization implementation, SDS 930 computer installation into the Mars Deep Space Station, precision antenna gain measurements, very long baseline interferometry, electromagnetic field survey at the Pioneer Deep Space Station, and new phase-lock receiver installation at the Microwave Test Facility.

J02 DSN Progress Report for September–October 1971: DSN Research and Technology Support

E. B. Jackson

Technical Report 32-1526, Vol. VI, pp. 147–148,
December 15, 1971

Accomplishments and progress during the major current activities of the Development Support Group at both the Venus Deep Space Station and the Microwave Test Facility are described. Activities include pulsar observations, planetary radar with very-high-resolution range measurement of the planet Mars, tricone support structure assembly, 100-kW clock synchronization implementation, precision antenna gain measurement on the 26-m antenna, Block IV receiver/exciter installation and testing, weak source observations of 13 sources, and observations of the planet Jupiter.

JET PROPULSION LABORATORY

J03 Proceedings of the Conference on Experimental Tests of Gravitation Theories, California Institute of Technology, Pasadena, California, November 11–13, 1970

Jet Propulsion Laboratory

Technical Memorandum 33-499, November 1, 1971

The Conference on Experimental Tests of Gravitation Theories was the result of the feelings of a number of people that technology, particularly that spawned by previous space activities, had made it possible to think realistically in terms of a long-range cooperative effort in the testing of general relativity and other modern theories of gravity. The conference was sponsored by NASA, the European Space Research Organization, and JPL. These proceedings, edited by R. W. Davies, present 33 papers that explore various competitive philosophies on both the operational and the theoretical level.

J04 Development and Testing of the Central Computer and Sequencer for the Mariner Mars 1971 Spacecraft

Jet Propulsion Laboratory

Technical Memorandum 33-501, October 15, 1971

The central computer and sequencer subsystem (CC&S) has been an important part of the Mariner series of interplanetary spacecraft since their inception. As with other spacecraft subsystems, the CC&S has increased in complexity and capability with each spacecraft project. This report describes the design, fabrication, and testing associated with the development of the Mariner Mars 1971 CC&S subsystem.

J05 **Development and Testing of the Pyrotechnic Subsystem for the Mariner Mars 1971 Spacecraft**

Jet Propulsion Laboratory

Technical Memorandum 33-502, December 15, 1971

The Mariner Mars 1971 pyrotechnic subsystem consists of the pyrotechnics switching assembly (PSA), the explosive squibs on the spacecraft, the spacecraft/Centaur release devices, and the pinpullers. Numerous small changes from the Mariner Mars 1969 design were effected in the PSA, but the basic capacitor-discharge approach remained the same. Two new squibs were developed; a completely new spacecraft/Centaur release device was designed, developed, and qualified; and minor design improvements were accomplished on the pinpullers for the Mariner Mars 1971 program. The basic support equipment hardware and approach were carried over from the Mariner Mars 1969 program. The purpose of this memorandum is to document the design, fabrication, and testing of the Mariner Mars 1971 pyrotechnic subsystem, with emphasis on changes from the Mariner Mars 1969 subsystem development.

J06 **Development and Testing of the S-Band Antenna Subsystem for the Mariner Mars 1971 Spacecraft**

Jet Propulsion Laboratory

Technical Memorandum 33-503, November 1, 1971

The Mariner Mars 1971 S-band antenna subsystem is used to transmit and receive S-band signals to and from the Deep Space Instrumentation Facility ground stations. The antenna subsystem consists of a low-gain antenna, a medium-gain antenna, a directional coupler, a high-gain antenna, and all transmission lines required to interconnect the antennas to the spacecraft radio frequency subsystem. The low-gain antenna is used to transmit signals during cruise and receive signals throughout the mission. The medium-gain antenna is coupled to the low-gain antenna via the directional coupler and is used to transmit and receive signals during Mars orbit insertion. The high-gain antenna is used to transmit high-data-rate signals primarily during Mars orbit.

J07 **Development and Testing of the Television Instrument for the Mariner Mars 1971 Spacecraft**

Jet Propulsion Laboratory

Technical Memorandum 33-505, November 1, 1971

This memorandum describes the Mariner Mars 1971 television instrument, with emphasis on those aspects that are different from

the Mariner Mars 1969 television subsystem. The various modes of operation are described, and functional descriptions of the major elements in the system are summarized. An electronic description of the circuits that differ from those of Mariner Mars 1969 is also presented, along with a brief description of the calibration and test sequences.

J08 A Reduced Star Catalog Containing 537 Named Stars

Jet Propulsion Laboratory

Technical Memorandum 33-507, November 15, 1971

This document is the first of a series presenting data, compiled by JPL, that are to be included in the JPL Astronautical Star Catalog. Positional and color magnitude data for the 537 named stars, which are to be included in the catalog, are given. A brief translation of the star names and the source language of the names are also presented.

J09 Development and Testing of the Data Automation Subsystem for the Mariner Mars 1971 Spacecraft

Jet Propulsion Laboratory

Technical Memorandum 33-508, November 15, 1971

The data automation subsystem serves as the data handling subsystem for the science payload. It provides basic timing and commands to control the instrument's modes and sequences. The instrument data are formatted for transmission to Earth in real time via the telemetry channel or stored on the tape recorder for playback in non-real time. The design, fabrication, and testing of the Mariner Mars 1971 data automation subsystem are described in this memorandum. Major changes are discussed relative to the Mariner Mars 1969 subsystem design.

J10 Development and Testing of the Infrared Interferometer Spectrometer for the Mariner Mars 1971 Spacecraft

Jet Propulsion Laboratory

Technical Memorandum 33-509, December 1, 1971

The primary purpose of the Mariner Mars 1971 infrared spectroscopy experiment is to determine values of atmospheric parameters and information pertinent to the solid surface of Mars. Both atmospheric and surface parameters can be derived by interpretation of thermal emission spectra, which will be observed from the orbiter as a function of time and location on the planet.

The Mariner interferometer, which was designed, fabricated, and tested by Texas Instruments, Inc., under the direction of the NASA Goddard Space Flight Center, is similar to the interferometer flown on the meteorological research satellites Nimbus 3 and 4 in 1969 and 1970. In this memorandum, the unique features of the Mariner interferometer are emphasized, with particular regard to the cesium iodide beamsplitter. The extended spectral range made possible with the cesium iodide beamsplitter is significant to the water vapor investigation. The major changes required to accommodate the increased performance and to adapt to the Mariner spacecraft environment are described.

J11 Mariner Mars 1971 Science Operational Support Equipment Final Report

Jet Propulsion Laboratory

Technical Memorandum 33-511, November 15, 1971

The Mariner Mars 1971 science operational support equipment (SOSE) was developed to support the checkout of the proof test model and flight spacecraft. This memorandum discusses the test objectives for the SOSE and how these objectives were implemented. Attention is focused on the computer portion, since incorporation of a computer in ground checkout equipment represents a major departure from the support equipment concepts previously used at JPL. The major hardware elements and the SOSE operational performance during spacecraft testing are described.

J12 DALG—A Program for Test Pattern Generation in Combinational Logical Circuits

Jet Propulsion Laboratory

Technical Memorandum 33-510, November 15, 1971

This memorandum is primarily a user's manual for a computer program DALG that generates test patterns for detecting faults in combinational logic circuits containing up to 200 logical gates. The gates may be of logical types AND, OR, NAND, NOR, NOT, or Exclusive OR. The faults may be any one gate or input stuck at a fixed value (0 or 1).

In addition to test pattern generation, DALG will also determine whether or not the given test pattern will detect given faults in a circuit. Sample problems are given along with input data sheets and printed output to illustrate the capabilities of the program.

JOHNSON, D.

J13 DSN Progress Report for July–August 1971: Combinational Complexity Measures as a Function of Fan-Out

D. Johnson, J. E. Savage (Brown University), and
L. R. Welch (University of Southern California)

Technical Report 32-1526, Vol. V, pp. 79–81,
October 15, 1971

If $C_s(f_1, \ldots, f_L)$ is the fan-out s combinational complexity of the functions $f_1, f_2, \ldots, f_L$ with respect to straight-line algorithms (or combinational machines) of fan-in r, then it is shown that

$$C_\infty(f_1, \ldots, f_L) \leqslant C_s(f_1, \ldots, f_L) \leqslant \left(\frac{d(r-1)}{s-1} + 1\right) C_\infty(f_1, \ldots, f_L) + \frac{d}{s-1}(L - N)$$

where N is the number of variables on which $f_1, \ldots, f_L$ depend and $d = C_s(I)$, where I is the identity function in one variable. Thus, a well-designed combinational machine or algorithm will not have a fan-out which is more than several times its fan-in.

JOHNSTON, A. R.

J14 Dispersion of Electro-Optic Effect in $BaTiO_3$

A. R. Johnston

J. Appl. Phys., Vol. 42, No. 9, pp. 3501–3507, August 1971

The dispersion of both the quadratic and linear electro-optic effects in flux-grown crystals of barium titanate ($BaTiO_3$) has been measured polarimetrically between 0.4 and 1.0 μ yielding $(g_{11}-g_{12})$ and

$$r_c = r_{33} - (n_a/n_c)^3 \, r_{13}$$

A strong dispersion was found: $(g_{11}-g_{12})$ increases to double its long-wave-length limit at 0.4 μ. Both unclamped (low frequency) and clamped measurements were made. Birefringence and the principal indices were also determined. A two-oscillator Sellmeier model, in which one oscillator frequency is polarization dependent, was shown to represent closely all the data. The unclamped

polarization potential, which specifies the magnitude of the oscillator frequency shift, was 3.9 eV m^4C^{-2}, while its clamped value was one-third as large. Ultraviolet reflectivity calculated from the model assuming reasonable values of empirical damping agrees with the observations of Cardona and Gahwiller.

JORDAN, J. F.

J15 Guidance and Navigation for Solar Electric Interplanetary Missions

K. H. Rourke and J. F. Jordan

J. Spacecraft Rockets, Vol. 8, No. 9, pp. 920–926, September 1971

For abstract, see Rourke, K. H.

KALFAYAN, S. H.

K01 Long-Term Aging of Elastomers: Chemical Stress Relaxation of Fluorosilicone Rubber and Other Studies

S. H. Kalfayan, A. A. Mazzeo, and R. H. Silver

JPL Quarterly Technical Review, Vol. 1, No. 3, pp. 38–47, October 1971

Elastomers have varied aerospace applications, including: propellant binders, bladder materials for liquid propellant expulsion systems, and fuel tank sealants, particularly for high-speed aircraft. Predicting the long-term behavior of these materials is of paramount importance. A comprehensive molecular theory for mechanical properties has been developed at JPL. It has only been tested experimentally in cases where chemical degradation processes are excluded. Hence, a study is underway to ascertain the nature, extent, and rate of chemical changes that take place in some elastomers of interest. The results can then be incorporated in the theoretical framework. This article reports progress on the investigations of chemical changes that may take place in the fluorosilicone elastomer, LS 420, which is regarded as a fuel and high-temperature-resistant rubber. The kinetic analysis of the chemical stress relaxation and gel permeation chromatography studies comprise the major portion of this article.

KATOW, M. S.

K02 DSN Progress Report for September–October 1971: S- and X-Band Feed System

M. S. Katow

Technical Report 32-1526, Vol. VI, pp. 139–141, December 15, 1971

The proposed S- and X-band feed system provides for simultaneous RF propagation from the 64-m antenna for both S- and X-band signals along the same boresight direction. The hardware for the tri-cone system consists of an ellipsoid reflector over the S-band horn and a dichroic reflector plate over the X-band cone. The ellipsoid reflector focuses the S-band signal in front of the dichroic plate. The dichroic plate is capable of transmitting an X-band signal through it and reflecting S-band. The dichroic plate, mounted in a position about 60 deg to the centerline of the X-band signal, then reflects the S-band signal coincident to the X-band signal. Preliminary hardware mounting schemes are outlined with probable operational requirements.

K03 DSN Progress Report for September–October 1971: Overseas 64-m RMS Program for SDS 920

D. McCarty and M. S. Katow

Technical Report 32-1526, Vol. VI, pp. 158–164, December 15, 1971

For abstract, see McCarty, D.

KAULA, W. M.

K04 Preliminary Results of Laser Ranging to a Reflector on the Lunar Surface

J. D. Mulholland, C. O. Alley (University of Maryland), P. L. Bender (Joint Institute for Laboratory Astrophysics), D. G. Currie (University of Maryland), R. H. Dicke (Princeton University), J. E. Faller (Wesleyan University), W. M. Kaula (University of California, Los Angeles), G. J. F. MacDonald (University of California, Santa Barbara), H. H. Plotkin (Goddard Space Flight Center), and D. T. Wilkinson (Princeton University)

Space Research XI, pp. 97–104, Akademie-Verlag, Berlin, 1971

For abstract, see Mulholland, J. D.

KHATIB, A. R.

K05 Dynamic Upper Atmospheric Force Model on Stabilized Vehicles for a High-Precision Trajectory Computer Program

A. R. Khatib

JPL Quarterly Technical Review, Vol. 1, No. 3, pp. 125–132, October 1971

This article summarizes the results of research carried out at JPL for the design and implementation of dynamic upper atmosphere and lift and drag models into the advanced Double-Precision Trajectory Program (DPTRAJ). The upper atmosphere model draws heavily on the behavior of the Earth's upper atmosphere which exhibits cyclic as well as irregular variations in density profile, temperature, pressure, and composition in unison with solar activities as deduced from the more recent land-based and satellite observations.

The lift and drag model is designed specifically for inertially stabilized vehicles of the Mariner class, with possible extension to gravity gradient stabilized vehicles of the GEOS class. The model considers operation in the free molecular flow regimes with large Knudsen numbers. The vehicle is considered a composite structure with basic components having well-defined shapes, each with its own surface characteristics in terms of temperature, reflectivity, and accommodation of free stream molecules. The model takes into account both the calculation of precise aerodynamic force coefficients in terms of expansion of modified Bessel functions in speed ratios and angle of attack, and approximate force coefficients when the speed ratios approach infinity. Other considerations include specular and diffused reflectivity, shielding, and shadow effects.

KINDER, W. J.

K06 DSN Progress Report for September–October 1971: DSN Telemetry System Tests

W. J. Kinder and R. S. Basset

Technical Report 32-1526, Vol. VI, pp. 10–12, December 15, 1971

The overall DSN System test plan, as edited for the DSN Multimission Telemetry System, is briefly described. Specific results, with delivered Mariner Mars 1971 telemetry software, are presented in relation to this test plan. Recommendations are included for future system demonstration, specifically as to system documentation and training.

KRON, M.

K07 DSN Progress Report for July–August 1971: Load Distribution on the Surface of Paraboloidal Reflector Antennas

M. Kron

Technical Report 32-1526, Vol. V, pp. 122–128, October 15, 1971

Wind pressure coefficients have been measured using wind tunnel models of parabolic reflectors. The application of this data and its conversion to useful form for structural deflection analysis within the "NASTRAN" Structural Analysis Computer Program and ultimately Root Mean Square (RMS) program is described in this article.

LACY, G. H.

L01 Farthest South Soil Microbial and Ecological Investigations

R. E. Cameron, G. H. Lacy, F. A. Morelli, and J. B. Marsh (University of California, Davis)

Antarctic J. U.S., Vol. VI, No. 4, pp. 105–106, July–August 1971

For abstract, see Cameron, R. E.

LAESER, R. P.

L02 DSN Progress Report for July–August 1971: Mariner Mars 1971 Mission Support

R. P. Laeser

Technical Report 32-1526, Vol. V, pp. 22–23, October 15, 1971

While continuing to provide the tracking and data acquisition function for Mariner 9 on its journey to Mars, the DSN is planning and practicing for the orbital operations. The final steps of implementation and the test plans for orbital operations are outlined in this article.

L03 DSN Progress Report for September–October 1971: Mariner Mars 1971 Mission Support

R. P. Laeser

Technical Report 32-1526, Vol. VI, pp. 33–36,
December 15, 1971

This article completes and updates the description of the planned DSN configuration for support of the Mariner 9 orbit insertion and orbital operations. Specifically covered are the S-band occultation experiment data handling, the planetary ranging configuration, and the simulation configuration.

LANDEL, R. F.

L04 Electrical Conductivity of Elastomeric TCNQ Complexes Under Mechanical Stress

A. M. Hermann (Tulane University), S. P. S. Yen, A. Rembaum, and R. F. Landel

J. Polym. Sci., Pt. B: Polym. Lett., Vol. 9, No. 8, pp. 627–633, August 1971

For abstract, see Hermann, A. M.

L05 Properties of a Highly Crosslinked Elastomer

R. F. Landel

Polymer Networks: Structural and Mechanical Properties, pp. 219–243, Plenum Publishing Corporation, New York, 1971

With the objective of enhancing understanding of the behavior of elastomers, the properties of a highly crosslinked polyurethane elastomer, based on ricinoleic acid (castor oil) as the backbone, have been measured. The rubber, termed Galcit I, has been proposed as a standardized, highly birefringent, nearly elastic rubber for use in testing new apparatus on a material with known properties and in checking or calibrating existing instruments. This article discusses the preparation and characterization of Galcit I.

LAYLAND, J. W.

L06 DSN Progress Report for September–October 1971: An Optimum Buffer Management Strategy for Sequential Decoding

J. W. Layland

Technical Report 32-1526, Vol. VI, pp. 106–111,
December 15, 1971

Sequential decoding has been found to be an efficient means of communicating at low undetected error rates from deep space probes, but a failure mechanism known as erasure or computa-

tional overflow remains a significant problem. The erasure of a block occurs when the decoder has not finished decoding that block at the time that it must be output.

The erasure rate can be unacceptably high, even when the decoder is spending over half of its time idly awaiting incoming data. By drawing upon analogies in computer time-sharing, this article develops a buffer management strategy that reduces the decoder idle time to a negligible level and, therefore, improves the erasure probability of a sequential decoder. For a decoder with speed advantage of 10 and buffer size of 10 blocks, operating at an erasure rate of 10^{-2}, use of the new buffer management strategy reduces the erasure rate to less than 10^{-4}.

LAYMAN, W. E.

L07 Development and Testing of the Beryllium Propulsion Support Structure for the Mariner Mars 1971 Spacecraft

J. H. Stevens and W. E. Layman

Technical Memorandum 33-517, January 1, 1972

For abstract, see Stevens, J. H.

LIKINS, P. W.

L08 Finite Element Appendage Equations for Hybrid Coordinate Dynamic Analysis

P. W. Likins

Technical Report 32-1525, October 15, 1971

The increasingly common practice of idealizing a spacecraft as a collection of interconnected rigid bodies to some of which are attached linearly elastic flexible appendages leads to equations of motion expressed in terms of a combination of: (1) discrete coordinates describing the arbitrary rotational motions of the rigid bodies, and (2) distributed or modal coordinates describing the small, time-varying deformations of the appendages; such a formulation is said to employ a *hybrid* system of coordinates. In this report, the existing literature is extended to provide hybrid coordinate equations of motion for a finite element model of a flexible appendage attached to a rigid base undergoing unrestricted motions, and some of the advantages of the finite element approach are noted. Transformations to the modal coordinates appropriate for the general case and various special cases are provided.

L09 Flexible Spacecraft Control System Design Procedures Utilizing Hybrid Coordinates

P. W. Likins, E. L. Marsh, and G. E. Fleischer

Technical Memorandum 33-493, September 15, 1971

Procedures for the practical implementation of the hybrid coordinate methods of dynamic analysis of flexible spacecraft in application to vehicles of realistic complexity are briefly documented, with supporting examples.

LINNES, K. W.

L10 DSN Progress Report for July–August 1971: Radio Science Support

K. W. Linnes

Technical Report 32-1526, Vol. V, pp. 42–44,
October 15, 1971

Since 1967 radio scientists have used the DSN 26- and 64-m antenna stations to investigate pulsars, to study the effects of solar corona on radio signals, and to observe radio emissions of X-ray sources. More recently, very long baseline interferometry (VLBI) techniques have been used for high resolution studies of quasars. During the reporting period, several proposals were received for extension of VLBI observations which had reported the startling expansion of quasar 3C279.

L11 DSN Progress Report for September–October 1971: Radio Science Support

K. W. Linnes

Technical Report 32-1526, Vol. VI, pp. 43–45,
December 15, 1971

Since 1967, radio scientists have used the DSN 26- and 64-m antenna stations to investigate pulsars, to study the effects of solar corona on radio signals, and to observe radio emissions from X-ray sources. More recently, very-long-baseline interferometry (VLBI) techniques have been used for high-resolution studies of quasars. During the reporting period, VLBI observations were made in support of investigations of quasars and the application of VLBI techniques to Earth physics problems. Support was also provided for preliminary investigation of the mapping of spiral galaxies.

L12 **DSN Progress Report for July–August 1971: Sequential Tests for Exponential Distributions**

G. Lorden (California Institute of Technology)

Technical Report 32-1526, Vol. V, pp. 82–90,
October 15, 1971

The problem is to test whether the frequency of random events (e.g., DSIF equipment failures) is at a nominally prescribed value. When the actual frequency is higher, a determination of this fact is to be made as quickly as possible. A test based on sequential maximum likelihood ratio methods is developed and approximations of its performance characteristics are derived. Results of Monte Carlo sampling demonstrate that these approximations are accurate and that high statistical efficiency is attained over a broad range of possible higher frequencies. Some applications to reliability and inventory policies for the DSIF are indicated.

MacDONALD, G. J. F.

M01 **Preliminary Results of Laser Ranging to a Reflector on the Lunar Surface**

J. D. Mulholland, C. O. Alley (University of Maryland),
P. L. Bender (Joint Institute for Laboratory Astrophysics),
D. G. Currie (University of Maryland),
R. H. Dicke (Princeton University), J. E. Faller (Wesleyan University), W. M. Kaula (University of California, Los Angeles), G. J. F. MacDonald (University of California, Santa Barbara), H. H. Plotkin (Goddard Space Flight Center), and D. T. Wilkinson (Princeton University)

Space Research XI, pp. 97–104, Akademie-Verlag, Berlin, 1971

For abstract, see Mulholland, J. D.

MacDORAN, P. F.

M02 **DSN Progress Report for July–August 1971: The Goldstone Interferometer for Earth Physics**

J. L. Fanselow, P. F. MacDoran, J. B. Thomas,
J. G. Williams, C. Finnie, T. Sato, L. Skjerve (Philco-Ford Corporation), and D. Spitzmesser

Technical Report 32-1526, Vol. V, pp. 45–57,
October 15, 1971

For abstract, see Fanselow, J. L.

McCARTY, D.

M03 DSN Progress Report for September–October 1971: Overseas 64-m RMS Program for SDS 920

D. McCarty and M. S. Katow

Technical Report 32-1526, Vol. VI, pp. 158–164,
December 15, 1971

With the completion of the 64-m antennas overseas and their performance testing, an important test measurement required is the reflector distortion RMS from gravity loading. In order to provide the paraboloid best-fitting capability for the available SDS 920 computers at overseas sites, the RMS program was modified to suit the typewriter-and-two-tape-units input–output capabilities of the computers. The program computes the RMS after paraboloid best fit from field angle readings using typed inputs. The constant data, such as coordinates of targets, are supplied in a data tape with the binary program supplied in a second tape.

McCLURE, J. P.

M04 DSN Progress Report for September–October 1971: GCF 50-kbps Wideband Data Error Rate Test

J. P. McClure

Technical Report 32-1526, Vol. VI, pp. 149–157,
December 15, 1971

During June 1971, a 7-day wideband data error test was conducted between the Space Flight Operations Facility communications terminal and the NASCOM Madrid Switch Center. The test, which was run at 50 kbits/s, was conducted to determine both long-term and short-term error data for a wideband circuit comparable to those expected to be used to support the Mariner Venus–Mercury 1973 Project. Long-term end-to-end error rates of 6×10^{-5} or better were measured in both directions. The hourly and 5-min error distributions indicate that the errors are grouped into bursts (as expected). Most of the time the error rate is substantially less than average.

McGINNESS, H.

M05 DSN Progress Report for September–October 1971: Movement of the Antenna Instrument Tower at DSS 14

H. McGinness

Technical Report 32-1526, Vol. VI, pp. 142–146, December 15, 1971

The motions of the top of the instrument tower and its surrounding windshield have been measured. A relationship between a static horizontal displacement and an angular displacement of the tower have been established through the use of optical apparatus. Displacements during excitation of the windshield have been determined by the use of accelerometers. The nature of the coupling between the windshield and tower is discussed. The conclusion reached is that the coupling is primarily an acoustical one.

McLYMAN, W. T.

M06 Magnetic Materials Selection for Static Inverter and Converter Transformers

W. T. McLyman

Technical Memorandum 33-498, November 1, 1971

A program was conducted to study magnetic materials for use in spacecraft transformers used in static inverters, converters, and transformer–rectifier supplies. A comparative investigation of different magnetic alloys best suited for high-frequency and high-efficiency applications was conducted, together with an investigation of each alloy's inherent characteristics. The trade names and magnetic alloys of the materials evaluated were: Orthonol: 50% Ni, 50% Fe; Sq. Permalloy: 79% Ni, 17% Fe, 4% Mo; 48 alloy: 48% Ni, 52% Fe; Supermalloy: 78% Ni, 17% Fe, 5% Mo; and Magnesil: 3% Si, 97% Fe.

One characteristic of magnetic materials that is detrimental in transformer design is the residual flux density, which can be additive on turn-on and cause the transformer to saturate. Investigation of this problem led to the design of a transformer with a very low residual flux. Tests were performed to determine the dc and ac magnetic properties at 2400 Hz using square-wave excitation. These tests were performed on uncut cores, which were then cut for comparison of the gapped and ungapped magnetic properties. When the data of many transformers in many configurations were compiled, the optimum transformer was found to be that with the lowest residual flux and a small amount of air gap in the magnetic

material. The data obtained from these tests are described, and the potential uses for the materials are discussed.

MACIE, T. W.

M07 Solar Electric Propulsion System Technology

T. D. Masek and T. W. Macie

Technical Memorandum 33-510, November 15, 1971

For abstract, see Masek, T. D.

MARGOLIS, J. S.

M08 Recomputation of the Absorption Strengths of the Methane $3\nu_3$ J-Manifolds at 9050 cm^{-1}

J. T. Bergstralh (McDonald Observatory) and J. S. Margolis

J. Quant. Spectrosc. Radiat. Transfer, Vol. 11, No. 8, pp. 1285–1287, August 1971

For abstract, see Bergstralh, J. T.

MARSH, E. L.

M09 Flexible Spacecraft Control System Design Procedures Utilizing Hybrid Coordinates

P. W. Likins, E. L. Marsh, and G. E. Fleischer

Technical Memorandum 33-493, September 15, 1971

For abstract, see Likins, P. W.

MARSH, J. B.

M10 Farthest South Soil Microbial and Ecological Investigations

R. E. Cameron, G. H. Lacy, F. A. Morelli, and J. B. Marsh (University of California, Davis)

Antarctic J. U.S., Vol. VI, No. 4, pp. 105–106, July–August 1971

For abstract, see Cameron, R. E.

MARTONCHIK, J. V.

M11 Absorption by Venus in the 3–4-Micron Region

R. Beer, R. H. Norton, and J. V. Martonchik (University of Texas)

Astrophys. J., Vol. 168, No. 3, Pt. 2, pp. L121–L124, September 15, 1971

For abstract, see Beer, R.

M12 Astronomical Infrared Spectroscopy With a Connes-Type Interferometer: II. Mars, 2500–3500 cm^{-1}

R. Beer, R. H. Norton, and J. V. Martonchik (University of Texas)

Icarus: Int. J. Sol. Sys., Vol. 15, No. 1, pp. 1–10, August 1971

For abstract, see Beer, R.

MASEK, T. D.

M13 Solar Electric Propulsion System Technology

T. D. Masek and T. W. Macie

Technical Memorandum 33-510, November 15, 1971

As the number of possible applications for primary solar-powered electric propulsion grows, the burden of demonstrating this technology grows in proportion. The solar electric propulsion system technology (SEPST) program at JPL is focusing on such a demonstration. This memorandum reports the progress of the present JPL hardware program (SEPST III) and discusses certain propulsion-system–spacecraft interaction problems being investigated.

The basic solar electric propulsion system concept and elements are reviewed. Hardware is discussed only briefly, relying on detailed fabrication or assembly descriptions reported elsewhere. Emphasis is placed on recent performance data, which are presented to show the relationship between spacecraft requirements and present technology.

MATHUR, F. P.

M14 Reliability Estimation Procedures and CARE: The Computer-Aided Reliability Estimation Program

F. P. Mathur

JPL Quarterly Technical Review, Vol. 1, No. 3, pp. 17–26, October 1971

Ultrareliable fault-tolerant onboard digital systems for spacecraft intended for long mission life exploration of the outer planets are under development. The design of systems involving self-repair and fault-tolerance leads to the companion problem of quantifying and evaluating the survival probability of the system for the mission under consideration and the constraints imposed upon the system. Methods have been developed to (1) model self-repair and fault-tolerant organizations; (2) compute survival probability, mean life, and many other reliability predictive functions with respect to various systems and mission parameters; (3) perform sensitivity analysis of the system with respect to mission parameters; and (4) quantitatively compare competitive fault-tolerant systems—various measures of comparison are offered. To automate the procedures of reliability mathematical modeling and evaluation, the CARE (computer-aided reliability estimation) program was developed. CARE is an interactive program residing on the UNIVAC 1108 system, which makes the above calculations and facilitates report preparation by providing output in tabular form and graphical 2-dimensional plots and 3-dimensional projections. The reliability estimation of fault-tolerant organization by means of the CARE program is described in this article.

MAZZEO, A. A.

M15 Long-Term Aging of Elastomers: Chemical Stress Relaxation of Fluorosilicone Rubber and Other Studies

S. H. Kalfayan, A. A. Mazzeo, and R. H. Silver

JPL Quarterly Technical Review, Vol. 1, No. 3, pp. 38–47, October 1971

For abstract, see Kalfayan, S. H.

MILLER, L. F.

M16 DSN Progress Report for July–August 1971: Comparison of Faraday Rotation Measurements of the Ionosphere

L. F. Miller and B. D. Mulhall

Technical Report 32-1526, Vol. V, pp. 58–65, October 15, 1971

An evaluation of the mapping techniques employed to provide ionospheric charged particle calibration for post-flight analysis and for Mariner Mars 1971 tracking system analytical calibration oper-

ations was performed. Comparisons based on Faraday rotation data from geostationary satellites were made between various satellites as recorded at the Venus Deep Space Station and by Stanford Center for radar astronomy.

MORELLI, F. A.

M17 Farthest South Soil Microbial and Ecological Investigations

R. E. Cameron, G. H. Lacy, F. A. Morelli, and J. B. Marsh (University of California, Davis)

Antarctic J. U.S., Vol. VI, No. 4, pp. 105–106, July–August 1971

For abstract, see Cameron, R. E.

MOYNIHAN, P. I.

M18 TOPS Attitude Propulsion Subsystem Technology

P. I. Moynihan

JPL Quarterly Technical Review, Vol. 1, No. 3, pp. 48–56, October 1971

This article summarizes the JPL Thermoelectric Outer-Planet Spacecraft (TOPS) Attitude Propulsion Subsystem effort through the end of fiscal year 1971. It includes the tradeoff rationale that went into the selection of anhydrous hydrazine as the propellant, followed by a brief description of three types of 0.445-N (100-mlbf) thrusters that were purchased for in-house evaluation. A discussion is also included of the 0.2224-N (50-mlbf) JPL-developed thrusters and their integration with a portable, completely enclosed, propulsion module that was designed and developed to support the TOPS single-axis attitude control tests in the JPL Celestarium. The article concludes with a synopsis of further work which will be accomplished prior to the onset of an outer-planet mission.

MUDGWAY, D. J.

M19 DSN Progress Report for September–October 1971: Viking Mission Support

D. J. Mudgway

Technical Report 32-1526, Vol. VI, pp. 37–42,
December 15, 1971

The Tracking and Data System Functional Specification and the NASA Support Plan have been completed for the Viking Project. A complex scheduling problem, created by the Viking Project request for mission design verification tests in late 1974 and early 1975, has been solved by reworking early agreements on responsibility for software development.

The Viking Project poses the problem of simultaneous multiple RF links to the DSN for the first time. Consequently, it has been necessary to introduce multiple-link requirements into the current DSN techniques for single-link RF compatibility testing. The effect of these new requirements, with particular reference to Viking, is discussed in this article.

MULHALL, B. D.

M20 DSN Progress Report for July–August 1971: Comparison of Faraday Rotation Measurements of the Ionosphere

L. F. Miller and B. D. Mulhall

Technical Report 32-1526, Vol. V, pp. 58–65,
October 15, 1971

For abstract, see Miller, L. F.

MULHOLLAND, J. D.

M21 Preliminary Results of Laser Ranging to a Reflector on the Lunar Surface

J. D. Mulholland, C. O. Alley (University of Maryland), P. L. Bender (Joint Institute for Laboratory Astrophysics), D. G. Currie (University of Maryland), R. H. Dicke (Princeton University), J. E. Faller (Wesleyan University), W. M. Kaula (University of California, Los Angeles), G. J. F. MacDonald (University of California, Santa Barbara), H. H. Plotkin (Goddard Space Flight Center), and D. T. Wilkinson (Princeton University)

Space Research XI, pp. 97–104, Akademie-Verlag, Berlin, 1971

The first Lunar Ranging Experiment (LURE) retroreflector array was placed on the lunar surface during the Apollo 11 mission. Prior to this event, a special high-precision lunar ephemeris (designated LE 16) was developed by means of a composite numeric/analytic process, so as to provide more accurate predictions for use at the

telescope. First returns were observed at the Lick Observatory on August 1, 1969 and at the McDonald Observatory shortly thereafter. The observing program is to continue for several years. Preliminary use of these data consists of their comparison with the LE 16 ephemeris, preparatory to a differential correction of the lunar elements. Present indications are that the ephemeris must undergo order-of-magnitude improvements before the full power of the laser data can be utilized. Other parameters in the predictive process are also capable of being corrected; an improvement in the coordinates of the Lick Observatory 120-in. telescope is already indicated.

NASH, D. B.

N01 Lunar Fines and Terrestrial Rock Powders: Relative Surface Areas and Heats of Adsorption

F. P. Fanale, D. B. Nash, and W. A. Cannon

J. Geophys. Res., Vol. 76, No. 26, pp. 6459–6461, September 10, 1971

For abstract, see Fanale, F. P.

NEUGEBAUER, M.

N02 Computation of Solar Wind Parameters From the OGO-5 Plasma Spectrometer Data Using Hermite Polynomials

M. Neugebauer

Technical Memorandum 33-519, December 15, 1971

This memorandum presents the method used to calculate the velocity, temperature, and density of the solar wind plasma from spectra obtained by attitude-stabilized plasma detectors on the Earth satellite Orbiting Geophysical Observatory 5 (OGO-5). The method, which uses expansions in terms of Hermite polynomials, is very inexpensive to implement on an electronic computer compared to the least-squares and other iterative methods often used for similar problems in the past.

NOGUCHI, H.

N03 Electrical Properties of 7,7′,8,8′-Tetracyanoquinodimethane Salts of Ionene Polymers and Their Model Compounds

V. Hadek, H. Noguchi, and A. Rembaum

Macromolecules, Vol. 4, No. 4, pp. 494–499, July–August 1971

For abstract, see Hadek, V.

NORTON, R. H.

N04 Absorption by Venus in the 3–4-Micron Region

R. Beer, R. H. Norton, and J. V. Martonchik (University of Texas)

Astrophys. J., Vol. 168, No. 3, Pt. 2, pp. L121–L124, September 15, 1971

For abstract, see Beer, R.

N05 Astronomical Infrared Spectroscopy With a Connes-Type Interferometer: II. Mars, 2500–3500 cm^{-1}

R. Beer, R. H. Norton, and J. V. Martonchik (University of Texas)

Icarus: Int. J. Sol. Sys., Vol. 15, No. 1, pp. 1–10, August 1971

For abstract, see Beer, R.

ODLYZKO, A. M.

001 DSN Progress Report for September–October 1971: Data Storage and Data Compression

A. M. Odlyzko

Technical Report 32-1526, Vol. VI, pp. 112–117, December 15, 1971

In this article, a sharp upper bound on the best possible data rate achievable is computed as a function of data storage capability in certain very general situations. The result shows that a dramatic increase in rate can be caused by a small increase in storage capability.

ONDRASIK, V. J.

002 DSN Progress Report for September–October 1971: The Repetition of Seasonal Variations in the Tropospheric Zenith Range Effect

K. L. Thuleen and V. J. Ondrasik

Technical Report 32-1526, Vol. VI, pp. 83–98,
December 15, 1971

For abstract, see Thuleen, K. L.

003 Analysis of Mariner VII Pre-encounter Anomaly

H. J. Gordon, S. K. Wong, and V. J. Ondrasik

J. Spacecraft Rockets, Vol. 8, No. 9, pp. 931–937,
September 1971

For abstract, see Gordon, H. J.

OTOSHI, T. Y.

004 DSN Progress Report for July–August 1971: Antenna Noise Temperature Contributions Due to Ohmic and Leakage Losses of the DSS 14 64-m Antenna Reflector Surface

T. Y. Otoshi

Technical Report 32-1526, Vol. V, pp. 115–119,
October 15, 1971

This article presents approximate formulas useful for computing antenna noise temperature contributions due to ohmic and leakage losses of a parabolic antenna reflector surface. The total noise temperature contributions due to ohmic and leakage losses for the DSS 14 64-m antenna were calculated to be 0.1, 0.3, and 0.6 K at 2.295, 8.448, and 15.3 GHz, respectively.

005 DSN Progress Report for September–October 1971: Further Studies of Microwave Transmission Through Perforated Flat Plates

T. Y. Otoshi and K. Woo

Technical Report 32-1526, Vol. VI, pp. 125–129,
December 15, 1971

This article presents approximate formulas useful for predicting transmission loss characteristics of a circular hole array in a metallic flat plate having finite thickness. The formulas apply to perpendicular and parallel polarizations of an obliquely incident plane wave. The approximate formulas are experimentally verified by free space measurements made on a sample of the mesh material used on the 64-m antenna at the Mars Deep Space Station.

PHEN, R. L.

P01 Application of Hybrid Propulsion Systems to Planetary Missions

J. P. Don and R. L. Phen

Technical Memorandum 33-483, November 1, 1971

For abstract, see Don, J. P.

PLOTKIN, H. H.

P02 Preliminary Results of Laser Ranging to a Reflector on the Lunar Surface

J. D. Mulholland, C. O. Alley (University of Maryland), P. L. Bender (Joint Institute for Laboratory Astrophysics), D. G. Currie (University of Maryland), R. H. Dicke (Princeton University), J. E. Faller (Wesleyan University), W. M. Kaula (University of California, Los Angeles), G. J. F. MacDonald (University of California, Santa Barbara), H. H. Plotkin (Goddard Space Flight Center), and D. T. Wilkinson (Princeton University)

Space Research XI, pp. 97–104, Akademie-Verlag, Berlin, 1971

For abstract, see Mulholland, J. D.

POULSON, P.

P03 Computer Program for the Automated Attendance Accounting System

P. Poulson and C. Rasmusson

JPL Quarterly Technical Review, Vol. 1, No. 3, pp. 27–32, October 1971

The Automated Attendance Accounting System (AAAS) was developed under the auspices of the Space Technology Applications Office at JPL. The task is basically the adaptation of a small digital computer, coupled with specially developed pushbutton terminals located in school classrooms and offices for the purpose of taking daily attendance, maintaining complete attendance records, and producing partial and summary reports. Especially intended for high schools, the system will relieve both teachers and office personnel from the time-consuming and dreary task of recording and analyzing the myriad classroom attendance data collected throughout the semester. In addition, since many school district budgets are related to student attendance, the increase in account-

ing accuracy is expected to augment district income. A major component of this system is the real-time AAAS software system, which is described in this article.

PRICE, T. W.

P04 Long-Duration Firings of a Mariner Mars 1969 Catalytic Reactor

T. W. Price

JPL Quarterly Technical Review, Vol. 1, No. 3, pp. 57–66, October 1971

Two long-duration tests were conducted with a surplus Mariner Mars 1969 monopropellant hydrazine reactor in an attempt to induce the "washout" phenomenon. The Mariner Mars 1969 reactor was chosen because it has a long development history and thus is well characterized. No "washout" occurred during either of the two 1000-s tests, although slow transients were observed in the reactor operation during what were nominally steady-state conditions. The 2000 s of operating time represents nearly an order of magnitude increase over the rated life of the engine.

QUINN, R.

QC DSN Progress Report for July–August 1971: Tracking and Data Acquisition Elements Research: Low Noise Receivers: Microwave Maser Development

R. C. Clauss and R. Quinn

Technical Report 32-1526, Vol. V, pp. 102–108, October 15, 1971

For abstract, see Clauss, R. C.

RASMUSSON, C.

R01 Computer Program for the Automated Attendance Accounting System

P. Poulson and C. Rasmusson

JPL Quarterly Technical Review, Vol. 1, No. 3, pp. 27–32, October 1971

For abstract, see Poulson, P.

REID, M. S.

R02 DSN Progress Report for September–October 1971: Improved RF Calibration Techniques: System Operating Noise Temperature Calibrations

M. S. Reid

Technical Report 32-1526, Vol. VI, pp. 130–138, December 15, 1971

The system operating noise temperatures of the S-band research operational cone at the Venus Deep Space Station and the polarization diversity S-band cone at the Mars Deep Space Station are reported for the period June 1, 1971 through September 30, 1971. In addition, the performance of the multi-frequency X- and K-band (MXK) cone on the ground at the Venus Deep Space Station is reported for X-band operation, as well as for X-band operation on the 64-m antenna at the Mars Deep Space Station for the same period. Also presented are system operating noise temperature calibrations of the K-band system in the following configurations: before installation in the MXK cone (approximately 23 K), installed in the cone, with the cone on the ground (approximately 25 K), and with the cone installed on the 64-m antenna at the Mars Deep Space Station (approximately 29 K).

REILLY, H. F., JR.

R03 DSN Progress Report for September–October 1971: Microwave Maser Development

R. C. Clauss and H. F. Reilly, Jr.

Technical Report 32-1526, Vol. VI, pp. 118–122, December 15, 1971

For abstract, see Clauss, R. C.

REMBAUM, A.

R04 Onset of Superconductivity in Sodium and Potassium Intercalated Molybdenum Disulphide

R. B. Somoano and A. Rembaum

JPL Quarterly Technical Review, Vol. 1, No. 3, pp. 33–37, October 1971

For abstract, see Somoano, R. B.

R05 **Electrical Conductivity of Elastomeric TCNQ Complexes Under Mechanical Stress**

A. M. Hermann (Tulane University), S. P. S. Yen, A. Rembaum, and R. F. Landel

J. Polym. Sci., Pt. B: Polym. Lett., Vol. 9, No. 8, pp. 627–633, August 1971

For abstract, see Hermann, A. M.

R06 **Electrical Properties of 7,7′,8,8′-Tetracyanoquinodimethane Salts of Ionene Polymers and Their Model Compounds**

V. Hadek, H. Noguchi, and A. Rembaum

Macromolecules, Vol. 4, No. 4, pp. 494–499, July–August 1971

For abstract, see Hadek, V.

R07 **Superconductivity in Intercalated Molybdenum Disulfide**

R. B. Somoano and A. Rembaum

Phys. Rev. Lett., Vol. 27, No. 7, pp. 402–404, August 16, 1971

For abstract, see Somoano, R. B.

RENZETTI, N. A.

R08 **DSN Progress Report for July–August 1971: DSN Functions and Facilities**

N. A. Renzetti

Technical Report 32-1526, Vol. V, pp. 1–3, October 15, 1971

The DSN, established by the NASA Office of Tracking and Data Acquisition and under the system management and technical direction of JPL, is designed for two-way communications with unmanned spacecraft traveling approximately 16,000 km (10,000 mi) from earth to planetary distances. The objectives, functions, and organization of the DSN are summarized, and its three facilities—the Deep Space Instrumentation Facility, the Ground Communications Facility, and the Space Flight Operations Facility—are described.

R09 **DSN Progress Report for September–October 1971: DSN Functions and Facilities**

N. A. Renzetti

Technical Report 32-1526, Vol. VI, pp. 1–4,
December 15, 1971

The DSN, established by the NASA Office of Tracking and Data Acquisition and under the system management and technical direction of JPL, is designed for two-way communications with unmanned spacecraft traveling approximately 16,000 km (10,000 mi) from Earth to planetary distances. The objectives, functions, and organization of the DSN are summarized, and its three facilities—the Deep Space Instrumentation Facility, the Ground Communications Facility, and the Space Flight Operations Facility—are described.

REY, R. D.

R10 DSN Progress Report for September–October 1971: Angle Tracking Analysis and Test Development

R. D. Rey

Technical Report 32-1526, Vol. VI, pp. 170–187,
December 15, 1971

The angle tracking systems are currently being analyzed, and tests are being developed to measure their performance. This article presents the progress made on the analysis and testing of the standard 26-m-diam antenna station automatic angle tracking system. The model is discussed, and certain important system constants are developed. Simulation runs of the model were performed, and comparisons are made with preliminary tests performed at the Echo Deep Space Station. The article also outlines the design of the test and software processing.

RHO, J. H.

R11 Grating Anomalies in Porphyrin Spectra

J. H. Rho

Geochim. Cosmochim. Acta, Vol. 35, No. 7, pp. 743–747,
July 1971

Experimental evidence is presented to show that porphyrin spectra are modified by grating anomalies to such an extent that interpretation is difficult. The anomalies appear in a definite wavelength region which depends on the optical properties of individual grating monochromators, and are associated with polarization effects. The presence of light-scattering material in the samples of any fluorescent compounds may induce the formation of grating anomalies in their fluorescence spectra. The anomalies may easily be mistaken for porphyrin peaks, especially in samples which

contain light-scattering material such as those from geological sources.

RINDERLE, E. A.

R12 DSN Progress Report for July–August 1971: A Comparison of Cowell's Method and a Variation-of-Parameters Method for the Computation of Precision Satellite Orbits

S. S. Dallas and E. A. Rinderle

Technical Report 32-1526, Vol. V, pp. 74–78, October 15, 1971

For abstract, see Dallas, S. S.

RODRIGUEZ, C. F.

R13 Simulation of Mariner Mars 1971 Spacecraft

N. E. Ausman, Jr., N. K. Simon, and C. F. Rodriguez

JPL Quarterly Technical Review, Vol. 1, No. 3, pp. 67–78, October 1971

For abstract, see Ausman, N. E., Jr.

ROUKLOVE, P.

R14 Parametric Testing of an Externally Configured Thermionic Converter

K. Shimada and P. Rouklove

Technical Memorandum 33-504, November 1, 1971

For abstract, see Shimada, K.

ROURKE, K. H.

R15 Guidance and Navigation for Solar Electric Interplanetary Missions

K. H. Rourke and J. F. Jordan

J. Spacecraft Rockets, Vol. 8, No. 9, pp. 920–926, September 1971

This article makes a practical analysis of closed-loop guidance of a solar electrically thrusted interplanetary spacecraft. A first-order guidance algorithm is used that allows easy interpretation yet rigorous treatment of trajectory terminal constraints. Interplane-

tary orbit determination is assumed to be provided by Earth-based radio (doppler) tracking. Guidance and orbit determination are evaluated with respect to given trajectories and then combined to yield information on the encounter accuracies and guidance cost—in terms of additional power consumption, control deviations, and payload penalty—expected from given injection and thruster performance dispersions. The results are presented in terms of two representative cases: a Jupiter flyby/orbiter mission and a comet rendezvous mission in the late 1970s.

SATO, T.

S01 DSN Progress Report for July–August 1971: The Goldstone Interferometer for Earth Physics

J. L. Fanselow, P. F. MacDoran, J. B. Thomas, J. G. Williams, C. Finnie, T. Sato, L. Skjerve (Philco-Ford Corporation), and D. Spitzmesser

Technical Report 32-1526, Vol. V, pp. 45–57, October 15, 1971

For abstract, see Fanselow, J. L.

SAVAGE, J. E.

S02 DSN Progress Report for July–August 1971: Combinational Complexity Measures as a Function of Fan-Out

D. Johnson, J. E. Savage (Brown University), and L. R. Welch (University of Southern California)

Technical Report 32-1526, Vol. V, pp. 79–81, October 15, 1971

For abstract, see Johnson, D.

S03 DSN Progress Report for July–August 1971: Contributions to a Mathematical Theory of Complexity

L. Harper (University of California, Riverside) and J. E. Savage (Brown University)

Technical Report 32-1526, Vol. V, pp. 91–98, October 15, 1971

For abstract, see Harper, L.

S04 **DSN Progress Report for July–August 1971: Some Results on the Matrix Multiplication Problem**

L. Harper (University of California, Riverside) and
J. E. Savage (Brown University)

Technical Report 32-1526, Vol. V, pp. 99–101,
October 15, 1971

For abstract, see Harper, L.

SAWYER, C. D.

S05 **DEXTER—A One-Dimensional Code for Calculating Thermionic Performance of Long Converters**

C. D. Sawyer

Technical Report 32-1545, November 15, 1971

This report describes a versatile code for computing the coupled thermionic electric–thermal performance of long thermionic converters in which the temperature and voltage variations cannot be neglected. The code is capable of accounting for a variety of external electrical connection schemes, coolant flow paths, and converter failures by partial shorting. Sample problem solutions are included, along with a user's manual.

SCHORN, R. A. J.

S06 **Comments on "The Venus Spectrum: New Evidence for Ice"**

R. A. J. Schorn and L. D. G. Young

Icarus: Int. J. Sol. Sys., Vol. 15. No. 1, pp. 103–109,
August 1971

In a recent article in *Icarus*, Plummer has attempted to show that high-altitude infrared spectra obtained by Kuiper's group exhibit evidence for ice-crystal clouds on Venus. He also asserts that these data are consistent with ground-based spectroscopic work which indicates ~100 ppt μm of water vapor "above the clouds" of Venus. Such an interpretation of the high-altitude spectra is not required by the data and, in fact, raises more problems than it answers. The bulk of ground-based observations indicate an H_2O abundance of much less than 100 ppt μm.

In this article, no conclusions are made about the composition of the clouds of Venus. It is merely pointed out that the airborne and ground-based spectra offer no convincing evidence for an ice-cloud composition.

SHIMADA, K.

S07 Parametric Testing of an Externally Configured Thermionic Converter

K. Shimada and P. Rouklove

Technical Memorandum 33-504, November 1, 1971

As described in this memorandum, a 25.4-cm-long externally configured converter was performance-tested at JPL by electrically heating the emitter to simulate reactor thermal power input. The measured maximum output power was limited by the maximum input power available from the electric RF induction heater. With maximum heater input power, the converter electric output was 178 W (1.95 W/cm^2) at an emitter temperature of 1946 K. This electric output power was smaller than expected. The power output during acceptance testing at the contractor's site was 5 W/cm^2 at a 2000-K emitter temperature. The converter withstood 46 controlled shutdowns and 13 abrupt shutdowns without shorting and without loss of cesium.

A reactor-core-length (25.4-cm-long) cylindrical thermionic converter could be used as a full-length thermionic fuel element. Obtaining high output power and maintaining the emitter-to-collector gap without shorting are of major importance to the feasibility of a 25.4-cm-long reactor fuel element. The emitter of the converter is located externally to the collector to increase the fuel-volume fraction and to allow redundant collector cooling in a reactor configuration.

S08 Measurements of Plasma Parameters in a Simulated Thermionic Converter

K. Shimada

JPL Quarterly Technical Review, Vol. 1, No. 3, pp. 97–109, October 1971

Cesium-filled thermionic energy converters are being considered as candidate electrical energy sources in future spacecraft requiring tens to hundreds of kilowatts of electrical power. The high operating temperatures necessary for a large specific power and high efficiency inevitably impose stringent constraints on the converter fabrication to achieve the desired reliability of the power system. The converter physics for reducing operating temperatures and cesium plasma losses are being studied to achieve high reliability without sacrificing the power performance of the converters. Various cesium parameters which affect the converter performance are: (1) electron temperatures, (2) plasma ion densities, and (3) electric potential profiles. These were investigated using a Lang-

muir probe in a simulated converter. The parameters were measured in different cesium discharge modes.

SHIRLEY, D. L.

S09 An Approach to Automated Drug Identification

D. L. Shirley

J. Forensic Sci., Vol. 16, No. 3, pp. 359–375, July 1971

The process of selecting one approach to the automation of drug screening tests is outlined. A systems analysis was performed which determined the requirements of forensic science laboratories for an automated drug identification system, and these requirements were compared with a set of model systems. A system that matched the most representative set of requirements was refined by the selection of more detailed approaches. An approach selected for initial hardware development and critical technology testing involved: (1) wet chemical sample preparation; (2) gas chromatographic separation, presumptive identification, and quantitation of drugs; (3) infrared spectrophotometric identification of drugs; and (4) computer control and data analysis.

SIEGMETH, A. J.

S10 DSN Progress Report for July–August 1971: Pioneer Mission Support

A. J. Siegmeth

Technical Report 32-1526, Vol. V, pp. 4–16,
October 15, 1971

A description of the planned configuration and data flow methodology of the Mark III Deep Space Network System is given. This system will support the Pioneer F and G missions and the successive projects of the NASA mission set of the 1970s. Block diagrams graphically illustrate the planned functions of the DSN Telemetry, Tracking, and Command Systems including their capabilities of being compatible with the forthcoming project requirements. The basic interfaces between subsystems of the three DSN facilities are defined.

S11 DSN Progress Report for September–October 1971: Pioneer Mission Support

A. J. Siegmeth

Technical Report 32-1526, Vol. VI, pp. 13–24,
December 15, 1971

The DSN plans to use the Mark III system configuration for tracking and data acquisition support of the Pioneer F and G missions. As a continuation of the description of the network systems, the configurations of the Simulation, Monitoring, and Operations Control Systems are given. Block diagrams show the planned functions, data flow methodology, and interfaces between the subsystems and the three DSN facilities.

SILVER, R. H.

S12 Long-Term Aging of Elastomers: Chemical Stress Relaxation of Fluorosilicone Rubber and Other Studies

S. H. Kalfayan, A. A. Mazzeo, and R. H. Silver

JPL Quarterly Technical Review, Vol. 1, No. 3, pp. 38–47,
October 1971

For abstract, see Kalfayan, S. H.

SIMON, N. K.

S13 Simulation of Mariner Mars 1971 Spacecraft

N. E. Ausman, Jr., N. K. Simon, and C. F. Rodriguez

JPL Quarterly Technical Review, Vol. 1, No. 3, pp. 67–78,
October 1971

For abstract, see Ausman, N. E., Jr.

SKJERVE, L.

S14 DSN Progress Report for July–August 1971: The Goldstone Interferometer for Earth Physics

J. L. Fanselow, P. F. MacDoran, J. B. Thomas,
J. G. Williams, C. Finnie, T. Sato, L. Skjerve (Philco-Ford Corporation), and D. Spitzmesser

Technical Report 32-1526, Vol. V, pp. 45–57,
October 15, 1971

For abstract, see Fanselow, J. L.

SOMOANO, R. B.

S15 Onset of Superconductivity in Sodium and Potassium Intercalated Molybdenum Disulphide

R. B. Somoano and A. Rembaum

JPL Quarterly Technical Review, Vol. 1, No. 3, pp. 33–37, October 1971

Molybdenum disulfide in the form of natural crystals or powder has been intercalated at −65 to −70°C with sodium and potassium using the liquid ammonia technique. All intercalated samples were found to show a superconducting transition. A plot of the percent of diamagnetic throw versus temperature indicates the possible existence of two phases in the potassium intercalated molybdenum disulfide. The onset of superconductivity in potassium and sodium intercalated molybdenite powder was found to be ≅6.2 and ≅4.5 K, respectively. The observed superconductivity is believed to be due to an increase in electron density as a result of intercalation.

S16 Superconductivity in Intercalated Molybdenum Disulfide

R. B. Somoano and A. Rembaum

Phys. Rev. Lett., Vol. 27, No. 7, pp. 402–404, August 16, 1971

In an attempt to investigate superconductors which are two-dimensional in nature, molybdenum disulfide has been intercalated with sodium and potassium. Both natural crystals of molybdenite and synthetic crystals were used, and measurements made on the intercalated products indicate a superconducting transition temperature of ~1.3°K for sodium and ~4.5°K for potassium.

SPITZMESSER, D.

S17 DSN Progress Report for July–August 1971: The Goldstone Interferometer for Earth Physics

J. L. Fanselow, P. F. MacDoran, J. B. Thomas, J. G. Williams, C. Finnie, T. Sato, L. Skjerve (Philco-Ford Corporation), and D. Spitzmesser

Technical Report 32-1526, Vol. V, pp. 45–57, October 15, 1971

For abstract, see Fanselow, J. L.

STEVENS, J. H.

S18 Development and Testing of the Beryllium Propulsion Support Structure for the Mariner Mars 1971 Spacecraft

J. H. Stevens and W. E. Layman

Technical Memorandum 33-517, January 1, 1972

In November 1971, the Mariner 9 spacecraft will be injected into Martian orbit by a 574-kg (1265-lbm) propulsion system. Support for that system is provided by an 8.9-kg (19.5-lbm) truss assembly consisting of beryllium tubes adhesively bonded to magnesium end fittings. Beryllium was selected for the tubular struts in the truss because of its exceptionally high stiffness-to-weight ratio. Adhesive bonding, rather than riveting, was utilized to join the struts to the end fittings because of the low toughness (high notch sensitivity) of beryllium. Magnesium, used in the end fittings, resulted in a 50% weight savings over aluminum, since geometric factors in the fitting design resulted in low stress areas where magnesium's lower density was a benefit. This memorandum describes the design, development, testing, and fabrication procedures and problems associated with the development of the Mariner 9 propulsion support truss structure.

STRAND, L. D.

S19 Low-Acceleration Solid-Propellant Rocket Ignition Study

L. D. Strand

Technical Memorandum 33-506, December 1, 1971

A study was conducted to develop a solid-propellant rocket igniter system that would build up thrust at a controlled rate of less than 0.2 g/s. The system consisted of a long-burning, regressive-burning, controlled-flow igniter and an inhibited progressive-burning surface in the main rocket motor. The igniter performed the dual role of igniting, under vacuum back-pressure and low L^* conditions, the nonrestricted portion of the propellant and providing the mass addition necessary to sustain combustion until the propellant burning area had increased sufficiently to provide a stable motor-chamber pressure. Two series of tests were conducted with existing small test motor hardware to: (1) demonstrate the feasibility of the concept, (2) determine the important parameters governing the system, and (3) obtain design guidelines for future scaled-up motor tests. A quasi-steady-state mass balance for the ignition system was written and programmed for use as a motor design tool.

S20 **Quenching of Solid-Propellant Rockets by Water Injection**

L. D. Strand and W. Gerber (Lockheed Aircraft Service Co.)

J. Spacecraft Rockets, Vol. 8, No. 9, pp. 992–996, September 1971

In other programs, command termination of solid-propellant motors by water quench has been demonstrated in motors having propellant weights up to 8600 kg. However, most attempts to correlate extinguishment data have given questionable results. Three mechanisms have been proposed: (1) rapid cooling of gases causes a dP/dt sufficient for extinction; the water then wets the surface, cooling it to prevent reignition; (2) cooling of the gases below some threshold value lowers heat feedback to the propellant below that necessary for self-supported combustion; and (3) a water film covers the entire surface of the propellant, cooling it below the temperature required for burning.

The study described in this article was initiated to improve understanding of the quench mechanism and to determine the optimum method of water injection. The slab-burning window motor used is capable of accepting several different types of water injectors: head-end injectors, multiple injectors impinging normal to the propellant surface, and sheet injectors which lay a thin sheet of water onto the propellant surface. The spray form varied from a fine mist to a solid stream. High-speed movies were taken during water injection and quenching.

THOMAS, J. B.

T01 **DSN Progress Report for July–August 1971: The Goldstone Interferometer for Earth Physics**

J. L. Fanselow, P. F. MacDoran, J. B. Thomas, J. G. Williams, C. Finnie, T. Sato, L. Skjerve (Philco-Ford Corporation), and D. Spitzmesser

Technical Report 32-1526, Vol. V, pp. 45–57, October 15, 1971

For abstract, see Fanselow, J. L.

THORMAN, H. C.

T02 **DSN Progress Report for September–October 1971: DSN Simulation System**

H. C. Thorman

Technical Report 32-1526, Vol. VI, pp. 5–9,
December 15, 1971

The DSN Simulation System provides real-time insertion of simulated Tracking, Telemetry, Command, Monitor, and Operations Control Systems data into the DSN. Data flows originating from the system are used extensively in testing and training activities to prepare the DSN and its users for coverage of planned missions. This article describes the upgrading of the Simulation System that was accomplished to provide support of DSN development, testing, and training activities in 1970 and 1971.

THULEEN, K. L.

T03 DSN Progress Report for September–October 1971: The Repetition of Seasonal Variations in the Tropospheric Zenith Range Effect

K. L. Thuleen and V. J. Ondrasik

Technical Report 32-1526, Vol. VI, pp. 83–98,
December 15, 1971

Using radiosonde balloon data taken from sites close to the DSN tracking stations, the tropospheric zenith range effect $\Delta\rho_z$ has been computed throughout 1967 and 1968. The behavior of $\Delta\rho_z$ has definite seasonal trends that are similar in both years. With the modification of the tropospheric model, which is used to calibrate radio tracking data to include these seasonal trends, the navigational errors, produced by inaccuracies in representing the zenith range effect, may possibly be reduced by as much as 40%.

TRAJMAR, S.

T04 Differential and Integral Cross Sections for the Electron-Impact Excitation of the $a^1\Delta_g$ and $b^1\Sigma_g^+$ States of O_2

S. Trajmar, D. C. Cartwright (The Aerospace Corporation), and W. Williams

Phys. Rev., Pt. A: Gen. Phys., Vol. 4, No. 4, pp. 1482–1492, October 1971

Electron-impact energy-loss spectra of O_2 have been analyzed for incident electron energies from 4 to 45 eV, scattering angles from 10 to 90 deg, and energy losses from 0 to 5 eV. The inelastic processes observed were the excitation of the $a^1\Delta_g$ and $b^1\Sigma_g^+$ electronic states and vibrational excitation in some cases to $v'' = 13$. The excitation cross sections at each energy were made absolute by normalizing the sum of the integral cross sections (all

inelastic, ionization, and elastic) to measured electron-O_2 total cross sections. The differential cross sections for the $a^1\Delta_g$ and $b^1\Sigma_g^+$ states show nearly isotropic behavior, as expected for optically spin-forbidden transitions. The elastic differential cross sections are strongly forward peaked at higher energies, but become only slightly forward peaked at the lower energies. The integral cross sections for the excitation of the $a^1\Delta_g$ and $b^1\Sigma_g^+$ states reach their maxima near 7 eV and are more than an order of magnitude larger than previous estimates. The integral elastic cross section reaches its maximum at around 10 eV.

TUSTIN, D. G.

T05 DSN Progress Report for September–October 1971: Network Allocation Schedules

D. G. Tustin

Technical Report 32-1526, Vol. VI, pp. 168–169, December 15, 1971

This article reviews the reasons and needs for the Network Allocation Schedules and briefly describes the make-up of these schedules and how they are used. The major emphasis is placed on the implementation of these schedules, including new special-purpose software. This software makes use of an existing file management program and IBM 360 utility programs.

VON ROOS, O. H.

V01 DSN Progress Report for September–October 1971: Analysis of Dual-Frequency Calibration for Spacecraft VLBI

O. H. von Roos

Technical Report 32-1526, Vol. VI, pp. 46–56, December 15, 1971

In this article, a feasibility study is undertaken and a detailed analysis is made of a wide-band very-long-baseline interferometer (VLBI) for the purpose of ranging and tracking a spacecraft. The system works on two frequencies (S- and X-band). By a new correlation technique, it is shown that it is possible to extract information on the total electron content with a rather high degree of accuracy, an accuracy certainly impossible to achieve with tracking modes currently in use. The total electron content and its time variation are valuable quantities on their own; they give important information on the solar wind. It is also shown that, at the same time, the declination and right ascension of a spacecraft

can potentially be determined much more accurately than by existing procedures.

V02 DSN Progress Report for September–October 1971: Tropospheric and Ionospheric Range Corrections for an Arbitrary Inhomogeneous Atmosphere (First Order Theory)

O. H. von Roos

Technical Report 32-1526, Vol. VI, pp. 99–105, December 15, 1971

In this article, a simple and concise expression is presented for the range correction for an atmosphere that possesses arbitrary radial, lateral, and azimuthal gradients of the index of refraction. The validity of this expression hinges only on the assumption that the index of refraction is close to unity, an assumption that is well-satisfied for the Earth's atmosphere. Furthermore, it is shown that the range corrections for a simple model of the Earth's troposphere, including typical lateral variations, are in close agreement with existing computer solutions.

WAHLQUIST, H. D.

W01 Hamiltonian Cosmology

F. B. Estabrook and H. D. Wahlquist

Phys. Lett., Vol. 35A, No. 6, pp. 453–454, July 12, 1971

For abstract, see Estabrook, F. B.

WELCH, L. R.

W02 DSN Progress Report for July–August 1971: Combinational Complexity Measures as a Function of Fan-Out

D. Johnson, J. E. Savage (Brown University), and L. R. Welch (University of Southern California)

Technical Report 32-1526, Vol. V, pp. 79–81, October 15, 1971

For abstract, see Johnson, D.

WIEBE, E.

W03 DSN Progress Report for July–August 1971: Superconducting Magnet for a Ku-Band Maser

R. Berwin, E. Wiebe, and P. Dachel

Technical Report 32-1526, Vol. V, pp. 109–114,
October 15, 1971

For abstract, see Berwin, R.

WILKINSON, D. T.

W04 Preliminary Results of Laser Ranging to a Reflector on the Lunar Surface

J. D. Mulholland, C. O. Alley (University of Maryland), P. L. Bender (Joint Institute for Laboratory Astrophysics), D. G. Currie (University of Maryland), R. H. Dicke (Princeton University), J. E. Faller (Wesleyan University), W. M. Kaula (University of California, Los Angeles), G. J. F. MacDonald (University of California, Santa Barbara), H. H. Plotkin (Goddard Space Flight Center), and D. T. Wilkinson (Princeton University)

Space Research XI, pp. 97–104, Akademie-Verlag, Berlin, 1971

For abstract, see Mulholland, J. D.

WILLIAMS, J. G.

W05 DSN Progress Report for July–August 1971: The Goldstone Interferometer for Earth Physics

J. L. Fanselow, P. F. MacDoran, J. B. Thomas, J. G. Williams, C. Finnie, T. Sato, L. Skjerve (Philco-Ford Corporation), and D. Spitzmesser

Technical Report 32-1526, Vol. V, pp. 45–57,
October 15. 1971

For abstract, see Fanselow, J. L.

WILLIAMS, W.

W06 Differential and Integral Cross Sections for the Electron-Impact Excitation of the $a^1\Delta_g$ and $b^1\Sigma_g^+$ States of O_2

S. Trajmar, D. C. Cartwright (The Aerospace Corporation), and W. Williams

Phys. Rev., Pt. A: Gen. Phys., Vol. 4, No. 4, pp. 1482–1492, October 1971

For abstract, see Trajmar, S.

WINKELSTEIN, R.

W07 Minicomputer-Controlled Programmed Oscillator

R. Winkelstein

JPL Quarterly Technical Review, Vol. 1, No. 3, pp. 79–87, October 1971

The programmed oscillator is a telecommunications receiver or transmitter subsystem which compensates for the known doppler frequency effect produced by the relative motion between a spacecraft and a tracking station. Two such programmed oscillators have been constructed, each using a low-cost minicomputer for the calculation and control functions, and each contained in a single rack of equipment. They are capable of operation in a phase-tracking mode as well as a frequency-tracking mode. When given an ephemeris suitable for the planet Venus, these units maintained phase coherence of better than 5 deg rms at 2388 MHz.

WONG, S. K.

W08 Analysis of Mariner VII Pre-encounter Anomaly

H. J. Gordon, S. K. Wong, and V. J. Ondrasik

J. Spacecraft Rockets, Vol. 8, No. 9, pp. 931–937, September 1971

For abstract, see Gordon, H. J.

WOO, K.

W09 DSN Progress Report for September–October 1971: Further Studies of Microwave Transmission Through Perforated Flat Plates

T. Y. Otoshi and K. Woo

Technical Report 32-1526, Vol. VI, pp. 125–129, December 15, 1971

For abstract, see Otoshi, T. Y.

WOO, R.

W10 A Multiple-Beam Spherical Reflector Antenna

R. Woo

JPL Quarterly Technical Review, Vol. 1, No. 3, pp. 88–96, October 1971

A spherical reflector with multiple feeds is an attractive possibility for application in future communications satellite systems. Data are presented which show that spherical reflectors possessing relatively high gain (40 dB) and very small phase path error ($<\lambda/32$) are feasible. A design of a spherical reflector utilizing corrugated horn feeds is considered. Radiation patterns are computed using the physical-optics technique. The designed antenna is approximately 60λ in diameter. Calculations performed for this antenna with three beams indicate that each beam has a gain of about 42 dB, a beamwidth of 1.4 deg, and sidelobes that can be expected to be at least 28 dB down. These results indicate that the feature of low sidelobes makes the spherical reflector a promising candidate for a multiple-beam communications satellite antenna.

YANG, J.-N.

Y01 Maximum Dynamic Response and Proof Testing

J.-N. Yang and E. Heer (NASA Headquarters)

J. Eng. Mech. Div., Proc. ASCE, Vol. 97, No. EM4, pp. 1307–1313, August 1971

Recent flight data show that the major spacecraft excitations during any one flight are not only highly transient, but are associated with considerable statistical variation from one flight to another. However, the flight data are usually insufficient for the statistical characterization of random excitation inputs, so other means of characterization are being attempted. In the time-domain analysis presented in this article, an approach is taken that yields an upper bound of the maximum dynamic response as well as a dynamic proof-testing excitation that, in turn, will produce the expected upper bound of the maximum response. Although a structure with a single input is considered in this article, extension of the technique to a structure with multi-excitations appears to be possible.

YASUI, R. K.

Y02 Effects of Storage Temperatures on Silicon Solar Cell Contacts

P. A. Berman and R. K. Yasui

Technical Report 32-1541, October 15, 1971

For abstract, see Berman, P. A.

Y03 **Supporting Data Package for TR 32-1541, Effects of Storage Temperatures on Silicon Solar Cell Contacts**

P. A. Berman and R. K. Yasui

Technical Memorandum 33-497, October 15, 1971

For abstract, see Berman, P. A.

YEN, S. P. S.

Y04 **Electrical Conductivity of Elastomeric TCNQ Complexes Under Mechanical Stress**

A. M. Hermann (Tulane University), S. P. S. Yen, A. Rembaum, and R. F. Landel

J. Polym. Sci., Pt. B: Polym. Lett., Vol. 9, No. 8, pp. 627–633, August 1971

For abstract, see Hermann, A. M.

YOUNG, A. T.

Y05 **Interpretation of Interplanetary Scintillations**

A. T. Young

Astrophys. J., Vol. 168, No. 3, Pt. 1, pp. 543–562, September 15, 1971

In this article, radio observations of interplanetary scintillations are interpreted by means of a theory previously used for the detailed interpretation of optical observations of atmospheric scintillations. The theory allows a number of restrictive assumptions to be removed, and thus gives a more realistic picture of the interplanetary medium and a more accurate representation of the observations. Observers are requested to report power spectra of the *logarithm* of the intensity, to avoid artifacts due to "spikes."

YOUNG, L. D. G.

Y06 **Comments on "The Venus Spectrum: New Evidence for Ice"**

R. A. J. Schorn and L. D. G. Young

Icarus: Int. J. Sol. Sys., Vol. 15, No. 1, pp. 103–109, August 1971

For abstract, see Schorn, R. A. J.

Y07 Calculation of the Partition Function for $^{14}N_2{}^{16}O$

L. D. G. Young

J. Quant. Spectrosc. Radiat. Transfer, Vol. 11, No. 8, pp. 1265–1270, August 1971

In calculating the transmission of the Earth's atmosphere in the infrared, it is necessary to include the effects of such minor atmospheric constituents as H_2O, CO_2, CH_4, N_2O, CO, and O_3. Before the line intensities for a given band can be accurately calculated, the partition function must be known. The most common isotope of nitrous oxide, $^{14}N_2{}^{16}O$, has been the subject of many high-resolution laboratory studies, and the best values of the molecular constants for this isotope have been tabulated elsewhere. In this article, internal and vibrational partition functions are tabulated for $^{14}N_2{}^{16}O$ for the temperature range 200–350°K at 10°K intervals. Rotational partition functions are also computed for the five lowest vibrational states.

ZANDELL, C.

Z01 DSN Progress Report for July–August 1971: CPS Sustaining Engineering

C. Zandell

Technical Report 32-1526, Vol. V, pp. 129–131, October 15, 1971

The Sustaining Engineer Program for the Central Processing System (CPS) of the Mark IIIA Space Flight Operations Facility is based on optimizing flight support capabilities. This is being achieved by testing hardware responses during simulated critical conditions, by supporting software development, and by monitoring system performance. This article defines the major hardware/software problem areas and reports the results of studies made to resolve these problem areas.

Subject Index

Subject Categories

Subjects

Publication Index

Technical Reports

DSN Progress Reports for July–October 1971 (Technical Report 32-1526, Vols. V and VI)

Technical Memorandums

Open Literature Reporting

NASA — JPL — Coml., L.A., Calif.